Université Nice Sophia Antipolis - UFR Sciences

Ecole Doctorale de Sciences Fondamentales et Appliquées

THESIS

pour obtenir le titre de

Docteur en Sciences

de l'Université Nice Sophia Antipolis

Discipline : Sciences de la Planète et de l'Univers

présentée et soutenue par

Álvaro ROJAS-ARRIAGADA

Study of the Galactic bulge with the Gaia-ESO Survey

Thèse dirigée par Alejandra Recio-Blanco & Patrick de Laverny

soutenue le 9 Septembre 2016

Jury :

Mme.	Françoise Combes	Astronome	Rapporteur
M.	Gerard Gilmore	Professeur	Rapporteur
Mme.	Francesca Matteucci	Professeur	Examinatrice
Mme.	Paola Di Matteo	Astronome adjointe	Examinatrice
Mme.	Livia Origlia	Professeur	Examinatrice
Mme.	Alejandra Recio-Blanco	Astronome adjointe	Directrice de thèse
M.	Patrick de Laverny	Astronome	Directeur de thèse

Study of the Galactic bulge with the Gaia-ESO survey

Abstract :

The chemical abundance and kinematic patterns of long-lived low mass stars represent an open book for reading the history and physical mechanisms involved in the formation and chemodynamical evolution of the different stellar populations assembling the present-day Milky Way. The Galactic bulge, being a massive structural component of the Galaxy, is crucial in our observational quest to understand galaxy evolution as a whole. Paradoxically, as observational evidence steadily accumulates, the nature of the Galactic bulge has proven to be rather complex, with structural, kinematic and chemical properties leading to conclusions often contradictory.

In this thesis, we made use of data coming from the Gaia-ESO survey (GES) to conduct a detailed study on the properties of the bulge, as well as of the thin and thick disks. The goal is to provide a state-of-the-art observational characterization of the bulge in the context of other Galactic components, placing it in the framework of the most recent formation models.

Concerning the disk system, we confirm that, given a good quality dataset, a gap/dip feature in the abundance-metallicity plane allows to separate stars into low-α and high-α sequences standing for the thin and thick disks. From a comparative analysis of their spatial, chemical and kinematic distributions we found, in agreement with recent studies, that metal-poor thin disk stars with [Fe/H] < -0.25 dex might have been formed and evolved in parallel and/or dissociated from the inside-out formation taking place in the inner thin disk.

We then studied a steadily increasing dataset of bulge red clump stars (~ 1200 and ~ 2500 stars from the first and fourth internal data releases of GES, respectively) in eleven bulge fields sampling the area $-10^\circ \leq l \leq +10^\circ$ and $-10^\circ \leq b \leq -4^\circ$. The bulge metallicity distribution function is found to be bimodal across the whole sampled area, with a narrow metal-rich ($\langle$[Fe/H]$\rangle \approx +0.2$ dex) and a broader metal-poor ($\langle$[Fe/H]$\rangle \approx -0.4$ dex) component whose relative size changes as a function of the latitude, determining a negative vertical metallicity gradient. The metal-rich population exhibits bar-like kinematics, displays the double RC feature and overlaps the metal-rich end of the thin disk sequence in the [Mg/Fe] vs. [Fe/H] plane. We associate these stars with the bar boxy/peanut bulge formed as the product of secular evolution of the early thin disk. On the other hand, the metal-poor population presents isotropic hot kinematics and does not participate in the X-shaped bulge. When compared to the thick disk, bulge stars seem to mimic their distribution in the [Mg/Fe] vs. [Fe/H] plane. When comparing the metallicity position of the so called "knee", that of the bulge is found to be at [Fe/H] $= -0.37 \pm 0.09$ dex, being 0.6 dex higher than that of the thick disk. A chemical evolution model suitably fits the whole bulge sequence by assuming a fast (< 1 Gyr) intense burst of star formation taking place at early epochs. The origin of the metal-poor bulge still remains unconstrained, but further research should allow to distinguish between violent processes or secular evolution for its origin.

Keywords: Milky Way, chemical abundances, Galaxy formation, Galactic archaeology. Galaxy: bulge, thin disk, thick disk.

Contents

1 Introduction **1**

1.1 A brief history of the Milky Way . . . 2
1.2 A cosmological interlude . . . 6
1.3 An overview of the main Galactic components . . . 7
1.3.1 The thin disk . . . 8
1.3.2 The thick disk . . . 8
1.3.3 The halo . . . 9
1.3.4 The bulge . . . 9
1.4 Galactic archaeology . . . 10
1.4.1 Chemical abundances . . . 11
1.4.2 Chemical evolution and the time-delay model . . . 11
1.5 The bulge . . . 14
1.5.1 Formation models . . . 14
1.5.2 Metallicity distribution function . . . 17
1.5.3 Structure and kinematics . . . 20
1.5.4 Chemical enrichment levels . . . 23
1.5.5 Age . . . 26
1.6 The nature of the disk system in the context of bulge formation . . . 30
1.7 The Gaia mission . . . 34
1.7.1 Layout and observation principles . . . 35
1.7.2 On-board instrumentation . . . 35
1.7.3 Gaia scientific yields . . . 37
1.8 The Gaia-ESO Survey . . . 38
1.9 Other current and future Galactic surveys . . . 40
1.9.1 APOGEE . . . 41
1.9.2 LAMOST . . . 41
1.9.3 GALAH . . . 42
1.9.4 WEAVE . . . 42
1.9.5 4MOST . . . 43
1.9.6 MOONS . . . 43
1.9.7 VVV . . . 43
1.10 Goal of this thesis . . . 44
1.11 Works published during the course of this thesis . . . 45

2 The Gaia-ESO Survey disk and bulge dataset **47**

2.1 The Gaia-ESO survey selection function for disk and bulge fields . . . 48
2.1.1 Milky Way disk/halo field target selection . . . 49
2.1.2 Bulge target selection . . . 50
2.2 Spectroscopic data, adopted setups and general quality . . . 52
2.3 Determination of fundamental parameters . . . 54

2.4 Measurement of elemental abundances . . . 56
2.4.1 Available node results . . . 57
2.4.2 A comparison between HR10|HR21 vs. HR21 abundance measurements . . . 58
2.4.3 Reference abundance scale . . . 58
2.4.4 Combined abundances in HR10|HR21 and HR21 into the benchmark scale . . . 61
2.4.5 Final calibrated combined abundances . . . 61
2.5 Summary . . . 64

3 Analysis tools 67
3.1 Distance determinations . . . 68
3.1.1 The code . . . 69
3.1.2 Tests with models . . . 72
3.1.3 Tests with Hipparcos data . . . 74
3.1.4 Tests with clusters . . . 77
3.1.5 Distances for the Gaia-ESO Survey targets . . . 79
3.2 Gaussian Mixture Models and other ways to disentangle substructure in the abundance-metallicity plane . . . 79
3.2.1 Gaussian Mixture Models . . . 80
3.2.2 Separating disk sequences in the abundance-metallicity plane . . . 83
3.3 Summary . . . 84

4 The Galactic disk system: disentangling disk sequences and chemical substructures 87
4.1 Data samples . . . 88
4.1.1 Gaia-ESO survey sample . . . 88
4.1.2 APOGEE sample . . . 89
4.2 Distribution of disk stars in the metallicity-abundance plane . . . 91
4.3 GMM decompositions of GES and APOGEE samples . . . 92
4.3.1 GES working sample . . . 93
4.3.2 GMM results for different stellar luminosity classes . . . 95
4.3.3 Comparison with APOGEE-RC data . . . 98
4.4 The metal-poor thin disk . . . 100
4.4.1 Definition of a robust-membership subsample . . . 101
4.4.2 Vertical distribution of disk stars . . . 102
4.4.3 Galactic rotational velocity of disk stars . . . 105
4.5 Implications for disk formation models . . . 107
4.6 Summary and conclusions . . . 110

5 The richness of diversity: Unveiling the composite nature of the Galactic bulge 113
5.1 Data sample . . . 114
5.1.1 Selected bulge fields . . . 114
5.1.2 Fundamental parameters . . . 115

5.1.3 Distances and reddenings . . . 118
5.2 Metallicity distribution function . . . 119
5.2.1 Samples in Baade's window . . . 120
5.2.2 Bimodality of the bulge MDF . . . 120
5.2.3 MDF variations with spatial location . . . 123
5.2.4 Double RC in magnitude distributions . . . 124
5.2.5 Metal-poor stars . . . 125
5.3 Trends in the [Mg/Fe] vs. [Fe/H] plane . . . 127
5.3.1 The metal-poor bulge knee . . . 129
5.4 Kinematics of chemically defined components . . . 129
5.4.1 Bulge rotation curve . . . 130
5.4.2 Kinematics at the peaks of the double RC . . . 131
5.4.3 Velocity dispersion . . . 132
5.4.4 Interpretation of metal-rich stars kinematics . . . 134
5.4.5 Interpretation of metal-poor stars kinematics . . . 134
5.5 Summary . . . 134

6 The bulge stellar populations and formation as seen by the GES 137
6.1 How many bulge components? . . . 138
6.2 The bulge MDF in the literature . . . 139
6.3 Metallicity gradients in perspective . . . 141
6.4 Beyond a metallicity characterization: the origin of bulge populations . . . 141
6.4.1 The metal-rich bulge . . . 142
6.4.2 The metal-poor bulge . . . 142
6.5 A dissipative collapse origin of the bulge? . . . 143
6.5.1 Interpretation of bulge chemical patterns from a chemical evolution model . . . 143
6.6 A secular origin of the bulge? . . . 145
6.6.1 Chemical similarities between the thick disk and the bulge . . . 145
6.7 Summary . . . 152

7 General conclusions, perspectives and future work 155
7.1 General summary and conclusions . . . 155
7.2 Towards solving the puzzle of bulge formation . . . 157
7.3 Future work prospects . . . 160

A Comparison of iDR1 and iDR4 fundamental parameters 165

B The bulge comparison sample 169

C Mathematical bits 171
C.1 Covariance Matrix . . . 171
C.2 Bivariate normal distribution . . . 173
C.3 Anderson-Darling test . . . 174
C.4 p-values . . . 174
C.5 Student t-test . . . 174

Bibliography 177

List of Figures

1.1 The first map of the Milky Way: William Herschel's model of the Galaxy 5
1.2 Schematic view of the main structural components of the Milky Way . . 8
1.3 Sketch of the evolution of [α/Fe] as a function of [Fe/H] 13
1.4 Examples of different kinds of bulges 15
1.5 Early bulge's MDF determinations 17
1.6 [Zoccali *et al.* 2008] MDFs in three fields along the bulge's minor axis . . 18
1.7 Bulge's photometric mean metallicity map of [Gonzalez *et al.* 2013] . . . 19
1.8 MDFs constructed by [Ness *et al.* 2013a] from strips of field at latitudes $b = -5, -7.5$ and -10 20
1.9 Annotated longitude-velocity (lv diagram of the CO (1-0) emission of [Dame *et al.* 2001]) 21
1.10 COBE/DIRBE contour maps of the bulge region in three different bands 22
1.11 Bulge RC count density maps of [Wegg & Gerhard 2013] 23
1.12 Bulge rotation and velocity dispersion curves from the ARGOS survey . 24
1.13 Bulge and disk(s) sequences in the abundance-metallicity plane 25
1.14 Bulge globular clusters compared with bulge field giants 26
1.15 [Zoccali *et al.* 2003] CMD comparison between bulge field stars and the halo globular cluster NGC 6528 27
1.16 CMD of proper motion selected bulge stars from [Clarkson *et al.* 2008] . 28
1.17 Age vs. metallicity for the microlensed dwarf sample of [Bensby *et al.* 2013] 30
1.18 Discovering the thick disk: Spatial density distribution vs. distance from the Galactic plane 31
1.19 Toomre diagram for a disk stellar sample classified with a kinematic criteria 32
1.20 Solar neighborhood FGK dwarf stars in the [α/Fe] vs. [Fe/H] plane. A black dotted line depict the chemical division into thin and thick disk populations adopted by [Adibekyan *et al.* 2013]. Figure reproduced from [Adibekyan *et al.* 2013]. 33
1.21 Configuration of Gaia instruments and scanning law 35
1.22 Gaia's end-of-mission pattern of transits from the nominal scanning law 36
1.23 Gaia-ESO survey schematic working flow diagram 40
1.24 Bulge and disk area sampled by the VVV survey 44

2.1 Distribution of GES disk and bulge fields across the sky, as observed up to the fourth internal data release 48
2.2 Photometric selection function for Milky Way disk/halo field stars . . . 49
2.3 Photometric selection function for bulge stars 51
2.4 Examples of spectra obtained with the HR10 and HR21 setups 53
2.5 Signal-to-noise distribution of Milky Way disk/halo field and bulge spectra 54
2.6 Three spectra of bulge stars with SNR equal to the lowest, the mean and the highest of the sample 55

2.7 Comparison between HR10|HR21 and HR21-only abundance measurements for the SME-LUMBA node . . . 57
2.8 Comparison between HR10|HR21 and HR21-only abundance measurements for the ASM-Nice node . . . 58
2.9 Illustration of the procedure followed to determine the relation to transform ASM-Nice abundances into the SME-LUMBA scale in the HR10|HR21 setup combination . . . 59
2.10 Comparison between ASM-Nice and SME-LUMBA abundances from the HR10|HR21 setup . . . 62
2.11 Comparison between ASM-Nice and SME-LUMBA abundances from the HR21-only setup . . . 63
2.12 [X/Fe] vs [Fe/H] for the final abundances from the HR21 setup . . . 64
2.13 [X/Fe] vs [Fe/H] for the final abundances from the HR10|HR21 setup . . . 65
2.14 Comparison between HR10|HR21 and HR21-only final combined and calibrated abundances . . . 66

3.1 Characterization of isochrones as an ingredient for distance determinations 70
3.2 Distance and reddening estimates for a TRILEGAL synthetic catalog . . . 73
3.3 Comparison of spectro-photometric distances with respect to trigonometric values . . . 76
3.4 Spectro-photometric distances and reddenings computed for some GES open and globular clusters . . . 78
3.5 Calculated distances versus surface gravities for GES stars in disk and bulge fields . . . 80
3.6 Performance of a GMM classification on a sample simulating disk sequences in the abundance-metallicity plane . . . 83
3.7 Separation of simulated disk sequences on the abundance-metallicity plane by applying a k-means clustering algorithm in narrow metallicity bins . . . 85

4.1 GES iDR2 disk sample in the [Mg/Fe] vs. [Fe/H] plane . . . 90
4.2 HR diagram of the GES iDR2 disk working sample . . . 91
4.3 Density distribution of disk stars in the [Mg/Fe] vs. [Fe/H] plane . . . 92
4.4 GMM best model for the GES iDR2 disk data distribution in the [Mg/Fe] vs. [Fe/H] plane . . . 94
4.5 GMM decomposition of iDR2 GES disk stars of different luminosity classes 96
4.6 GMM decomposition of Gaia-ESO survey and APOGEE samples in the [α/M] vs. [M/H] plane . . . 99
4.7 Spatial distribution of GES iDR2 disk working sample . . . 101
4.8 Responsibilities from GMM components for stars in the [Mg/Fe] vs. [Fe/H] plane . . . 102
4.9 Vertical distribution of GES iDR2 disk stars as a function of [Fe/H] and [Mg/Fe] . . . 104
4.10 V_ϕ velocity distributions of the GMM groups . . . 105
4.11 Azimuthal velocity component V_ϕ as a function of the Galactocentric radius R_{GC} . . . 106

5.1 Finding chart for iDR1 and iDR4 bulge fields. 115
5.2 HR and CMD diagrams of the bulge sample. 116
5.3 Color distribution of GES bulge RC targets 118
5.4 Galactocentric radial distance distribution of GES bulge RC targets . . 119
5.5 MDF for comparison and GES samples at Baade's window 120
5.6 MDFs of the bulge sample in two latitude strips 121
5.7 Individual MDFs of the 11 bulge fields 122
5.8 Magnitude distribution of bulge RC stars 124
5.9 Location in the HR diagram of metal-poor bulge working sample stars . 126
5.10 Distribution of bulge stars in the [Mg/Fe] vs. [Fe/H] plane 128
5.11 Determination of the bulge "knee" position in the [Mg/Fe] vs. [Fe/H] plane 130
5.12 Bulge rotation curves from GES, GIBS and BRAVA samples 131
5.13 Velocity dispersion of metal-rich and metal-poor stars in bulge fields . . 133
5.14 Velocity dispersion distribution in the [Mg/Fe] vs. [Fe/H] plane 133
5.15 Velocity dispersion vs. metallicity profile for the metal-poor bulge 135

6.1 GMM decomposition of bulge MDFs taken from literature 140
6.2 Comparison between bulge data and the adopted CEM in the [Mg/Fe] vs. [Fe/H] plane 145
6.3 HR diagram of the selected sample of disk stars 146
6.4 Selected disk subsample in the [Mg/Fe] vs. [Fe/H] plane 147
6.5 Bulge sample compared with disk profiles 148
6.6 Spatial distribution of the bulge and disk samples in the $|Z_{GC}|$ vs. R_{GC} plane 149
6.7 Determination of the "knee" in the [Mg/Fe] vs. [Fe/H] plane for the thick disk 150

7.1 [La/Eu] vs. [Fe/H] distributions for several samples compiled from literature 157
7.2 161

A.1 Calibration of iDR1 parameters respect to the benchmark sample 166
A.2 HR diagram of stars present in iDR1 and iDR4 samples 167
A.3 Comparison of fundamental parameters of bulge stars from iDR1 and iDR4 167

B.1 Comparison of metallicity determinations from GES and literature for the bulge comparison sample 170

C.1 Bivariate distributions. From left to right: white noise of non correlated normal distributed data. Uncorrelated data with the dispersion in the x axis scaled by 2. Positive correlated data 173
C.2 Illustration of the p-value of an observed sample result. The vertical axis is the probability density of each possible outcome of the statistic test computed under the null hypothesis H_0. The $p-$value corresponds to the shaded area under the curve from the observed result towards more "extreme" results. 175

List of Tables

2.1 Zero points with respect to the benchmarks of the three HR21 setup analysis nodes . . . 57
2.2 Coefficients of the polynomials used to transform ASM-Nice abundances into the SME-LUMBA scale in the HR10|HR21 setup combination . . . 60
2.3 Coefficients of the polynomials used to transform ASM-Nice abundances into the SME-LUMBA scale, in the HR21-only setup . . . 60
2.4 Zero points of the SME-LUMBA scale relative to the benchmark scale . 61

4.1 Centroids and marginalized dispersions of the GMM modes for the different disk samples . . . 94
4.2 Slopes of the linear models fitted to the data in Fig. 4.5 . . . 97

5.1 Characteristics of the bulge fields . . . 117
5.2 Parameters of the best GMM model for each field where two components were found. MP and MR subscripts refer to the metal-poor and metal-rich Gaussian components, respectively. . . . 123
5.3 Galactocentric velocities of stars located in the bright and faint peaks of the metal-rich magnitude distribution in bulge fields displaying the double RC feature . . . 132

Chapter 1

Introduction

Contents

1.1 A brief history of the Milky Way . . . 2
1.2 A cosmological interlude . . . 6
1.3 An overview of the main Galactic components . . . 7
1.3.1 The thin disk . . . 8
1.3.2 The thick disk . . . 8
1.3.3 The halo . . . 9
1.3.4 The bulge . . . 9
1.4 Galactic archaeology . . . 10
1.4.1 Chemical abundances . . . 11
1.4.2 Chemical evolution and the time-delay model . . . 11
1.5 The bulge . . . 14
1.5.1 Formation models . . . 14
1.5.2 Metallicity distribution function . . . 17
1.5.3 Structure and kinematics . . . 20
1.5.4 Chemical enrichment levels . . . 23
1.5.5 Age . . . 26
1.6 The nature of the disk system in the context of bulge formation 30
1.7 The Gaia mission . . . 34
1.7.1 Layout and observation principles . . . 35
1.7.2 On-board instrumentation . . . 35
1.7.3 Gaia scientific yields . . . 37
1.8 The Gaia-ESO Survey . . . 38
1.9 Other current and future Galactic surveys . . . 40
1.9.1 APOGEE . . . 41
1.9.2 LAMOST . . . 41
1.9.3 GALAH . . . 42
1.9.4 WEAVE . . . 42
1.9.5 4MOST . . . 43
1.9.6 MOONS . . . 43
1.9.7 VVV . . . 43
1.10 Goal of this thesis . . . 44
1.11 Works published during the course of this thesis . . . 45

Abstract: In this chapter we introduce a number of general ideas and concepts relevant to the development of this thesis. After a general description of the main components of the Milky Way, and the ideas behind Galactic archaeology, the Galactic bulge is reviewed from the observational and theoretical points of view. The nature of the disk system is also reviewed in detail. In addition, a description of the Gaia mission, the Gaia-ESO survey, and other current and future Galactic surveys aiming to decode the nature, origin and chemodynamical evolution of the bulge and other Galactic components is provided. The chapter ends with a list of works published during the course of this thesis.

In a clear night in a dark place far from the lights of big cities, we can experience the astonishing natural spectacle offered by the Milky Way, the white diffuse band of light and dark clouds crossing the sky. This streak of light is the projected perspective, that from our particular vantage point, we have of our host galaxy. The understanding of its nature has a long and honorable history and it is tightly related to the development of astronomy in general. In fact, most of what we can see with the naked eye corresponds to objects, stars, dust, clusters and glowing gas that belongs to our Galaxy.

The present thesis was carried on thanks to the exquisite data set of stars from different Galactic components offered by the Gaia-ESO survey. Our primary focus is the Galactic bulge, its detailed study and comparison with respect to other Galactic components, in particular with the thick disk. This endeavor offers to us an invaluable opportunity to disentangle and understand the physical processes driving bulge formation and evolution, seeding our understanding on the Milky Way formation. In turn, since our Galaxy might be a normal representative of objects of its class, we hope at understanding galaxy formation in general.

In this chapter we present an introductory background to put the study conducted during this thesis in a general context. Subsequent chapters will deal with more technical details about the Gaia-ESO survey and the characteristics of our observational sample, to finally deal with the detailed analysis and interpretation. So, let's start with a bit of history.

1.1 A brief history of the Milky Way

The first ideas about the nature of the Milky Way go back to the magic/mythological conceptions envisaged by probably every single civilization since the dawn of history. The spectacular belt of diffuse white light, glowing patches and dark clouds has been the subject of many interpretations and projections of both worldly an magic symbolisms. It is the *silver river* for the Chinese, the *Nile in the sky* for the ancient Egyptians, the *way which has shadow* for Bengali people, the *merchants way* for Arabs, the *way of birds* as dubbed in Baltic countries, the *road to Santiago* in Spain, or the *Via Lactea* -literally, the Milky Way- as called by the Romans. Moreover, in between the pre-columbian civilizations of the New World, which had a particular privileged vantage point to the

Galactic bulge, the Milky Way was not unnoticed at all; *Willka Mayu*, the heavenly river for the Incas, *Wakah Chan*, the tree of the world, for the Mayan, and *Wenuleufu*, the river of above, for the Mapuches in the south of Chili.

Last but not least is to mention that the very word *Galaxy* comes from *galaktos*, the Greek word for milk, in reference to the myth according to which the Milky Way comes from spilled milk from the breast of Hera, feeding Heracles.

It is exciting to imagine all the cultural implications and magic/philosophical/mythical ways of thinking that the view of the Milky Way has inspired in people throughout history. But here, by the sake of concision, we made a time leap up to the 15th century.

The modern conception of the Milky Way starts with the first telescopic observations performed by Galileo in 1610. Up to this time, the glow of the Milky Way was interpreted as due to the concentration of some sort of celestial fluid. Galileo instead, demonstrated that actually the diffuse light comes from the unresolved contribution of a vast number of faint crowding stars. In this way, the status of the Milky Way as a stellar system was established once and forever.

The following leap in the development of ideas came mostly from the field of philosophical speculative conjectures, and refers to the ideas concerning to the whole universe. The Cartesian model of the universe, as exposed in the Descartes treatise *The world* (1636), consists in a system of rotating celestial bodies, in analogy to the bodies in the solar system. This rotation would be imprinted into the celestial bodies by the stream motions of the aether. Thomas Wright published in 1750 *An original theory or new hypothesis of the universe* in which the Sun was one more of many stars orbiting around the so called "divine center" of the universe. A matured version of theses ideas was presented by Immanuel Kant in his *The Universal Natural History and Theory of Heaven* of 1755. In this treatise, Kant expanded previous ideas by putting the structure of the stellar system in the context of other fuzzy patches of light observable in the sky, the so called nebulae. For Kant, who also presented a cosmogony devised to explain the origin of the solar system (the nebular hypothesis), the rotation of the solar system would be mimicked by the whole Galaxy, but in a much larger scale. The rotation of the stellar system would be necessary to compensate for the attractive gravitational pulling from the center. In turn, this general rotation would made the system to be naturally flat, which given our vantage point somewhere within it, would determine a projected view of the system as a band performing a great circle in the sky, just as observed. In addition, Kant pushes these ideas further by proposing the first fractal system of the Universe; according to him, the Galaxy is merely one of many "island universes", with the nebulae being the other systems. The absence of detectable relative motions in the sky of both, stars and the other island universes, would be explainable as a consequence of the extremely large distances involved.

All these philosophical disquisitions have the virtue of coming mainly from deep foresight rather than from interpretation of available data. Posterior observational validation will probe some of these ideas to be in fact qualitatively correct.

As observational techniques steadily improved, the possibilities of conducting detailed studies of both the distribution of stars and the cataloging of nebulae made progress. In between the firsts lists of nebulae is the one assembled by the French comet-hunter Charles Messier. His famous list of 103 objects was created as an effort

to identify bright patchy sources which could be confused with comets, separating in this way transient from permanent visually diffuse objects in the sky. A great increase in the number of cataloged sources is owed to the patient work of William Herschel. Equipped with a 20-foot reflector telescope working as a transit instrument -a large one for that epoch- and assisted by his sister Caroline and his son John, he observed and classified ~ 2500 nebulae in the sky reachable from their position at Slough, near London. The southern sky exploration was conducted later by John Herschel from a site in Cape of Good hope in South Africa. This heroic observational effort is the base from which John Dreyer assembled and published his *New General Catalog of Nebulae and Clusters of Stars* (NGC) of ~ 5000 objects in 1888. It was followed by a number of index catalogs expanding the number of entries to almost 15000 nebulous objects. In hindsight, we know that the objects listed in the NGC are a mixture of stars clusters, true gas nebulae, planetary nebulae and galaxies.

William Herschel himself was convinced that nebulae were the other island universes postulated by Kant. The fact of not being able to distinguish individual stars, as in the case of the Milky Way, was attributed by him just to the eventual large distances separating these objects from us. A flaw in this assumption came with the reconnaissance that some of these objects -the planetary nebulae- appear as a spherical shell of glowing gas at the center of which a single star could be detected. He assumed that these objects would be an exception, in the sense of being local portions of glowing incandescent gas. The definitive different nature of these objects was demonstrated with the spectroscopic observations of W. Huggins.

Another different open problem was the determination of the large scale distribution of stars in the Milky Way. Once again, we own one of the first important efforts to observationally define the spatial distribution of stars to W. Herschel. His star-gaging approach was based in a number of assumptions 1) all the stars have the same intrinsic luminosity, 2) the stars are uniformly distributed in the Galaxy, 3) all stars are observable out to the edges of the system, and 4) there is not any source of dimming of the star light (i.e. interstellar extinction). On this conceptual basis, he conducted a meticulous set of observations, counting the number of stars per magnitude interval in several directions of the sky. The product of this patient effort is his famous map of the Milky Way stellar distribution, which is reproduced in Fig. 1.1. In his view, the Galaxy is a flattened system with a diameter about five times larger than its thickness, and with the Sun close to its center. He could not determine absolute dimensions for the system given the unavailability of distance standards to calibrate his method.

Shortly after, Herschel become aware of few flaws in his model. He was aware of the fact that possibly the stars didn't have, as assumed, an intrinsic constant luminosity. A warning in this sense was raised by John Micell, who around that time developed some statistical methods to suggest that binary stars and star clusters could be physical associations rather than random associations. Taking this into account, the internal variations in apparent magnitude in these systems would translate into equal differences in their intrinsic values. Herschel eventually convinced himself about this by observations he conducted on binary systems. A second problem arose when he repeated star counts with a larger 40-foot telescope; in fact, the fainter he went, the more stars he counted. He ended eventually by loosing faith in his large scale star distribution model.

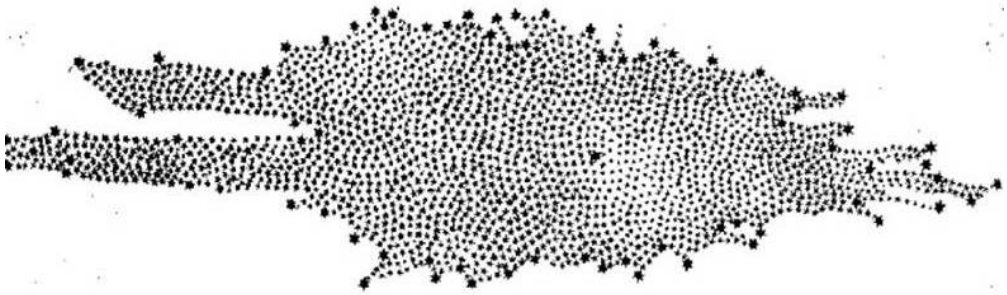


Figure 1.1: The first map of the Milky Way: William Herschel's model of the Galaxy (1785) based on star-gaging ([Herschel 1785]). The Sun is located close to the center of the disc of stars and depicted with a black point.

In the same vein, the XX century brought the final steps towards what we judge now as the correct description of the Galaxy. As the product of an international observational campaign, a new model of the distribution of stars in space was proposed by J. Kapteyn in 1922. This approach, rather similar to the star-gaging of Herschel, was performed under three assumptions: 1) the distribution of absolute magnitudes (i.e. luminosity function) of the stars is the same everywhere, 2) there is not a preferred motion direction in space, and 3) there is not absorption of starlight. After determining the (local) luminosity function and calibrated distances based in parallaxes, he produced a model in which the Milky Way consists on a flatten stellar system of 1500 pc thick and about 8 times this size in the plane, with the Sun slightly off from the center. Around the same time, H. Shapley devised a different approach to tackle this problem. Shapley noted that the globular clusters, up to this time classed as nebulae but with round shape and individual resolved stars, are well distributed in the sky, although with a concentration towards the constellation of Sagittarius where the brighter part of the Milky Way is also located. In this sense, Shapley judged that globular clusters should be a major structural component of the Milky Way, and in consequence symmetrically distributed around its center. He studied its distribution by computing their line-of-sight distances thanks to the recently period luminosity relation of RR Lyraes. What he found, is that the system was in fact approximately spherical, with the Sun at ~ 16 kpc off from its center. This lead Shapley to propose a model with a much larger scale than the Kapteyn one.

The issue of the structure of the Galaxy, together with that of the nature of the nebulae, gave origin to the so called "great debate" between Shapley and Curtis of 1920. The two issues where discussed, and at some point became interrelated. Shapley defended that the nebulae are a subsystem of the Galaxy because no stars were possible to be resolved in them (so, they were not stellar systems), they present lower surface brightness than the Galaxy and tend to be bluer than it. Additionally, Shapley gave credibility to the observations conducted by A. van Maanen, who claimed to have detected rotation in some nebulae. If these systems where far away, and with sizes similar to the Milky Way, then the detected rotation would imply a tangential velocity at heir edges larger than the speed of light.

With time, it was demonstrated that both positions were partially wrong; the interstellar extinction, the main source of discrepancies was observationally established just in 1923. On the other hand, E. Hubble detected cepheids in Andromeda, setting the scale of the universe at sizes never before speculated.

1.2 A cosmological interlude

The attempts to understand the large scale structure of the Universe continued all along the XXth century. What emerged from these efforts as a satisfactory model is the so called Big Bang cosmology. In order to account for the processes driving the formation of structures in the Universe, a parametrization of this model should be adopted. The currently most accepted paradigm is the lambda-cold-dark-matter (ΛCDM) cosmology, which is briefly introduced below.

A Gaussian field of quantum fluctuations accounts for the primordial density enhancements in the early Universe. These fluctuations were expanded to galaxy-sized scales during inflation, setting the conditions for the subsequent formation of structures. In principle, this process can take two different tracks. In the first one, the so called *top-down formation* scenario, galaxies can form as the product of the fragmentation of large structures composed by hot dark matter (HDM), i.e. dark matter which had relativistic internal velocities at the epoch of radiation-matter equality. In this scenario, low mass objects are the last structures to be formed in the Universe. In the second scenario, or *bottom-up formation* scenario, cold dark matter (CDM) condensates forming halos in a variety of mass scales when the matter era begins. Galaxies are subsequently formed from the assembling of these smaller components in a hierarchical sequence.

The ΛCDM is the standard model/parametrization of Big Bang cosmology. It explains the formation of structures as a bottom-up process in a Universe which contains a cosmological constant Λ, accounting the dark energy, plus cold dark matter. Dark energy is needed to explain the accelerated expansion of the Universe ([Perlmutter *et al.* 1999]) while cold dark matter is introduced to properly account for some observations at large scale, such as the flat rotation curve of galaxies, gravitational lensing and the enhanced clustering of galaxies, which are not fully explained by the gravitational effects of visible matter. The most recent determination of cosmological parameters for the ΛCDM model, from the Planck collaboration ([Planck Collaboration *et al.* 2015]), advocates for a flat geometry and an energy composition where dark energy is dominant: density parameters, $\Omega_\Lambda = 0.6911$, $\Omega_{\rm DM} = 0.2589$, $\Omega_b = 0.0486$, Hubble constant $h = 0.6774$, and Age $= 13.799$ Gyr.

In a ΛCDM cosmology context, small perturbations in the early Universe collapsed producing dark matter halos which accrete baryons. These virialized dark matter halos, with their respective baryonic content, aggregate progressively to form larger haloes in a hierarchical growth of structure. In this sense, small structures, such as dwarf galaxies and globular clusters, were assembled first and can be regarded as the remaining building blocks of the formation of larger present day galaxies such as the Milky Way.

The ΛCDM cosmology is a well tested model which successfully explains a wide

range of observations: the CMB temperature fluctuations, the large-scale mass power spectrum (as traced by the spatial distribution of galaxies and clusters of Galaxies), the chemical abundance imprint of Big Bang nucleosynthesis (abundances of H, D, He and Li, [Cyburt *et al.* 2016]), and the statistical properties of strong gravitational lensing. Despite these impressive successes, at smaller spatial scales, where the dissipative physics of baryons is dominant, ΛCDM is challenged by a number of observations which are not readily explainable by the hierarchical nature of galaxy formation implied by ΛCDM ([Scannapieco *et al.* 2012, Famaey & McGaugh 2013]).

For instance, models predict a larger number of dwarf galaxies than those observed around the Milky Way and other large galaxies of the Local Group. This is the so called *missing satellites problem*. Moreover, dwarf galaxies around the Milky Way ([Kroupa *et al.* 2010]) and Andromeda ([Ibata *et al.* 2013]) are found to be distributed as a rotationally supported relatively flat disk. This contrasts with the expected isotropic distribution which naturally emerges from merger dynamics.

The merger history and the transference of angular momentum from the disk to the halo in models produce galaxies with a specific baryonic angular momentum which is too small compared with what is observed. In the same line, ΛCDM models of galaxy formation have problems to produce bulgeless disk galaxies. In fact, major mergers typically create prominent bulges that are a particular imprint of the hierarchical nature of these models ([Abadi *et al.* 2003]).

Observational evidence are fundamental to put solid constraints on the detailed prescription of the ΛCDM cosmology. An adequate understanding of how a galaxy as the Milky Way formed and evolved, accounting for the complex physics of baryons which is relevant at these scales, might help to fix the flaws of the theory to make it consistent with observations. The content of this thesis can be viewed as a piece of this work.

1.3 An overview of the main Galactic components

The Milky Way is a gravitationally bound system of stars, gas, dust and dark matter. According to its global morphology is classified as a SB(rc)bc galaxy, i.e. a spiral barred galaxy. On the other hand, according to current estimations of it global mass and star formation rate ([Licquia *et al.* 2015]), the Milky Way falls in the so called "green valley", the transition region in the color-magnitude diagram of galaxies in between the red sequence and the blue cloud where galaxies are forming stars in a declining rate. Moreover, the Milky Way looks particular with respect to galaxies of similar mass when considering the nature of its current accretion events. In fact, it has been estimated that galaxies of the luminosity of the Milky Way are barely found currently accreting massive satellites as the Magellanic clouds ([Robotham *et al.* 2012]). The case is even strengthen if we take into account that these satellites are moreover strongly forming stars. Apart of these peculiarities, the application of the Copernican principle tells us that we should expect the Milky Way to be a fair good example of a large barred disk galaxy to study it in situ and in detail.

The Milky Way stellar content is given by the spatial arrangement of several different structures, which were probably assembled into the system at different epochs and

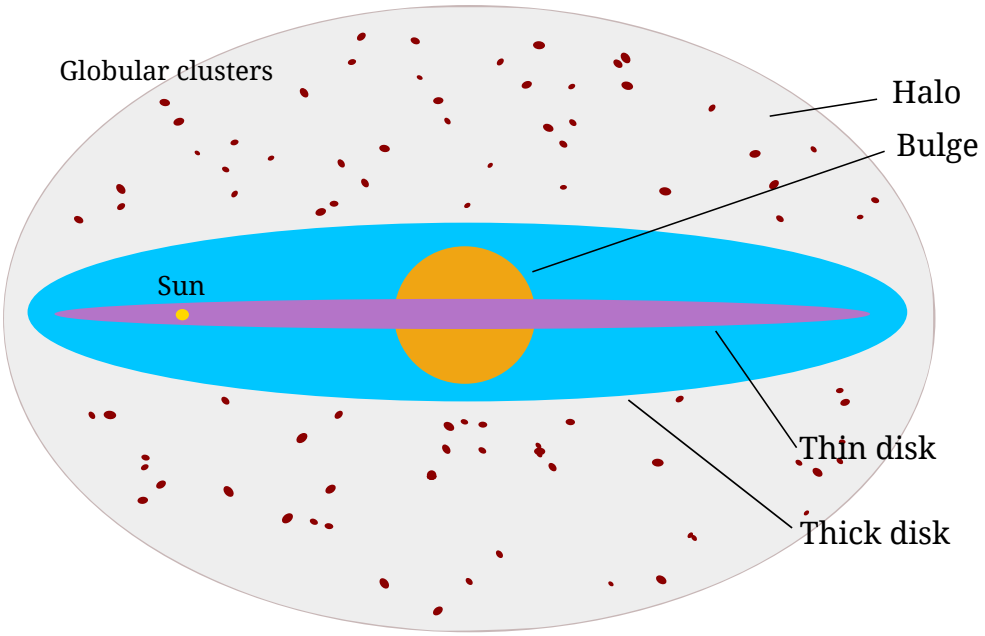


Figure 1.2: Schematic view of the main structural components of the Milky Way.

timescales during the Galaxy formation. The characteristics of the stellar content in each one of these components are tightly related to the concept of stellar populations, first suggested by Baade in 1944. In Fig. 1.2, we display a sketch of the main components of the Galaxy, which are described below.

1.3.1 The thin disk

It is the component where the majority of the stars, both field and in open clusters, reside in (stellar mass $M = 4 \pm 1 \times 10^{10}$ $M_{\odot}$, [Bland-Hawthorn & Gerhard 2016]). They are young, with typical ages $\lesssim 8$ Gyr, and metal-rich stars of population I. The great majority of the gas, atomic and molecular hydrogen concentrates here, which also determines that it is in this component where the vast majority of the sites of current stellar formation are located. Its metallicity distribution ranges approximately from $-0.6 \leq$ [Fe/H] $\leq +0.5$ dex[1], with [α/Fe] enhancements going from slightly larger than solar to subsolar values. In structural terms, the thin disk constitutes a flat distribution with exponential number density profiles, both in the vertical (scaleheight of $z \sim 300$ pc, e.g. [Jurić *et al.* 2008]) and radial (scalelenght of $R \sim 2.6$ kpc, e.g. [Jurić *et al.* 2008]) directions. It is supported mainly by circular orbits, with small dispersion and rotational velocities of the order of 210 km s^{-1} (e.g. [Recio-Blanco *et al.* 2014]).

1.3.2 The thick disk

Thick disks as separate structural components of galaxies were discovered in the late 70s from the impossibility to account for the light profiles of some edge-on external

[1] The bracket notation for chemical abundances is defined in Sect. 1.4.1

galaxies with single exponential profiles ([Tsikoudi 1979, Burstein 1979]). In the case of the Milky Way, the confirmation of the existence of a thicker disk component came into light though deep star-counts towards the Galactic poles ([Yoshii 1982, Gilmore & Reid 1983]). Since that time, it has been demonstrated that the thick disk also differentiates from the thin disk in its chemistry, age distribution and kinematics. The thick disk is rotationally supported, although kinematically hotter than the thin disk, containing about five times less mass than the thin disk ($M = 8 \pm 3 \times 10^9$ $M_\odot$, [Bland-Hawthorn & Gerhard 2016]). It is more vertically extended (scaleheight $z \sim 900$ pc, [Jurić *et al.* 2008]) but more centrally concentrated (scalelenght $R \sim 2.0$ kpc, [Bland-Hawthorn & Gerhard 2016]) than the thin disk. It is composed fundamentally by field stars with ages ≥ 8 Gyr ([Haywood *et al.* 2013]). The metallicity range spanned by its stars ranges from [Fe/H] ≈ -1.0 dex to approximately solar values, with [α/Fe] enhancements systematically higher than those displayed by the thin disk at a given metallicity. There is not currently observational evidence for a radial metallicity gradient, but a shallow vertical gradient has been detected ([Mikolaitis *et al.* 2014]).

1.3.3 The halo

We distinguish here the stellar halo from the dark matter halo (baryonic and non-baryonic) which is supposed to surround and dominate the mass content of the Galaxy, as predicted by ΛCDM cosmological models. The stellar halo encompasses about 1% of the Galactic stellar content, including globular clusters and field stars. Halo stars constitute an extended spheroidal distribution, supported by random motions in eccentric orbits and with just a small possible net rotation. Essentially, all its stars are older than 10 Gyr, metal-poor ([Fe/H] $\leq$ 1.0 dex) and α-enhanced. Indications of a dual halo have been presented from spatial distribution, kinematic and chemical analysis. [Hartwick 1987] showed than the distribution of metal-poor halo RR Lyrae stars depicted a two-component halo, with a flattened inner component and a more spherical outer component. Subsequent analysis has confirmed the presence of two broadly overlapping subcomponents, a high-α inner halo with zero or some prograde rotation, and a mean metallicity of [Fe/H]=-1.5 dex, and a low-α outer halo with retrograde rotation and mean metallicity of [Fe/H]=-2.2 dex ([Carollo *et al.* 2010, Nissen & Schuster 2010]). In this context, the low-α stars might correspond to an accreted component, while the high-α would be formed in situ in the halo. The slope break of the radial density distribution between the two components is located at about $R = 30$ kpc ([Sesar *et al.* 2011]). When a smooth density model is subtracted from maps of stellar counts, a rich variety of unrelaxed substructure is revealed, showing that the accretion of small satellites should account for a relevant fraction of its stellar content.

1.3.4 The bulge

This Galactic component is the primary object of study of this thesis. The bulge can be morphologically defined in simple terms as the bulk of stars swelling out from the exponential profile of the disk star density at the Galactic center. Historically, studies of this region have been complicated due to extreme dust absorption, accounting for

up to 30 magnitudes in visible wavelengths. A number of studies looking at some regions where the extinction is lower, and in the last years, thanks to the exploitation of observations in near infrared, have been contributed to construct a new picture of the bulge and to progressively reveal a very complex structure. In general terms, the Galactic bulge is a massive component comprising about a quarter of the Galaxy's stellar mass ($M_{bulge} = 2.0 \pm 0.3 \cdot 10^{10}$ $M_{\odot}$, [Valenti *et al.* 2013]). The metallicity of its stars ranges $-1.5 \leq$ [Fe/H] $\leq +0.5$ dex, with enhancement levels similar or higher than those of thick disk stars.

In the following sections, we will provide a detailed account of the main observations and theoretical works concerning this Galactic component.

1.4 Galactic archaeology

Low mass stars are ubiquitous in the Galaxy dominating by number with respect to high mass stars. The slow pace of the thermonuclear reactions taking place in their interiors determines that stars of progressively lower mass have increasing lifetimes, even comparable to the age of the Galaxy. As a matter of fact, stars with mass similar to, or less than that of the Sun have main-sequence lifetimes of at least 10 Gyr ([Schaller *et al.* 1992]).

Because of such long lifetimes, old low mass stars have witnessed the very early formation history of the Milky Way, and contain a detailed record of the past chemo-dynamical events which shaped its current observable properties. Galactic archaeology is a research field which aims to decode these fossil records by characterizing chemical and kinematical patterns of stellar populations. The ultimate goal is to understand the origin and evolution of the stellar populations assembled in the Milky Way, which in turn represents a way to understand galaxy formation in general.

The past evolution of a stellar system can be reconstructed by a careful analysis of its detailed pattern of chemical abundances, plus a proper kinematical characterization. If a group of low-mass stars was formed at the same time from the same cloud, they will present matching patterns of photospheric chemical abundances, independently of their kinematical distributions after several Gyr of galactic evolution. In this sense, a chemical tagging of stars finding these matching chemical patterns, provides an opportunity to identify the remnants of ancient building blocks of the Galaxy even is they are currently dispersed in the position-velocity phase-space ($\mathbf{x}$,$\mathbf{v}$).

All this valuable information can be read in the Milky Way from detailed photometric and/or spectroscopic observations of its resolved stellar populations. In particular, the Milky Way bulge is the only bulge we can resolve into individual stars down to the bottom of the main-sequence. The star-by-star study of its stellar content, together with the great degree of detail that is possible to achieve with the current large aperture telescopes and multiobject spectroscopy, have turned the Galaxy into an opportunity to perform "near field cosmology" in order to test any envisaged scenario of galaxy formation.

1.4.1 Chemical abundances

Auguste Comte was a French philosopher living in the XIX century. He was quoted as saying "There are some things of which the human race will remain in ignorance, for example the chemical constitution of the heavenly bodies". This intuitive and logic assertion was proven to be wrong just after a lapse of few decades. In fact, the introduction of spectroscopy marked the beginning of astrophysics, and thus, the possibility of studying the physical properties of celestial bodies by means of the analysis of the light received from them. In this way, we learned that the stars, in particular the photospheres from which the spectra we observe comes from, contains known chemical species. Taking the Sun as an example, it is composed roughly of 74% percent of hydrogen atoms, 25% of helium atoms and the remaining 01% of the so called metals, namely all the elements with mass number larger than A = 12. The later calculation, from the present-day solar photospheric composition of [Grevesse *et al.* 2007]. Chemical abundances are determined in stars by measuring the strength of absorption lines imprinted on their continuum spectral energy distributions by the different elements present in the star atmospheres.

The photospheric abundance of a given element X in a star is commonly expressed as

$$\mathrm{A(X)} = 12 + \log(\mathrm{X/H}),$$

where X/H is the ratio of the abundance by number between the considered element and hydrogen. In studies of stellar populations, photospheric abundances are customarily expressed in relation to the solar chemical composition as

$$[\mathrm{Fe/H}] = \log(\mathrm{X/H}) - \log(\mathrm{X/H})_{\odot},$$

where abundances can be expressed either by number or by mass. By definition, Solar abundances are [X/H] = 0 dex.

1.4.2 Chemical evolution and the time-delay model

To stars alchemy is trivial. In fact, it is in the stellar interiors, or during the last evolutionary stages of stars, where the baryonic content of the Universe beyond carbon -the so called metals- is synthesized. Big bang nucleosynthesis accounts for the formation of hydrogen, helium and small amounts of lithium, but the physical conditions for the production of elements beyond this point were not reached in the progressively colder expanding universe.

The quiescent burning of elements in the core and burning layers of massive stars ($M > 10\ M_{\odot}$) produces most of the O, Ne, Mg, Si, S, Ca and Ti, which are then released into the interstellar medium (ISM) via type II supernovae (SN II) explosions. On the other hand, iron peak elements (Vn, Cr, Mn, Fe, Co and Ni) are mostly produced through explosive nucleosynthesis, mainly during type Ia supernovae (SN Ia) explosions (which have progenitors of masses lower than 8 $M_{\odot}$ in binary systems). Clearly, both nucleosynthetic channels are not exclusive, and elements like Si, S and Ca are also produced in a non-negligible amount during SN Ia explosions. An exception to this is given by O and Mg which are believed to the produced exclusively in massive stars.

Heavy elements (with Z > 30) are produced by neutron capture during last stages of stellar evolution ([Sneden *et al.* 2008]). The slow (relative to the rate of β decay) neutron-capture *s*-process elements, are produced at the relative low neutron density environments of cool giant stars, in particular during the mixing episodes in the course of AGB evolution. They are deposited into the ISM through stellar winds. On the other hand, rapid neutron capture *r*-process elements are produced during core collapse SN II explosions. Again, these two channels are not exclusive and elements can be produced in different fractions by both processes.

There is a wealth of information encoded in the chemical patterns of stars, as they represent a record of the detailed processes and relative timescales driving the evolution of different stellar populations. In the case of the Milky Way, the careful study of abundance ratio distributions of stars residing at different Galactic components might allow to reconstruct the chemo-dynamical history of the Galaxy, specially when considered together with structural, kinematic and/or age information. The advent of large spectroscopic surveys obtaining spectra at resolution high enough for detailed chemical diagnosis, as well as the introduction of automated procedures to cope with the analysis of such increasingly large datasets, has represented a leap from sample sizes on the order of hundreds to tens of thousands of stars. The analysis of stars in the abundance-metallicity plane allows for the identification and characterization of sequences and/or gaps displayed by stars belonging to different Galactic components. The lessons learned from this kind of analysis are shedding light over fundamental problems, such as the relation and/or continuity between the thin and the thick disk, the relation between the halo and thick disk, or the relation between the disk(s) and bulge stellar populations. The study of abundance-metallicity distributions together with kinematics is in the heart of the work conducted in this thesis.

The interpretation of the information provided by the abundance-metallicity distribution of stars belonging to different stellar populations has required the elaboration of models intended to reproduce the growth of the metal fraction with time, the so called chemical evolution models.

Chemical evolution models are a powerful tool to put constraints on the formation timescale of any stellar population (see [Pagel & Patchett 1975, Audouze & Tinsley 1976, Tinsley 1976] for a view of the early development of ideas). Analytical and then numerical models have greatly evolved, allowing to interpret the chemical enrichment patterns of the different Milky Way components as well as those of external galaxies.

A chemical evolution model (CEM) follows the growth history of the small but important fraction of chemical elements with mass number $A \geq 12$, which as mentioned before, correspond to all elements produced not by big bang primordial nucleosynthesis but as the product of processing in stars. This stellar nucleosynthesis can be whether quiescent (burning of elements in the core, or burning layers, inside stars) or explosive (during explosion of stars at the end of their lifetimes). The chemical enrichment of the interstellar medium (ISM) is drawn mainly by the interplay among supernovae of type Ia and II (SN Ia and SN II) contributions. The early evolution of the gas enrichment is driven by the output of core collapse SN II, whose progenitors are massive (> 10 $M_{\odot}$) short-lived stars which start exploding soon after the onset of stellar formation. They pollute the gas mainly with α-elements plus a small fraction of iron. A larger amount

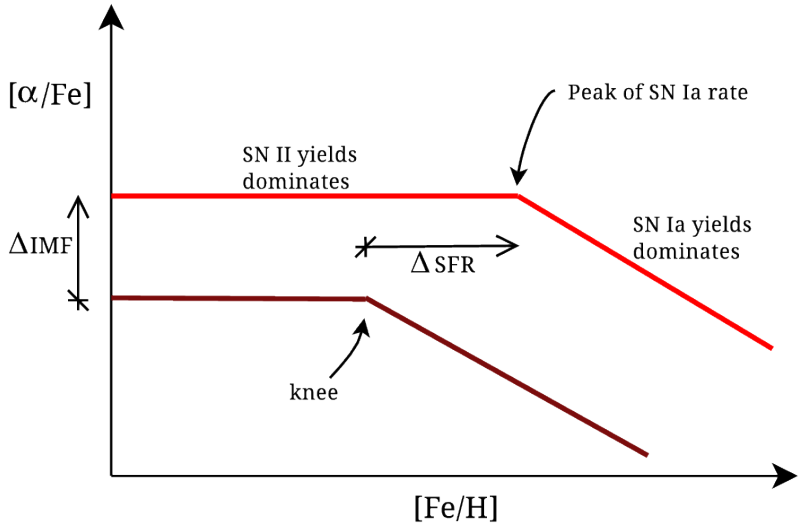


Figure 1.3: Sketch of the evolution of [α/Fe] as a function of [Fe/H].

of iron and iron-peak elements is deposited into the ISM by type Ia supernovae, which are believed to be the product of the explosive deflagration of C-O white dwarfs (with progenitors of masses lower than about 6-8 $M_\odot$) in binary systems. Being the product of low mass star evolution, SN Ia start exploding after $\sim$ 30 Myr, with the time of the maximum of their explosion rate ($\sim$ 70 Myr, [Matteucci & Recchi 2001]) being determined by the initial mass function (IMF) and the star formation rate (SFR) of the stellar system.

These somehow different timescales implied in the ISM pollution are the conceptual basis of the so called *time-delay model* of chemical enrichment, which is illustrated in Fig. 1.3. After the formation of the system, massive stars will pollute the gas at high [α/Fe] levels. The value at which the ISM will be enriched depends critically on the fraction of massive stars born out of the gas, namely, on the IMF. In Fig. 1.3 this is illustrated by the different vertical position of the two represented tracks. A chemical evolution dominated by more massive stars determine a higher [α/Fe] level of the α-elements "plateau". Chemical enrichment proceeds with increasing metallicity up to the time where the maximum of SN Ia frequency is reached. From this point afterward the larger amounts of iron deposited into the ISM by SN Ia will imprint a decrease of the α-element fraction with increasing metallicity. This change of enrichment regime determines the metallicity at which the so called "knee", the turndown point at which the α-element ratio starts to decrease strongly with metallicity, is imprinted in the [α/Fe] vs. [Fe/H] plane sequence. If the star formation rate is high, because of a deep potential well and/or high gas surface density, the metallicity at which the "knee" happens will move to larger metallicity values, as illustrated in Fig. 1.3.

In a nutshell, stars born from gas with primordial or pre-enriched composition, synthesize metals and deposit them back to the ISM at the end of their lives. The exact characteristics of such process determines the temporal chemical evolution of the gas. Low mass stars, because of their long lifetimes, lock up gas out of this enrichment

process. In this way, the photospheric chemical composition of low mass stars, which is assumed to be a fair representation of the gas at the time they born, is a fundamental source of information to understand Galaxy formation and evolution.

1.5 The bulge

The Galactic bulge is the Rosseta stone for our understanding of galaxy formation and evolution. Bulges are very common structures in galaxies, which in cosmological terms harbor approximately 70% of the stellar mass ([Fukugita *et al.* 1998]). Because they consist of most of the oldest stars in a galaxy, studying bulges represent a valuable opportunity to understanding the chemo-dynamical processes involved in the general formation of their host galaxies.

Being a major Galactic component, comprising around a quarter of the Milky Way stellar mass ($M_{bulge} = 2.0 \pm 0.3 \times 10^{10}\ M_{\odot}$, [Valenti *et al.* 2015]), and covering around 500-600 square degrees in the sky, the Galactic bulge provides us with the closest example of this kind of frequent galactic structure. As a predominantly old stellar population, it has witnessed the very early formation history of the Milky Way, and its stars contain a detailed record of the past chemo-dynamical events which shaped its current observable properties. Furthermore, because of its proximity, the Galactic bulge represents an ideal opportunity of performing detailed observations for hypothesis-testing on a star-by stat basis, an advantage that is not available for external bulges, except for M31. Ironically, this great advantage is at the same time a potential limitation in our ability to properly account for the global properties of the system. A detailed mapping of the stellar populations in the bulge region implies the observation of about 600 square degrees, clearly a huge observational challenge. In the recent years, new generation of multi-object spectrographs (MOS) at the largest facilities, as well as wide and deep photometric surveys, have opened new research opportunities, determining a flourishing tine of progress in bulge studies. In the following, we present an account of the bulge properties as seen and interpreted both from the observational as from the theoretical point of view.

1.5.1 Formation models

In general terms, two main formation scenarios have been proposed to explain bulge formation; i) violent formation through the monolithic collapse of a primordial gas cloud at early times or through hierarchical merging of substructures, and ii) secular dynamical evolution of the early disk.

Violent processes

To account for the first of these scenarios, we have to go back to the classical model of Eggen, Lynden Bell and Sandage (the ELS model, [Eggen *et al.* 1962]). In this work, they analyzed metallicity and stellar movements of an in-situ halo sample, concluding that a monolithic collapse would account for its formation. Under these ideas, the observed properties of the bulge would be well explained by assuming an in situ formation via

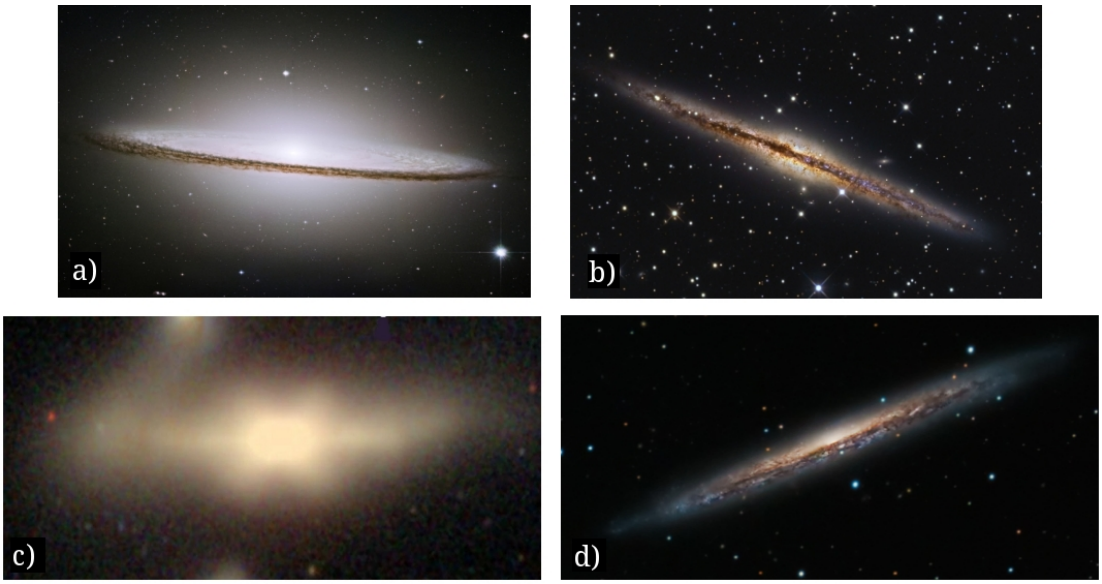


Figure 1.4: Examples of different kinds of bulges. *Panel a:* The prominent classical bulge of the Sombrero Galaxy NGC 4594. *Panel b:* The boxy shape bulge of NGC 891. *Panel c:* The extreme X-shape bulge of NGC 128. *Panel d:* The edge-on spiral galaxy NGC 5907 appears to have a negligible bulge.

dissipative gravitational collapse of a primordial gas cloud in a free-fall dynamical time scale. This rapid formation takes place in early stages of Galaxy formation, triggering a violent star formation -essentially in a star-burst regime- which produces virtually the whole stellar content of the bulge in less than 0.1 Gyr. From the chemical evolution point of view, such a quick violent formation process determines a chemical enrichment dominated by massive stars, with the α-enhanced imprint of SN II nucleosynthesis [Matteucci & Brocato 1990]. Considering these ideas in a ΛCDM context, it has been proposed that merger-driven bulge formation can be accounted by the accretion of dark matter clumps carrying baryons and gas [Elmegreen 1999, Abadi *et al.* 2003], external building blocks [Scannapieco & Tissera 2003], or multiple chemically distinct disk fragments of massive clumps of star and gas [Immeli *et al.* 2004]. All in all, this kind of formation predicts bulges with a stellar content predominantly old, spatially extended, dynamically supported by random motion with just a small net rotation, and with a broad MDF and general high-α enhancements. This kind of bulges, sometimes thought as small elliptical living in the center of a disk, are called classical bulges. The prominent round bulge of the Sombrero galaxy, displayed in Fig. 1.4, is a clear example of a classical bulge. Violent process dynamics accounts for the characteristic $r^{1/4}$ law light distribution profiles in classical bulges, as that of Sombrero galaxy ([Barnes 1988]).

Secular evolution

A new taxonomy of galactic bulges emerged from morphological studies of external galaxies. In fact, some bulges present characteristics departing from what is expected for a classical spheroid; they are flatter with peanut or boxy shape, their rotational to

random velocity ratio is high and they present nearly exponential light profiles. These characteristics, resembling more a disk than a classical bulge, lead to the proposition of a different kind of structures, masquerading classical bulges but with a disk-like structure, the so called *pseudobulges* [Kormendy & Kennicutt 2004].

It is known that boxy/peanut (B/P) bulges in late type galaxies are associated with the presence of bars ([Kuijken & Merrifield 1995, Bureau & Freeman 1999]). Moreover, about 60% of disk galaxies presents some kind of barred structure at their centers as seen in NIR images ([Marinova & Jogee 2007]). In this sense, pseudobulges might be common structures in galaxies.

Pseudobulges are believed to be the product of dynamical secular evolution of a massive rotating disk through bar formation and buckling ([Combes & Sanders 1981, Raha *et al.* 1991, Athanassoula 2005]). Dynamical instabilities in the inner parts of the disk scramble stellar orbits which lose angular momentum and form a bar. This structure subsequently undergoes vertical instabilities, buckling and fattening by redistributing stars in the vertical direction. The final structure, reach a dynamical equilibrium given by the assembling of different families of resonant orbits, and constitutes a central stellar density looking like a pseudobulge.

As described by N-body simulations, secular evolution produces structures than when seen edge-on display a characteristic boxy/peanut, and even in extreme cases, X-shaped light surface distributions ([Martinez-Valpuesta *et al.* 2006]). Two examples of these kind of structures are given in the panels *b* and *c* of Fig. 1.4. In addition, the same models predict that B/P bar bulges rotates cylindrically, namely, that the mean stellar velocity is independent of the distance from the plane, as for a rigid body.

Concerning ages, the presence of a rotating non axisymmetric mass distribution given by the bar distorts the galactic potential, inducing loss of angular momentum in portions of gas which fall to the center and triggers star formation ([Coelho & Gadotti 2011, Ellison *et al.* 2011]). In this sense, the presence of a young stellar component in B/P bulges is expected. On the other hand, from the studies of [Sheth *et al.* 2008, Sheth *et al.* 2012], it is known that bars can be found in galaxies already at $z = 1$. Moreover, bars are long lived structures that can survive to $z = 0$, unless massive amount of gas are present in the disk ([Bournaud & Combes 2002, Athanassoula 2005, Bournaud *et al.* 2005, Kraljic *et al.* 2012]). A look-back time of 8 Gyr for $z = 1$ sets a minimum age for the stars trapped in the bar potential, which are expected to be the bulk of its stellar content.

Composite bulges

As it can be seen from the above discussion, there are a number of physical processes that might be responsible for shaping the different present-day kinematic, chemical and structural properties observed in the Galactic bulge. While it is true that the mechanisms leading to the formation of a spheroidal or a pseudobulge component are very different in nature, they are not necessarily exclusive phenomena. Dual bulges, including spheroidal and pseudobulge components, have been observed in a number of external galaxies ([Prugniel *et al.* 2001, Peletier *et al.* 2007, Erwin *et al.* 2015, Fisher & Drory 2016]), as well as predicted by numerical simulations ([Fux 1999, Samland &

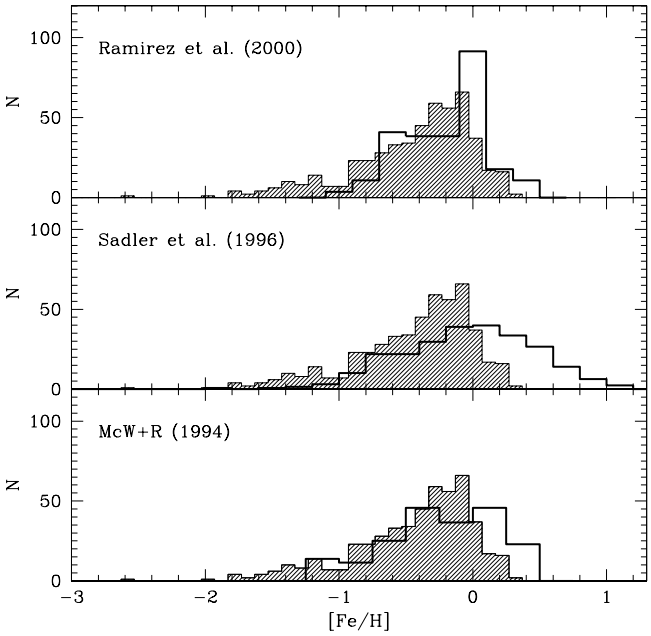


Figure 1.5: Early bulge's MDF determinations. The photometric MDF of [Zoccali *et al.* 2003] (shaded histogram) is compared with those derived by three low-resolution studies ([Sadler *et al.* 1996, Ramírez *et al.* 2000, McWilliam & Rich 1994]). Figure reproduced from [Zoccali *et al.* 2003]

Gerhard 2003, Nakasato & Nomoto 2003, Obreja *et al.* 2013]). The proportion in which both structures contribute to the central stellar overdensity is variable, but qualitatively validate the feasibility of mixed formation scenarios.

It is worth to mention that there are large disk galaxies that seem to be bulgeless (e.g. NGC 5907, panel *d* Gig. 1.4). This demonstrates that it is possible, even for large disk galaxies, to avoid all the different mechanisms of bulge formation.

1.5.2 Metallicity distribution function

The bulge metallicity distribution function (MDF) represents a fundamental piece of information to constraint its formation history, and place it in the context of the general assembling of structures in the Milky Way. The definition of its true shape and range across the bulge region has been a long -and still ongoing- observational challenge. This is mainly due to the large area to be sampled, and the problem which is posed when trying to target a population lying 8 kpc away across the disk, which plagues any sample with foreground contaminants, and large amounts of dust absorption.

The first studies on the stellar content of the bulge, mainly focused in the study of the low extinction region around $(l, b) = (1, 4)$ -the Baades's window- provided circumstantial evidence indicating for wide range of metallicity. In fact, [Baade 1951] discovered RR Lyrae variables in Baade's Window, while late M giants where also found to be very abundant in the same region ([Nassau & Blanco 1958]). The coexistence of evolved M giants and RR Lyrae stars is possible only if the stellar population has a underlying large enough range of metallicity.

The first observational efforts to define the bulge MDF come from low resolution campaigns, which at the epoch required patient star-by-star observations to build up a statistically significant spectroscopic sample. The early Baade's window CMD of [Arp 1965] (based on photographic photometry), allow for the first target selections

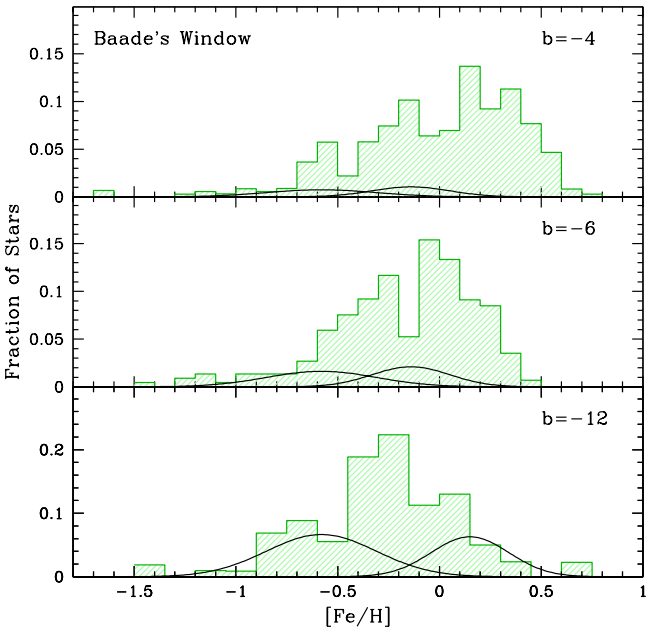


Figure 1.6: [Zoccali *et al.* 2008] MDFs in three fields along the bulge's minor axis. The two overplotted black gaussians have the mean and sigma values characteristics of the thick ([Reddy *et al.* 2006]) and the thin disk ([Nordström *et al.* 2004]). Figure reproduced from [Zoccali *et al.* 2008].

feeding low-resolution spectroscopic follow up ([Whitford & Rich 1983, Rich 1988, Sadler *et al.* 1996, Ramírez *et al.* 2000, McWilliam & Rich 1994]). From all these first attempts targeting giant stars, a concordant picture emerged in which the bulge is made up of stars with a wide range of metallicity of $-1 <$ [Fe/H] $< +1$ dex, with the peak around solar metallicity (see Fig. 1.5).

The MDF of [Zoccali *et al.* 2003] confirmed this picture by adopting a different technique. From the combination of optical (Wide Field Imager WFI camera at the MPG/ESO 2.2 meter telescope) and near infrared (2MASS) photometry in the bulge, a $(M_K, V-K)$ CMD was constructed. In order to reduce the impact of overlying disk stars, a control disk field CMD was used to statistically subtract disk features from the bulge CMD. The MDF was then derived from the comparison with respect to a set of RGB templates. In Fig. 1.5, this photometric MDF is compared with respect to those obtained from early low resolution studies.

A star-by-star observation of bulge stars make very expensive any effort of building up larger samples to perform studies with a good statistical significance. This situation improved dramatically with the advent of multi-object spectrographs, which allow for the simultaneous observation of hundreds of stars in a single shot. This new technique was adopted in [Zoccali *et al.* 2008] to determine the shape of the MDF in three fields along the bulge minor axis by observing about 900 K giants. The resulting distributions are reproduced in Fig. 1.6. This study represents the first high resolution observational effort to define the MDF, homogeneously comparing it at different locations in the Galactic bulge.

In addition, the MDFs of [Zoccali *et al.* 2008] demonstrated the existence of a vertical metallicity gradient of 0.6 dex/kpc along the bulge minor axis, a signature already suggested by [Minniti *et al.* 1995]. This vertical gradient is clearly visible in the broader picture offered by the photometric metallicity map of [Gonzalez *et al.* 2013]. In this work, the same technique of [Zoccali *et al.* 2003] was used to compute the mean metallicity

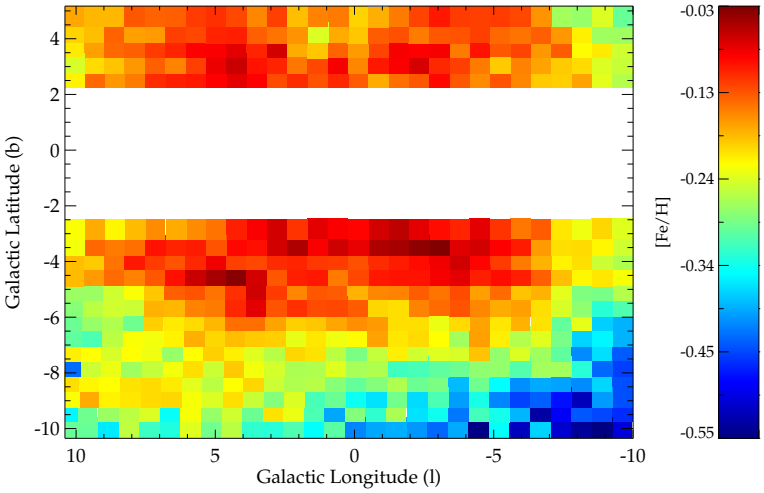
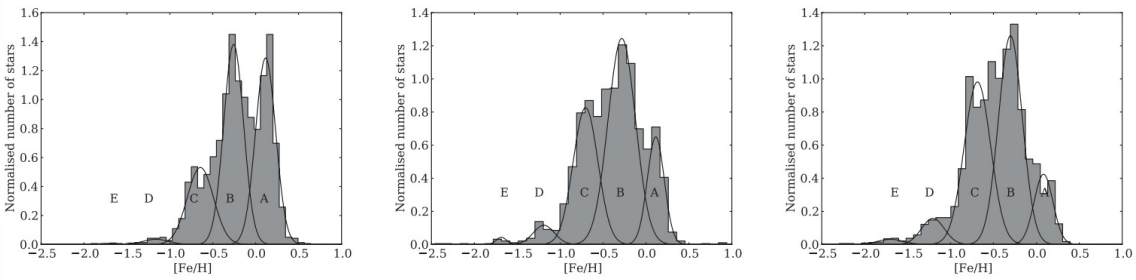


Figure 1.7: Photometric map of the mean metallicity across the bulge area sampled by the VVV survey. Figure reproduced from [Gonzalez *et al.* 2013]

in small spatial parcels mapping all the bulge area available from the VVV survey. In the resulting map, reproduced in Fig. 1.7, clear trends of decreasing metallicity with latitude are visible. From these results, [Gonzalez *et al.* 2013] estimate a vertical gradients of ~ 0.28 dex/kpc, smaller than the gradient derived by [Zoccali *et al.* 2008]. An increasing number of spectroscopic studies further complemented and confirmed this picture (see for example the compilation of literature results in [Johnson *et al.* 2012a]). The presence of a vertical gradient outside Baade's window became a firmly established result. However, the shape of the MDF determined in few fields at $|b| < 4$ from high-resolution near-infrared spectroscopy, suggest that the metallicity gradient could be null in the inner 700 pc from the plane [Ramírez *et al.* 2000, Rich *et al.* 2007a, Rich *et al.* 2012].

The presence of a vertical gradient in the bulge has been interpreted as a clear signature of classical bulge formation by dissipative collapse in the early stages of the Galaxy. In the same vein, it was argued that the presence of a vertical metallicity gradient rules out the possibility of the bulge being the product of disk secular evolution. In fact, disk dynamical heating has no means to discriminate stars by their metallicity, so that in principle they should end mixed in the resulting vertical structure ([Friedli *et al.* 1994]). However, recent N-body simulations of secular bulge formation have demonstrated that a vertical metallicity gradient can arise as an effect of the mapping in the vertical direction of horizontal [Martinez-Valpuesta & Gerhard 2013], vertical [Bekki & Tsujimoto 2011], or a mix of both [Di Matteo *et al.* 2015] metallicity gradients initially present in the disk.

The steadily increasing amount of high-resolution based studies allowed for the emergence of an alternative empirical interpretation of the vertical metallicity gradient. In the study of [Hill *et al.* 2011], 219 stars where selected from the Baade's window RC and observed at $R \sim 20000$ at the VLT FLAMES/GIRAFFE. The resulting MDF, clearly bimodal, was decomposed into two Gaussian populations of roughly the same size, with a metal-poor broad component centered at [Fe/H] $= -0.30$ dex, and a narrow metal-rich component centered at [Fe/H] $= +0.32$ dex. A qualitatively similar result was found by [Uttenthaler *et al.* 2012] from a sample of 400 K giants observed at $(l, b) = (0, 10)$,



(a) $l \pm 15°, b = -5°$ (b) $l \pm 15°, b = -7.5°$ (c) $l \pm 15°, b = -10°$

Figure 1.8: MDFs constructed by [Ness *et al.* 2013a] from strips of field at latitudes $b = -5$, -7.5 and -10. The five component decomposition claimed in this work is illustrated by the black gaussians, identified with letters from A to E with decreasing metallicity. Figure reproduced from [Ness *et al.* 2013a].

except that in this case the metal-rich component was found to account just for the 30% of the total sample.

More recently, from a large sample of 28000 low to medium-resolution ($R \sim 11000$) spectra from the ARGOS survey, [Ness *et al.* 2013a] presented a detailed MDF study suggesting that the bulge MDF might be built up by five component populations. The ARGOS survey targeted stars in 28 fields sampling the area $-30 < l < +30$, $-10 < b < -5$, but a smaller subset of completed fields was used. The primary targets of the ARGOS survey are RC stars. The advantage of using RC stars is that they have a narrow range of absolute magnitude and color which weakly depends on metallicity (with a mean of $M_K = -1.61$ and a dispersion of 0.22 mag, [Alves 2000]). This fact was used to compute distances complementing estimations done by isochrone fitting. A subsample of stars likely located at the bulge distance was selected by imposing a cut off of $R_{GC} < 3.5$ kpc. The resulting sample of 14000 stars was used to construct the MDF from the combination of fields in three latitude strips ($b = -5$, -7.5 and -10). The bayesian information criterion (BIC) benefit in each case models fitting the data with a combination of 4-5 gaussians. The constructed MDFs and fitted models in each latitude strip are reproduced in Fig. 1.8. From this figure, and the analysis of [Ness *et al.* 2013a], the bulge vertical metallicity gradient is interpreted as the product of the variation of the relative strength of the three most metal-rich components with distance from the plane. In fact, the size of the metal-rich component A decreases systematically from $b = -5$ to $b = -10$ while the metal-poor component C increases. The intermediate metallicity component B seem to be equally represented at all studied latitudes.

In this sense, the vertical metallicity gradient is produced by a change of the MDF shape and not by a solid shift of it with latitude, an interpretation already suggested by [Zoccali *et al.* 2008].

1.5.3 Structure and kinematics

The shape and kinematics of the Milky Way bulge both support the existence of a bar. First evidences of the presence of a bar came from the analysis of gas dynamics ([de

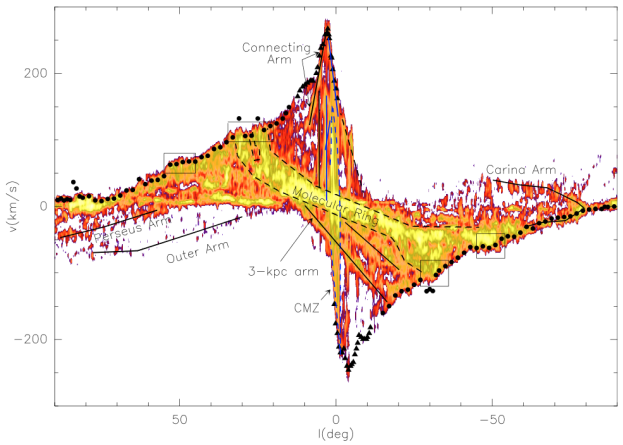


Figure 1.9: Annotated longitude-velocity (lv diagram of the CO (1-0) emission of [Dame *et al.* 2001]). Figure reproduced from [Rodriguez-Fernandez & Combes 2008].

Vaucouleurs 1964]). Large positive and negative line-of-sight velocities in the 21-cm line profiles near the Galactic center were found, indicating large departures from circular motions. The characteristic "8" shape visible in the longitude-velocity (lv) diagram, as the one reproduced in Fig. 1.9 ([Rodriguez-Fernandez & Combes 2008]), revealed the complex gas flows in the inner regions, and were taken as evidence of the presence of an axisymmetric rotating bar-like potential. This characteristic feature in the lv-plane was also used as a way to associate B/P bulges with bars in external galaxies ([Kuijken & Merrifield 1995, Bureau & Freeman 1999]). The presence of a bar was subsequently confirmed, and further characterized, by several studies using different probes and techniques; 21-cm line emission kinematics ([Liszt & Burton 1980]), infrared imaging ([Blitz & Spergel 1991]), AGB star counts ([Weinberg 1992]), miras distribution ([Whitelock & Catchpole 1992]), and COBE/DIRBE infrared imaging ([Weiland *et al.* 1994]).

The Galactic bulge presents a boxy/peanut appearance as displayed in 2MASS star counts [López-Corredoira *et al.* 2005] and COBE/DIRBE near-infrared light distribution [Dwek *et al.* 1995]. In Fig. 1.10 we reproduce from [Dwek *et al.* 1995] the contour maps of the bulge region as seen in three DIRBE bands. From here, the boxy shape of the bulge is evident, as well as an asymmetry in the sense that the vertical extension of the bulge is larger and brighter at positive than at negative longitudes. Several models have subsequently interpreted this boxy structure as an edge-on buckled bar [Zhao 1996, Fux 1999, Shen *et al.* 2010].

In the same line, star counts using RC stars has been used to explore the spatial distribution of the bulge stellar content. In fact RC, intrinsic luminosities have little variation with age and metallicity, turning them into good distance tracers. In extensive analysis using star counts of RC in a large area, [McWilliam & Zoccali 2010] using 2MASS, and [Nataf *et al.* 2010] using OGLE-III, took advantage of the standard candle nature of RC star to characterize their spatial density number distribution in several lines-of-sight towards the bulge region. These authors found bimodal RC luminosity distributions in several fields with $|b| > 5.5°$, which is interpreted as the line-of-sight intersecting two overdensities located at different distances. The magnitude difference between the peaks change with (l,b), unveiling an underlying X-shape structure. The 3D density maps of [Saito *et al.* 2011], using 2MASS, and [Wegg & Gerhard 2013], us-

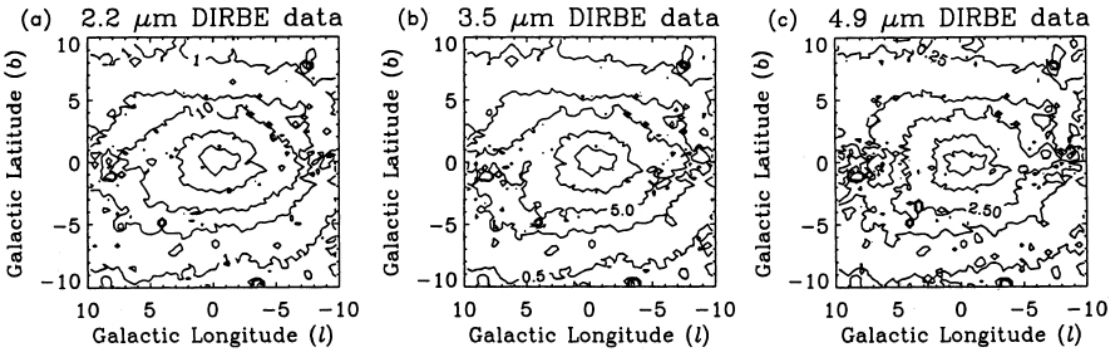


Figure 1.10: COBE/DIRBE contour maps of the bulge region at 2.2 μm, 3.5 μm and 4.9 μm. Figure reproduced from [Dwek *et al.* 1995].

ing VVV RC star counts (reproduced in Fig. 1.11), confirmed and enlarged this picture by mapping the X-shape morphology across several slices in latitude. The underlying X-shaped structure is seen as boxy/peanut from the Sun position because of the almost edge-on perspective. Some dynamical models predict X-shaped bulges as extreme cases of boxy/peanut bulges (e.g. [Athanassoula 2005, Martinez-Valpuesta *et al.* 2006, Debattista *et al.* 2006]). In addition, this type of structure has also been observed in external galaxies ([Bureau *et al.* 2006]). All this morphological evidence has been interpreted as in favor of a bar-driven secular evolution origin of the bulge.

The bar is currently characterized as a triaxial structure of ~ 3.5 kpc in length with axis ratios of 1:0.4:0.3. Its near side points towards positive Galactic longitudes, with a position angle of $\sim 25°$ with respect to the Sun-Galactic center direction ([Rattenbury *et al.* 2007, Wegg & Gerhard 2013]).

Boxy bulges present a characteristic cylindrical rotation, namely, a nearly constant stellar rotation speed with height above the Galactic plane. Classical bulges rotate more slowly at increasing height ([Falcón-Barroso *et al.* 2004]). Several different stellar probes have been used to try to characterize the bulge kinematics beyond what is seen in gas dynamics.

Planetary nebulae (PNe) are relatively rare, but they were used by [Beaulieu *et al.* 2000] to trace the bulge kinematics in a wide range of l and b. PNe were found to trace an underlying cylindrical rotation for the bulge that was fit by bar models as that of [Fux 1999]. The OH/IR maser emission stars are very common in a layer close to the plane, and specially abundant towards the Galactic center. Their distribution in the lv-plane, approximately following that of gas, was modeled using orbit reconstruction by [Habing *et al.* 2006], who found evidence for the presence of the bar as well as of a co-rotation resonance at 3.3 kpc. Old K giants were used by [Minniti *et al.* 1992] to construct a rotation curve by observing stars off the minor axis.

The first and recent large data set of systematically collected radial velocities of giant stars in the Galactic bulge was assembled by the BRAVA project ([Rich *et al.* 2007b, Kunder *et al.* 2012]). They found that K giants display indistinguishable rotation curves in strips at $b = -4°$, $b = -6°$, and $b = -8°$ ($l \pm 10$). BRAVA velocities are fitted nicely by the model of [Shen *et al.* 2010], which is able to reproduce a boxy/peanut bulge just

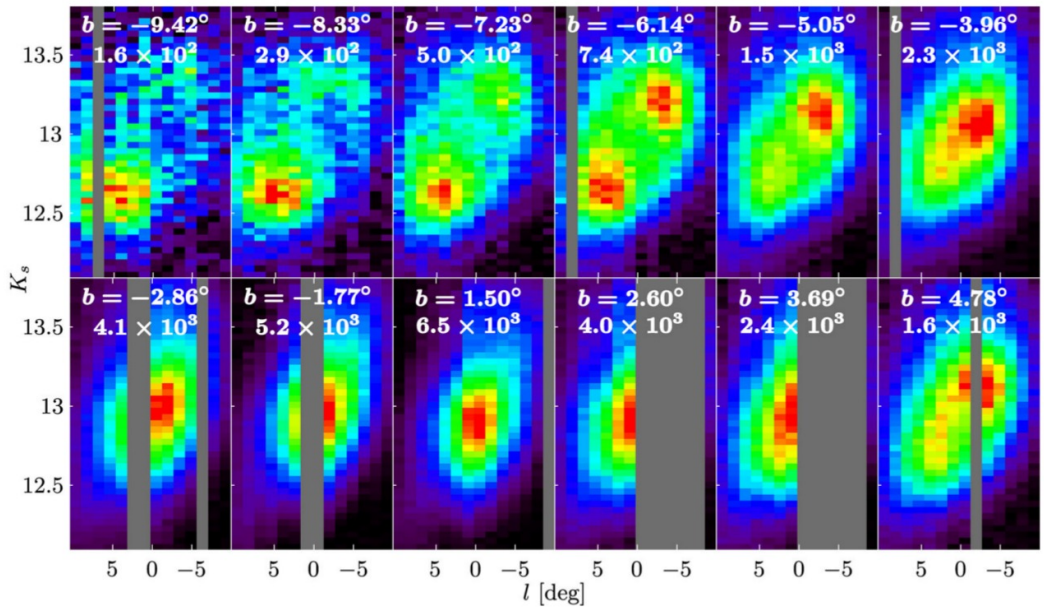


Figure 1.11: Bulge RC count density maps of [Wegg & Gerhard 2013]. They are based in photometry from the first data release of the Vista Variables in the Vía Láctea (VVV) project. The different slices are labelled by their central latitude. Figure reproduced from [Wegg & Gerhard 2013].

from accreted stars from the disk, and constrains any possible classical component to be less than 8% of the disk mass. This fact might challenge attempts to detect it, even in large data samples.

More recently, the ARGOS survey, with its large sample of ~ 14000 confirmed likely bulge RC stars, yielded a detailed characterization of the kinematic behavior of bulge star in the context of the different MDF components found by [Ness *et al.* 2013a]. In Fig. 1.12, we reproduce from [Ness *et al.* 2013b] the rotation and velocity dispersion curves for stars separated in three bins of metallicity, broadly accounting for the A, B and C MDF components. The mean rotation of stars in the Galactic bulge area ($-10 < l < 10$) is close to cylindrical, and keeps increasing outside this range to values as high as 150 km s^{-1}. Component B seem to rotate faster than A, and displays a velocity dispersion profile which looks as a kinematically hot replica of that of component A. Since both populations are in the same potential, this is interpreted as the stars in component A being more centrally concentrated that those in component B. On the other hand, stars in component C seem to co-rotate with respect to their more metal-rich counterparts, but display a much uniform and high velocity dispersion profile.

1.5.4 Chemical enrichment levels

Detailed comparisons between the bulge and other Galactic components, in particular, the thick disk in the [α/Fe] vs. [Fe/H] plane can provide a direct way to try to understand the origin of the metal-poor bulge. Early attempts in this direction ([McWilliam

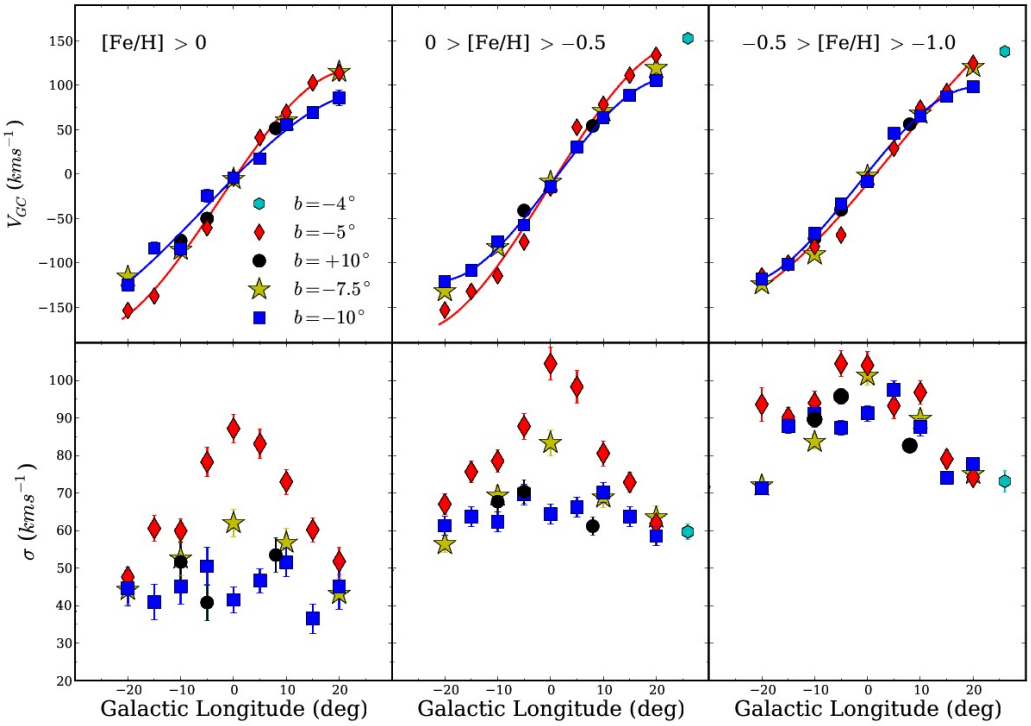


Figure 1.12: Bulge rotation and velocity dispersion curves from the ARGOS survey. Figure reproduced from [Ness *et al.* 2013b].

& Rich 1994, Rich & Origlia 2005, Zoccali *et al.* 2006, Lecureur *et al.* 2007, Fulbright *et al.* 2007]) claimed that bulge stars were more α-enhanced than thick disk stars of the same metallicity. [Meléndez *et al.* 2008] and [Alves-Brito *et al.* 2010] attributed this result to systematic effects arising from the comparison of giant and dwarf samples, given their different temperature and gravity regimes. Their homogeneous sample of bulge and thick disk giants display similar trends in the [α/Fe] vs. [Fe/H] plane, and presumably comparable location of the "knee" in the sequences of both populations. Similarities between the bulge and the thick disk have been also found by studying microlensed bulge dwarf stars in comparison with a local sample of thick disk dwarfs and subgiants ([Bensby *et al.* 2013, Bensby *et al.* 2014]).

The previous discussion shows that safer comparisons and conclusions might rest on the analysis of stars with similar physical parameters. It also emphasizes the importance of performing comparisons between stars in different populations on the basis of samples homogeneously analyzed. A direct comparison of different literature results might be affected by systematics arising from the different data and analysis methodologies employed to derive abundance levels. The eventual different chemical evolutionary histories of the bulge and thick disk may be encoded in subtle differences in the distribution of their stars in the abundance-metallicity plane, and in general in their detailed abundance patterns, and consequently, it is just by performing strict homogeneous comparisons that these differences can be revealed. In the same line, a rigorous study of the

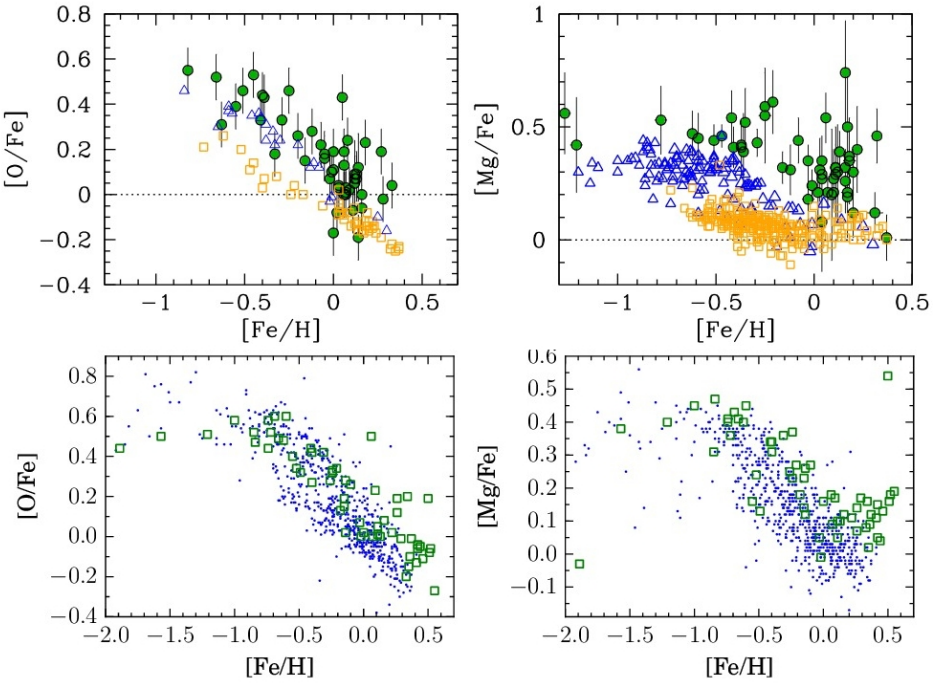


Figure 1.13: Bulge and disk(s) sequences in the abundance-metallicity plane. *Upper panels:* oxygen and magnesium ratios over iron of K giants from [Zoccali *et al.* 2006] and [Lecureur *et al.* 2007] (green circles) are compared with a sample of dwarf disk stars from [Reddy *et al.* 2006] and [Bensby *et al.* 2004, Bensby *et al.* 2005] (orange squares and blue triangles). Figure reproduced from [Zoccali & Minniti 2009]. *Lower panels:* the dwarf disk sample of [Bensby *et al.* 2014] (blue points) is compared with the sample of microlensed bulge dwarfs of [Bensby *et al.* 2013] (green squares) in the [O/Fe] vs. [Fe/H] and [Mg/Fe] vs. [Fe/H] planes.

detailed chemical abundance patterns based on statistically significant samples, can shed light on the initial conditions, physical processes and relative timescales characterizing formation and evolution of the bulge and thick disk populations.

The study of bulge field stars is complicated by the large spread in age and distance, and by the contamination from disk field stars interlopers in the lines of sight. In addition, the transition between the inner disk and the bulge is still not totally understood. In this context, the study of globular clusters as tracers of the bulge populations is a valuable tool because they provide clear points in the age-metallicity-distance distributions. Even if globular clusters are not necessarily representative of the field stellar populations, they must be properly accounted in any envisaged bulge formation scenario. A large number of high resolution studies on bulge GCs has steadily been accumulated. As an example, we display in Fig. 1.14 (from [Rojas-Arriagada *et al.* 2016b]) a comparison between bulge field stars and a compilation of bulge globular clusters from the literature. Their distribution in the abundance metallicity plane seem to favor an early prompt chemical enrichment . Unfortunately, up to now, comparisons are possible just at a qualitative level given the lack of studies systematically targeting field bulge stars

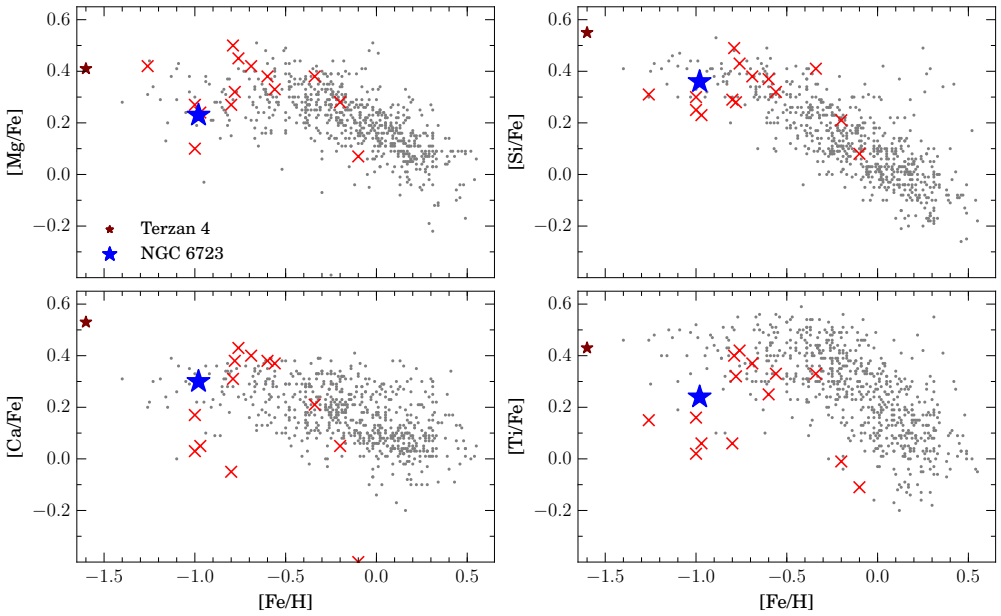


Figure 1.14: Bulge globular clusters compared with bulge field giants. Alpha-elements Mg, Si, Ca and iron-peak Ti are displayed in the [X/Fe] vs. [Fe/H] plane in the for panels. The different results for clusters and field stars are compiled from literature. Figure reproduced from [Rojas-Arriagada *et al.* 2016b].

and globular clusters. With such a dataset, systematics from the chemical analysis could be safely neglected. And of course GCs are interesting object at this own right, important to understand the place they take in the general assembling of the Milky Way.

1.5.5 Age

From the very early identification of RR Lyrae stars towards bulge by Baade ([Baade 1951]), the Galactic bulge has been regarded as an old population dominated by globular cluster-age like stars. However, efforts looking for tracers of young stellar populations have revealed the presence of a possible significant number of young stars, mainly in the central parsecs at the Galactic center, but recently also suggested to be present all across the bulge region. In order to understand bulge formation, a crucial piece of information is given by the age distribution of its stellar content.

Age from the color magnitude diagram

An important constraint on the mean age of the bulge comes from the comparison of bulge field stars with globular clusters, which in general can be taken as clean points in the abundance-distance-age space. This approach exploits the fact that the magnitude difference between the RC and the main-sequence turn-off is a proxy for the age of a stellar population, hence allowing for relative age comparisons. [Ortolani *et al.* 1995] first demonstrated that the stellar population at Baade's window is as old as the globular

cluster 47 Tucanae. Using HST photometry, [Ortolani *et al.* 1995] found that the main-sequence locii of the two metal-rich bulge globular clusters NGC 6528 and NGC 6553 are essentially the same when compared with the well studied halo cluster 47 Tucanae. They further demonstrated that NGC 6528 and NGC 6553 are coeval with the bulge stellar population at Baade's window. When the RC of the bulge and the clusters is forced to coincide (eliminating the effects of reddening and distance differences), the field luminosity peak at the position of the main-sequence turn-off matches that of the clusters.

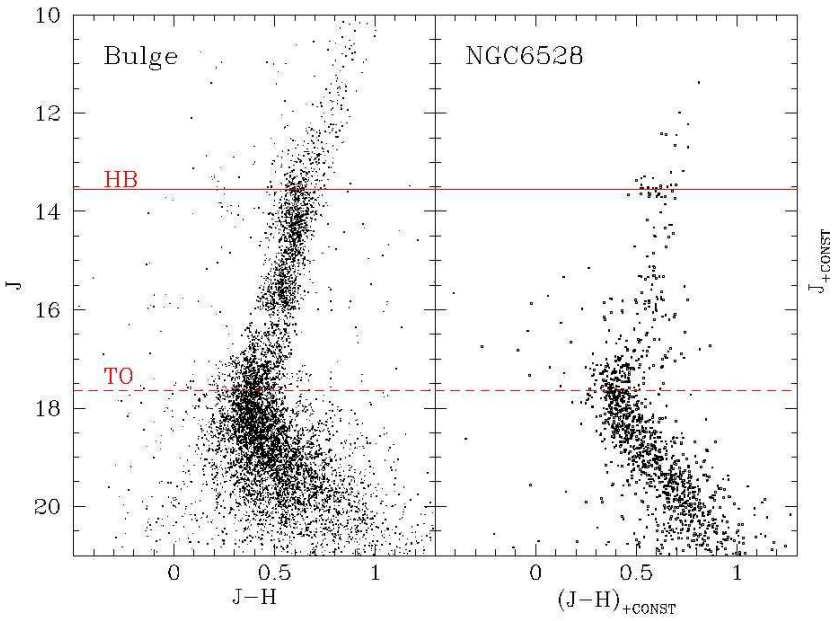


Figure 1.15: [Zoccali *et al.* 2003] CMD comparison between bulge field stars and the halo globular cluster NGC 6528. A control disk field at $(l, b) = (30°, 0°)$ is used to statistically clean the CMD at Baade's window, which in turn is compared with that of NGC 6528. A striking coincidence in the position of the RC and the main-sequence turn-off argues for a bulge age $\gtrsim 10$ Gyr. Figure reproduced from [Zoccali *et al.* 2003].

In general, the lines of sight towards the Galactic bulge are largely effected by the contamination of foreground disk stars. In a typical bulge CMD, the plume of disk main-sequence stars spreads in magnitude as an effect of increasing distance, falling on top of the bulge turn-off, making difficult to determine its precise location. A way to overcome this problem was proposed by [Zoccali *et al.* 2003], who made use of a disk field at $(l, b) = (30, 0)$, which has little or not bulge population, to statistically subtract the disk main-sequence feature from the CMD observed at Baade's window. The comparison of this cleaned CMD with that of the halo globular cluster NGC 6528,

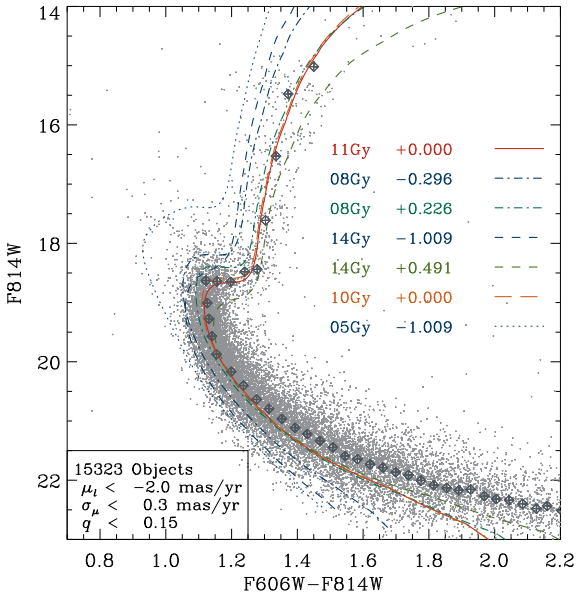


Figure 1.16: CMD of proper motion selected bulge stars from [Clarkson *et al.* 2008]. A sequence of isochrones at metallicity [Fe/H]=(-1.009, -0.226, +0.491) and ages (8, 10, 14) Gyr are displayed. Figure reproduced from [Clarkson *et al.* 2008].

pointed for a mean age of 10 Gyr for the bulk of the bulge stars, with no trace of a young or intermediate age population. In Fig. 1.15, this procedure is illustrated (taken from [Zoccali *et al.* 2003]). The same technique has been recently employed to explore the age at the corners of the B/P bulge (where less crowding and reddening facilitates the analysis) by [Valenti *et al.* 2013]. They found that the CMD of the two studied fields are consistent with their stellar population being older than 10 Gyr, in agreement with [Zoccali *et al.* 2003].

The availability of deep photometry and accurate proper motions from HST observations allowed for the introduction of a second approach to overcome the problem of disk contaminants. By studying the distribution of proper motions of field stars towards the bulge, disk stars can be identified and removed because of their larger longitudinal μ_l proper motions, as expected for a population rotating in front of the bulge. After the pioneering work of [Kuijken & Rich 2002], the most recent analysis of proper motion-selected bulge stars is given by the works of [Clarkson *et al.* 2008] and [Clarkson *et al.* 2011]. Observing at the SWEEPS field at $(l, b) = (1.25, -2.65)$, a strict proper motion selection yields the cleanest available CMD diagram of the bulge down to the main-sequence. In Fig. 1.16 we reproduce the cleaned CMD presented in [Clarkson *et al.* 2008]. The locus of the sequence above the turn-off is well reproduced by a solar metallicity α-enhanced isochrone of 11 Gyr. In particular, from the blue straggler study of [Clarkson *et al.* 2011], it is argued that no more than 3.4% of bulge stars are younger than about 5 Gyr.

Using the same data, a different interpretation has been recently proposed by [Haywood *et al.* 2016]. They argue than in order to reproduce the small spread in color of the CMD turn-off, given the metallicity distribution of bulge stars, a wide range of ages should be spanned by them. In fact, if the tight CMD sequence hides an age-metallicity relation, the spread in color is small only if metal-rich stars are predominantly young. In particular, just a 34% of bulge stars might have ages larger than 9 Gyr, which strongly contrast with all the aforementioned studies.

As discussed before, globular clusters can be used as probes of the stellar population they are associated with. An old age is systematically derived from bulge clusters, both at low metallicity ([Barbuy *et al.* 2006, Barbuy *et al.* 2007, Barbuy *et al.* 2009]) and high metallicity ([Lagioia *et al.* 2014]).

Young stars in the bulge

The chemical composition of the bulge provides also indications of a rapid formation. In fact, the α-element enhancements are a feature expected from a population whose chemical enrichment has proceeded fast and dominated by massive stars (c.f Sect. 1.5.4). Certainly, a mean old age is expected if the bulge is the product of a early prompt formation, either by dissipative collapse or hierarchical merging. On the contrary, a significant amount of young stars are expected to be part of the stellar content of the bulge if it is the product of a secular evolution of the disk. As we have seen, bar instabilities produce not only inward displacements of younger disk stars by loss of angular momentum, but also gas which can eventually trigger in-situ star formation. The issue of the existence of a young stellar component in the bulge has been a long standing concern, and a number of indications for its presence have been discussed in the literature.

The presence of mid-age and very young stars at the central parsecs of the bulge is a well established fact. However, several attempts have been conducted to find young stars elsewhere in the bulge area by using luminous evolved stars as tracers of young stellar populations. From VLA observations covering the central degrees of the bulge, [Lindqvist *et al.* 1992a, Lindqvist *et al.* 1992b] searched for the presence of OH/IR stars as maser sources. Their analysis, pointed out that stars with larger shell expansion velocities, associated with younger ages, are more concentrated towards the Galactic center. This finding is the starting point of a number of works seeking for these stars in the Galactic center ([Sjouwerman *et al.* 1998, Vanhollebeke *et al.* 2006]). In the same line, the study of Mira stars has shown that those with longer periods -indicative of younger ages- are mostly concentrated to the Galactic center ([Lloyd Evans 1976, Whitelock *et al.* 1991, Blommaert & Groenewegen 2007]). Additionally, several studies using AGB and planetary nebulae probes points for an age distribution with a peak around 3 Gyr ([Whitelock *et al.* 1991, Matsunaga *et al.* 2009, Gesicki *et al.* 2014]). Moreover, a population of young stars have been traced over the whole bulge region from ISOGAL data [van Loon *et al.* 2003]. Finally, numerous classical cepheids, young stars with ages < 100 Myr, have been detected close to the Galactic mid-plane ($-1.7 < b < 2.0$) and distributed along the whole bulge longitudinal extent ([Dékány *et al.* 2015]).

Main sequence stars at the distance of the bulge are too faint to be reasonable targets for spectroscopy. A way to circumvent this limitation, is to systematically monitor the bulge to detect microlensing events magnifying these faint sources. In fact, the high stellar density towards the bulge guarantees a relatively high rate of such events. The magnification can reach several magnitudes, making possible to allocate a fiber and obtain a spectrum. The high resolution spectroscopy of highly magnified bulge dwarfs, first used by [Minniti *et al.* 1998], has allowed to obtain an increasing list of bulge dwarfs through a long program of target-of-opportunity observations at VLT ([Bensby

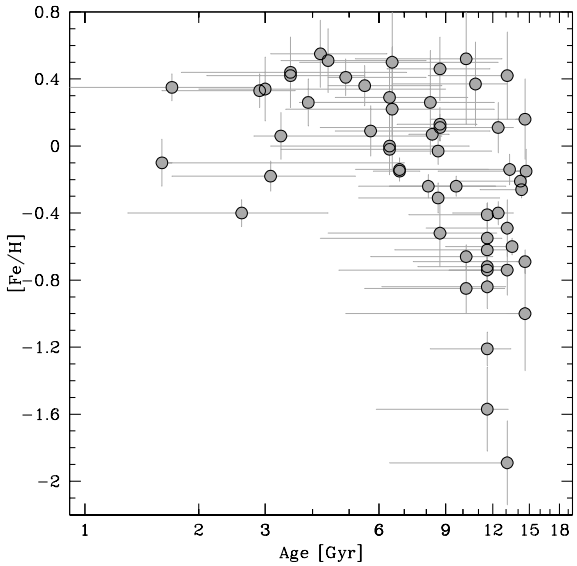


Figure 1.17: Age vs. metallicity for the microlensed dwarf sample of [Bensby *et al.* 2013]. Figure reproduced from [Bensby *et al.* 2013].

et al. 2013]). Using this sample, the presence of a significant amount of young stars all across the bulge region has been suggested. If fact, from the latest collected sample of 58 dwarf and subgiant stars, it has been shown that while metal-poor stars are uniformly old, at high metallicity the age spread increase considerably (Fig. 1.17). The metal-rich stars with [Fe/H] $\geq$ 0.1 dex display a wide range of ages, going from 2 to 12 Gyr with a dominant peak around 4-5 Gyr and a tail towards older ages.

This evidence is found to be spectacularly inconsistent with the results derived from CMD studies, and posses a challenge to be appropriately explained by any proposed model of bulge formation. It has been suggested than the presence of young stars in an old bulge, located predominantly near the plane, would be a natural consequence of the secular evolution of the Galaxy ([Ness *et al.* 2014]).

1.6 The nature of the disk system in the context of bulge formation

A significant new piece in our understanding of the global structure of the Milky Way was added around 20 years ago with the discovery of the thick disk ([Yoshii 1982, Gilmore & Reid 1983]). Detected from a double exponential fit to the vertical number density distribution of disk stars (see Fig. 1.18), the thick disk was characterized as a distinct structural component, with a larger scale height and hotter kinematics than the younger thin disk. Subsequent works have characterized it with kinematic and chemical properties in between those of the halo and thin disk populations (e.g. [Feltzing *et al.* 2003, Reddy *et al.* 2006, Navarro *et al.* 2011, Kordopatis *et al.* 2011, Fuhrmann 2011, Bensby *et al.* 2014, Recio-Blanco *et al.* 2014]). However, a large part of the observational work aiming at characterizing the two disks has been based in the analysis of local samples of the solar neighborhood. Only recently it has been possible to begin to extend the spatial coverage of samples, thanks to a new generation of surveys spanning larger radial regions: SEGUE ([Yanny *et al.* 2009]), RAVE ([Steinmetz *et al.* 2006]), APOGEE

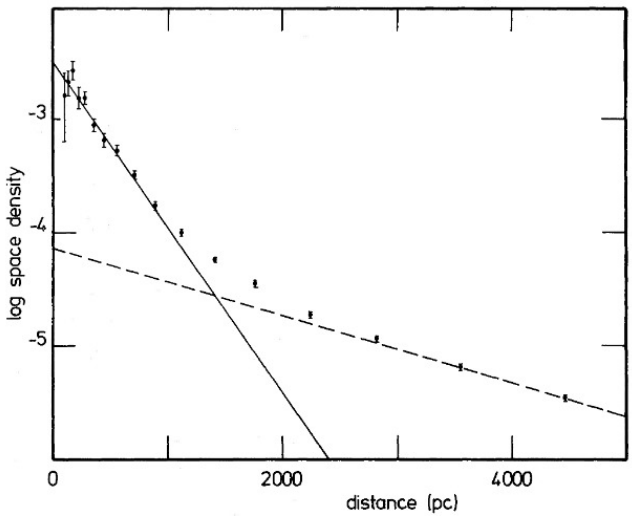


Figure 1.18: Discovering the thick disk: Density distribution of stars with distance from the Galactic plane for stars with $4 \leq M_V \leq 5$. The profile is well reproduced by the combination of two exponential profiles with scale heights of 300 pc (solid line) and 1350 pc (dashed line). Figure reproduced from [Gilmore & Reid 1983].

([Eisenstein *et al.* 2011]), and the Gaia-ESO survey ([Gilmore *et al.* 2012]).

A main question in all studies tackling the problem of characterizing the two Galactic disks is the way the thin and thick disk star samples are defined and separated. The adopted criterion is, at the same time, a definition of what we understand by thin and thick disk, and has an impact on the distribution of other properties characterizing them. The chosen parameter or criterion should allow describing the large-scale distribution of stars in both disks.

Star-count-based characterizations of the disk system are prone to systematics arising from degeneration in age-color relations or from the adoption of a single scale height to model the thick disk in all its radial extension. These effects can lead to spurious results, blurring other properties by the cross contamination of thick and thin disk stars in the samples.

A kinematic selection criteria ([Soubiran *et al.* 2003, Bensby *et al.* 2014]) has been proposed to separate samples by assigning membership probabilities, modeling the Galactic space velocities U_{LSR}, V_{LSR} and W_{LSR} as Gaussian distributions (Fig. 1.19). This kind of sample selection allows to obtain cleaner distributions in other parameters, but some superposition still exists.

Recently, it has been proposed to use chemical information to separate disk samples by the relative enhancement in α-elements (e.g. [Navarro *et al.* 2011, Adibekyan *et al.* 2013, Recio-Blanco *et al.* 2014, Mikolaitis *et al.* 2014, Kordopatis *et al.* 2015]). The chemical composition of a star is a more stable property than the kinematics or spatial distributions during the complex evolution of a stellar system ([Freeman & Bland-Hawthorn 2002]). The idea is to define thin and thick disk stars from their location in the α-abundance metallicity plane, which is conceptually equivalent to understanding them as dual different star formation rates ([Chiappini 2009]). When the data quality is good enough, the identification of two distinct sequences of α-poor and α-rich stars, associated with the thin and thick disks, allow to separate samples with remarkable results in spatial, kinematics, and age distributions.

In a different interpretation of SEGUE data, [Bovy *et al.* 2012] discarded the existence of a thick disk as a different structural component. There is no necessity of a

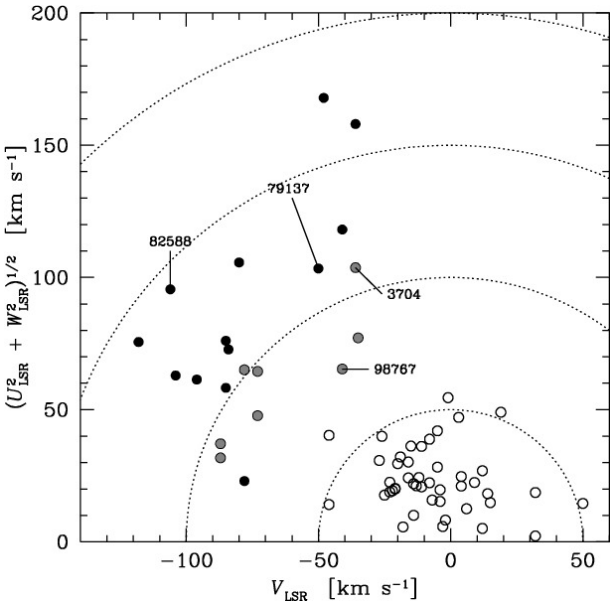


Figure 1.19: Toomre diagram for a disk stellar sample classified with a kinematic criteria. Solid lines indicate constant values of the total space velocity $v_{tot} = \sqrt{U_{LSR}^2 + V_{LSR}^2 + W_{LSR}^2}$ in steps of 50 km s^{-1}. Thin and thick disk stars are depicted by open and full circles, respectively. Figure reproduced from [Bensby *et al.* 2003].

double exponential to explain the vertical stellar density profile in their mass-weighted scale-height distribution. In this sense, they interpreted the observed bimodality in the [α/Fe] vs. [Fe/H] plane as an effect of the lack of correction of the spectroscopic sample to account for the survey selection function, otherwise affected by the survey-specific spatial and mass sampling of the underlying stellar populations.

The case for a clear gap outside the solar neighborhood (a low density region in the number density distribution) between thin and thick disk sequences in the [α/Fe] vs. [Fe/H] plane was presented by [Recio-Blanco *et al.* 2014], based on data from the first nine months of the Gaia-ESO survey. In the same line, [Anders *et al.* 2014], using the first year of APOGEE data, confirmed the existence of the gap, not only in the solar distance bin, but also in two other radial bins in the inner and outer parts of the galactic disk. These authors argued that in APOGEE the target selection would not be enough to create such a gap. This was later on confirmed by [Nidever *et al.* 2014] using a red clump (RC) sample for which the uncertainties in the distances could be reduced from the typical 20% uncertainties to a $\sim$ 5% level, as claimed in [Bovy *et al.* 2014].

In the thin and thick disk sequences framework, ages were determined by [Haywood *et al.* 2013] to further characterize the HARPS local neighborhood sample of [Adibekyan *et al.* 2013]. They identified the thin and thick disk sequences with two epochs in the formation history of the Milky Way, with different timescales, different enrichment rates, and different assembling mechanisms. Their age-based classification into thin and thick disk agrees remarkably well with the location of those stars in the two sequences of the abundance-metallicity plane.

Using a sample of $\sim$ 10000 RC stars from the SDSS-III/APOGEE, [Nidever *et al.* 2014] traced patterns in the [α/Fe] vs. [Fe/H] plane through a large Galactocentric radial domain. The thick disk displays a relatively constant trend in this plane with radial distances, while the thin disk distribution is more radially dependent. They suggested that while in the inner Galaxy stars in both disks could be explained by a single chemical

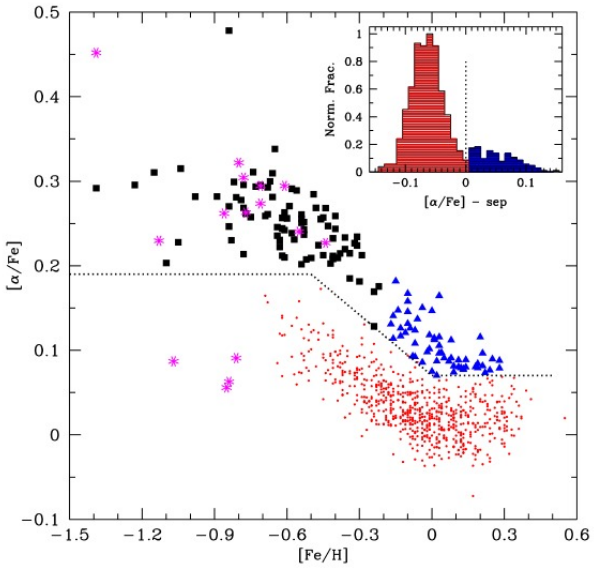


Figure 1.20: Solar neighborhood FGK dwarf stars in the [α/Fe] vs. [Fe/H] plane. A black dotted line depict the chemical division into thin and thick disk populations adopted by [Adibekyan *et al.* 2013]. Figure reproduced from [Adibekyan *et al.* 2013].

evolutionary track, more complicated assumptions are needed to explain their distributions in outer regions. These results were confirmed over a larger distance range in [Hayden *et al.* 2015] by using a sample of red giant stars from APOGEE DR12.

Other recent studies have characterized the thick disk as a structure with negative vertical and flat radial metallicity gradients ([Mikolaitis *et al.* 2014]). The thin disk instead, presents gradients in both directions ([Hayden *et al.* 2014, Recio-Blanco *et al.* 2014, Mikolaitis *et al.* 2014]), an imprint predicted by the inside-out disk formation paradigm, first proposed by [Larson 1976].

In the same line, observations of open clusters as tracers of young stellar populations (which makes them a good proxy for the current metallicity of the ISM) show that outside the solar radius, at distances $R_{GC} > 9 - 10$ kpc and subsolar metallicity, the radial metallicity gradient flattens ([Bragaglia *et al.* 2012, Yong *et al.* 2012, Frinchaboy *et al.* 2013]). This shallow slope is consistent with determinations based on Cepheids ([Genovali *et al.* 2014]). In this context, the existence of an external distinct region of the thin disk (with [Fe/H]<-0.25 dex) has been proposed. From age and kinematics considerations, [Haywood *et al.* 2013] have proposed a different chemodynamical history for this region, whose properties seem to be intermediate to those of the internal thin disk and the thick disk. The presence of such metal-poor thin disk stars in their local sample is explained in their scenario as an effect of the Sun being at the interface of the two regions of the disk ([Snaith *et al.* 2015]), so without the necessity of invoking churning, but maybe some degree of blurring radial migration processes.

The detailed understanding of the nature of the thin and thick disks, their age, chemical and spatial distributions, and their correlations, is important to set a context in which the nature and origin of the bulge can be understood.

As mentioned above, the characterization of the solar neighborhood sample of [Haywood *et al.* 2013] lead the authors to propose an alternative interpretation of the high- and low-α sequences of disk stars in the abundance-metallicity plane. Thick disk and metal-rich thin disk stars are dominant inside the solar radius, so that they can be con-

sidered as constituting an inner disk sequence. On the other hand, metal-poor think disk stars dominates outside the solar neighborhood, constituting an outer disk sequence.

In [Ness *et al.* 2013a], the three main components of the bulge MDF, A, B and C (see Fig. 1.8) are interpreted as composed by stars from the young thin disk, the old thin disk and the thick disk, trapped in the bar potential. In this sense, the Milky Way bulge is thought to be the result of a pure thin disk instability. In this context, N-body simulations of bulge formation via bar formation and buckling showed that just an initial thin disk is enough to reproduce global bulge properties such as the metallicity distribution ([Martinez-Valpuesta & Gerhard 2013]) and the velocity rotation and dispersion curves ([Shen *et al.* 2010]). This picture has been challenged by [Di Matteo *et al.* 2015] by arguing that pure thin disk formation models fail in reproducing the detailed chemo-kinematic relations of bulge stars (see also the review of [Di Matteo 2016]). Instead, they propose than the bulge might be the result of the mapping of the inner disk sequence of [Haywood *et al.* 2013] (so, thick and metal-rich thin disk) into the B/P bulge structure by the bar instability event. Such scenario, allows to establish a parenthood between the metal-poor bulge and the thick disk, and finds support in a number of observational evidences, in particular by the chemical similarities between stars belonging to these two populations (see Fig. 1.13).

All in all, the interpretation of the stellar distribution in the metallicity-abundance plane in the context of disk structures is a current hot topic of debate. Separating the relative contribution of thick/thin, inner/outer disks, and understanding the variations of their properties with R_{GC} and Z, is an important step to reconstruct the formation history of the disk as a complex entity during the assembly of the Milky Way.

1.7 The Gaia mission

A great deal of progress in many areas of the astrophysics was triggered and feeded over the last two decades by the enormous astrometric dataset provided by the Hipparcos mission ([Perryman *et al.* 1997]). In the same line, the Gaia mission was conceived as one of the most ambitious ESA space missions. The satellite was successfully launched from Kourou (French Guiana) in December 2013, and is currently in operations at the second Lagrange point, at 1.5 million kilometers from Earth, for a nominal five years mission period. Gaia will determine positions, proper motions, parallaxes and radial velocities for more than one billion stars with $V < 20.7$ mag, representing approximately 1% of the stellar content of the Galaxy in a significant fraction of its volume ([Perryman *et al.* 2001]).

For a fraction of the targeted stars, Gaia will moreover determine fundamental parameters, metallicity and elemental abundances. The unprecedented amount and precision of the end-of-mission data provided by Gaia will allow for a three dimensional spatial and dynamical cartography of a major volume of the Milky Way. The impact over several areas of astrophysics promises to be enormous and revolutionary.

We outline below some general characteristics of the Gaia instruments and observing modes to be performed by Gaia, as well as the expected scientific yields, in particular for Galactic archaeology.

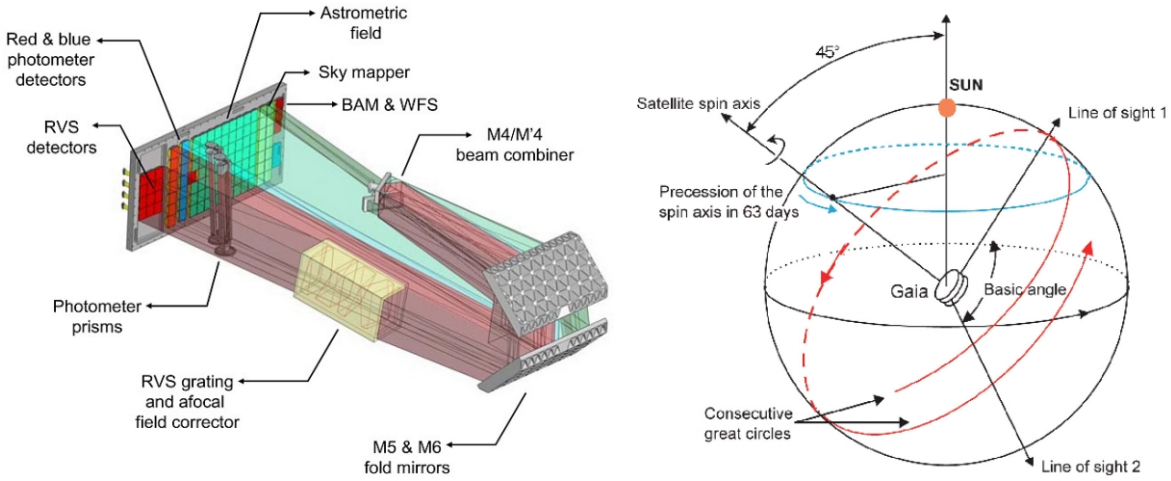


Figure 1.21: *Left panel:* Configuration of Gaia instruments (credit: EADS Astrium). *Right panel:* Diagram of the scanning law for the Gaia's two field-of-view observing motion.

1.7.1 Layout and observation principles

In simple terms, the Gaia observations rely on a pattern of repeated and systematic observations of the sky in a cyclic scanning motion. Over the five years mission, this means that a given sky region will be observed several times. The satellite has two primary mirrors of 1.45×0.5 m^2 (along scan $\times$ across scan direction) with a basic angle of 106.5 degrees (see left panel of Fig. 1.21). The collected light is combined in the focal plane by a set of secondary mirrors. The observations are conducted according to a carefully prescribed scanning law, which is illustrated in the right panel of Fig. 1.21. The satellite continuously spin around its axis at a rate of one revolution every 6 hours. Additionally, the rotation axis slowly precesses with an average period of 63 days. The angle between the slowly precessing axis and and the Sun-Earth line is maintained at 45 degrees ([Mouret *et al.* 2007]). This angle is a compromise in order to simultaneously have the largest possible angle with respect to the Sun direction while obtaining a sky sampling as uniform as possible. Under this scanning law, Gaia will steadily map all the sky, performing an average of 70 observations per source in the 5 year nominal mission operation lifetime. In Fig. 1.22 we display the resulting density of observations pattern from this nominal scanning law.

1.7.2 On-board instrumentation

As an astrometric, photometric and spectroscopic mission, the Gaia satellite hosts a number of instruments specifically designed to accomplish these different aspects. A diagram of the Gaia on-board instruments described below is given in Fig. 1.21.

- **Astrometric instrument ASTRO:** It made use of the global astrometry concept of Hipparcos, by measuring the relative separation of stars simultaneously present in the combined fields of view of the two primary mirrors. As the satellite

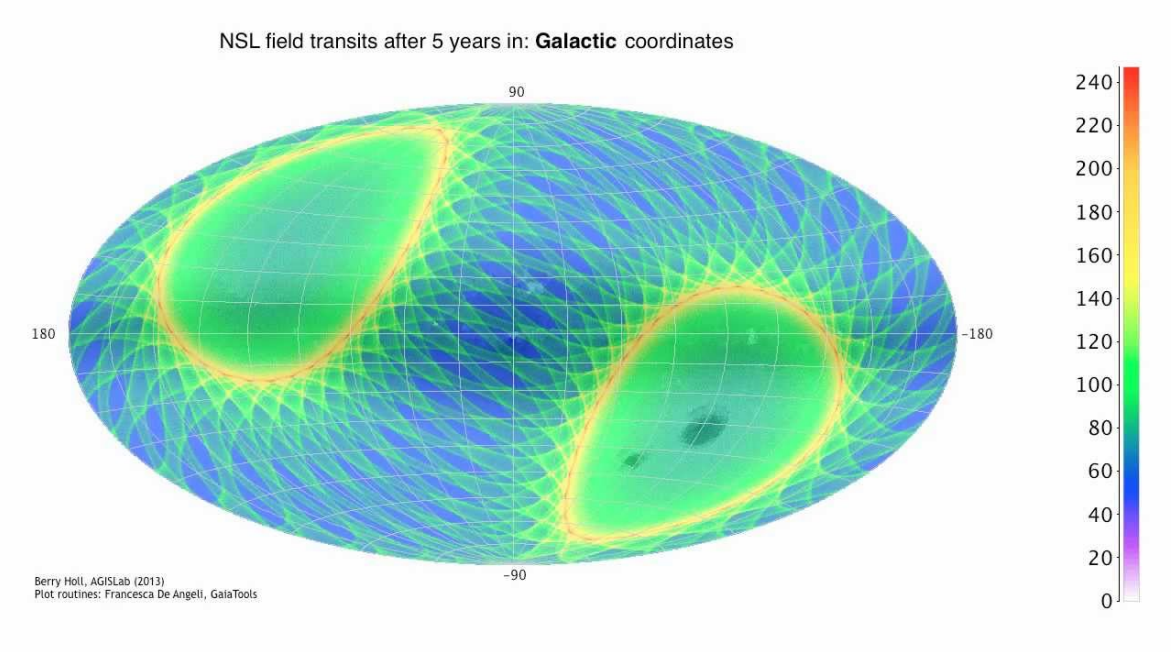


Figure 1.22: Gaia's end-of-mission pattern of transits from the nominal scanning law. Credits, Berry Holl.

spins about its rotation axis, a continuous stream of relative angles is measured as the field of view sweeps across the sky. Parallaxes are expected to reach end-of-mission precision levels of 7 μas at $V = 10$, 20-25 μas at $V = 15$, and 100-350 μas at $V = 20$ ([Jordi *et al.* 2010]).

- **Spectro-photometric instrument:** two low resolution prisms, the blue and red photometers (BP, RP, see left panel of Fig. 1.21), located between the main mirrors and the focal plane, cross disperse all the light entering in the field of view. The blue photometer will disperse light covering the wavelength range 3300-6800 Å with a sampling of 30-270 Å per pixel, while the red photometer will sample the 6400-10500 Å range with a sampling of 70-150 Å per pixel. In this way, the spectral energy distribution will be sampled for all sources down to a flux limit of $G = 20$, where G is the Gaia passband ([Jordi *et al.* 2006]). These low resolution spectra will allow the determination of fundamental parameters $T_{\rm eff}$, $\log(g)$ and global metallicity [M/H] for an expected number of 10^9 stars. For FGKM stars at $G = 15$ ($V = 15$-17), it is expected to estimate $T_{\rm eff}$ within 100 K precision, 0.25 dex for $\log(g)$ and 0.2 dex for metallicity ([Bailer-Jones *et al.* 2013]).

- **Radial velocity spectrometer:** The radial velocity spectrometer (RVS) is a mid-resolution integral field spectrograph designed to perform fast observations as the satellite scans the sky, obtaining $R \sim 11200$ spectra at a rate of 100 per second. In the five years mission lifetime, this high observing rate will yield about 15 billion spectra. The primary goal of the instrument is the determination of radial velocities. To this end, the RVS samples a spectral region centered around

the CaII triplet feature (8470-8710 Å), and will obtain spectra with a sufficient high SNR to derive $V_{\rm rad}$ for all stars with $G_{\rm RVS} \lesssim 16$ (where $G_{\rm RVS} \lesssim 16$ is the Gaia magnitude through the RVS filter), or 150 million stars. This will provide the full three-dimensional space motions of stars when combined with the Gaia proper motions.

With this spectral resolution, the region around the calcium triplet provides a number of distinguishable weak features of SiI, TiI and FeI. This provides an opportunity to be exploited through the parametrization of the brighter stars to complement what it is performed independently from the two lower resolution BP and RP spectro-photometers. In this sense, all stars brighter than $G_{\rm RVS} \approx 14$, or several tens of millions, will be analyzed by one of the coordination units (CU8) of the Gaia Data procession and Analysis Consortium (DPAC) through the GSP-Spec pipeline ([Recio-Blanco *et al.* 2016]). This pipeline consists on the combination of MATISSE, DEGAS and GAUGIN, and will eventually include other analysis approaches such as artificial neural networks ([Fustes *et al.* 2012]). The GSP-Spec pipeline will be optimized to classify and deal with different types of the stars, ensuring that a robust and homogeneous parametrization can be produced for all of them. For all stars brighter than $G_{\rm RVS} \approx 14$, $\rm T_{eff}$, $\log(g)$, [M/H] and [α/Fe] will be determined. In addition, detailed abundances of Fe, Ca, Ti and Si are expected to be determined for about 5 million sources with $G_{\rm RVS} \lesssim 12$.

1.7.3 Gaia scientific yields

The primary goal of Gaia is to determine the structure, formation and evolution of the Milky Way. The 6D position-velocity phase space (**x**,**v**) vectors will be accurately determined for tens of millions of stars thanks to the combination of positions, parallaxes, proper motions and radial velocities. The determination of fundamental parameters will allow to further estimate ages. With this dataset it will be possible to decode the star formation history of the Galaxy and understand the involved physical processes and the temporal sequence in which the different structures assembled to form the present day Milky Way. Specific questions concerning the hierarchical or secular origin of the bulge, the formation by dynamical heating of accretion of building blocks for the thick disk, and the assembling history of the stellar halo will be possible to be addressed with an unprecedented detail.

In a broader sense, Gaia will make possible to deal with many issues which go beyond the main goal of the mission. It will allow to revise and refine ideas concerning stellar structure and evolution. In a local scale, a solar system census will be possible, discovering small wondering objects such as asteroids and transneptunian objects. The first step of the distance ladder rely on the proper calibration of standard candles with trigonometric distances. Gaia will enable this through the precise determination of luminosity of cepheids as well as refining the distance to the Magellanic Clouds. It is expected that Gaia will discover thousands of large extrasolar planets to 200-500 pc around the Sun, both via the astrometric detection of the primary star wobbling or by photometric transit, and will even allow for orbital characterization for many of

them. In the same way, tens of thousands of white dwarfs, brown dwarfs, as well as thousands of extragalactic supernovae and quasars are expected to be detected. It is even expected that the unprecedented precision level of Gaia measurements will contribute to fundamental physics, for example enabling to perform tests on the General Relativity by characterizing the bending of light by the larger solar system planets and the Sun. Last, but not least, the availability of precise proper motions for stars all the way to the bulge will allow to obtain clean samples of bulge objects for detailed study and further spectroscopic follow up. Moreover, the availability of radial velocities will allow for 6D dynamical studies based on unprecedented large samples. A very detailed structural and dynamical picture of the bulge will subsequently emerge from the synergies of Gaia data and further photometric and spectroscopic follow up campaigns. Without any doubts exiting times are coming.

1.8 The Gaia-ESO Survey

The Gaia-ESO survey is an ESO public spectroscopic survey ([Gilmore *et al.* 2012]), which in 3000 hours of observation over a period of five years (December 2011-December 2016) has the goal of observing 10^5 stars distributed in the main components of the Milky Way: The bulge, the disks, including clusters, and the halo. The Gaia-ESO survey is the product of the coordinate effort of more than 300 scientist in over 90 institutions. The primary goal of the survey is to perform an homogeneous overview of the distribution of kinematics and elemental abundances over a large Galactic volume.

The observations are performed with the FLAMES facility at the ESO/VLT UT2 (Kueyen) 8.2 meter telescope, using both GIRAFFE (in MEDUSA mode) as well as the UVES spectrographs. The employed GIRAFFE setups are optimized in relation with the nature of the targets and the scientific goals of the different survey portions, as outlined below.

- **Bulge:** the primary targets are red clump giants, which are selected from the field CMD diagrams by adopting VVV photometry. The selection function is described in Chap. 2 of this thesis. The selected stars are observed using the HR21 GIRAFFE setup, which provides spectral coverage in the region around the calcium triplet (8484-9001 Å, $R \sim 16\,200$). A sample of foreground brighter giants is simultaneously observed with UVES (4700-6840 Å, $R \sim 47\,000$) by allocating these fibers on bright stars in each field. The goal is to characterize the stellar populations residing in the central kiloparsecs of the Galaxy by means of a detailed chemical characterization coupled with kinematics.

- **Disk(s) and halo:** the primary targets are FGK stars. The target selection is done using VISTA photometry, as described in the next chapter. The selected stars are observed both with the HR10 (5339-5619 Å, $R \sim 19\,800$) and HR21 GIRAFFE setups, with a companion smaller portion of stars simultaneously observed with UVES. The goal is to understand the chemical distribution of thin and thick disk stars to highlight their differences, as well as characterize their potential radial and/or vertical gradients in metallicity and/or chemical abundances. These results

might help to understand at which degree, if any, radial migration dominates the dynamical evolution of the Galactic disk.

- **Clusters:** the targets are clusters spanning a broad age an metallicity range, from young open clusters of a few Myr (but no embedded clusters) to old open and globular (which are observed for calibration purposes) clusters. Several GIRAFFE settings are employed to observe stars according to the specific characteristics of the star sample. The photometric selection is done from 2MASS photometry and ESO archival data. The aim is to understand the processes of formation, early chemical and dynamical evolution, and the processes driving their posterior dissolution. This is important since it is possible that most of the disk field stars come from diluted open clusters.

The Gaia-ESO survey is organized on the basis of working groups on charge of the different tasks, from target selection and observation, to the derivation of the different fundamental parameters and abundances required to achieve the scientific goals of the survey. In Fig. 1.23, a schematic chart of the working flow inside the consortium is shown. The target selection process is customized to meet the requirements of the different science cases. A detailed description of the selection function of disk/halo fields and bulge stars adopted in this thesis is presented in the next chapter. Once spectra are obtained, a processing cascade reduces the data, removes instrument features and telluric lines, calibrates spectra and estimates radial velocities. The estimation of fundamental parameters is performed by different working groups depending on the instrument (GIRAFFE/UVES) and the nature of the studied targets (field stars/clusters).

The Gaia-ESO survey provides radial velocities, fundamental parameters, metallicity and detailed chemical abundances for several elements Al, Mg, Si, Ca, Ti, Cr, Mn, Fe, Co and Ni (depending of the instrument/setup) for a large number of stars distributed in a large volume of the disk, the bulge and the halo.

In addition to its stand alone scientific value, we can think the Gaia-ESO survey as a pre-follow-up and complement of the Gaia mission. In fact, as presented above, Gaia will provide precise positions, parallaxes and proper motions for all observed stars down to $V = 20.7$ mag, while radial velocities will be available just for stars down to $V \sim 17$ (that in any case will be less precise than proper motions at that magnitude). In this sense, the Gaia-ESO survey will provide radial velocities filling the gap of Gaia to provide three dimensional motions for a large number of stars down to $V = 20$. In this way, the Gaia-ESO survey will increase the dimensionality which will be possible to analyze for a large number of stars. Moreover, the six dimensional phase-space ($\mathbf{x}$,$\mathbf{v}$) provided by Gaia and GES data, will be complemented by the chemical space given by the detailed abundances derived from GES spectra. The relative spatial distributions and the correlations between chemistry and kinematics are fundamental to understand the way how different stellar populations assembled to form the Milky Way. We can expect to be able to reconstruct the spatial and temporal evolution of chemistry and kinematics in order to determine at which point the formation of different structures, for example the thick disk and the bulge, are interconnected. The combination of Gaia-ESO survey and Gaia datasets promise to yield a wealth of information, enabling us to perform a chemo-dynamical cartography of a large volume of the Galaxy.

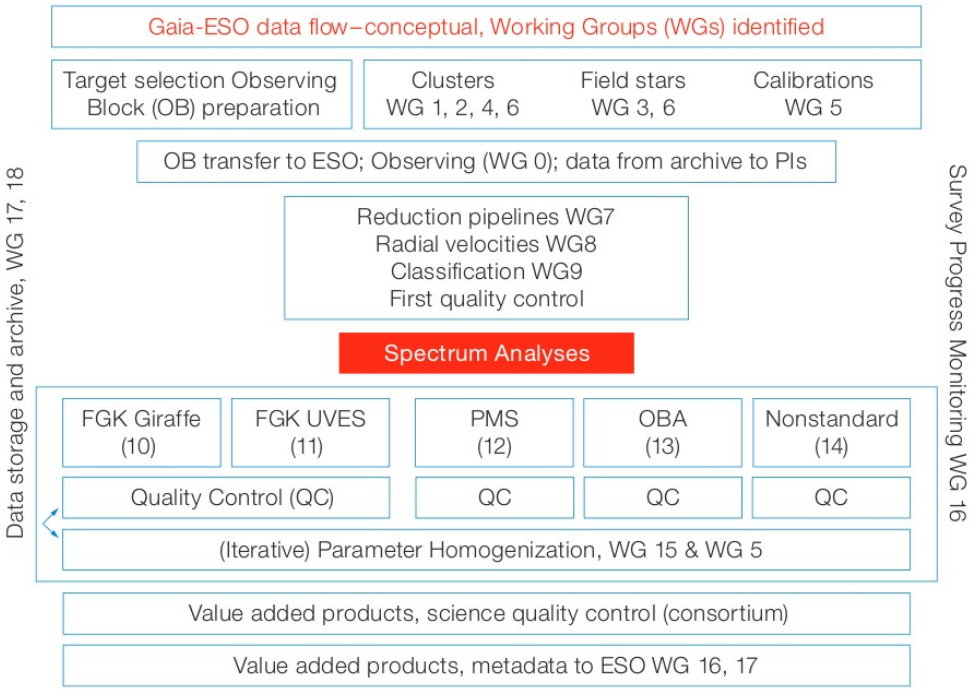


Figure 1.23: Gaia-ESO survey schematic working flow diagram. The GES consortium has a working group structure that manages the data flow from target selection through data reduction, quality control, fundamental parameters and detailed abundances determination, and homogenization, to produce the final data products for scientific analysis. The different layers of this processing cascade, and the working groups in charge of the different tasks are depicted in the chart.

Concerning the bulge, it would be desirable to have a dataset providing spectra of high signal-to-noise, high resolution -enough to perform detailed chemical diagnostics- and a broad spatial coverage, with sample sizes at each observed field of sufficient statistical weight. The Gaia-ESO survey provides such a dataset. In fact, as it will be described in the next chapter, the general spectra quality and the footprint of GES bulge fields is designed to provide a detailed overview of the stellar populations at several southern Galactic latitudes, both along the bulge minor axis as well as in off-axis positions. The importance of studying a dataset allowing detailed analysis at specific positions, as well as the comparison of trends across the bulge region is evident and represents an opportunity not provided by previous surveys.

1.9 Other current and future Galactic surveys

The Galaxy is an ideal laboratory to conduct detailed studies of its resolved stellar populations to understand galaxy formation and evolution. A new era of large sample-based studies is given by the transition from PI-based observing campaigns, targeting samples of the order of hundreds, to large survey astronomy aiming at observe samples of hundred thousands, and in the forthcoming years, millions of stars. This revolution

is partly boosted by the large all sky photometric surveys providing homogeneous and deep photometry from which all these spectroscopic surveys can feed their target lists. In the following, we provide a brief overview of some of the most recent and relevant surveys for the development of this thesis.

1.9.1 APOGEE

The Apache Point Observatory Galactic Evolution Experiment (APOGEE, [Majewski *et al.* 2015]) is a large scale systematic and homogeneous spectroscopic survey designed to observed 10^5 giant stars across the main Galactic components. Observations are performed at bright time with a dedicated 300-fiber cryogenic high resolution ($R \sim 22500$) spectrograph operating in the near infrared at the H band (1.51-1.70 μm). By observing at NIR wavelengths, APOGEE overcomes the limitations imposed by the large amount of dust extinction in the Galactic plane and towards the bulge, which have historically limited optical studies in these inner areas. The main targets of APOGEE are giant stars (RGB, AGB and RC), intrinsically luminous tracers present in stellar populations of all ages. They are selected adopting 2MASS photometry and are observed down to a flux limit of H=12.2. The high resolution and high SNR (typically larger than 100 per resolution element), allow to obtain precise radial velocities (< 100 m s^{-1}) and to determine stellar parameters and chemical abundances of 15 elements (α-elements, iron-peak and Z-odd) up to 0.1 dex of precision. This data set is intended to provide deep insights on the dynamical structure and chemical evolution of the Galaxy, allowing to study the evolution of chemical elements as a function of time and location. Despite the fact of observing at low latitudes, APOGEE targets stars in the main Galactic components, the bulge the thin disk, the thick disk, and halo. This sampling provides the opportunity to study in detail at which point the stellar populations in all these components compares or differ with respect to each other, broadening our understanding of the physical processes driving Galactic assembling and chemodynamical evolution. The APOGEE survey (2011-2014), observing at the Apache Point Observatory (New Mexico), will be complemented with southern hemisphere observations from a twin instrument installed in the Du Pont telescope at Las Campanas Observatory in Chile (APOGEE-2, 2014-2020).

1.9.2 LAMOST

The Large sky Area Multi Object fibre Spectroscopic Telescope (LAMOST, [Zhao *et al.* 2012]) survey is conceived to observe, over a period of 5-6 years, 10 million of Milky Way stars distributed in most of the northern sky area. Observations are performed down to a flux limit of $r = 19$ with a 4 meter Schmidt telescope, which provides a wide field of view of 5 square degrees. Up to 4000 fibers are allocated to feed a set of spectrographs which provide spectra in the spectral range $3700 \leq \lambda \leq 9100$ Å, with a resolution of $R \sim 1800$. The resolution and general spectra quality are intended to attain a radial velocity and metallicity precision of $\sigma V_{rad} \sim 7$ km s^{-1} and σ[Fe/H] ~ 0.3 dex, similar to those of the SDSS-III/SEGUE (Sloan Extension for Galactic Understanding and Exploration). The Galactic portion of the LAMOST survey (LAMOST Experiment

for Galactic Understanding and Exploration - LEGUE) includes a search for metal-poor halo stars and expect to be the source of several serendipitous discoveries given the vast volume of data. The first data release ([Luo *et al.* 2015]) includes $\sim$ 3 000 000 stars, for which fundamental parameters and metallicities have been derived though dedicated pipelines developed for the survey.

1.9.3 GALAH

The GALactic Archaeology with HERMES (GALAH) survey ([Freeman 2012, De Silva *et al.* 2015]) is a large optical spectroscopic survey designed with the goal of observing 10^6 stars over most of the southern hemisphere with $|b| > 10°$ and $\delta < +10°$. The main targets of the survey are disk and bulge stars. Observations are performed at the 3.9-meter Anglo-Australian Telescope (AAT), which allows the allocation of targets over a 2 degree field-of-view. The targets are selected from 2MASS photometry to be observed down to a faint flux limit of $V = 14$. The multiplexing capabilities of the HERMES spectrograph allows to allocate up to 400 fibers to obtain stellar spectra in four non-contiguous optical bands at a resolution of $R \sim 28000$. The selected spectral windows are optimized to obtain spectral features of a maximized number of chemical species, and covers about 1000 Å in the range 4718-7890 Å. From the resulting high quality spectroscopic dataset (SNR > 100), the GALAH survey is expected to yield a detailed chemical characterization, measuring abundances for up to 15 chemical elements. The main objective of the survey, is to apply the principles of chemical tagging to identify stars coming from common ancient star formation sites from their matching abundance patterns. This endeavor, might allow to reconstruct the detailed star formation history and dynamical evolution of the Milky Way. The survey started observations in late 2013, and up to the time of writing of this thesis, has observed 175000 stars in more than 500 different fields.

1.9.4 WEAVE

WEAVE is a new wide-field optical MOS (multi-object spectroscopy) facility proposed for the prime focus of the 4.2-meter William Herschel Telescope, La Palma, Spain ([Dalton *et al.* 2012]). The instrument has a multiplexing capability of $\sim$ 1000 targets per shot, distributed in a field-of-view of 2 degrees in diameter. The targets can be observed in low ($R \sim 5000$) or high spectral resolution ($R \sim 20\ 000$). Several surveys have been proposed to exploit the capabilities of this instrument, with scientific goals covering a wide range of research fields. The Galactic Archaeology survey is planned to complement and fully exploit Gaia data by providing precise radial velocity and chemical element measurements for targets that are too faint for the Gaia RVS. In this sense, millions of stars will be observed, providing radial velocities for stars fainter than $V = 15$ (with $R \sim 5000$ in the range $V = 17$-20, and $R \sim 20\ 000$ for $V < 18$), and chemical abundances for those fainter than $V = 12$. As a northern hemisphere survey, WEAVE has the privileged vantage point to explore the outer Milky Way disk. Moreover, because of its technical capabilities, WEAVE will provide a unique dataset in terms of depth and resolution, something which is not provided by any current or planed optical

spectroscopic survey. In general, the Galactic Archaeology survey will address a number of issues concerning Milky Way structure and evolution; determination of its mass and mass assembling over time, the 3D Galactic potential, the origin of the stellar thick disk, characterization of halo stellar streams, determination of the fraction of halo stars originated in accreted systems, etc. The observations are expected to start in early 2018.

1.9.5 4MOST

The 4-meter multiobject spectroscopic telescope (4MOST, [de Jong *et al.* 2012]) is a MOS instrument designed to enter in operations at the VISTA telescope, Paranal, Chili, in early 2022. Given its capabilities and scientific goals, 4MOST can be considered as the southern hemisphere counterpart of the WEAVE instrument. In fact, its spectroscopic observations, covering the full optical wavelength region, will complement measurements of Gaia by providing radial velocities to ~ 1 km s^{-1} accuracy down to the depth of Gaia astrometric limits, and detailed abundances for stars brighter than $V = 16$ for million of stars. The multiplexing capabilities of 4MOST, in its 4.1 square degree field-of-view, depends on the selected resolution mode. In the low-resolution mode, 1624 fibers can be allocated, covering the wavelength range 3700-9500 Å with a spectral resolution of $R \sim 4000 - 7800$ per sampling element. On the other hand, observations in the high-resolution mode allow for the observation of up to 821 targets with $R \sim 18500$, covering the spectral range 3926-6790 Å in three non overlapping regions (3926-4355 Å, 5160-5730 Å, 6100-6790 Å).

1.9.6 MOONS

The Multi-Object Optical and Near-infrared Spectrograph (MOONS, [Cirasuolo *et al.* 2011]) is a third generation instrument for the VLT. Similarly to the Galactic surveys planned for WEAVE and 4MOST, the Galactic Archaeology science to be performed with MOONS is expected to provide an adequate follow-up to Gaia and other ground based surveys by measuring radial velocities, metallicities and chemical abundances for several millions of stars. The instrument will allow to allocate up to 1024 fibers over a field-of-view of ~ 500 square arcmin. The targets can be observed in a medium-resolution mode ($R \sim 4000 - 6000$) with a wavelength coverage of 6400-18 000 Å, or in a high-resolution mode obtaining spectra in three bands simultaneously (7700-9000 Å at $R = 9000$, 11 700-12 600 Å at $R = 20\,000$ and 15 200-16 300 Å at $R = 20\,000$). The instrument's first light is expected for 2018-2019.

1.9.7 VVV

The Vista Variables in the Vía Láctea (VVV, [Minniti *et al.* 2010, Saito *et al.* 2012]) survey is an infrared variability survey of the Milky Way bulge and an adjacent stripe of the disk. The surveyed bulge area extends $-10 \leq l \leq +10.4$, $-10.3 \leq b \leq +5.1$, while the disk stripe that at $295 \leq l \leq 350$, $-2.25 \leq +2.25$. They are outlined in Fig. 1.24. The observations are performed at the 4.1 meter Visible and Infrared Telescope for Astronomy (VISTA), with the near infrared VIRCAM camera in five passbands, Z,

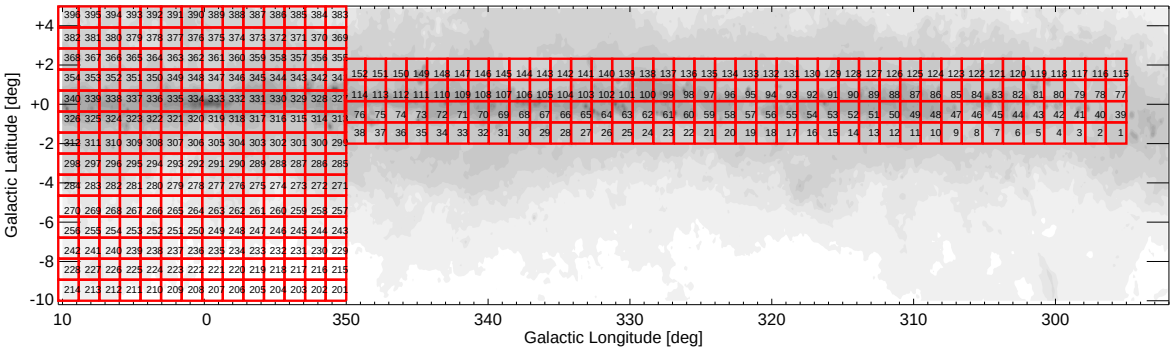


Figure 1.24: Total area sampled by the VVV survey. The red lines depict the bulge and adjacent disk area and its division into tiles, which are numbered. Figure reproduced from [Saito *et al.* 2012].

Y, J, H and K_s. With a total observation time of 1920 hours, the VVV is conceived to perform repeated observations over the period 2010-2015, covering a total area of 520 square degrees, and providing photometry for 10^9 point sources, from which 10^6 variable sources are expected to be identified. The resulting photometric catalogs will be complementary to 2MASS by the addition of the two extra Z and Y passbands and the fainter flux limits attained by VVV photometry. In fact, the VVV photometric catalogs reach saturation around $K_s = 12$ and go faint to a limiting magnitude of $Ks = 18$ in most of the fields (down to $K_s = 16.5$ even for the innermost bulge fields at $|b| \leq 1°$). The surveyed area is divided into tiles. There are 396 of them, 196 in the bulge and 152 in the disk area (Fig. 1.24).

The VVV will provide a deep three dimensional (or four dimensional, if we consider the time domain) map of the surveyed region, by using primary distance calibrations such as RR Lyrae stars. In between the main objectives of the survey are the determination of Galactic structure, detection of new variable sources (RR Lyrae, classical Cepheids, Cepheids of type II, Miras, semi irregular variables, etc), the search for microlensing events and the search for unobserved clusters hidden by the large dust extinction close to the plane. It will help to increase considerably the general physical understanding of star variability, and is expected to provide many serendipitous discoveries.

As a final, but relevant to us, point, the photometric selection function and ancillary photometric catalogs of the Gaia-ESO survey bulge fields, is based on VVV data, as presented in Chap. 2 (see Fig. 2.3).

1.10 Goal of this thesis

The main goal of this thesis is to understand the complex nature and physical processes involved in the formation of the Milky Way bulge. The Galactic bulge is not only an old but also a massive structural component which has witnessed the early history of Galactic assembling and chemical evolution. In this sense, a detailed study of the bulge's stellar content, kinematics, morphology and chemical abundances, may allow

us to unveil the different chemodynamical processes that shaped its current observable properties. Such a Galactic archaeological endeavor, aims at reading the fossil records imprinted in the stars to understand the role played by the different mechanisms proposed to explain the bulge formation. Is the Galactic bulge the product of a single formation mechanism? and in the same line, is the Galactic bulge a single stellar population? and if not, are other Galactic components related with the genesis of one/all the bulge stellar populations? Answering this kind of key questions is fundamental to understand the Galaxy formation, and since the Milky Way is an archetypal spiral galaxy, galaxy formation in general.

1.11 Works published during the course of this thesis

A number of papers have been published during the course of this thesis. As it is listed below, few of them are the direct product of the research conducted and described in this manuscript, while others are the product of related research projects, exploring other aspects of Galactic populations and going also beyond the spectroscopic approach.

First author papers directly related to this thesis:

- **Rojas-Arriagada, A.**, Recio-Blanco, A., Hill, V., de Laverny, P., Schultheis, M., Babusiaux, C., Zoccali, M., Minniti, D., Gonzalez, O. A., Feltzing, S., Gilmore, G., Randich, S., Vallenari, A., Alfaro, E. J., Bensby, T., Bragaglia, A., Flaccomio, E., Lanzafame, A. C., Pancino, E., Smiljanic, R., Bergemann, M., Costado, M. T., Damiani, F., Hourihane, A., Jofré, P., Lardo, C., Magrini, L., Maiorca, E., Morbidelli, L., Sbordone, L., Worley, C. C., Zaggia, S., Wyse, R. (2014) *The Gaia-ESO Survey: metallicity and kinematic trends in the Milky Way bulge*, A&A, 569, A103. Presented in Chap. 5 and 6.

- **Rojas-Arriagada, A.**, Recio-Blanco, A., de Laverny, P., Schultheis, M., Guiglion, G., Mikolaitis, S., Kordopatis, G., Hill, V., Gilmore, G., Randich, S., Alfaro, E. J., Bensby, T., Koposov, S. E., Costado, M. T., Franciosini, E., Hourihane, A., Jofré, P., Lardo, C., Lewis, J., Lind, K., Magrini, L., Monaco, L., Morbidelli, L., Sacco, G. G., Worley, C. C., Zaggia, S., Chiappini, C. (2016) *The Gaia-ESO Survey: Separating disk chemical substructures with cluster models. Evidence of a separate evolution in the metal-poor thin disk*, A&A, 586, A39. Presented in Chap. 4.

- **Rojas-Arriagada, A.**, Recio-Blanco, A., de Laverny, P., Mikolaitis, Š., Matteucci, F., Spitoni. E., Schultheis, M., Hayden, M., Hill, V., Zoccali, M., Minniti, D., Gonzalez, O., A., Gilmore, G., Randich, S., Feltzing, S., Alfaro, E., J., Babusiaux, C., Bensby, T., Bragaglia, A., Flaccomio, E., Koposov, S., E., Pancino, E., Carraro, G., Casey, A., R., Costado, M., T., Damiani, F., Donati, P., Franciosini, E., Hourihane, A., Jofré, P., Lardo, C., Lewis, J., Magrini, L., Morbidelli, L., Sacco, G., G., Worley, C., C., Zaggia, S. (2016) *The Gaia-ESO Survey: Exploring the complex nature and origins of the Galactic bulge populations*, A&A submitted. Presented in Chap. 5 and 6.

Other first author papers:

- **Rojas-Arriagada, A.**, Zoccali, M., Vásquez, S., Ripepi, V., Musella, I., Marconi, M., Grado, A., Limatola, L. (2016) *High resolution spectroscopic analysis of seven giants in the bulge globular cluster NGC 6723*, A&A, 587, A95.

Other projects in which I contributed:

- Angeloni, R. Contreras Ramos, R., Catelan, M., Dékány, I., Gran, F., Alonso-García, J., Hempel, M., Navarrete, C., Andrews, H., Aparicio, A., Beamín, J. C., Berger, C., Borissova, J., Contreras Peña, C., Cunial, A., de Grijs, R., Espinoza, N., Eyheramendy, S., Ferreira Lopes, C. E., Fiaschi, M., Hajdu, G., Han, J., Helminiak, K. G., Hempel, A., Hidalgo, S. L., Ita, Y., Jeon, Y.-B., Jordán, A., Kwon, J., Lee, J. T., Martin, E. L., Masetti, N., Matsunaga, N., Milone, A. P., Minniti, D., Morelli, L., Murgas, F., Nagayama, T., Navarro, C., Ochner, P., Pérez, P., Pichara, K., **Rojas-Arriagada**, A., Roquette, J., Saito, R. K., Siviero, A., Sohn, J., Sung, H.-I., Tamura, M., Tata, R., Tomasella, L., Townsend, B., Whitelock, P. (2014) *The VVV Templates Project Towards an automated classification of VVV light-curves. I. Building a database of stellar variability in the near-infrared*, A&A, 567, A100.

- Zoccali, M., Gonzalez, O. A., Vasquez, S., Hill, V., Rejkuba, M., Valenti, E., Renzini, A., **Rojas-Arriagada, A.**, Martinez-Valpuesta, I., Babusiaux, C., Brown, T., Minniti, D., McWilliam, A. (2014) *The GIRAFFE Inner Bulge Survey (GIBS). I. Survey description and a kinematical map of the Milky Way bulge*, A&A, 562, A66.

- Zoccali, M., Gonzalez, O. A., Vásquez, S., Hill, V., Rejkuba, M., Valenti, E., Renzini, A., **Rojas-Arriagada, A.**, Babusiaux, C., Brown, T., Minniti, D., McWilliam, A. (2015) *The GIRAFFE Inner Bulge Survey (GIBS)*, The Messenger,159, 36.

- Gonzalez, O. A., Zoccali, M., Vasquez, S., Hill, V., Rejkuba, M., Valenti, E., **Rojas-Arriagada, A.**, Renzini, A., Babusiaux, C., Minniti, D., Brown, T. M. (2015) *The Giraffe Inner Bulge Survey (GIBS) II. Metallicity distributions and alpha element abundances at fixed Galactic latitude*, A&A, 584, A46.

Chapter 2

The Gaia-ESO Survey disk and bulge dataset

Contents

2.1 The Gaia-ESO survey selection function for disk and bulge fields 48
2.1.1 Milky Way disk/halo field target selection . . . 49
2.1.2 Bulge target selection . . . 50
2.2 Spectroscopic data, adopted setups and general quality 52
2.3 Determination of fundamental parameters . . . 54
2.4 Measurement of elemental abundances . . . 56
2.4.1 Available node results . . . 57
2.4.2 A comparison between HR10|HR21 vs. HR21 abundance measurements . . . 58
2.4.3 Reference abundance scale . . . 58
2.4.4 Combined abundances in HR10|HR21 and HR21 into the benchmark scale . . . 61
2.4.5 Final calibrated combined abundances . . . 61
2.5 Summary . . . 64

Abstract: After the general description of the Gaia-ESO survey provided in the previous chapter, we present here a more detailed description of the bulge and disk datasets adopted in this thesis. The photometric selection functions and the rational behind their design is described. The general quality of the obtained data is described and illustrated, and the determination of fundamental parameters and elemental abundances is presented in detail.

The Gaia-ESO survey was designed to target stars in all the main components of the Milky Way. Given the different nature of the observed populations and scientific questions to be addressed, the way how stars are selected for observation has been conveniently customized. In this thesis, we exploit the richness of the Milky Way disk/halo and bulge samples. It is important to properly understand the way in which stars are selected from a given Galactic component, as it allow us to anticipate the qualitative composition of the sample, and correct if needed, any sort of bias introduced by that selection.

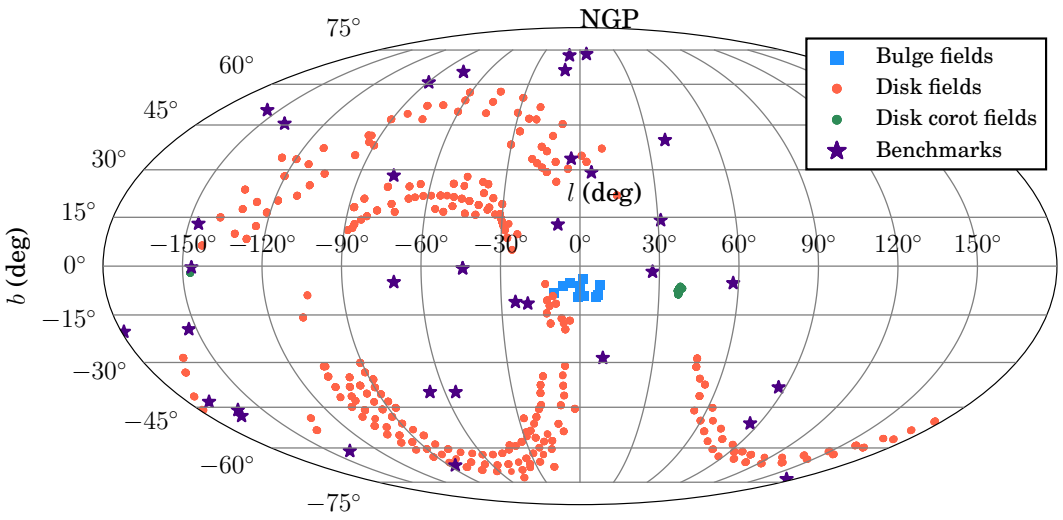


Figure 2.1: Distribution of disk and bulge fields across the sky, as observed up to the fourth internal data release. A Mollweide projection in Galactic coordinates, with the Galactic center in the middle, is adopted. Red circles (green for the few Corot fields) and blue squares depict disk and bulge pointings. The position of individual benchmark stars are depicted by purple stars.

In this chapter, we present a general description of the bulge and disk datasets adopted in this thesis. We devote next section to describe the photometric selection functions used to pick up bulge and disk/halo targets from their location in the CMD. Then we cope with the description of observations, setups, resolution, and general quality of the obtained data. Finally, we describe the processing cascade, from data reduction to the determination of fundamental parameters and elemental abundances.

2.1 The Gaia-ESO survey selection function for disk and bulge fields

A large -and still increasing- number of stars have been observed at several disk and bulge pointings (e.g. $\sim$ 30000 disk field and $\sim$ 2500 bulge stars up to the fourth internal data release). The footprint of such disks and bulge fields is illustrated in Fig. 2.1. From here, we can see how the distribution of Milky Way disk/halo field pointings avoid low latitude regions where dust obscuration and differential reddening can be large. Bulge fields, on the other hand, are distributed at lower latitudes, but still avoiding regions at $b \geq -4°$.

Let's examine the ways how stars are selected in each case.

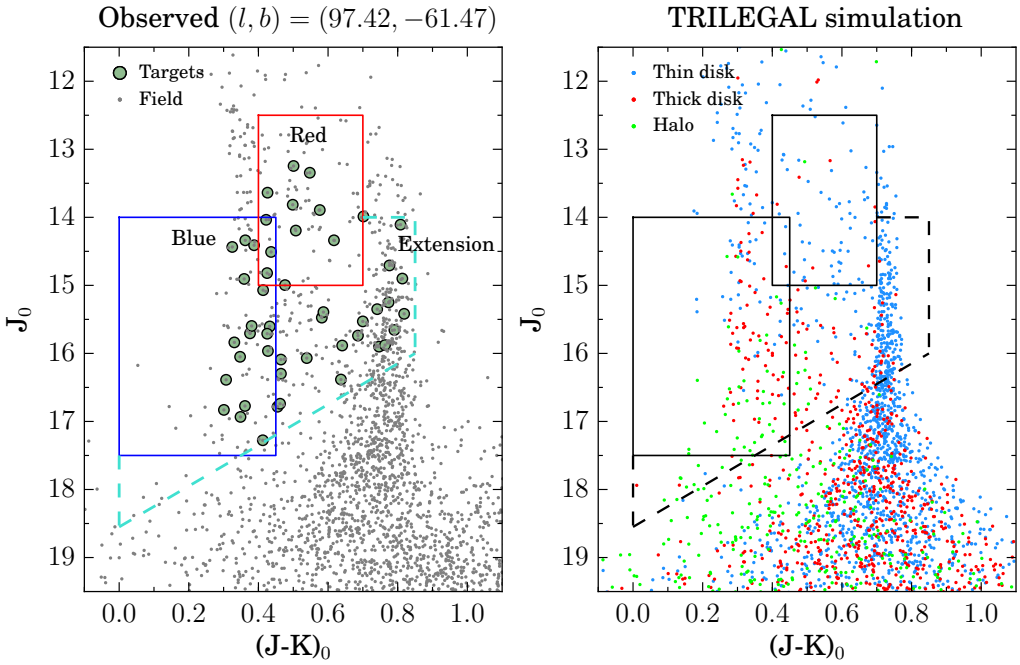


Figure 2.2: Photometric selection function for Milky Way disk/halo field stars. *Left panel :*CMD diagram of the disk field located at (l,b)=(97.42,-61.47). Green circles stand for the observed targets. The stars in an area 0.5° around the center of the field are displayed with gray points. The blue and red boxes, as well as the target selection extension are drawn with blue, red and cyan lines, respectively. *Right panel:* CMD diagram of a TRILEGAL simulation of the same observed field. The disk, thin disk and halo stars are depicted with different colors. Curves of photometric error in J and K bands were fitted to the data in the left panel and applied to the simulated magnitudes.

2.1.1 Milky Way disk/halo field target selection

We describe here the main characteristics of the photometric selection function for Milky Way disk/halo field stars. A detailed description can be found in [Stonkutė *et al.* 2016].

The GES target selection for halo and disk(s) field stars is based on the disk-to-halo transition seen in SDSS at $g \sim 18$ and $0.2 < g - r < 0.4$ (for example [de Jong *et al.* 2010], their Fig. 3). Guided by this feature, stars are selected according to their color and magnitude by using photometry from the VISTA Hemisphere Survey (VHS, [McMahon *et al.* 2013]). The main selection is defined in two nominal boxes:

- Blue box: $0.00 \leq$ J-K ≤ 0.45; $14.0 \leq$ J ≤ 17.5
- Red box: $0.40 \leq$ J-K ≤ 0.70; $12.5 \leq$ J ≤ 15.0

Targets are selected in the boxes in a proportion of 80% in the blue box and 20% in the red box. The effective position of the boxes is adjusted in color according to the field extinction, as given by the Schlegel dust maps [Schlegel *et al.* 1998]. To this end, E(J-K) = 0.5·E(B-V) is adopted, derived by assuming the extinction law of [Rieke

& Lebofsky 1985]. No adjustment is made in J magnitude. The left panel of Fig. 2.2 shows the CMD of a typical disk/halo field towards a low extinction high latitude region. Gray points depict the stars present in an area comparable to that of a FLAMES FoV. The position of the blue and red boxes is illustrated, as well as the distribution of spectroscopic targets observed in this field. The plume of stars at J-K $\simeq$ 0.4 is composed mostly by main-sequence turn-off old stars of about 10 Gyr. Thick disk stars dominate over halo ones at bright magnitudes, with a break in the vertical sequence given by the difference in mean metallicity between these two populations (with halo stars toward bluer colors). On the other hand, the dense vertical plume of stars sitting at J-K $\simeq$ 0.75 correspond mostly to local metal-rich thin disk stars, except in the faint end which can be also populated by a relevant number of thick disk stars.

The primary selection given by the blue and red boxes is extended in those cases where the star surface density in the observed field is to low to allocate all the available fibers. These second priority targets are selected as defined by the following relations:

$$0.0 \leq \text{J-K} \leq 0.45 + \Delta_{\text{J-K}}$$

$$\text{J} \geq 14.0$$

$$\text{J} + 3.0 \cdot ((\text{J-K})0.35) \leq 17.50,$$

where $\Delta_{\text{J-K}}$ corresponds to the extension in color. The exact value of $\Delta_{\text{J-K}}$ vary slightly from field to field, as described and tabulated in [Stonkutė *et al.* 2016]. This selection extension is depicted by the dashed cyan line in the left panel of Fig. 2.2. We can see that in fact, this allows to compensate for the insufficient number of targets falling into the blue and red boxes, completing the sample by including stars mostly located in the vertical sequence of thin disk stars at at J-K $\simeq$ 0.75 mag.

In the right panel of Fig. 2.2 we display a synthetic CMD computed with the TRILEGAL model[1] at the same (l, b) location and area as the observed field in the left panel. The photometric selection is displayed on top of the field stars, which are color coded according to the Galactic component they belong to. From here, we can see that the selection allows for a mixture of thin and thick disk stars, including a non negligible fraction of halo members. It is also expected from here, that the red box will contain a larger proportion of thin disk stars than the blue one.

2.1.2 Bulge target selection

Bulge targets were selected according to a customized photometric selection function, which made use of J, H and K_s photometry available from the Vista Variables in the Via Lactea project (VVV, [Minniti *et al.* 2010]). This selection function, which is very different in nature than the one presented above to select disk/halo field stars, is illustrated in Fig. 2.3. A generic color cut selects stars with $(\text{J-K}_s)_0 > 0.38$, which is imposed on the dereddened photometry in each field according to the values estimated from the reddening maps of [Gonzalez *et al.* 2011][2]. This cut, defining the left border

[1] http://stev.oapd.inaf.it/cgi-bin/trilegal

[2] These maps, derived from VVV and 2MASS photometric data, are accessible at http://mill.astro.puc.cl/BEAM/calculator.php.

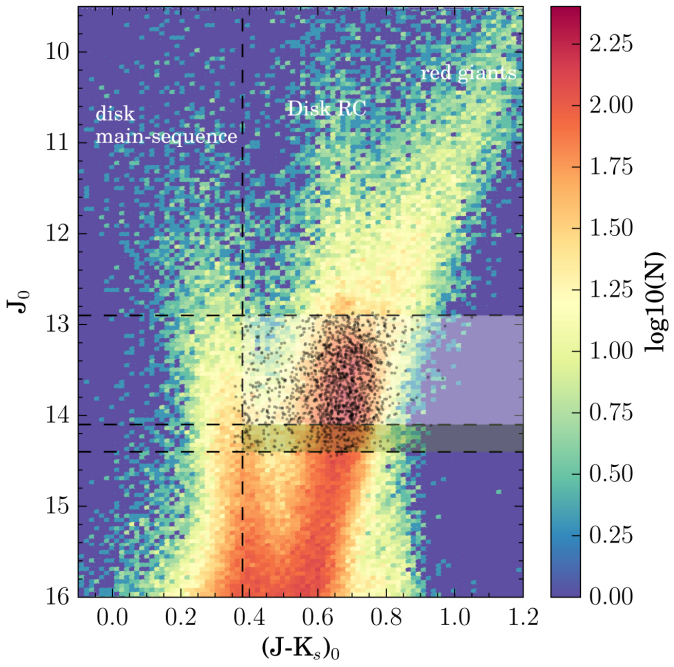


Figure 2.3: Photometric selection function for bulge stars. The background density count map depicts a generic CMD in the bulge region from VVV photometry. Prominent sequences are labeled. A shaded white area depicts the main selection function, with color and magnitude cuts of $(\mathrm{J\text{-}K}_s)_0 > 0.38$ and $12.9 < \mathrm{J}_0 < 14.1$, respectively. The green shaded area depicts the magnitude extension implemented in fields where the double red clump feature is visible. The whole spectroscopic sample collected up to the GES iDR4 is displayed with black dots.

of the selection box in Fig. 2.3, is blue enough to allow metal-poor bulge stars to be included in the sample, with the drawback of including a number of foreground dwarf main-sequence stars. This sample contamination enters in a variable proportion according to the field extinction. The latter because the dwarf disk stars are distributed in the CMD mostly in a vertical band at the blue side of the bulge RC. This blue plume is on average less affected by the reddening than the bulge RC, so that the difference in color between the two features depends on the specific field extinction. In Fig. 2.3, the dwarf thin disk plume is visible at $J - K_0 \sim 0.35$ mag, while the one corresponding to the disk RC at $J - K_0 \sim 0.65$ mag. Since RC stars are good standard candles, the RC sequence clumps in magnitude whenever these stars clump spatially. This happens at $J_0 = 13.5$, which in fact, corresponds to the mean apparent magnitude of a RC star located in the Galactic bulge.

On the other hand, a generic magnitude cut selects stars with $(14.1 - 1.2) < \mathrm{J}_0 < 14.1$. This 1.2 mag interval, is in general large enough to select stars located in the bulge RC peak of the field luminosity function, accounting for the spatial distance spread of the bar and the change of the RC mean magnitude with longitude because of the bar position angle. In a number of fields where the double RC feature is observed in the luminosity function, the magnitude cut would not fit the entire magnitude extension of the bar. In these cases, an extension of the magnitude limit was allowed to include up to 30% of targets in an extra 0.3 mag below the nominal cut.

As we can see, this selection function is designed to sample RC bulge stars of all metallicities. A fraction of dwarf thin disk stars is expected to contaminate the sample, specially at the blue end of the color distribution. Nonetheless, a bluer color cut is important since metal-poor stars in the bulge region are interesting as they can be members of the inner stellar halo, but specially, because simulations predict that fist

stars should be located in the inner regions of the Galaxy ([Tumlinson 2010]).

2.2 Spectroscopic data, adopted setups and general quality

The Gaia-ESO survey collects data by observing with the Fiber Large Array Multi Element Spectrograph (FLAMES, [Pasquini *et al.* 2000]) facility. This is a multi-object intermediate and high resolution spectrograph mounted at the ESO VLT-UT2 (Kueyen) of Paranal Observatory, Chile. The instrument is designed to perform multi-object observations, accessing targets over a field-of-view of 25 arcmin in diameter, by simultaneously fiber-feeding two spectrograph, the low to mid resolution GIRAFFE and the high resolution UVES. When using GIRAFFE in its MEDUSA mode, this multiplexing capabilities translate into the possibility to observe up to 140 objects simultaneously, with 132 GIRAFFE fibers and 8 UVES fibers. As a result of this instrument configuration, the bulk of GES targets are obtained in GIRAFFE, with a small sample of higher resolution spectra ($R \sim 40\,000$) coming from UVES parallels. Since the exposure time is fixed by the requirements given by GIRAFFE targets, the UVES sample is mostly composed by local stars, which are bright in the respective CMDs.

The Milky Way disk/halo field and bulge portions of the Gaia-ESO survey observations are conducted using two GIRAFFE setups, the HR10 and HR21. Field disk/halo stars are observed with both setups while bulge targets are observed though the HR21 alone. The HR10 setup provides a spectral coverage spanning from 5339 to 5619 Å with a resolving power of $R \sim 19\,800$. In the upper panel of Fig. 2.4 we display the HR10 spectrum of a disk star. On the other hand, the HR21 setup provides a spectral coverage approximately centered at the Calcium triplet feature, spanning from 8484 to 9001 Å with a resolving power of $R \sim 16\,200$. In the lower panel of Fig. 2.4 we display the HR21 spectrum of a bulge star.

The raw data reduction and extraction of GIRAFFE spectra is performed at the Cambridge Astronomy Survey Unit (CASU) using the instrument-specific ESO reduction pipelines as well as private special purpose pipelines. Radial velocities are computed using a spectral fitting technique through cross correlation against real and synthetic spectra developed for the GES (Koposov in prep). Typical uncertainties from this procedure are of around 0.3-0.4 km s^{-1}.

In Fig. 2.5 we display the signal-to-noise distributions of all the disk field and bulge spectra obtained up to the fourth internal data release. We separate disk/halo and bulge stars in different panels. The different selection functions and observing strategies drive to different general quality distributions. In the case of field stars, the reported SNR is the average between those measured in the HR10 and HR21 spectra for each individual star (with that of HR21 being about twice as high as that of HR10). We can see that the SNR distribution of field stars is weighted towards low values, with the bulk of the stars having ratios lower than 80 per resolution element. If we consider the SNR distribution of all observed stars (left panel, black histogram), we can see that it goes all the way down to SNR ≈ 0, with a strong peak at about SNR ~ 10. From this, it can be anticipated that trustworthy stellar parametrizations might be difficult to obtain at the low SNR regimes. The red histogram in the left panel of Fig. 2.5

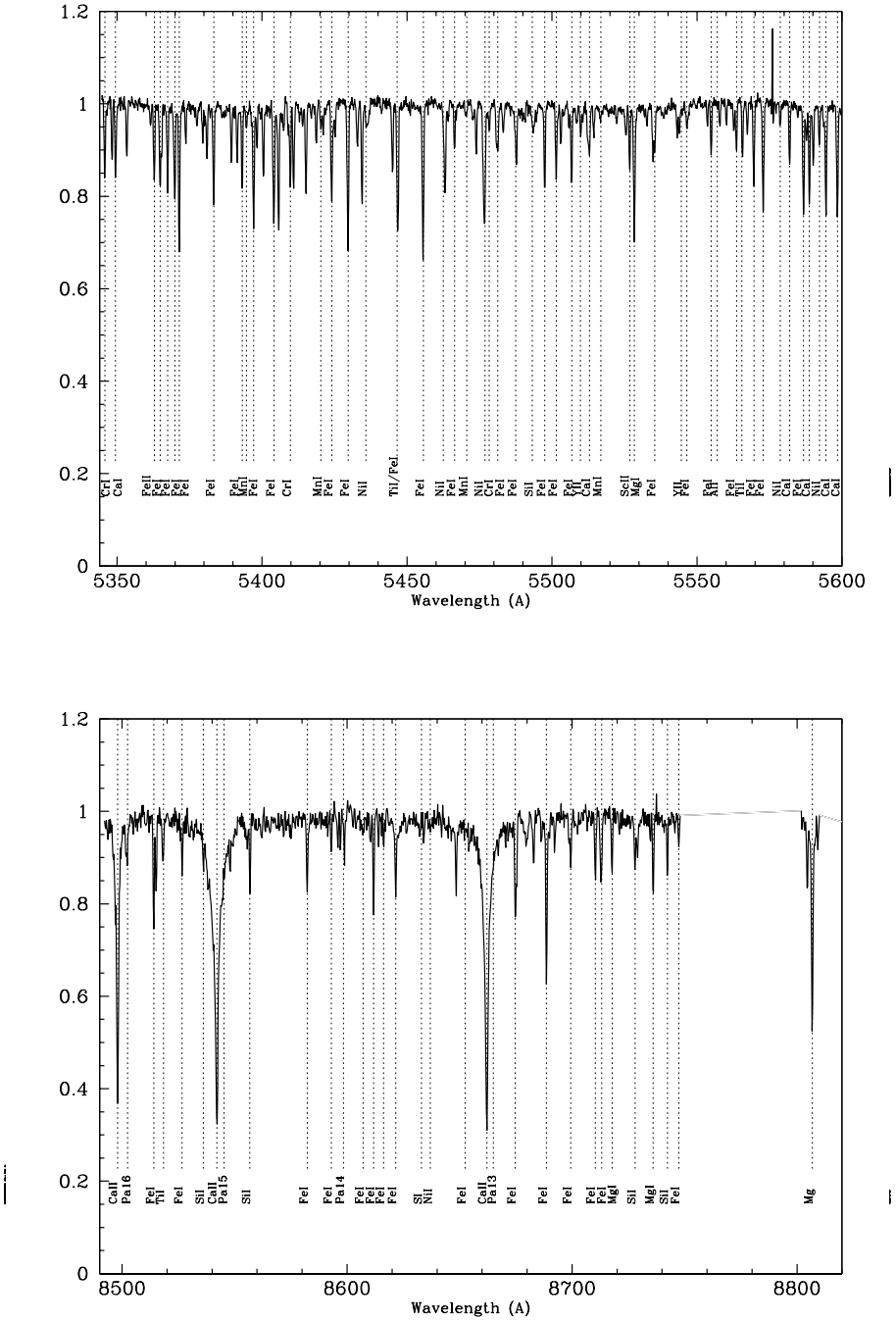


Figure 2.4: Examples of spectra obtained with the HR10 and HR21 setups. *Upper panel:* HR10 spectrum of a disk star with $T_{\rm eff}$ = 5944 K, $\log(g)$ = 4.15 dex and [Fe/H] = −0.41 dex. *Lower panel:* HR21 spectrum of a bulge star with $T_{\rm eff}$ = 4675 K, $\log(g)$ = 2.87 dex and [Fe/H] = −0.49 dex. In each case, the main lines used for abundance determinations are labeled.

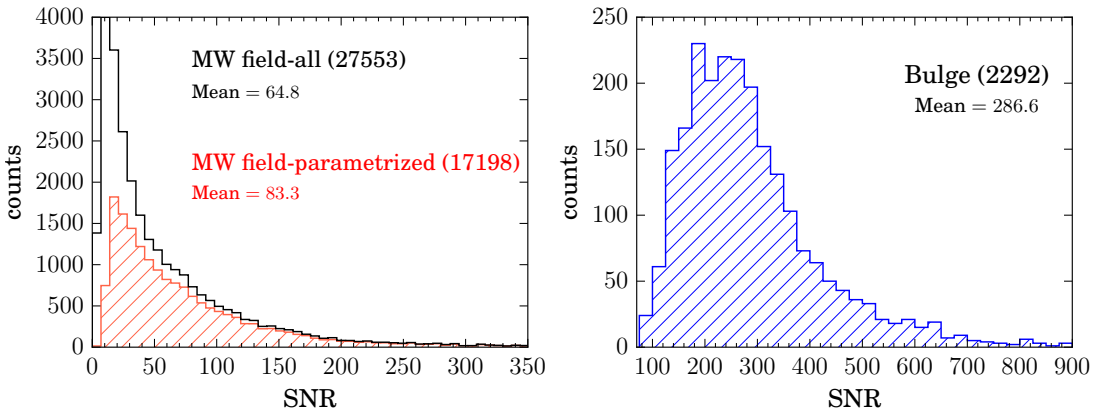


Figure 2.5: Signal-to-noise distribution of Milky Way disk/halo field and bulge spectra. For the field spectra, two distributions, corresponding to the total amount of observed stars and the fraction for which fundamental parameter determination was possible, are displayed.

shows that this is in fact the case. If we consider the SNR distribution of stars with available stellar parametrization from the GES analysis cascade, we see that it contains considerably less stars at the low SNR end, with the peak of the distribution being around SNR $\approx$ 20. This effect might modify the sample drawn by the survey selection function (Fig. 2.2). In fact, stars with lower SNR are expected to be at the faint tail of the magnitude distribution in each field. Considering the TRILEGAL simulation displayed in the right panel of Fig. 2.2, we can see that this effect translates into a bias against halo stars in each field. This analysis is just qualitative, but should be the object of a detailed investigation. The Gaia-ESO study of [Stonkutė *et al.* 2016], describes in detail the selection function of disk fields and propose corrections for some sampling biases. However, they do not take into account the effects of removing from the observed sample a considerable number of stars for which it is not possible to obtain a robust parametrization. A proper consideration of this effect might allow to understand the *effective* Gaia-ESO survey selection function of field disk stars in contrast with the nominal one. The latter, might be still be valid in studies considering radial velocities that in fact are measured for most of the stars, even for those with low SNR.

On the other hand, the bulk of bulge stars were obtained with high SNR, with an average of about 290 per resolution element. There are not spectra with SNR lower than 70-80. The good quality of the bulge spectra is illustrated in Fig. 2.6, were we display three spectra corresponding to the stars with the lowest, the mean and the highest ratios of the sample. We can see that even in the case of the lowest SNR, the main spectral features are clearly distinguishable.

2.3 Determination of fundamental parameters

The determination and compilation of a recommended set of atmospheric parameters and elemental abundances is performed by the Gaia-ESO survey working group 10

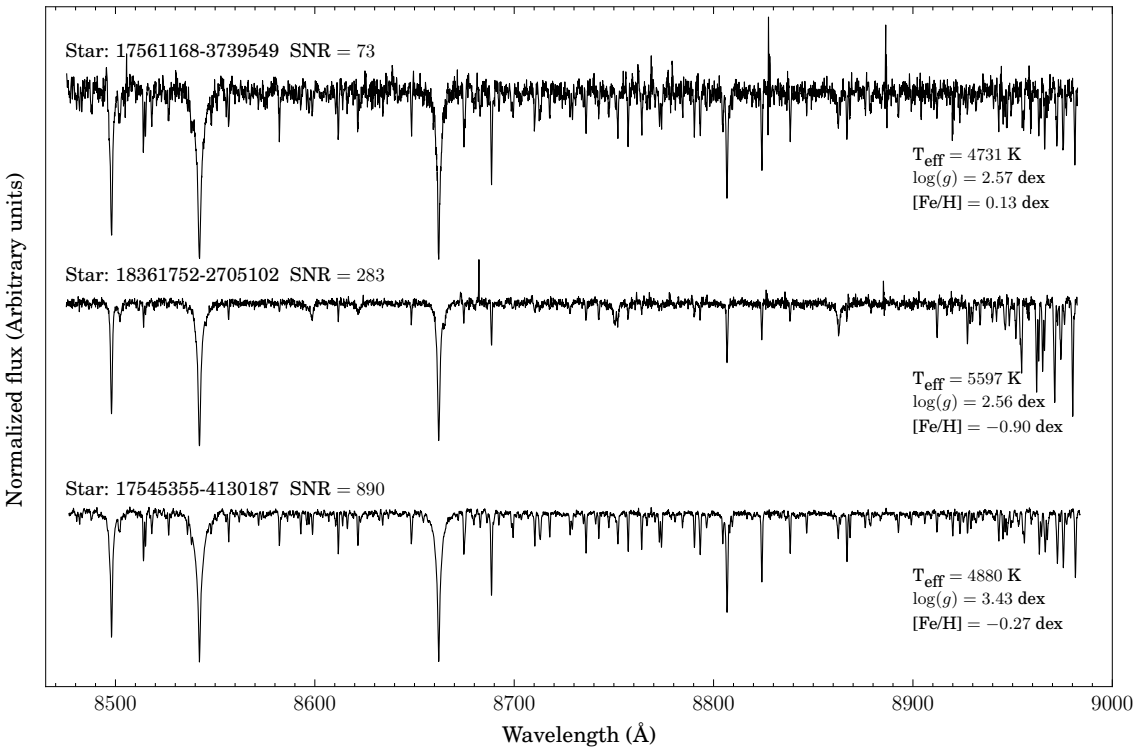


Figure 2.6: Three spectra of bulge stars with SNR equal to the lowest, the mean and the highest of the sample.

(WG10, see Sect. 1.8 and Fig. 1.23) for all the FGK-type stars observed with GIRAFFE (about 70% of the GES targets). There are some differences and progressive improvements in the procedures throughout the successive data releases. What we describe here corresponds to the adopted strategy to produce recommended fundamental parameters for the fourth internal data release.

The individual extracted, sky subtracted, radial velocity corrected and normalized spectra are analyzed by three independent approaches: Spectroscopy Made Easy (SME-LUMBA[3], [Valenti & Piskunov 1996]), FERRE-IAC[4] ([Allende Prieto *et al.* 2006]) and MATISSE ([Recio-Blanco *et al.* 2006]). The SME-LUMBA code works by computing synthetic spectra "on the fly", while FERRE-IAC and MATISSE rely on the comparison of the observed spectra against a grid of synthetic spectra. A common grid was generated for the analysis of Gaia-ESO survey spectra in a four-dimensional space:

- $3000 \leq \mathrm{T_{eff}} \leq 8000$ K
- $0.0 \leq \log(g) \leq 5.5$ dex
- $-5 \leq [\mathrm{M/H}] \leq +1$ dex

[3]LUMBA stands for Lund-Uppsala-MPA-Bordeaux-ANU
[4]IAC stands for Instituto de Astrofísica de Canarias

- $[\alpha/\mathrm{Fe}] = 0.4$ dex for $[\mathrm{M/H}] \leq -1.0$ dex, and $[\alpha/\mathrm{Fe}] = -0.4 \cdot [\mathrm{M/H}]$ for $-1 \leq [\mathrm{M/H}] \leq 0$

As a first step, $\mathrm{T_{eff}}$, $\log(g)$, [M/H] and $[\alpha/\mathrm{Fe}]$ are determined by the three nodes.

A set of spectroscopic benchmark stars selected for the Gaia-ESO survey are observed and analyzed in the same way as the main sample. This set is described in detail in [Jofré *et al.* 2015], and their distribution across the sky is depicted by violet stars in Fig. 2.1. From this point forward, the determination of recommended fundamental parameters proceeds slightly different for bulge and field disk/halo stars.

For field disk/halo stars, the random errors in the individual parameter determinations from SME-LUMBA, FERRE-IAC and MATISSE is reduced by putting them into a common scale. To this end, the deviation of results of each node with respect to the nominal parameters of the benchmark stars is compared, and the one with the smallest zero-points is taken as a reference. Then, multilinear transformations as a function of $\mathrm{T_{eff}}$ and $\log(g)$ are used to map the results of the two other nodes into the scale of the reference one. These transformations are of the form

$$\Delta\theta = \theta_p - \theta_{ref} = c_0 + c_1 \cdot \mathrm{T_{eff},}_p + c_2 \cdot \log(g_p),$$

where θ is one of the parameters $\mathrm{T_{eff}}$, $\log(g)$, [M/H], or $[\alpha/\mathrm{Fe}]$, and the subscripts stand for the reference procedure (ref) and the other two (p). Once the results of all the nodes are transformed into the common scale (the one of SME-LUMBA for the iDR4), they are combined as a weighted average, with the weights corresponding to the inverse of the square root of the scatter with respect to the reference node. Finally, the zero-points of the reference node with respect to the benchmarks are removed from the combined parameters. The corresponding parameter errors are estimated from the standard deviation of the three node results for each star. These final parameters and associated errors constitute the recommended set of fundamental parameters by the Gaia-ESO survey consortium for the disk/halo field stars.

For bulge stars, the procedure is simplified with respect to the one described above, and it was performed as part of this thesis. For the individual parameter determinations with SME-LUMBA, FERRE-IAC and MATISSE, the zero-points with respect to the benchmarks are determined and removed (Table 2.1). The node results for the bulge sample are corrected by removing these small zero-points. After this, the results are combined as a unweighted average to produce a unique set of atmospheric parameters while reducing the random errors of individual determinations. The corresponding errors are computed as the node-to-node dispersion. They constitute the recommended set of fundamental parameters by the Gaia-ESO survey consortium for the bulge.

2.4 Measurement of elemental abundances

The determination of elemental abundances is performed on the basis of individual line measurements. In Fig. 2.4 the majority of the lines used to measure abundances in HR10 and HR21 setups are labelled. An homogenization process, as the one described above for the estimation of recommended fundamental parameters, is performed, and it was done for the fourth internal data release as part of this thesis. For this reason,

Node	ZP(T_{eff}) K	ZP($\log g$) *cgs*	ZP([Fe/H]) dex
FERRE-IAC	285	0.51	0.21
SME-LUMBA	53	-0.06	0.08
MATISSE	147	0.08	0.26

Table 2.1: Zero points with respect to the benchmarks of the three HR21 setup analysis nodes.

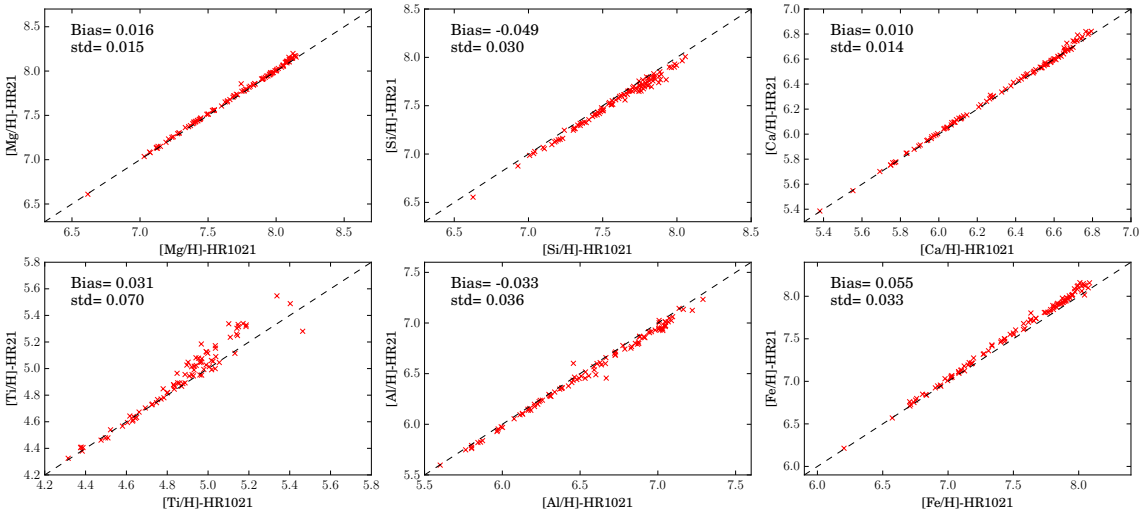


Figure 2.7: Comparison between HR10|HR21 and HR21-only abundance measurements (MgI, SiI, CaII, TiI, AlI and FeI) for the SME-LUMBA node. The sample corresponds to 114 red clump bulge stars in common with the sample of [Hill *et al.* 2011]. Dashed black lines indicate the 1:1 relation.

we provide here a more detailed explanation of the technical aspects involved in this procedure.

2.4.1 Available node results

Using the recommended parameters (T_{eff}, $\log(g)$ and [M/H]), the Gaia-ESO survey linelist (Heiter et al. in prep) and the MARCS model atmospheres ([Gustafsson *et al.* 2008]), abundances for several elements (Mg, Al, Si, Ca, Ti, Cr, Mn, Co, Ni and Fe) have been calculated from the setup combinations HR10|HR21 (field stars) and HR21-only (bulge stars). These chemical abundances have been estimated from both neutral and ionized lines (c.f Fig. 2.4) using SME-LUMBA and an automated spectral synthesis method (hereafter ASM-Nice, [Mikolaitis *et al.* 2014]).

The size of the sample is $\sim$ 30 000 spectra in the HR10|HR21 setup combination and $\sim$ 2500 for the bulge sample in HR21-only. We homogenized results from the HR10|HR21 and from HR21-only setups separately. Whenever needed, we adopted the solar composition by [Grevesse *et al.* 2007], which is the adopted standard by the GES.

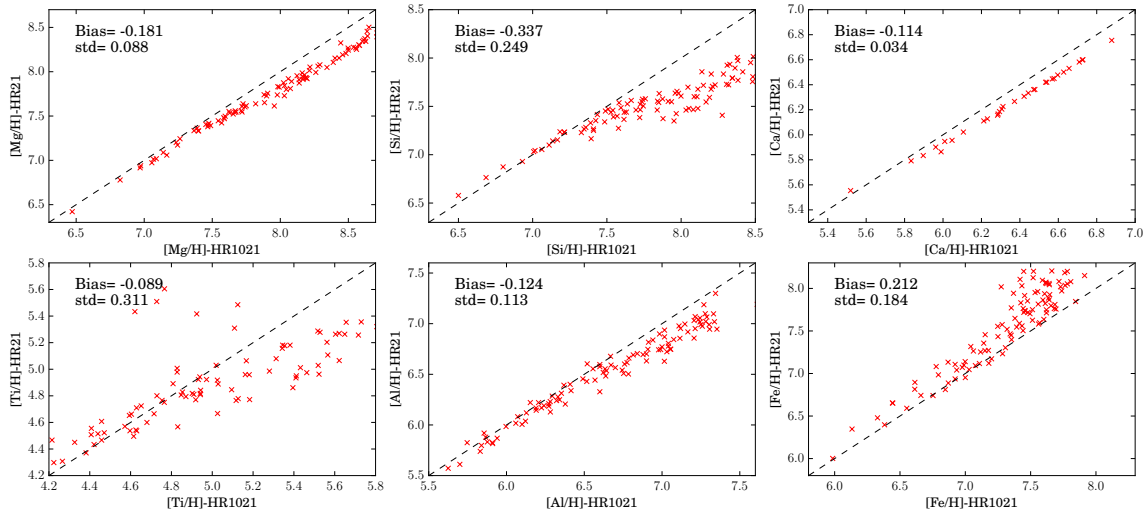


Figure 2.8: Comparison between HR10|HR21 and HR21-only abundance measurements (MgI, SiI, CaII, TiI, AlI and FeI) for the ASM-Nice node. The sample corresponds to 114 red clump bulge stars in common with the sample of [Hill *et al.* 2011]. Dashed black lines indicate the 1:1 relation.

2.4.2 A comparison between HR10|HR21 vs. HR21 abundance measurements

As part of the bulge observations, a sample of 228 stars was selected from the Baade's window studies of [Zoccali *et al.* 2008] and [Hill *et al.* 2011], and observed with both, HR10|HR21 (114 stars from [Hill *et al.* 2011]) and HR21-only (114 stars from [Zoccali *et al.* 2008]) for comparison purposes (See Chap. 5). This data set (in particular the half observed with HR10|HR21) provides us with an opportunity to test the internal consistency of the abundance measurements obtained from both setup combinations. Figure 2.7 displays the comparison for the SME-LUMBA node. There is a good agreement between abundances determined for both setups, with distributions closely following the 1:1 line. Dispersion and bias are small. On the other hand, in Fig. 2.8, we present the same comparison for the ASM-Nice node. We verify the presence of small biases and trends for Si (I) and Ti (I) measurements.

We can see that SME-LUMBA abundance measurements from both setup combinations are more consistent than those provided by the ASM-Nice node.

2.4.3 Reference abundance scale

Considering the above discussion, we choose to transform ASM-Nice abundances into the SME-LUMBA scale. In order to perform such transformation, we compare for each element (for HR10|HR21 and HR21-only separately) the relation between SME-LUMBA and ASM-Nice results. Since bulge HR21 spectra have very good signal-to-noise levels, we use all the available stars in this comparison. On the other hand, spectra in HR10|HR21 setup combination are in a broad range of SNR values (Fig. 2.5), so we perform the comparisons between nodes in this setup combination using stars

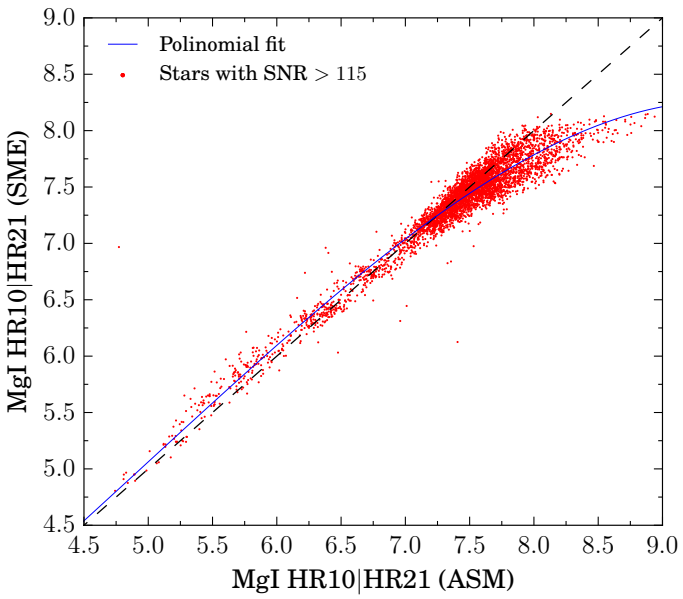


Figure 2.9: Illustration of the procedure followed to determine the relation to transform ASM-Nice abundances to the SME-LUMBA scale in the HR10|HR21 setup combination. A 4th degree polynomial (blue solid line) is enough to fit the the distribution followed by MgI results from the two nodes. Only stars with SNR > 115 are used.

with SNR> 115. In general, the distributions are close to the 1:1 line, specially in the HR21 setup. Whenever deviations appear between the nodes, they are stronger in the metal-rich and metal-poor ends. For some elements, a constant shift seems to be enough to put ASM-Nice measurements into the SME-LUMBA scale, but in other cases, more complex relations appear. We use linear, and up to 5th degree polynomials to fit the distributions and transform ASM-Nice results into the SME-LUMBA scale. Higher polynomials are needed to deal with the sometimes strong deviations in the metal-rich end of the abundance distributions. Since these deviations present a low dispersion around the trend, a more complex fit is justified to correct them. We verified that the use of high order polynomials does not introduce any modulation or trend in the transformed abundances. They just correct the metal-rich and metal-poor deviations. We also verified that in each case, a linear fit to the region excluding the metal-rich and metal-poor ends of the distributions is in good agreement with the polynomial fit in that range. Figure 2.9 displays an example of one of these high order polynomial fits. Tables 2.2 and 2.3 present the coefficients of the relations used to transform ASM-Nice measurements into the SME-LUMBA scale. We note that higher order polynomials were needed mostly in HR10|HR21, while simpler bias or linear corrections were enough in the case of HR21-only measurements.

For Titanium measurements (TiI and TiII), we found in HR10|HR21 that the dispersion and characteristics of the metal-rich end impede us to construct reliable relations between ASM-Nice and SME-LUMBA abundances. We decided then to cut the samples with a limit of $A(Ti_{ASM\text{-}Nice}) < 5.2$ dex, in both cases.

Figure 2.10 and 2.11 display a comparison of node abundances for both setups after transforming ASM-Nice abundances into the SME-LUMBA scale. We see a good agreement between nodes, with smaller bias and dispersion than before transformations. In the HR10|HR21 setup combination, we see that the stars still deviating from the 1:1 relation after scale transformation are those with lower SNR levels.

	$\mathcal{O}(5)$	$\mathcal{O}(4)$	$\mathcal{O}(3)$	$\mathcal{O}(2)$	$\mathcal{O}(1)$	$\mathcal{O}(0)$
FeI					0.925	0.606
MgI		-8.111e-4	3.499e-3	6.792e-2	5.119e-1	8.746e-1
AlI			-0.013	0.123	0.901	-1.064
SiI	-1.157e-4	1.499e-4	6.085e-3	,6.025e-2	3.788e-1	8.802e-1
CaI	1.869e-4	-2.078e-3	-6.315e-3	8.450e-2	9.829e-1	-9.723e-2
CaII						-0.052
TiI		-0.003	0.012	0.104	0.403	0.851
TiII	-8.656e-4	1.812e-3	1.945e-2	6.890e-2	1.009e-1	1.799
CrI			-6.845e-4	-1.194e-2	1.060	2.765-1
MnI				-0.086	1.757	-1.685
CoI		-0.012	0.097	0.105	-1.414	4.929
NiI						-0.05

Table 2.2: Coefficients of the polynomials used to transform ASM-Nice abundances into the SME-LUMBA scale in the HR10|HR21 setup combination.

	$\mathcal{O}(5)$	$\mathcal{O}(4)$	$\mathcal{O}(3)$	$\mathcal{O}(2)$	$\mathcal{O}(1)$	$\mathcal{O}(0)$
FeI						0.014
AlI						0.011
MgI	-3.173e-4	2.238e-3	1.670e-2	-4.573e-3	-6.321e-1	5.968
SiI						0.023
CaII						0.008
TiI						0.026

Table 2.3: Coefficients of the polynomials used to transform ASM-Nice abundances into the SME-LUMBA scale, in the HR21-only setup.

Ion	HR10|HR21	HR21	Ion	HR10|HR21	HR21
MgI	-0.035	-0.056	CrI	-0.102	–
SiI	0.081	0.116	MnI	0.076	–
CaI	-0.037	–	FeI	0.026	-0.067
CaII	0.091	0.062	CoI	0.046	–
TiI	0.059	-0.077	NiI	-0.028	–
TiII	0.036	–	AlI	0.081	0.081

Table 2.4: Zero points of the SME-LUMBA scale relative to the benchmark scale. As aluminium measurements are not provided by [Jofré *et al.* 2015], the reported zero point is given with respect to the solar composition of [Grevesse *et al.* 2007]. The same value is tabulated for both setups because aluminium is measured just from one line located in the HR21 setup spectral range, so that HR10 setup in the HR10|HR21 setup combination does not provide extra information.

Once ASM-Nice abundances were shifted into the SME-LUMBA scale, we computed the combined abundances by averaging them. We end with two sets of combined abundances, one for HR10|HR21 and one for HR21. In order to provide an estimate of the quality of these combined results, we compute an errorbar as half of the absolute difference between node results for each element and each star. This quantity correlates well with the SNR level, as can be seen in figures 2.10 and 2.11.

2.4.4 Combined abundances in HR10|HR21 and HR21 into the benchmark scale

The combined results from each setup have to be translated into the benchmark scale. To do this, the abundances of benchmark stars, with nominal values provided in [Jofré *et al.* 2015], were measured for HR10|HR21 and HR21 in the same way as for the rest of the GES sample. Since the node-combined abundances for each setup are in the SME-LUMBA scale, we just need a calibration relating this scale with that of the benchmarks. To estimate these zero points, we compare for each measured element, the SME-LUMBA results with the nominal values given in [Jofré *et al.* 2015]. In general just small bias corrections are necessary to transform results from SME-LUMBA into the benchmark scale. Aluminium is not provided for the benchmarks in [Jofré *et al.* 2015], so we just calculate a zero point with respect to the Sun. The zero points in each setup are provided in Table 2.4. We note here that the bias with respect to the benchmarks were computed for all ions individually. In this sense, we have FeI, MgI, SiI, CaII, TiI and AlI bias estimations for HR21 and MgI, AlI, SiI, CaI, CaII, TiI, TiII, CrI, MnI, FeI, CoI and NiI bias estimations for HR10|HR21.

2.4.5 Final calibrated combined abundances

The final HR10|HR21 abundances include measurements for the following number of spectra: MgI (18587), AlI (12183), SiI (14109), CaI (13123), CaII (12658), TiI (12402), TiII (7921), CrI (9109), MnI (8774), CoI (3750), NiI (5003) and FeI (18660) stars, from

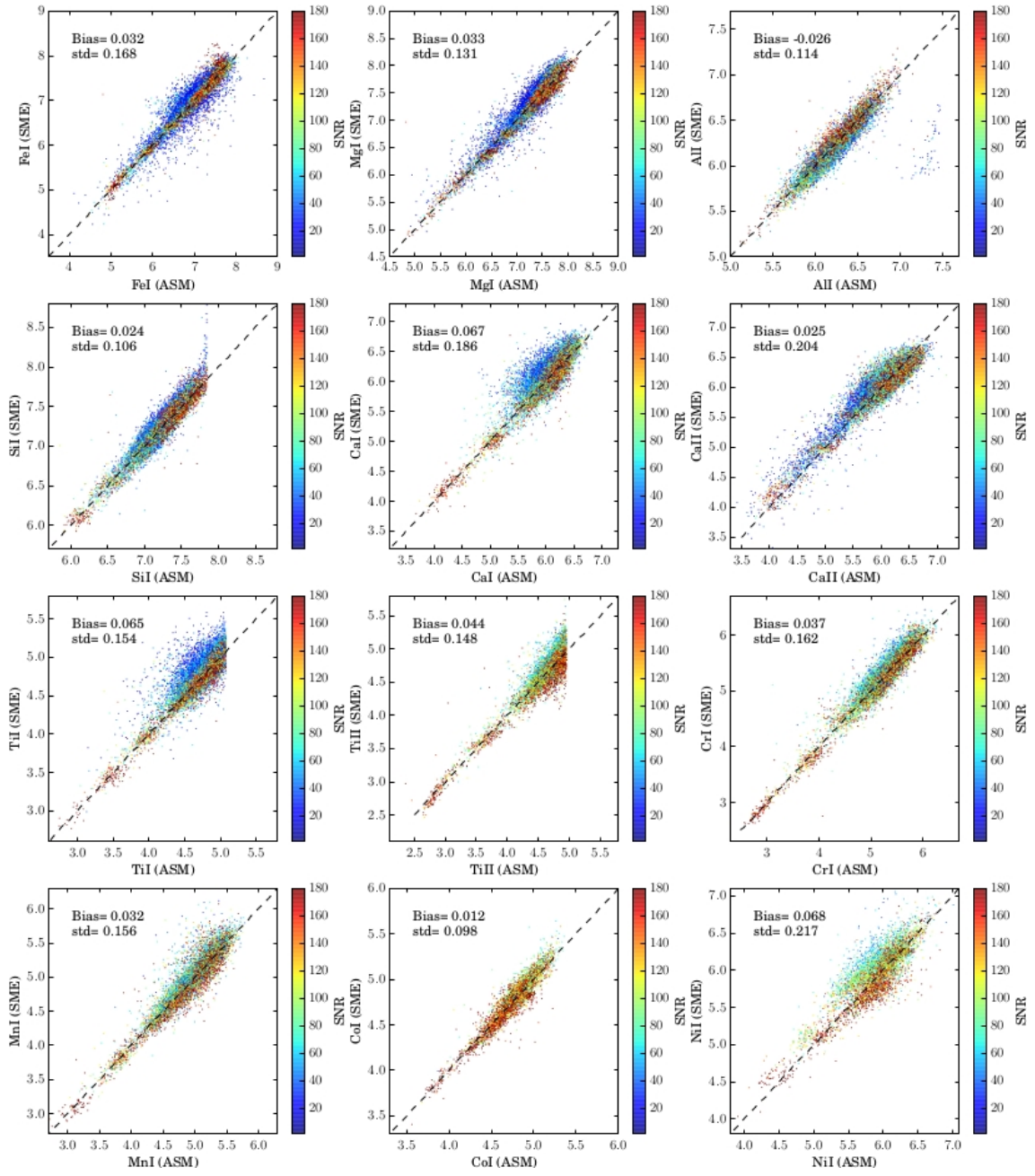


Figure 2.10: Comparison between ASM-Nice and SME-LUMBA abundances from the HR10|HR21 setup. ASM-Nice abundances are transformed into the SME-LUMBA scale using polynomials with the coefficients given in table 2.2. Dashed black lines depict the 1:1 relation in each panel.

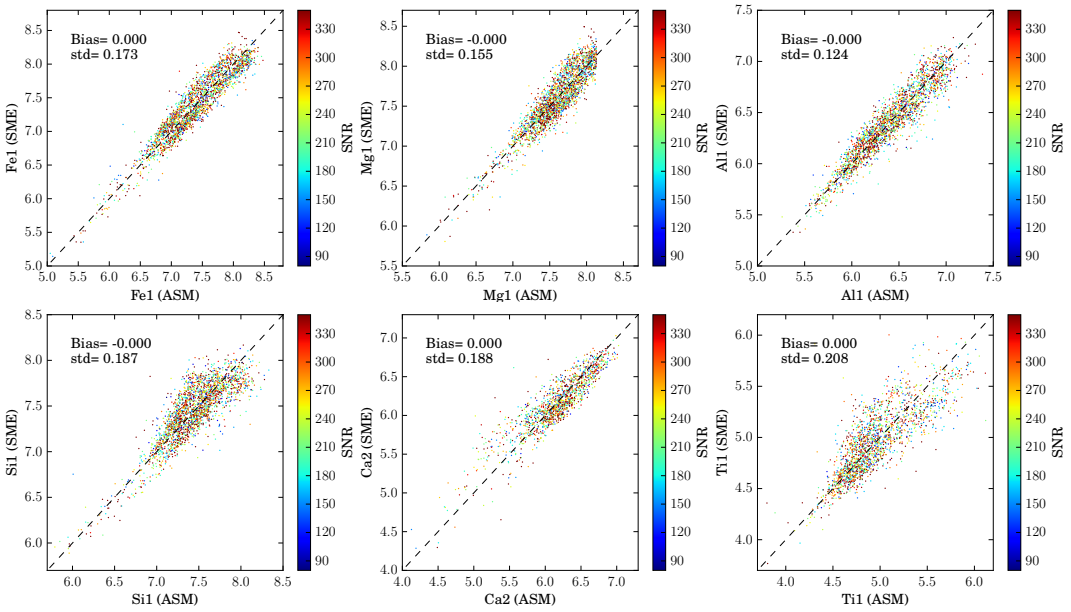


Figure 2.11: Comparison between ASM-Nice and SME-LUMBA abundances from the HR21-only setup. ASM-Nice abundances are transformed into the SME-LUMBA scale using polynomials with the coefficients given in table 2.2. Dashed black lines depict the 1:1 relation in each panel.

an original set of 20114 stars with WG10 recommended fundamental parameters (T_{eff}, $\log(g)$, [M/H] and [α/Fe]).

On the other hand, the final HR21 abundances contains measurements for: MgI (2292), SiI (2268), CaII (1373), TiI (1864), AlI (2196) and FeI (2292) stars, from an original set of 2511 stars with WG10 recommended fundamental parameters (T_{eff}, $\log(g)$, [M/H] and [α/Fe]).

In Fig. 2.12 for HR21 and Fig. 2.13 for HR10|HR21 we display the set of final abundances in the [X/Fe] vs. [Fe/H] plane.

If Fig. 2.14 we display the comparison between HR10|HR21 and HR21-only final combined and calibrated abundances (MgI, SiI, CaII, TiI, AlI and FeI) for the 114 bulge stars with measurements performed in both setups. We can see that the general agreement for all the elements, with the exception of titanium, is quite good. This is important to ensure an homogeneous analysis while comparing abundance distributions of bulge (abundances from HR21 setup) and disk (abundances from HR10|HR21 setup) stars (See Chap. 6). The dispersion of points around the 1:1 relation in Fig. 2.14 come from the differences in the homogenization procedures adopted for the HR10|HR21 and HR21 setups. The fact that dispersions are small, shows that despite these homogenization differences, the final results are quite consistent: Consistence is preserved while the errors associated to the combined abundances in each setup are reduced with respect to the results from the individual analysis nodes (ASM-Nice and SME-LUMBA).

We recall here that the procedure described in this section concerns directly what was done to homogenize the abundances of the fourth internal data release. The results

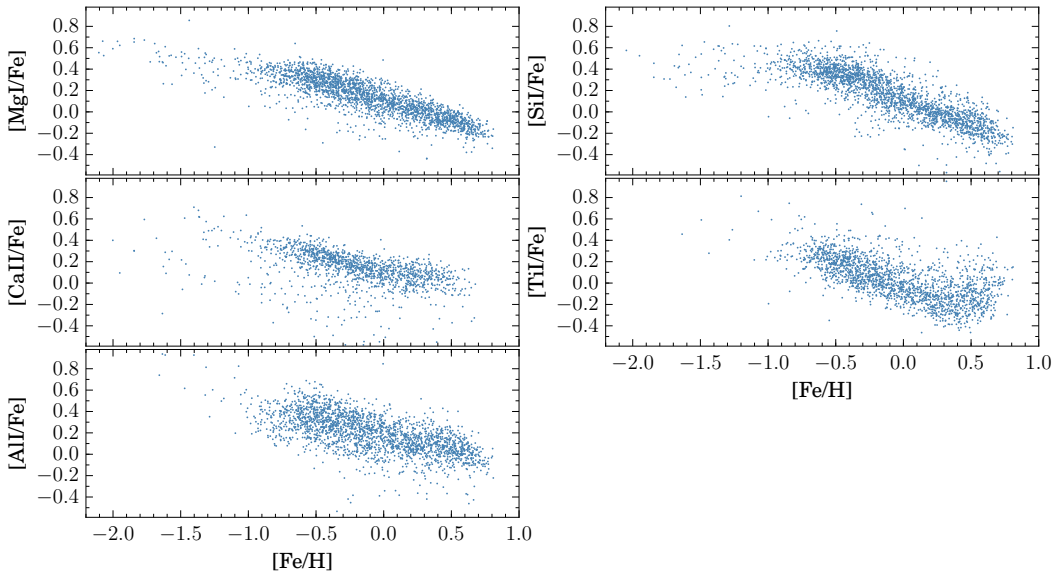


Figure 2.12: [X/Fe] vs. [Fe/H] for the final abundances from the HR21 setup.

obtained from the analysis of this data set are presented in Chap. 5. In any case, this procedure is roughly the same as those implemented in previous data releases, including the iDR2, which we adopted to conduct the disk study presented in the next chapter.

2.5 Summary

We presented in this chapter a detailed description of the Gaia-ESO survey photometric selection functions used to draw the bulge and field disk samples. We also described the general quality and characteristics of obtained data, as well as the procedures used to derive fundamental parameters and elemental abundances.

In summary:

1. About 30000 disk field stars have been observed up to the fourth internal data release. They are selected from two nominal CMD boxes sampling the disk-to-halo transition seen in SDSS at $g \sim 18$ and $0.2 < g - r < 0.4$.

2. About 2500 stars in pointings towards the bulge have been observed up to the fourth internal data release. They are selected from the red clump as seen in the CMD diagram from VVV photometric data. The selection function aims to target stars all along the magnitude (distance) spread of the bulge, as well as towards blue colors, where the most-metal poor stars should be located.

3. All stars are observed with the FLAMES/GIRAFFE spectrograph. Disk field stars are observed with both the HR10 and HR21 setups, while bulge stars just using the HR21 one.

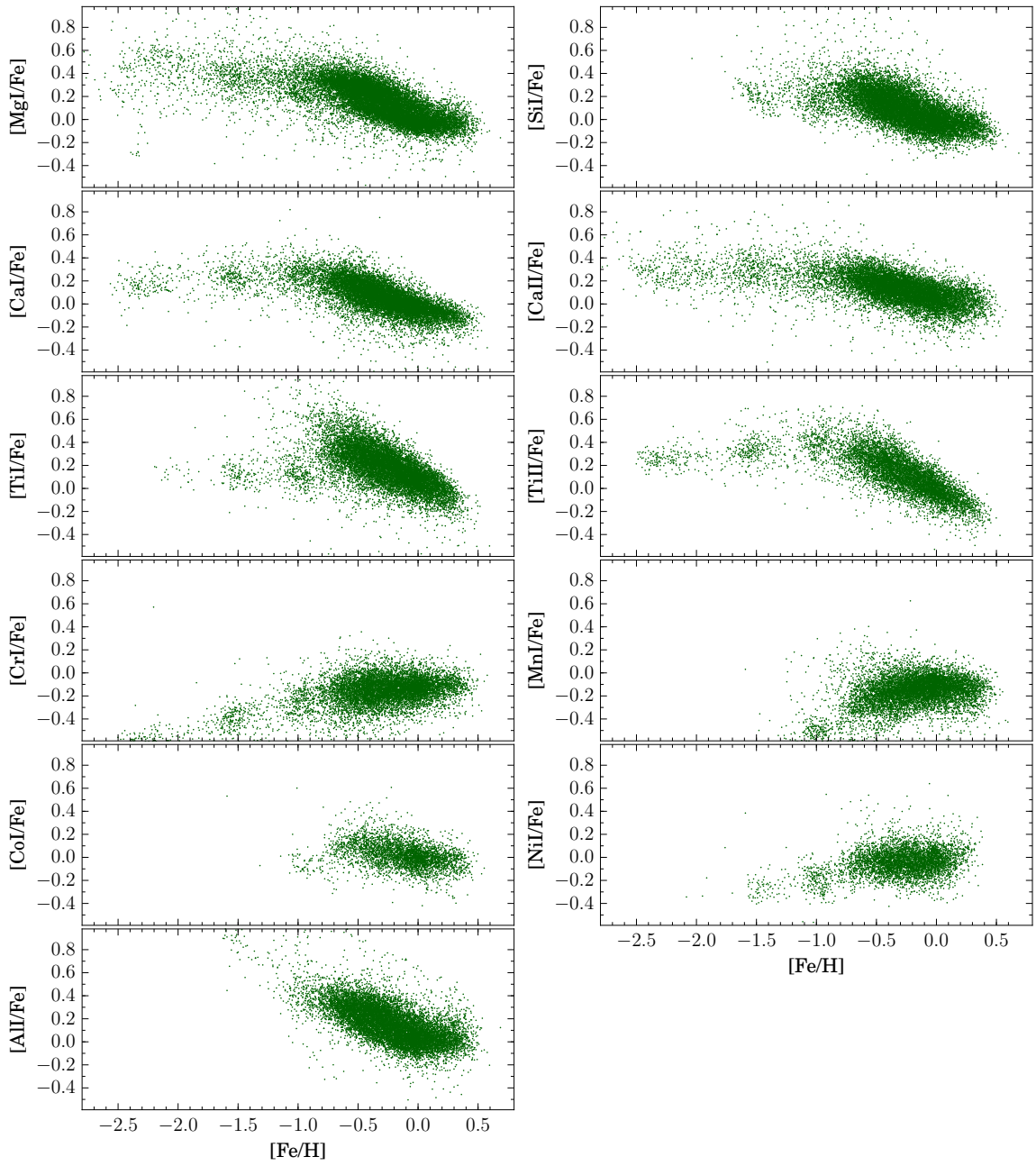


Figure 2.13: [X/Fe] vs. [Fe/H] for the final abundances from the HR10|HR21 setup.

4. Fundamental parameters $T_{\rm eff}$, $\log(g)$, metallicity [M/H] and α-element ratio [α/Fe] are determined by three independent nodes of analysis. An homogenization process is conducted to generate recommended parameters which are in the scale of the GES spectroscopic benchmark stars.

5. Using the recommended parameters, elemental abundances of several elements are measured by two independent nodes, and homogenized to produce a recommended

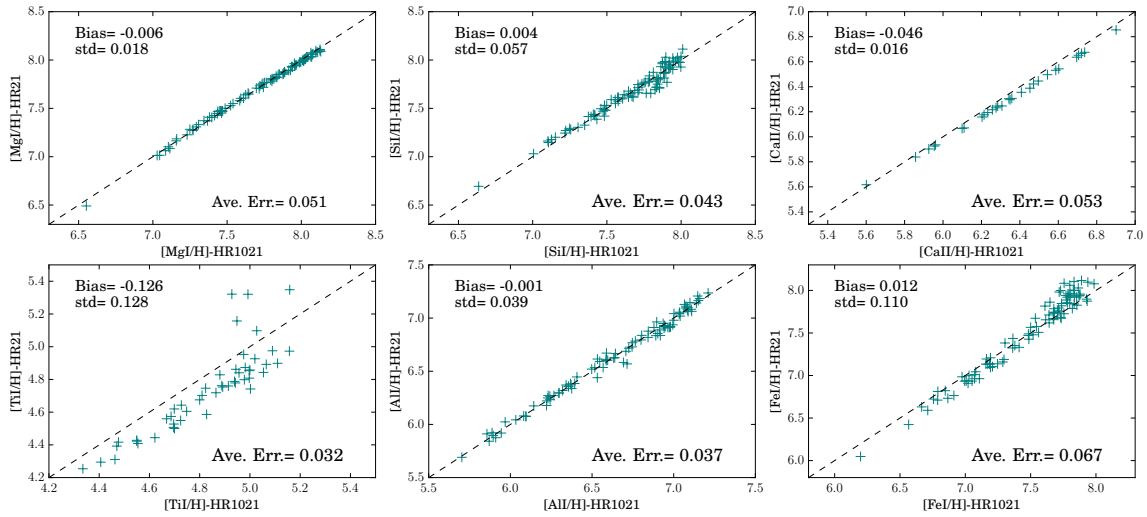


Figure 2.14: Comparison between HR10|HR21 and HR21-only final combined and calibrated abundances for MgI, SiI, CaII, TiI, AlI and FeI. The sample corresponds to 114 red clump bulge stars in common with the sample of [Hill *et al.* 2011]. Dashed black lines indicate the 1:1 relation.

set of values in the benchmark scale.

6. Care was taken to ensure that abundances derived from the HR10|HR21 setup combination (disk field stars) are compatible with those measured from the HR21 setup only (bulge stars).

Chapter 3

Analysis tools

Contents

3.1 Distance determinations 68

3.1.1 The code 69

3.1.2 Tests with models 72

3.1.3 Tests with Hipparcos data 74

3.1.4 Tests with clusters 77

3.1.5 Distances for the Gaia-ESO Survey targets 79

3.2 Gaussian Mixture Models and other ways to disentangle substructure in the abundance-metallicity plane 79

3.2.1 Gaussian Mixture Models 80

3.2.2 Separating disk sequences in the abundance-metallicity plane . . . 83

3.3 Summary 84

Abstract: During the development of this thesis, several tools and mathematical approaches were adopted to study the bulge and disk samples from the Gaia-ESO survey as well as from APOGEE. In this chapter, we present a description of the procedures and ideas adopted to estimate spectro-photometric distances as well as to separate thin and thick disk stars in the abundance-metallicity plane. A number of tests to demonstrate their applicability is also presented.

In the previous chapters we provided a general description of the Gaia-ESO survey, its selection function for disk and bulge fields, and the processing cascade going from observations to the final data products, fundamental parameters, metallicity, and abundance determinations. These samples, are the basis of the analysis of the bulge in the perspective of Galactic stellar populations conducted during this thesis, as discussed thoroughly in the next chapters.

Our aim here, is to provide an overview on the tools and mathematical approaches we used to analyze the observational data sets. In particular, we provide here a description of a method to compute spectro-photometric distances, and some approaches used to separate thin and thick disk samples using chemical abundance information.

3.1 Distance determinations

The determination of stellar distances is a fundamental, but not straightforward, ingredient to study Galactic structure. Trustworthy position vectors for a large number of stars are necessary to characterize the relative spatial distribution of the major Galactic structures and to complement kinematic characterizations. Here, we provide a brief non exhaustive sketch of the possible ways to obtain stellar distances.

A primary direct distance estimation is possible by measuring stellar parallaxes. As the Earth orbits Sun, stars will display small shifts with respect to more distant background stars. These parallactic motions, provide a direct way to geometrically determine distances given that we know the size of the Earth-Sun distance baseline. Distances are given in parsecs, where one parsec is the distance at which one star would display a parallactic angle of 1 arcsecond. As a reference, the closest star to the Sun, Proxima Centauri, is at 1.3 pc.

These geometrical distances are the ideal way to characterize Galactic populations, but the spatial volume where precise determinations are available depends on our ability to properly measure parallactic angles, always in the sub-arcsecond scale[1].

An alternative direct way to measure distances would be possible if the luminosity of stars were a known quantity. In this case, the inverse-square law of radiation would provide -in the absence of interstellar extinction- a direct way to link the known stellar luminosity and the flux measured on earth (i.e. it apparent magnitude) with a line-of-sight distance. In reality, stellar luminosity vary in a wide range, so that this procedure is possible just in some particular cases where absolute magnitude is known. This is the case of stellar pulsators (through period luminosity calibrations), RGB-tip stars, and RC stars.

In a general case, it is still possible to obtain an estimation of the absolute magnitude of a star, and so its distance, if we know its fundamental parameters and if we adopt a set of theoretical models relating the $\log(g)$-$T_{\rm eff}$ plane with the color-magnitude one. This is the idea behind the computation of spectro-photometric distances. For a given star, if we know its set of fundamental parameters $T_{\rm eff}$, $\log(g)$ and metallicity [M/H], we can use an isochrone of the appropriate metallicity to obtain the absolute magnitude in a desired passband. We can then compare this value with the apparent magnitude in the respective passband to compute a distance modulus, which in turn can be translated into a line-of-sight distance, if interstellar extinction is known.

This simple picture hides some of the complexities of the problem. Given statistical and systematic errors in the fundamental parameters, a star in the $\log(g)$-$T_{\rm eff}$ plane will usually not fall exactly on the locus of the respective isochrone: A way of finding the most likely location of the star in the theoretical $\log(g)$-$T_{\rm eff}$ plane should be devised.

The results we can obtain from this approach are not as accurate as for standard

[1] From an historical point of view, Tycho Brahe, although being the greatest observer in the pretelescopic era, was never able to measure a parallactic angle. In a clever interpretation, he attributed this to the fact that stars were simply to far away to allow for parallaxes to be measured rather than to assume that they were actually fixed sources in the celestial sphere. We had to wait till 1838 for the first successful measurement of a stellar parallax. It was Friederich Bessel, who determined from the measured parallax a distance of ~ 3.5 pc for 61 Cygni.

candles, and specially less than direct geometrical measurements. Nevertheless, its strength is the fact the in principle it is possible to apply it to a whole survey, if photometric and stellar parameters of enough quality are available. In this way, scarcity of precision is compensated by a large number statistics.

In the context of the analysis of bulge data coming from the fourth internal data release described in Chap. 5, we developed a code to compute distances by isochrone fitting. The adopted procedure make use of the fundamental parameters $T_{\rm eff}$, $\log(g)$, metallicity [Fe/H] (from FeI lines), VISTA J, H and K_s photometry, and associated errors to compute simultaneously the most likely line-of-sight distance and reddening by isochrone fitting with a set of PARSEC isochrones[2]. The general approach is similar to other methods in the literature (e.g. [Zwitter *et al.* 2010, Ruchti *et al.* 2011, Kordopatis *et al.* 2011]). In the following we describe it.

3.1.1 The code

Our approach estimates the absolute magnitude of a given star as the weighted mean (or median) of theoretical predictions given its ($\log g$, $T_{\rm eff}$) position with respect to all the available isochrones. This is done for as many photometric passbands as available. The details are as follows:

1. We consider a set of isochrones spanning ages from 1 to 13 Gyr in 1 Gyr steps, and metallicities from -2.2 to 0.5 dex in steps of 0.1 dex. In practice, each isochrone, for a given age and metallicity, consists in a sequence of model stars located along a track in the $\log(g)$ vs. $T_{\rm eff}$ plane with increasing mass, from the main-sequence till the AGB. Each model star is characterized by theoretical values of M_J, M_H and M_{K_s} absolute magnitudes. As an example, in panel *a* of Fig.3.1 isochrones of all ages are displayed for three different metallicity values. The bulk of disk and bulge stars have metallicities inside the range given by these isochrones. Consequently, the distribution of model stars in panel *a* provides an indication of the expected distribution of GES bulge/disk stars in he HR diagram.

   On the other hand, an observed star is characterized by a set of fundamental parameters and observed passband magnitudes (VISTA photometry in our case) $\{T_{\rm eff}, \log(g), [{\rm Fe/H}], J, H, K_s\}$, together with their associated errors. They are the observed quantities. Given the fundamental parameters $T_{\rm eff}$, $\log(g)$ and metallicity [Fe/H], a star can be placed in the $\log(g)$-$T_{\rm eff}$-[Fe/H] isochrone space.

2. We compute the distance from this observed star to the set of all model stars from the whole set of isochrones. To this end, we adopt the metric

$$d(a.m) = \frac{[T_{\rm eff\ *} - T_{\rm eff}(a,m)]^2}{\sigma^2_{T_{\rm eff\ *}}} + \frac{[\log(g)_* - \log(g)(a,m)]^2}{\sigma^2_{\log(g)\ *}} + \frac{[[{\rm Fe/H}]_* - [{\rm Fe/H}](a,m)]^2}{\sigma^2_{[{\rm Fe/H}]\ *}},$$

[2] Available at http://stev.oapd.inaf.it/cgi-bin/cmd

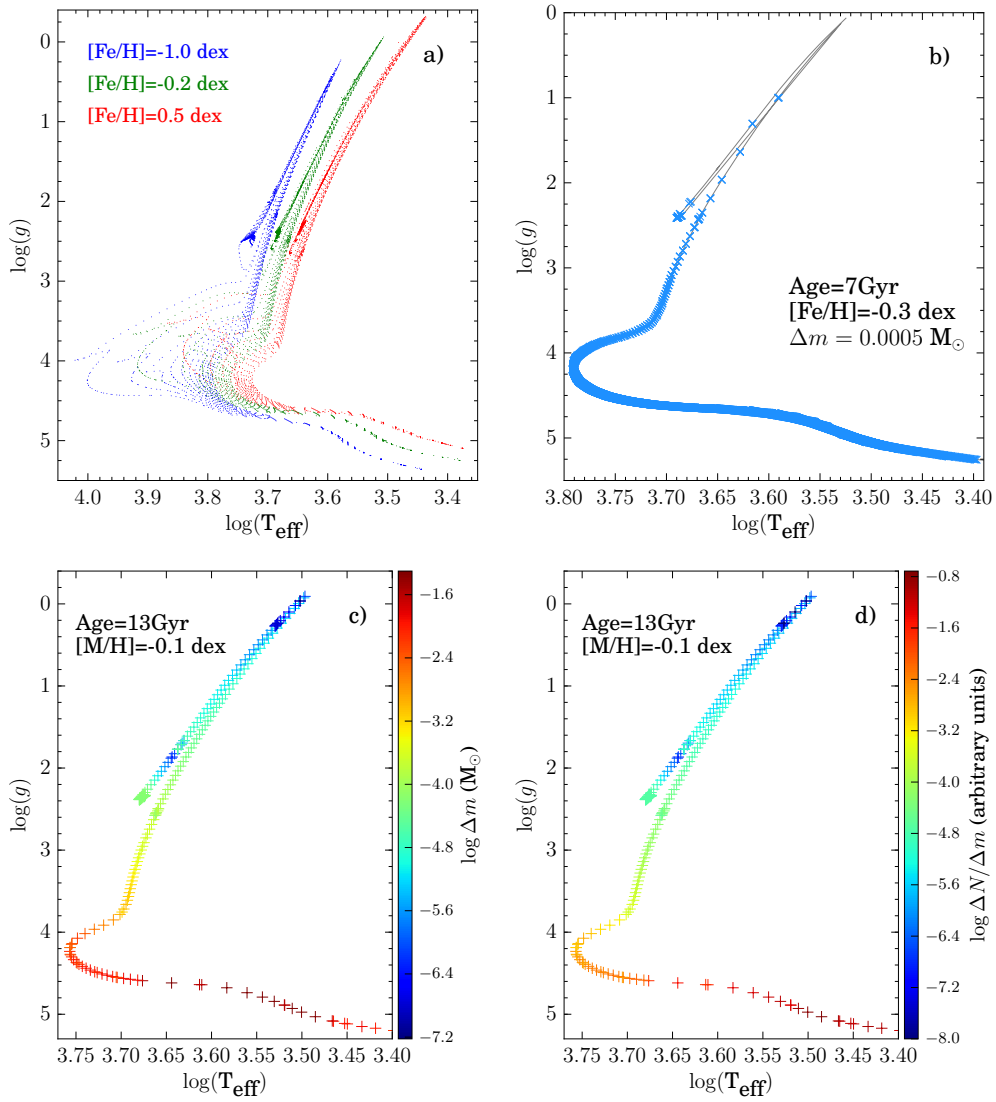


Figure 3.1: Characterization of isochrones as an ingredient for distance determinations. *Panel a:* isochrones of ages from 1 to 13 Gyr in steps of 1 Gyr are displayed for three different metallicities. This metallicity interval accounts for the vast majority of the GES stars used in this thesis. *Panel b:* an isochrone is interpolated to have a constant small mass step between consecutive model stars. Blue crosses stand for the interpolated model stars while the original isochrone track is depicted by the gray solid line. *Panel c:* isochrone model stars are color coded according to the average mass difference with respect to neighbor model stars. A logarithmic scale is used to highlight differences. *Panel d:* isochrone model stars are color coded according to the average difference in the integrated IMF along the isochrone. A logarithmic scale is used to highlight differences. All plots use the adopted PARSEC isochrones.

where $T_{\rm eff}(a,m)$, $\log(g)(a,m)$ and [Fe/H](a,m) are the fundamental parameters and metallicity,which depends of age a and mass m of the isochrone model stars. The quantities with a star subscript stand for the fundamental parameters and errors ($\sigma_{T_{\rm eff}\,*}$, $\sigma_{\log(g)\,*}$) of the observed star.

3. With this metric, we can compute weights associated with the match of the observed star to each point of the isochrone collection

$$W(a,m) = P_m P_{IMF} \left[e^{-d(a,m)}\right].$$

This weight is composed of three factors;

a. P_m accounts for the evolutionary speed of the model stars along the isochrone, which is proportional to the mass difference between contiguous model stars in the track. The isochrones are constructed in order to roughly place their model stars uniformly distributed along them in the $\log(g)$ vs. $T_{\rm eff}$ plane. This means that a simple unweighted statistic using all model stars will lead to overweight short evolutionary stages in detriment of long lived ones. This is illustrated in panels *b* and *c* of Fig. 3.1. If the isochrones were constructed with their model stars being spaced with a constant mass step, a typical track would look like the one displayed in panel *b*. It is evident that a uniform mass step would lead to place a large number of model stars in long lived stages, such as the main-sequence, in detriment of the RGB or AGB, were few model stars would be present even with a very small mass step. The color code of model stars in panel *c* emphasizes this fact. In the main-sequence, a large mass step produces a small shift in the position of the star along the track. Instead, a small mass step is enough to significantly shift a star in the shorter lived stages after the main-sequence turn-off, with the exception of the RC.

A way to correct for this effect in our computations, given the uniform spacing in the isochrones in the $\log(g)$ vs. $T_{\rm eff}$ plane, is to include a weight P_m proportional to the Δm between contiguous model stars, in order to assign more weight to the long lived evolutionary stages, where a randomly selected star is more likely to be in.

b. P_{IMF} accounts for the fact that, given a stellar population, the number of stars per mass interval dN/dm is not uniform. In fact, this distribution is given by the initial mass function (IMF). In practice, we made use of the PARSEC isochrone quantity int_IMF; the cumulative integral of the IMF along the isochrone. In fact, following [Girardi *et al.* 2000], we have that "the difference between any two values is proportional to the number of stars located in the corresponding mass interval". In panel *d* of Fig. 3.1 the model stars are color coded according to dN/dm.

c. The third factor is just an exponential weight associated with the distance of the observed star with respect to each model star, given the adopted metric.

We can use the weights $W(a,m)$ to compute any kind of weighted statistics.

4. Using the computed weights $W(a, m)$ for a given star, we calculate the likely values of its absolute magnitudes M_J, M_H and M_K as the weighted mean or weighted median of the respective values of all the model stars from the whole set of isochrones.

5. Additionally, we compute the line-of-sight reddening by comparing the theoretical color with the observed one $E(J-K) = (J_{obs} - K_{obs}) - (M_J - M_K)$. In some cases, when the reddening is small, uncertainties in the photometry and/or in our procedure, can lead to estimated reddenings slightly negative. In such cases, we set its value as the sum in quadrature of the uncertainties in J and K observed magnitudes, as an upper limit given these uncertainties.

6. Finally, from the computed absolute magnitudes and the estimated reddening, we compute the distance modulus and then line-of-sight distance in each passband as:

$$\mu = m_{obs} - M_\lambda$$
$$\mu_0 = \mu - A_\lambda$$
$$d = 10^{\frac{\mu_0}{5}+1} \text{ (pc)}$$

In the following, we present a selection of tests made to check the reliability of the distances obtained through this method.

3.1.2 Tests with models

The availability of Galaxy models to synthesize stellar populations provides us with an opportunity to check the general performance of our code while controlling quantities such as reddening and uncertainties in fundamental parameters. To perform this test, we made use of the TRILEGAL model[3], mainly because it uses PARSEC isochrones, just as our code does.

We generate a synthetic catalog of stars, including all Galactic components, with the following main characteristics:

- pointing: (l,b)=$(0°, -6°)$
- Area: $A = 4$ deg^2.
- Faint limit of apparent magnitude: $J_{\rm lim} = 16$.
- Binary fraction: null
- IMF from [Chabrier 2003].
- Extinction at infinite: $A_{V\infty} = 1.014$ mag.

The resulting catalog contains 246 302 stars.

We calculated distances for the whole catalog assuming three cases for the uncertainty levels in stellar parameters:

[3] Available at http://stev.oapd.inaf.it/cgi-bin/trilegal.

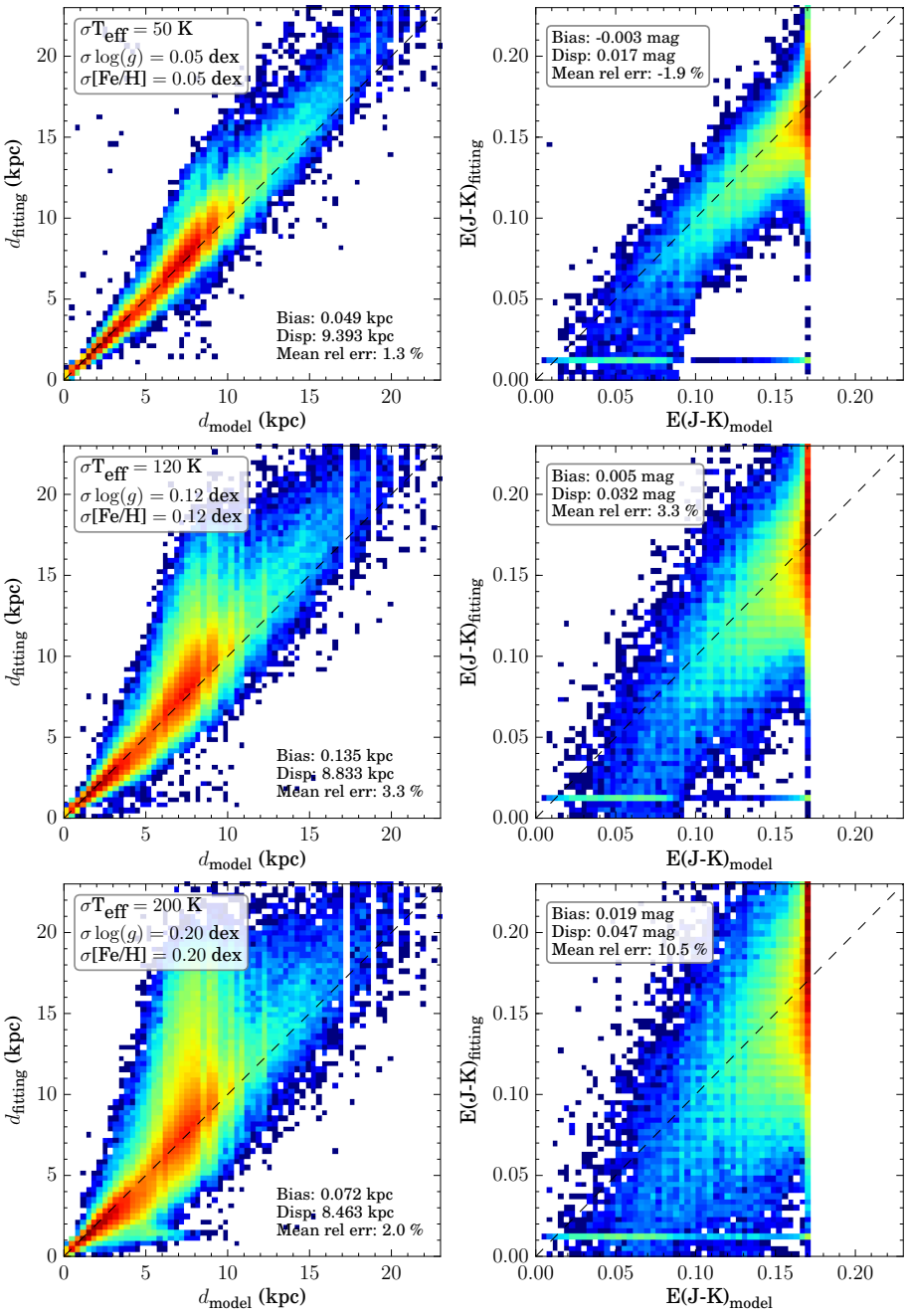


Figure 3.2: Distance and reddening estimates for a TRILEGAL synthetic catalog. *Left panels:* comparison of distances obtained with our code with respect to the nominal TRILEGAL values. Three different levels of uncertainties are applied to the fundamental parameters, as indicated in each panel. A logarithmic scale is used in the histogram color-code. *Right panels:* similar to left panels but for the reddening E(J-K) values.

- Low errors: $\Delta T_{eff} = 50$ K, $\Delta \log(g) = 0.05$ dex and Δ[Fe/H] $= 0.05$ dex.
- Regular errors: $\Delta T_{eff} = 120$ K, $\Delta \log(g) = 0.12$ dex and Δ[Fe/H] $= 0.12$ dex.
- High errors: $\Delta T_{eff} = 200$ K, $\Delta \log(g) = 0.20$ dex and Δ[Fe/H] $= 0.20$ dex.

To implement these uncertainty levels in the input catalogs we both, introduce Gaussian noise of the respective size in the parameters, and set error bar columns with the respective values.

The results of these experiments are displayed in Fig. 3.2, where estimated distances and reddenings are compared with respect to the nominal values given in the original TRILEGAL catalog. The histograms are color-coded according to a logarithmic scale on the number count density. The idea is to highlight the low fraction of stars lying departing from the 1:1 relation. In general, distances seem to be well recovered for a large fraction of the input stars. In fact, for all levels of noise in fundamental parameters, the higher density of number counts is closely located over the 1:1 relation (depicted as a gray dashed line in the panels). A slight tendency to overpredict distances is observed, but this effect is relatively large just for a small fraction of the input stars. The bias and dispersion of residuals quoted in each panel strength the case. As a matter of fact, the absolute relative distance error for the 80 percent of the sample is smaller than 11.6%, 21.4% and 35% for the three increasing levels of noise presented in Fig. 3.2.

Accurate reddening values seem somehow more difficult to obtain. In fact, the right panels of Fig. 3.2 shows that estimated reddening values tend to be underestimated for E(J-K) $\lesssim 0.05$ mag, specially in the high level uncertainties case. On the other hand, for larger reddening values -which are typical of pointings toward the bulge, for example- the comparison between estimated and nominal values is quite good.

Not to be overlooked though is the fact that while computing spectro-photometric distances, there is a hidden variable given by the fact that in general age is not know beforehand. Although average age values or distributions can be assumed for different stellar populations (for example, old ages for the halo or the bulge), in general ages are not available for all stars in a spectroscopic survey.

Fortunately, tests with synthetic data, as the one presented here, show that even without any age information distances can be reasonably estimated for a large fraction of input stars. The main effect of age spread in a given sample, might be just of increasing dispersion in relative distance errors, and in the case of introducing trends, they might be smaller than the typical uncertainties introduced by the photometric and spectroscopic errors.

3.1.3 Tests with Hipparcos data

We can test our code in a more realistic situation by calculating distances for stars with known values. Fortunately this is possible thanks to the availability of the Hipparcos catalog of trigonometric distances. Several studies based in medium to high resolution spectroscopy have been conducted on Hipparcos stars (planet searching, Galactic disk stellar populations), and fundamental parameters are publicly available. In the following, we compare trigonometric distances, adopting the new Hipparcos reduction by [van Leeuwen 2007], with results from our code for tree different datasets.

3.1.3.1 Casagrande et al 2011

As a first test, we study the distance distribution of stars in the the Geneva-Copenhagen Survey (GCS, [Nordström *et al.* 2004]). The Geneva-Copenhagen survey provides a catalog of 16 682 kinematically unbiased F, G (and in lesser extent, K) solar neighborhood stars brighter than $V \sim 8.3$ mag. To compute distances, we adopted the improved stellar parameters provided by [Casagrande *et al.* 2011]. The work of [Casagrande *et al.* 2011] provide fundamental parameters $T_{\rm eff}$, $\log(g)$ and metallicity, derived from photometry in combination with Hipparcos distances. The effective temperatures are obtained from a calibration based in the infrared flux method (their $ifrm$ sample). Metallicity is estimated from Strömgren $uvby\beta$ photometry. Finally, $\log(g)$ values are estimated by using the classical ($T_{\rm eff}$,L) relation, adopting absolute magnitudes which are in turn derived from the known trigonometric distances.

From the description above, we can see that the comparison of Hipparcos/computed distances for this catalog can be understood as an internal consistency test of our code. In fact, given that Hipparcos distances are used to obtain surface gravities, we expect to cleanly retrieve distances with our method, accounting for the inclusion of observational uncertainties. We calculate distances for all stars in the $ifrm$ subsample of [Casagrande *et al.* 2011] with relative error in parallaxes smaller than 10 percent and no flags in 2MASS photometry. The errors in fundamental parameters are adopted according to the characterization provided in [Casagrande *et al.* 2011], namely $\Delta T_{\rm eff} = 95$ K, $\Delta \log(g) = 0.025$ dex and Δ[Fe/H] $= 0.13$ dex.

In the upper left panel of Fig. 3.3 we display the comparison between geometrical and spectro-photometric distances for the CGS sample. We can see that the agreement is excellent, with negligible bias and dispersion of residuals, and a mean relative distance error of only $\sim 2\%$. The absolute relative distance error for the 80 % of the sample is smaller than 5%.

On the other hand, given that the bulk of stars in the GCS are are essentially reddening free -because of their short distances- a comparison with respect to the estimated values with our code in not performed.

3.1.3.2 Adibekyan et al 2013

Unlike the previous test, we compute now distances for a sample whose fundamental parameters come from a high resolution spectroscopy-based study. The sample, presented in [Adibekyan *et al.* 2012] and used to study kinematical and chemical properties of the Galactic disk in [Adibekyan *et al.* 2013], consists in 1111 solar neighborhood long-lived FGK dwarf stars from the HARPS GTO planet search program. To perform our distance calculations, we adopt 2MASS photometry, keeping stars with AAA quality flag. We also remove stars for which the relative parallax errors are larger than 20%. Finally, we eliminate all stars with $T_{\rm eff} > 6000$ K, since the parameters of stars in this range seem to be less robust ([De Pascale *et al.* 2014]). Typical errors in fundamental parameters are claimed in [Adibekyan *et al.* 2012] to be as small as $\Delta T_{\rm eff} = 30$ K, $\Delta \log(g) = 0.06$ dex and Δ[Fe/H]=0.03 dex. Instead, we adopt slightly inflated and more plausible spectroscopic errors as $\Delta T_{\rm eff} = 100$ K, $\Delta \log(g) = 0.15$ dex and Δ[Fe/H]=0.05 dex.

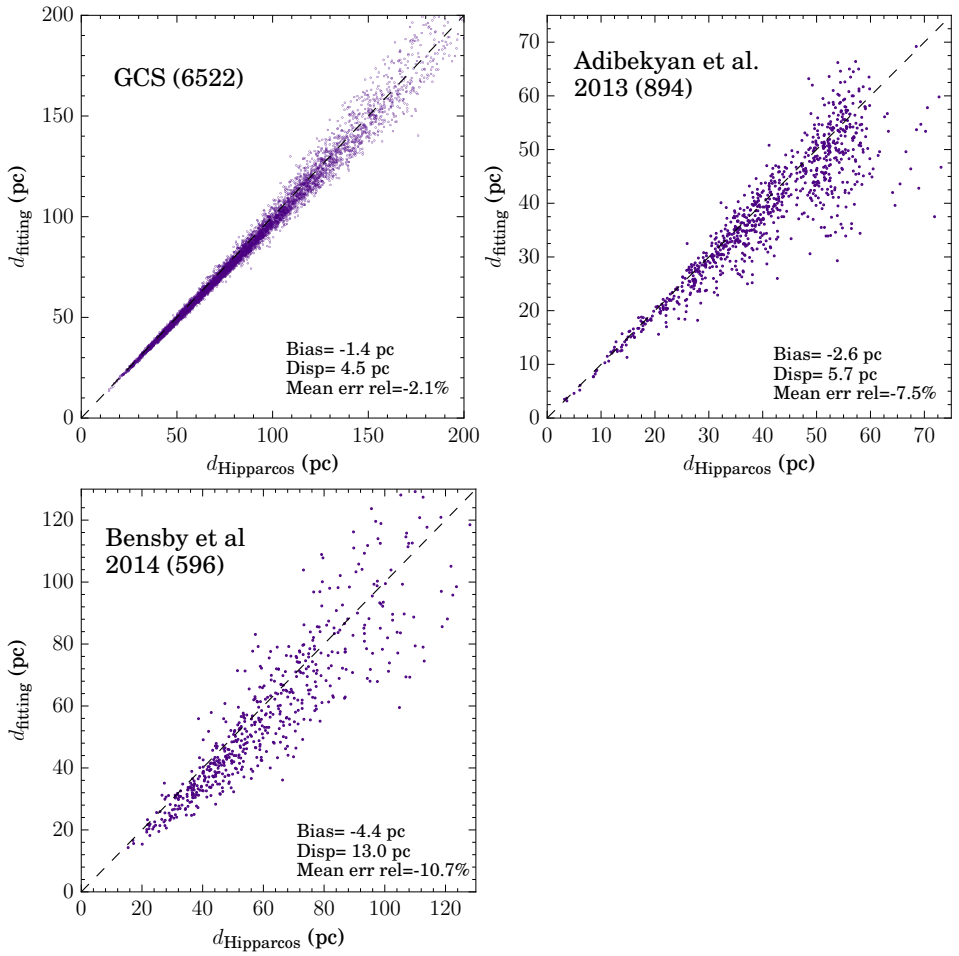


Figure 3.3: Comparison of spectro-photometric distances with respect to trigonometric values. *Upper left panel:* Hipparcos distances versus those calculated from the fundamental parameters of [Casagrande *et al.* 2011] for the Geneva Copenhagen Survey. *Upper right panel:* Hipparcos distances versus those estimated for the high-resolution spectroscopic sample of [Adibekyan *et al.* 2013]. *Lower panel:* Hipparcos distances versus those estimated for the high-resolution spectroscopic sample of [Bensby *et al.* 2014].

After applying the above cuts, we calculate distances for 894 stars. Their are compared with respect to the nominal Hipparcos distances in the upper right panel of Fig. 3.3. The general distribution falls nicely on top of the 1:1 line. The bias and dispersion are very small, as well as the mean relative error. The absolute relative distance error for the 80 % of the sample is smaller than 16%.

3.1.3.3 Bensby et al 2014

This sample consists of 714 kinematically selected F,G dwarf and sub-giant solar neighborhood stars. High quality spectra, with resolution $R = 40\ 000 - 110\ 000$ and SNR $= 150 - 300$ were obtained from a combination of different facilities (FEROS, SOFIN, FIES, UVES, HARPS and MIKE). As for the previous samples, we selected

stars with good quality flags in their 2MASS photometry and relative parallax errors smaller than 20%. The uncertainties in fundamental parameters are provided for each star in [Bensby *et al.* 2014]. Their mean values correspond to ΔT_{eff} = 61 K, $\Delta \log(g) = 0.09$ dex and Δ[Fe/H]=0.06 dex.

We calculate distances for 596 stars. The comparison with respect to Hipparcos distances is displayed in the lower panel of Fig. 3.3. The general trend of the data is quite satisfactory, with a small bias and dispersion. The mean relative error is of about 11%, while the absolute relative distance error for the 80% of the sample is smaller than 26%.

3.1.4 Tests with clusters

As described in chapter 7, the Gaia-ESO survey has devoted a significant fraction of its observing time to stars belonging to open and globular clusters. In practice, all stars belonging to a given cluster can be considered as being at the same distance. In this sense, they constitute an excellent opportunity to test the internal consistency of any method of distance determination in a star-by-star basis. They should in fact display a unimodal distribution around the cluster distance with a width accounting for observational uncertainties.

We selected all cluster targets and retrieve their fundamental parameters (as determined from the HR10|HR21 setup) from the fourth internal data release of the GES. This sample belongs to 14 globular and open clusters, namely M15, M2, NGC104, NGC1851, NGC1904, NGC2243, NGC2808, NGC362, NGC4372, NGC4833, NGC5927, NGC6705 and NGC6752.

As usual, it is possible that a fraction of the stars targeted in each cluster are foreground contaminants. To identify and remove these interlopers, we construct for each cluster the V_{Hel} vs. [Fe/H] diagram. Cluster stars naturally clump is this plane, so that an appropriate cut in velocity and metallicity around mean values is enough to select a clean sample of likely cluster members. After cleaning each cluster sample, we end up with a total of 632 stars, with an average of $\sim$ 50 stars per cluster (with a minimum of 9 and a maximum of 69). An HR diagram of the selected cluster members is displayed in the upper left panel of Fig. 3.4. We can see that the sample span a wide range of ages and phases of stellar evolution, well sampling the T_{eff}-$\log(g)$ plane.

We computed distances and line-of-sight reddenings for the whole selected sample. Final cluster distance and reddening values are estimated as the mean of the values of its member stars. A distance errorbar is computed in each case as the standard error of the mean. For comparison with independent estimates published in the literature, we retrieve cluster data from the [Harris 1996] (2010 edition) catalog of globular clusters and from the WEBDA database[4] for the two open clusters in our sample (NGC 6705 and NGC 2243).

In the upper right panel of Fig. 3.4, we display a comparison between our cluster line-of-sight reddening estimates with respect to the values reported in literature. For the majority of the clusters, which are located toward low extinction regions, our estimates

[4] Available at https://www.univie.ac.at/webda/

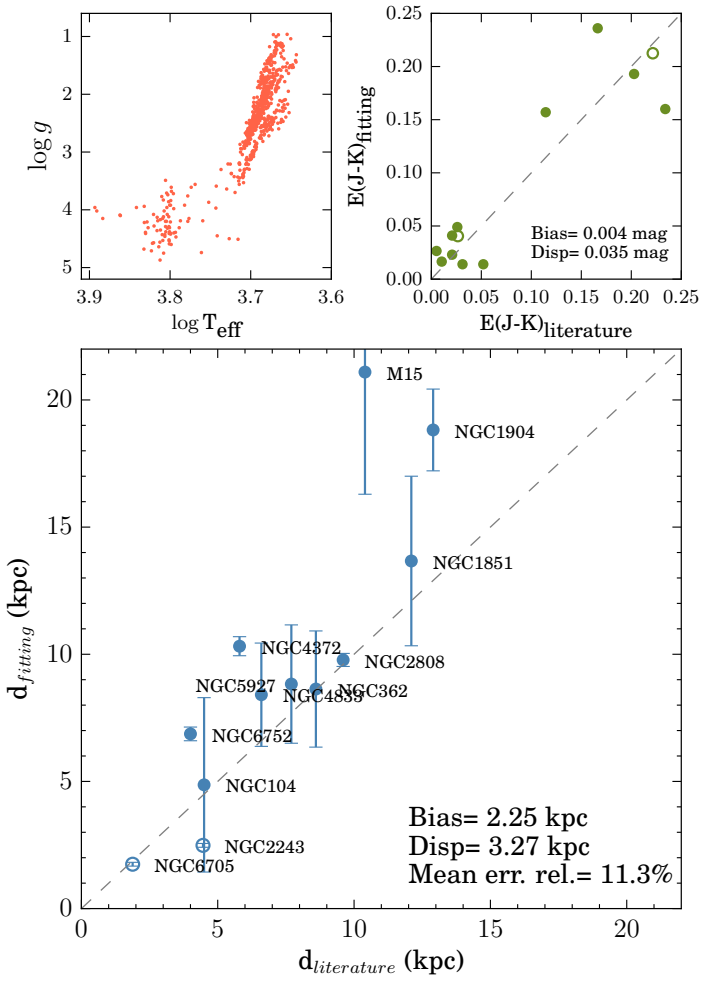


Figure 3.4: Spectro-photometric distances and reddenings computed for some GES open and globular clusters. *Upper left panel:* HR diagram of stars confirmed as cluster members. *Upper right panel:* the reddening values retrieved from literature for the clusters are compared to the mean values as determined from our spectro-photometric method. *Lower panel:* the mean spectro-photometric distances of all clusters are compared to the values published in literature. Errorbars depict the standard error of the mean. Open and filled symbols stand for open and globular clusters, respectively.

are consistent with the literature pointing to E(J-K) $\lesssim$ 0.05 mag for all of them. For clusters with higher reddening levels, the comparison is still satisfactory.

In the lower panel of Fig. 3.4, we compare our cluster mean distance estimates with those from literature. The latter are calculated from the mean V mag of the horizontal branch (V_{HB}) as primary distance indicator. In turn, the absolute calibration of the distance scale given by V_{HB} rely on distances measured more directly, such as main-sequence fitting, trigonometric parallaxes and RR Lyraes. Certainly, these estimates suffer of their own sources of errors, and shouldn't be considered as a ground truth. In fact, without the availability of accurate parallaxes it is not possible to have a refined

distance scale of globular clusters. Still, the comparison presented in Fig. 3.4 shows that our estimates does not severally diverge from other possible ways to determine distances. For all the clusters but M2 -displaying a strong deviation- the two sets of distance compares well, with just a slight tendency of our computed distances to be overestimated with respect to the literature values. In particular, we found that there is a net tendency of the difference between distance estimations to increase with decreasing cluster metallicity. Very metal-poor stars are more difficult to analyze, and consequently, the derived fundamental parameters and metallicity are prone to have larger errors. Moreover, the set of benchmark stars used to calibrate these results does not contain many metal-poor stars, so that the corrections applied to these stars might be less robust than those for more metal-rich stars. Larger errors in parameters and metallicity translate directly in larger errors in their distance estimations.

3.1.5 Distances for the Gaia-ESO Survey targets

We have computed spectro-photometric distances and reddening values for the whole bulge and disk samples with available [Fe/H] values from the fourth internal data release of the GES. By using (l,b) star positions, we further compute their Galactocentric Cartesian coordinates X_{GC}, Y_{GC} and Z_{GC}, and the cylindrical Galactocentric radial distance $R_{GC} = \sqrt{X_{GC}^2 + Y_{GC}^2}$. In Fig. 3.5 we compare line-of-sight distances with respect to surface gravity for the disk and bulge targets. Two different mean trends are visible, with bulge stars mostly crowding at the RC surface gravity position and at 8 kpc, as expected from its selection function (Chap. 2). Instead, disk stars display a shallower trend. with most of the stars lying at main-sequence gravities and inside 3 kpc of heliocentric distance. Figure 3.5 provides an overview, while a detailed analysis and exploitation of bulge and disk distances will be performed in detail in Chap. 5.

If we consider the typical uncertainty levels of fundamental parameters of disk and bulge datasets, as described in Chap. 2, and the results of the test performed on the code above, we can establish a conservative limit of 25-30% for the typical internal errors in distance. For our purposes these levels are acceptable, and in any case they are about the same precision level reached by other approaches in the literature. Only the advent of precise parallaxes by Gaia will substantially improve this picture.

3.2 Gaussian Mixture Models and other ways to disentangle substructure in the abundance-metallicity plane

Chemical tagging rely on the reasonable assumption that stars that born together at the same time and from the same gas cloud should display matching abundance patterns, regardless of they eventual different kinematics signatures imprinted by dynamical evolution of the system.

In this sense, the comparison of chemical patterns of stars in stellar populations represents a powerful tool of Galactic archaeology to unravel the perhaps common origin of groups of stars currently sitting at separate structural Galactic components. In this thesis, me made use of chemical information as the fundamental ingredient to

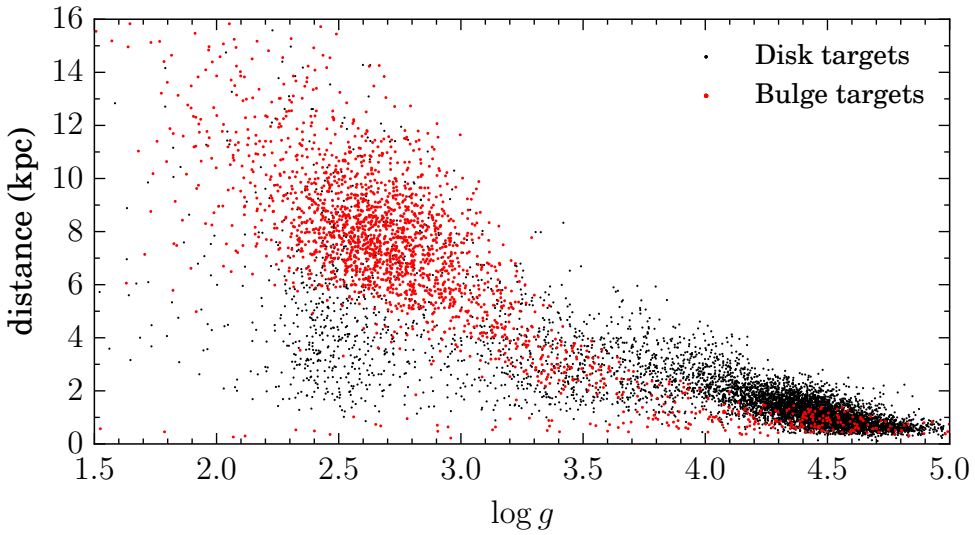


Figure 3.5: Calculated distances versus surface gravities for GES stars in disk and bulge fields.

study bulge and disk stars, which is then complemented with kinematic information. In order to classify stars based on their chemical signatures, metallicity alone or the joint metallicity+abundances, we adopted the formalism of Gaussian Mixture Models (GMM) to perform a clustering analysis searching for subgroups in the data. We briefly describe here its mathematical formalism, while in the rest of this section we will describe an alternative way we use in Chap. 5 to separate disk sequences in the abundance-metallicity plane.

3.2.1 Gaussian Mixture Models

A GMM is a parametric probability density function given by a weighted sum of Gaussian components. The GMM parameters, including the number of components and centroids, are estimated to better represent the analyzed data structure. Given a dataset with a certain number of features (points), a GMM algorithm constructs a generative model that is the specific Gaussian mixture that better predicts the data structure. Given this statistically optimal model with a specific number of clusters, we can separate the data into families according to the component that has the highest probability to have generated each feature. The cluster parameters can then be used to describe the data in terms of dispersion, correlations, or slopes. This unsupervised analysis approach does not require priors.

A mixture model (M) is a weighted sum of a number (k) of probability distribution functions (*pdf*). For a GMM in 2D, the mixture is defined by a sum of bivariate normal distributions (G) (see Annex C.2)

$$M(z|\mu,\Sigma) = \sum_{i=1}^{k} w_i G(z|\mu_i,\Sigma_i),$$

with means μ and covariance matrices Σ (see Annex C.1). The mixture model with

a specific set of parameters μ_i σ_i, and weights w_i for the components is an attempt to fit the data set z composed by N features. Given such data set, we wish to determine the parameters of the mixture of k Gaussian modes that better predict the data structure. A mixture model must satisfy

$$\sum_{i}^{k} w_i = 1$$

and should integrate to 1 over the data coordinate space.

The likelihood function of a mixture is defined as

$$L(z|\mu, \Sigma) = \prod_{j=1}^{\mathrm{N}} M(z_j|\mu, \Sigma).$$

Then, the log-likelihood corresponds to

$$\begin{aligned}\ln(L(z|\mu, \Sigma)) &= \ln\left(\prod_{j=1}^{N}\sum_{i=1}^{k} w_i G(z_j|\mu_i, \Sigma_i)\right) \\ &= \sum_{j=1}^{N} \ln \sum_{i=1}^{k} w_i G(z_j|\mu_i, \Sigma_i).\end{aligned}$$

The Expectation-Maximization algorithm maximizes the likelihood function (equivalent to minimize the negative of the log-likelihood), determining the set of parameters that defines the best mixture model $\hat{M}(z|\mu, \Sigma)$.

By fitting a GMM to a data set, we can characterize the individual modes of the probability distribution with their means and covariances. The Gaussian modes are a good way of clustering the data points into similar groups. When the fit is performed, it is then possible to check to which mode each data point belongs most probably, by calculating the responsibilities

$$R(i|z_j) = \frac{w_i G(z_j|\mu, \Sigma)}{\sum_m w_m G(z_j|\mu_m, \Sigma_m)}.$$

This means that for each datapoint there is a set of *a posteriori* probabilities to have been generated from each component of the mixture. A decision criterion, such as the highest of such responsibilities, can be used as a label to separate the sample into several data groups. More elaborated approaches can be devised to deal with the fact that some points with close equal probabilities to belong to several components can still be classified just in one with a simple criterion.

The Expectation-Maximization algorithm therefore allows us to determine the best parameters of a mixture model with a given number of modes. In a general case problem, we normally do not know a priori the number of components into which the data substructure separates. We thus need an extra loop of optimization to compare several maximum likelihood models with different number of components.

To do this, we adopted the Akaike information criterion (AIC)[5] as a cost function to assess the relative fitting quality in between different proposed mixtures. The AIC is a measure of the relative quality of a statistical model for a given set of data. It is designed to deal with the trade-off of the goodness of fit and the complexity of the model (number of GMM components). We can use it as a way to perform model selection, allowing us to determine the number of components that are presumably supported by the data. The AIC is given by

$$AIC = 2N_p - 2\ln(L_{max}),$$

where N_p is the number of parameters of the model and L_{max} is the maximized value of the likelihood function of the model (obtained through the Expectation-Maximization algorithm).

The AIC is a relative quantity in the sense that it is not a test for the null hypothesis. Indeed, it cannot tell us anything about the quality of the model in an absolute sense. The only significant information is the relative comparison of the AIC between different proposed models. As a consequence, the model with the lowest AIC value is the preferred one for a given data set. The quantity

$$P_{rel,i} = \exp\left[\frac{\mathrm{AIC}_{min} - \mathrm{AIC}_i}{2}\right]$$

gives us the relative probability that the i-th model minimizes the information loss. This is the relative likelihood of the model i.

In the next chapters we will use this mathematical approach to examine both one-dimensional data (metallicity distribution function) as well as bidimensional data in the abundance-metallicity plane. As an illustration, in Fig. 3.6 we present a general case of data in the abundance-metallicity plane by simulating distributions trying to reproduce plausible disk sequences. In the upper panel, a sample of 935 stars was generated randomly from a model consisting of a mixture of five bivariate Gaussians with different covariance matrices. Some degree of superposition between stars belonging to the different components is allowed, as visible from the different colors used to represent datapoints. The results of a GMM analysis on this dataset are displayed in the middle panel. The same color code is used but this time to depict the group membership of the stars according to the responsibilities. The five original components are found in the data. They are illustrated by gray ellipsoids depicting the regions containing the 90% of the probability density of the respective component. By comparing the upper and middle panels is clear that the sample substructure is nicely recovered.

As expected, the classification of stars in regions where two or more components overlaps is more uncertain. In general, the largest responsibility associated with one of the model components for a given data point will depend of both the distance with respect to the centroids of all the components and the relative weights of them in the composite model. On the other hand, under the assumption of Gaussian components

[5] Another alternative could be the Bayesian information criterion (BIC). It penalizes a solution with increasing level of complexity (i.e., larger number of modes in the mixture) more strongly than the AIC.

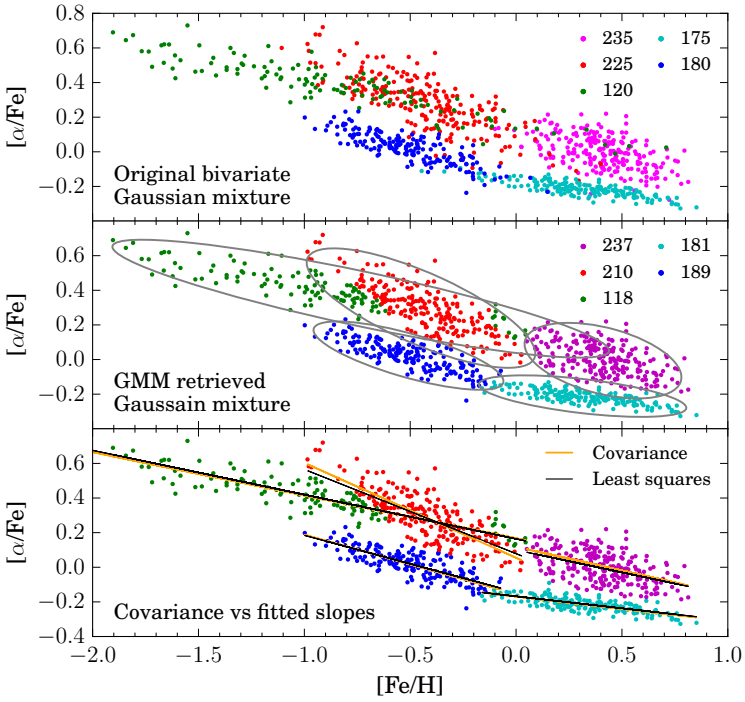


Figure 3.6: Performance of a GMM classification on a sample simulating disk sequences in the abundance-metallicity plane. *Upper panel :*random samplings from five bivariate Gaussian distributions are merged to compose the test dataset, as depicted by the different colors. *Middle panel:* data classification as determined from the best GMM model. Individual gray ellipses depict the area containing 90% of the probability density of each component of the model. *Lower panel :*slopes are computed for each data group directly from the data and using the covariance information of the best model.

made by the GMM approach, a deviation from Gaussianity, like a tail or a gap in metallicity or abundance, will produce a separation of data into an extra component. If the dispersion and superposition of data substructures is not large, the method is quite efficient in recovering the characteristics of the generative model of the simulated distributions.

3.2.2 Separating disk sequences in the abundance-metallicity plane

As explained above, a GMM analysis can be used to find substructure in the distribution of a stellar sample in the abundance-metallicity plane. In particular, it allow us to separate the α-rich and α-poor sequences -associated with the thin and the thick disk- in a way compatible with other approaches that separate them by following the minimum density of [α/Fe] in several metallicity bins ([Recio-Blanco *et al.* 2014, Mikolaitis *et al.* 2014]), or using a pure maximum likelihood procedure in narrow metallicity bins ([Kordopatis *et al.* 2015]). We refer to these papers for a detailed description of the respective procedures, as well as their results using samples from the first and third internal data releases of the Gaia-ESO survey.

We want to illustrate here a somehow different procedure to separate disk sequences which is also based in the examination of the [α/Fe] distribution in narrow metallicity bins. We will use it in Chap. 5 when attempting a comparison between the bulge and thick disk sequences. The idea is illustrated in Fig. 3.7, where we apply it to the synthetic data presented in Fig. 3.6. Given a data set in the abundance-metallicity plane, a number of metallicity bins are defined narrow enough to better define the separation of sequences as a function of metallicity and broad enough to contain a statistically significant number of data points. As shown in the upper panel of Fig. 3.7, we just consider the metallicity extent where two sequences are apparent in the data. A k-means algorithm is applied to the [Mg/Fe] distribution in each bin, with the motivated election of $k = 2$ clusters. From the individual bin-to-bin solutions (red crosses in upper panel), the position of the two sequences is determined along the metallicity extent of the sample, allowing to define a nominal separation, and to perform a classification of the stars in the sample (middle panel). At the metal-rich and/or metal-poor extremes, where the separation between sequences is not clear or the number statistics is not enough, we can extrapolate horizontally the [Mg/Fe] level of the separation at the closest defined metallicity bin (middle and lower panels).

3.3 Summary

In this chapter, we presented some tools and mathematical approaches adopted to study the bulge and disk datasets from GES and APOGEE in the course of this thesis.

In summary:

1. We can determine spectro-photometric distances by comparing the apparent magnitude of a given star with an estimation of its absolute magnitude computed from their fundamental parameters through a set of isochrones. Our implementation adopt PARSEC isochrones and an approach similar to other methods in the literature ([Zwitter *et al.* 2010, Ruchti *et al.* 2011, Kordopatis *et al.* 2011]).

2. From different test on the performance of the code, we establish that distances can be estimated within a conservative uncertainty of 25-30%.

3. We computed distances for the all disk and bulge stars observed by the Gaia-ESO survey up to its fourth internal data release.

4. We described two approaches we can use to separate thin and thick disk stars in the abundance-metallicity plane. We can use a Gaussian mixture models algorithm, or a simple search for the density minimum of [α/Fe] in several metallicity bins. Both procedures provide consistent results regarding the ability to split high-α and low-α sequence stars, if the quality of the data is good enough.

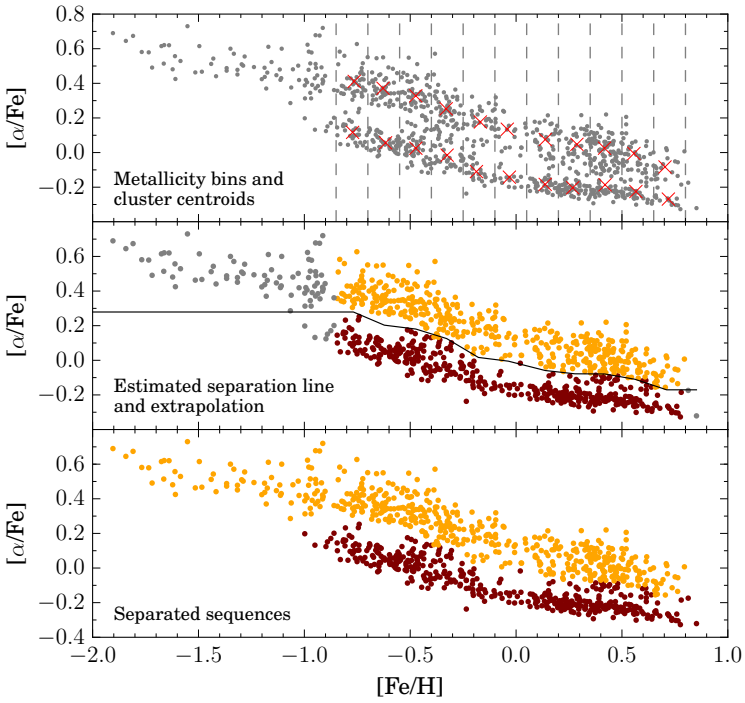


Figure 3.7: Separation of simulated disk sequences on the abundance-metallicity plane by applying a k-means clustering algorithm in narrow metallicity bins. *Upper panel:* the dataset is separated in several narrow metallicity bins in the range where the two disk sequences are apparent in the data. A k-means clustering with two nodes is run in each bin, and the resulting centroids are depicted by red crosses. *Middle panel:* from the cluster centroids, a separation line between the sequences is estimated (black solid line). It is horizontally extrapolated outside the metallicity range user to compute it. *Lower panel:* final classification of the sample into low- and high-α sequences.

Chapter 4

The Galactic disk system: disentangling disk sequences and chemical substructures

Contents

4.1 Data samples 88
4.1.1 Gaia-ESO survey sample 88
4.1.2 APOGEE sample 89
4.2 Distribution of disk stars in the metallicity-abundance plane . 91
4.3 GMM decompositions of GES and APOGEE samples 92
4.3.1 GES working sample 93
4.3.2 GMM results for different stellar luminosity classes 95
4.3.3 Comparison with APOGEE-RC data 98
4.4 The metal-poor thin disk 100
4.4.1 Definition of a robust-membership subsample 101
4.4.2 Vertical distribution of disk stars 102
4.4.3 Galactic rotational velocity of disk stars 105
4.5 Implications for disk formation models 107
4.6 Summary and conclusions 110

Abstract: Recent spectroscopic surveys have begun to explore the Galactic disk system on the basis of large data samples, with spatial distributions sampling regions well outside the solar neighborhood. We used data from the second data release of the Gaia-ESO survey to study the distribution of disk stars in the metallicity abundance plane. We use a Gaussian mixture models algorithm, separating the sample in five groups associated with major Galactic components; the metal-rich end of the halo the thick disk, and three subgroups for the thin disk sequence. The metal-intermediate and metal-rich subgroups of the thin disk sequence ($[Fe/H] > -0.25$ dex) highlight a change in the sequence's slope at solar metallicity, which holds true at different radial regions of the Galaxy. The metal-poor thin disk subgroup ($[Fe/H] < -0.25$ dex) presents a Galactocentric distance distribution shifted to larger distances than those of the more metal rich subgroups, a scale-height intermediate between those of the thick and the metal-rich thin disk, and

higher mean azimuthal velocity than the latter. These stars might have formed and evolved in parallel and/or dissociated from the inside-out formation taking place in the inner thin disk. Their enhancement levels might be due to their origin from gas pre-enriched by outflows from the thick disk or the inner halo. This chapter is based on results published in A&A, 586, 93 (Rojas-Arriagada et al., 2016).

A significant new piece in our understanding of the global structure of the Milky Way was incorporated around 20 years ago with the discovery of the thick disk ([Yoshii 1982, Gilmore & Reid 1983]). Since that time, a significant amount of observational evidence has triggered a very active research activity, which is reviewed in Chap. 7. First identified as a deviation in the assumed simple exponential density profile of the vertical number density distribution of disk stars, the separation between thin and thick disk stars has been proposed to be possible based on kinematics or chemical criteria. In particular, it is becoming increasingly clear that a separation based on the distribution of disk stars in the abundance-metallicity plane is a fruitful way to separate clean samples with less superposition in other properties.

The interpretation of the stellar distribution in the metallicity-abundance plane of disk stars is currently a hot topic of debate. Separating the relative contribution of thin/thick disks, and the variations in their properties with R_{GC} and z is an important ingredient to reconstruct the formation scenario of the disk as a complex entity during the assembly of the Milky Way. In this chapter, we present a discussion about what we learned about the disk system from the analysis of data coming from the second internal data release of the Gaia-ESO survey, and in particular, we discuss the usefulness of using non-supervised algorithms for searching sub-structures of data samples in the abundance-metallicity plane.

4.1 Data samples

As explained in Chapters 7 and 2 a major fraction of the Gaia-ESO survey pointings is devoted to observe disk fields both at high and low latitude. The idea is to provide a dataset of stars spanning a spatial volume large enough to explore the inner/outer Galaxy, thin/thick disk structure and the disk/halo transition. For the present work, we made use of data coming from the Gaia-ESO and APOGEE surveys. In both cases we only considered lines of sight corresponding to disk fields, excluding clusters and pointings toward the bulge. The GES data are those acquired up to the second internal data release. It comprises a subset of 8906 FGK field stars,

We describe below some specific details concerning the selection of working samples from GES and APOGEE.

4.1.1 Gaia-ESO survey sample

The GES dataset contains stars in 129 different lines of sight at high and low latitude fields. From the characteristics of the selection function, we expect the data to be composed of disk(s) and halo stars. Only the best-quality stellar parametrizations were kept by considering the smallest errors in fundamental parameters and elemental

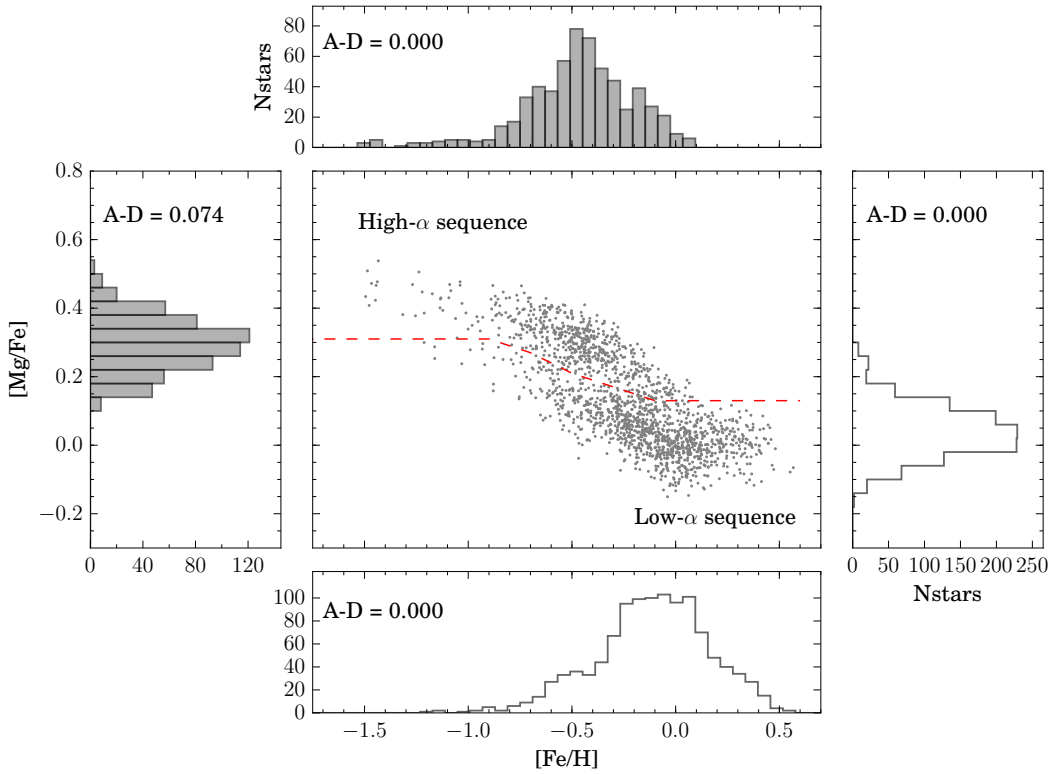


Figure 4.1: Working sample of GES iDR2 disk stars in the [Mg/Fe] vs. [Fe/H] plane. A red dashed line marks the separation between α-rich and α-poor sequences estimated by following the number count minimum of [Mg/Fe] in several intervals of metallicity. The four panels around the central one display the marginalized distributions in [Fe/H] and [Mg/Fe] corresponding to the alpha-rich and alpha-poor sequences. Filled histograms stand for the thick disk and step histograms for the thin disk. A $p-$value, derived from the Anderson-Darling test for Gaussianity, is quoted in each panel.

abundances. As another selection criterion, we used the signal-to-noise ratio measured in the spectra obtained with the HR10 setup of GIRAFFE. The corresponding SNR in the HR21 setup is about twice as high. To clean up the sample, we applied cuts to the 90^{th} percentile of the error distributions in stellar parameters, iron abundance, and magnesium abundance. These cuts correspond to $\Delta T_{\rm eff} = 136$ K, $\Delta \log(g) = 0.27$ dex, Δ[FeI/H]=0.14 dex, and Δ[MgI/H]=0.10 dex. Therefore, stars with errors simultaneously smaller than the respective cut values, and having a $\rm SNR_{HR10} > 33$ were kept. For the present analysis, we adopted the metallicity [Fe/H] and magnesium abundance ratio [Mg/Fe] as determined from FeI and MgI lines. Typical mean errors in these quantities are $\overline{\rm E[Fe/H]} = 0.06$ dex and $\overline{\rm E[Mg/Fe]} = 0.07$. The resulting clean working sample comprises 1725 stars and is shown in Fig. 4.1. It presents a fairly clean distribution in the plane [Mg/Fe] vs. [Fe/H], with only a small number of outliers. To ease the Gaussian mixture analysis, we removed them with a MAD-clipping algorithm. They are 12 stars in total, and are well distributed in the metallicity range of the data.

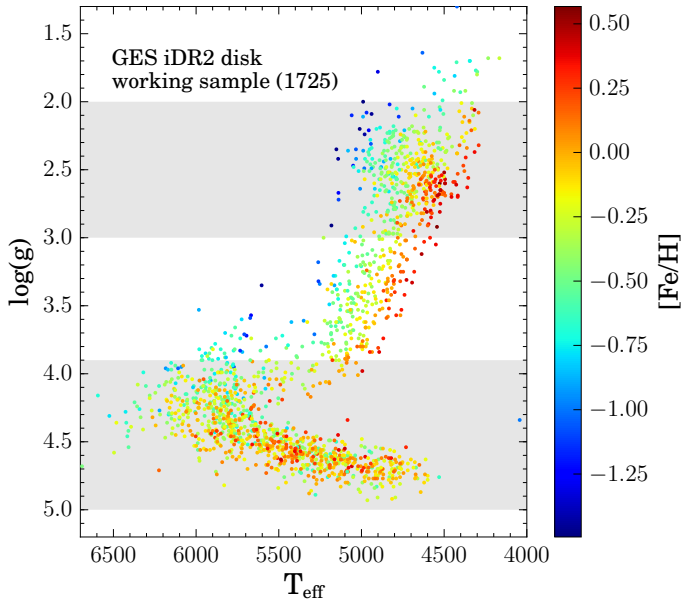


Figure 4.2: HR diagram of the GES iDR2 disk working sample. The points are color-coded according to the metallicity. Two horizontal gray bands depict the surface gravity ranges adopted to define dwarf and RC subsamples.

As shown in Fig. 4.2, our working sample covers all the main stellar evolutionary stages of low mass stars, the main-sequence, turn-off, RGB and the RC. Finally, distances were obtained via isochrone fitting using the method described in [Kordopatis *et al.* 2011] and [Schultheis *et al.* 2015]. This approach is similar to that presented in Chap. 3 which was developed in the context of the analysis of GES iDR4 data (see next chapter).

4.1.2 APOGEE sample

The APOGEE selection function is described and characterized in detail in [Zasowski *et al.* 2013]. In a nutshell, it selects stars satisfying the color-magnitude constraints $(J\text{-}K)_0 \geq 0.5$ and $7.0 \geq H \geq 13.8$. To this end 2MASS photometry is used. Colors are dereddened from the extinction derived using the Rayleigh Jeans color excess (RJCE) method [Majewski *et al.* 2011]. The color cut was set red enough to remove main-sequence stars, but blue enough to reduce the bias against metal-poor giants.

We used the APOGEE red clump catalog (APOGEE-RC) of 19937 stars described in [Bovy *et al.* 2014]. In that work, RC stars were selected from the general APOGEE DR12 catalog based on their position in the color-metallicity-T_{eff}-log(g) space. The classification method is calibrated using stellar evolution models and high-quality asteroseismology data. In this way, the derived distances for the sample are claimed to be accurate to 5-10 %.

In order to work with a clean sample, we made use of several flags provided by the APOGEE pipeline ASPCAP [Garcia Perez *et al.* 2014]. They characterize the quality of the spectra and fitting procedure, allowing us to remove stars with less robust parameters. In particular, we used ASPCAP $\chi^2 < 10$ and ASPCAPFLAGS containing a warning about any parameter as criteria to eliminate stars from the sample. We also selected stars with SNR > 220. By applying all these cuts, we obtained our APOGEE working sample composed of 6107 RC stars with good quality stellar parameters. The

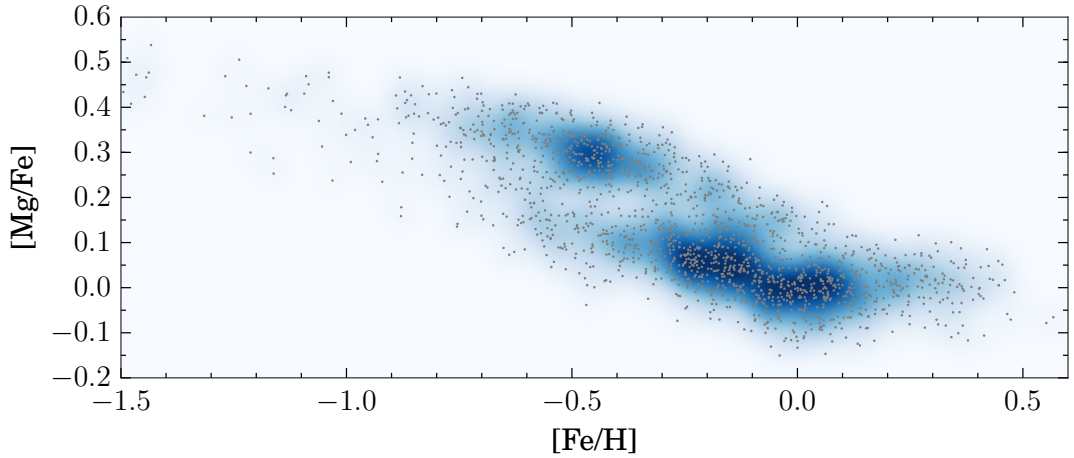


Figure 4.3: Density distribution of disk stars in the [Mg/Fe] vs. [Fe/H] plane. Small gray dots depict the distribution of the GES working sample. The background color map corresponds to the convolution of the star positions with a Gaussian kernel of 0.03 dex in both [Mg/Fe] and [Fe/H].

ASPCAP pipeline provides T_{eff}, $\log(g)$, [M/H], [C/M], [N/M], and [α/M]. A calibrated version of them is obtained by empirical comparisons to external spectroscopic references [Mészáros *et al.* 2013] and is provided in the public APOGEE-RC catalog. We adopted these calibrated stellar parameters for our analysis. Our idea is to use this sample, in particular adopting [M/H] and [α/M], to perform a qualitative comparison with the results obtained from Gaia-ESO survey data. Typical mean errors in these quantities are $\overline{\mathrm{E[M/H]}} = 0.03$ dex and $\overline{\mathrm{E}[\alpha/\mathrm{M}]} = 0.01$ dex.

4.2 Distribution of disk stars in the metallicity-abundance plane

We used the GES working sample to explore the possible chemical substructures in the [Mg/Fe] vs. [Fe/H] plane. We adopted this plane because the abundance determinations for the α-element Mg seem to be less affected by errors in stellar parameters and because visual inspection showed some evidence for a better separation of thin and thick disk sequences than for other elements. Moreover, together with oxygen, magnesium is thought to be almost entirely produced during the hydrostatic burning phases in massive stars ($M > 10M_{\odot}$) and restored into the ISM by SNII explosions [Matteucci & Chiappini 2001].

We used the procedure described in Chap. 3 to separate the sample into thin and thick disk sequences by following the minimum in the count density distribution of stars in [Mg/Fe] in several narrow metallicity bins. In Fig. 4.1, this separation into low- and high-alpha sequences is depicted by the red dashed lines. For each sequence, we constructed histograms of their marginalized distributions in [Fe/H] and [Mg/Fe]. They are displayed in the lateral panels of Fig. 4.1. A visual inspection shows that in each case the data cannot be represented by a single Gaussian distribution. In all cases, it is

possible to find visual evidence for substructures, secondary peaks, and departures from Gaussianity. To quantify them, we performed an Anderson-Darling test (see Appendix C.3) in each distribution. This statistic tests for normal distribution with unknown mean and variance. The corresponding p-values (see Appendix C.4) are quoted in each panel. We clearly see that, in almost every case, we can reject the null hypothesis that the sample comes from a normal distribution. The only exception might be the [Mg/Fe] distribution of the thick disk, with a p-value=0.07, although it is fairly close to the 5% limit.

A more explicit characterization of the number density distribution of our disk stars in the [Mg/Fe] vs. [Fe/H] plane is given in Fig. 4.3 where the stars are overplotted on a smoothed Gaussian density map. The underdensity between thin and thick disk sequences is clearly visible. A hiccup in density is visible in the thick disk sequence at [Fe/H] ~ -0.25 dex. In the same way, a bimodal overdensity is visible in the thin disk sequence with peaks at [Fe/H] ~ -0.3 and 0.05 dex, respectively.

This preliminary data overview is important to guide the adopted strategy for data analysis. As the statistical test shows, the marginalized distributions cannot be explained by a single Gaussian, but their general shape suggests a possible mixture of two or three peaked distributions. In the following, we will assume multiple Gaussianity as a reasonable simple approximation and verify a posteriori whether this adopted assumption satisfactorily reproduces the shape of the data, providing also physical insights.

4.3 GMM decompositions of GES and APOGEE samples

In view of the data properties revealed by the above exploratory inspection, we adopted the formalism of GMM to perform a clustering analysis searching for subgroups in the data. This unsupervised analysis approach does not require priors. As presented in Chap 3, a GMM is a parametric probability density function represented as a weighted sum of Gaussian component densities. The GMM parameters, including the number of components and centroids, are estimated to better represent the analyzed data structure. With this approach, we aim at detecting and characterizing the number density and slope variations of the different sequences in the abundance-metallicity plane.

4.3.1 GES working sample

We applied the GMM algorithm to our GES working sample in the [Mg/Fe] vs. [Fe/H] plane, searching for mixtures composed of up to 10 components. This is an overestimated number, since we expect the disks and halo to be represented by fewer components. Nonetheless, we test for such multi component solutions to ensure that the selected model based on the AIC (see Chap. 3) is the preferred one considering also potentially overfitted solutions. To avoid unphysical overfitted solutions, we set a minimum allowed value for the covariance[1] of the bivariate Gaussian[2] modes of the mixture. We adopted $\sigma_{min} = 0.05$ dex, which is permissive, but avoids unphysical narrow com-

[1] See Appendix C.1 for a description of the covariance matrix.
[2] See Appendix C.2 for a mathematical description of the bivariate normal distribution.

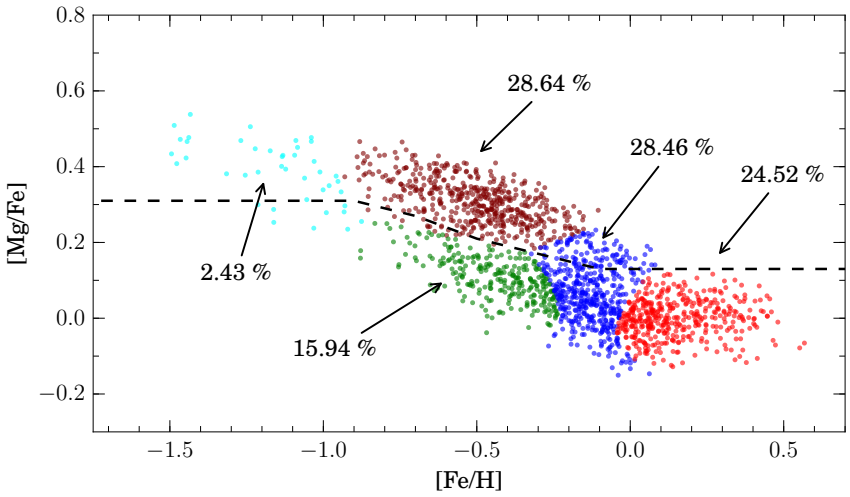


Figure 4.4: GMM best model for the GES data distribution in the [Mg/Fe] vs. [Fe/H] plane. The colors highlight the different data families corresponding to individual modes of the Gaussian mixture. Stars are classified according to the highest component-associated responsibilities. Three black dashed line segments displays the division into thin and thick disk sequences presented in in Fig. 4.1. We quote the percentage of the sample that each component encompasses.

ponents in the data. In this way, we avoid finding substructure with a size smaller than the typical errors in [Mg/Fe] or [Fe/H] ($\overline{\mathrm{E[Fe/H]}} \simeq 0.06$ dex and $\overline{\mathrm{E[Mg/Fe]}} \simeq 0.07$ dex).

In Fig. 4.4 we display the best model according to the AIC model selection criterion, and for comparison, the thin and thick disk division displayed in Fig. 4.1. The dataset is separated into five components. This number seems robust since the relative probabilities of GMM solutions with 4 and 6 components with respect to the one with 4 are 10^{-11} and 0.005, respectively. Different colors are used to visually tag the stars belonging to each of the five modes of the GMM model (hereafter, we keep these colors in all figures to better identify the different data groups). It is worth to mention here that this color classification is only indicative. In fact, as explained in Chap. 3, stars can be classified into the different modes of a GMM based on the highest associated responsibility, regardless of the relative importance of other components to explain that observation. This means that stars located in regions close to the borders between components can have nearly equal probabilities to belong to two or more components, which makes their classification uncertain. However, for a qualitative description of the GMM results, a highest probability tagging is enough. The centroids and marginalized dispersions of the Gaussian modes of the best model are listed at the left side of Table 4.1.

Three of the GMM components (red, blue and green symbols) constitute a low-α thin disk sequence. A high-α component (brown symbols) stands for the thick disk, and a high-α metal-poor component (cyan symbols) for the metal-poor tail of the thick disk and/or halo stars. The multimodal nature of the thin disk sequence qualitatively agrees with the non-Gaussianity of its marginalized distributions in [Fe/H] and [Mg/Fe], as

Group	GES-All		GES-RC		GES-Dwarfs		APOGEE	
	μ	σ	μ	σ	μ	σ	μ	σ
Cyan	(-1.09, 0.38)	(0.23, 0.09)	(-1.19, 0.39)	(0.22, 0.09)	(-0.50, 0.20)	(0.27, 0.12)	(—, —)	(—,—)
Brown	(-0.49, 0.30)	(0.18, 0.07)	(-0.49, 0.33)	(0.17, 0.07)	(-0.49, 0.28)	(0.18, 0.07)	(-0.29, 0.19)	(0.24, 0.05)
Green	(-0.35, 0.09)	(0.21, 0.08)	(-0.41, 0.15)	(0.12, 0.07)	(-0.26, 0.07)	(0.21, 0.08)	(-0.26, 0.07)	(0.14, 0.03)
Blue	(-0.12, 0.07)	(0.13, 0.09)	(-0.13, 0.11)	(0.07, 0.07)	(-0.10, 0.04)	(0.13, 0.09)	(-0.08, 0.05)	(0.08, 0.03)
Red	(0.11, 0.00)	(0.17, 0.06)	(0.19, 0.01)	(0.17, 0.06)	(0.10, 0.00)	(0.14, 0.06)	(0.11, 0.04)	(0.10, 0.02)

Table 4.1: Centroids and marginalized dispersions of the GMM modes for the different samples. The analysis was performed in the [Mg/Fe] vs. [Fe/H] plane for the GES samples and in the [α/M] vs. [M/H] for APOGEE.

seen in Fig. 4.1. Similarly, an indication of a unique strong high-α component was given by the Gaussian shape of the [Mg/Fe] distribution of the thick disk sequence, as seen in Fig. 4.1.

The low-α metal-rich end of the halo/thick disk GMM group merges at the metal-poor end of both disk components. This configures a region where the GMM classification of features is more difficult to assess given the aforementioned similitude between responsibilities associated to several GMM components overlie each other.

Between [Fe/H]=-0.8 and -0.3 dex, the agreement between the GMM groups and the separation of sequences by searching for the [Mg/Fe] number density minima in metallicity bins (dashed black line segments in Fig. 4.4), is quite satisfactory. In contrast, the blue GMM group at [Fe/H] > -0.25 dex includes both the thin disk and what is called high α metal-rich stars in [Adibekyan *et al.* 2013] and [Gazzano *et al.* 2013]. It is unclear from visual inspection whether these high α metal-rich stars are the metal-rich end of the thick disk merging the thin disk sequence around solar metallicities, or a different population. The GMM algorithm does not find a further separation accounting for such a component in GES data. The gap reported by [Adibekyan *et al.* 2013] at [Fe/H]$= -0.2$ dex that separates the thick disk sequence and the high α metal-rich stars is not visible in our data or in the APOGEE-RC sample, as presented below.

4.3.2 GMM results for different stellar luminosity classes

As shown in Fig. 4.2, our GES working sample covers all the main stellar evolutionary stages of low-mass stars. We wish to determine whether the GMM results (Table 4.1) are affected by the GES selection function given the different evolutionary stages selected in the sample. Figure 4.2 clearly shows that most of the stars are in the dwarf sequence or in the RC region. In the following, we adopt as RC stars those in the range $2.0 \leq \log(g) \leq 3.0$ dex[3] and as dwarfs those lying at $\log(g) \geq 3.9$ dex.

To perform our test, we considered the two subsamples defined above, one in the RC

[3]This range is wide enough to include all likely RC stars given the uncertainties in $\log(g)$. Moreover, this is the range normally adopted in other works (e.g. in the somehow more complex RC selection criteria of [Bovy *et al.* 2014]) to define RC samples, though that a detailed characterization of the range of RC physical parameters is a current quest (see the upcoming ARAA review on RC stars by Leo Girardi).

region (430 stars) and another in the dwarf sequence (990 stars). The resulting GMM decompositions in the [Mg/Fe] vs. [Fe/H] plane are shown in the mid and lower panels of Fig. 4.5. The results for the two subsamples agree qualitatively well with respect to the total sample shown in the upper panel.

In particular, we can conclude from Fig. 4.5 that

- RC and dwarf samples present the same qualitative data substructure, as highlighted by the respective GMM decompositions.
- The RC sample presents indications for a number underdensity in the thin disk sequence at [Fe/H]~ -0.25 and [Fe/H]~ 0.05 dex .
- The sequences drawn by RC stars seem to have less dispersion in [Mg/Fe] than those corresponding to dwarf stars: by comparing the different GMM groups, we see that the dispersions of RC stars around the linear fits of the GMM groups are in average around 10% smaller than those of dwarfs.

For the last point, we can verify whether the effect is due to larger errors in the abundances derived for dwarf stars or if it corresponds to a different behavior of the two populations. An examination of the error distributions of [Mg/Fe] and [Fe/H] in both groups of stars shows that, in general, RC stars have larger errors than dwarfs (i.e., mean errors of $\overline{\text{E[Fe/H]}} = 0.07$ dex; $\overline{\text{E[Mg/Fe]}} = 0.09$ dex for RC, and $\overline{\text{E[Fe/H]}} = 0.05$ dex; $\overline{\text{E[Mg/Fe]}} = 0.07$ dex for dwarfs), in contrast to the smaller dispersion in [Mg/Fe] observed in this group. As the errors in [Mg/Fe] measurements are of the same order of magnitude as the observed dispersions around the linear fits, no conclusions can be drawn with respect to a possible astrophysical difference in the dispersion of RC and dwarf stars.

Using the covariance information of the GMM results, we estimated linear trends of each group in the three samples shown in Fig. 4.5. They are depicted as solid color lines. We also estimated linear fits directly from the data in each GMM family group, using the Theil-Sen estimator. For these last estimates, we computed errors by bootstrapping. To do this, we resampled the respective data groups to generate 500 bootstrap samples. We calculated the slope for each resampling, estimating the final error as their standard deviation. The results for the three panels are presented in Table 4.2. These slopes, in particular for the subsolar metallicity part of the thin disk (blue and green groups), compare well to those determined by [Kordopatis *et al.* 2015] (cf. their Table 1).

In the thin disk sequence of the whole working sample, a break in slope is visible at solar metallicity, at the location of the boundary between the two metal-rich GMM components. This is equally visible in the dwarf subsample, but less so in the RC subsample. We computed the Student t-test (see Appendix C.5) for the slope difference significance of the complete sample, obtaining $t(912) = -6.615$ with an associated p-value~ 0, thus confirming its statistical significance. A similar result is obtained considering only the dwarf sample, with a p-value~ 0. For the RC distribution, the same analysis gives us a p-value$=0.39$, showing that, in this case, the difference between the slopes is not statistically significant. In particular, while comparing the two subsamples, the metal-rich GMM group presents a negative slope for RC, but a positive one for dwarf stars (Fig. 4.5 and Table 4.2).

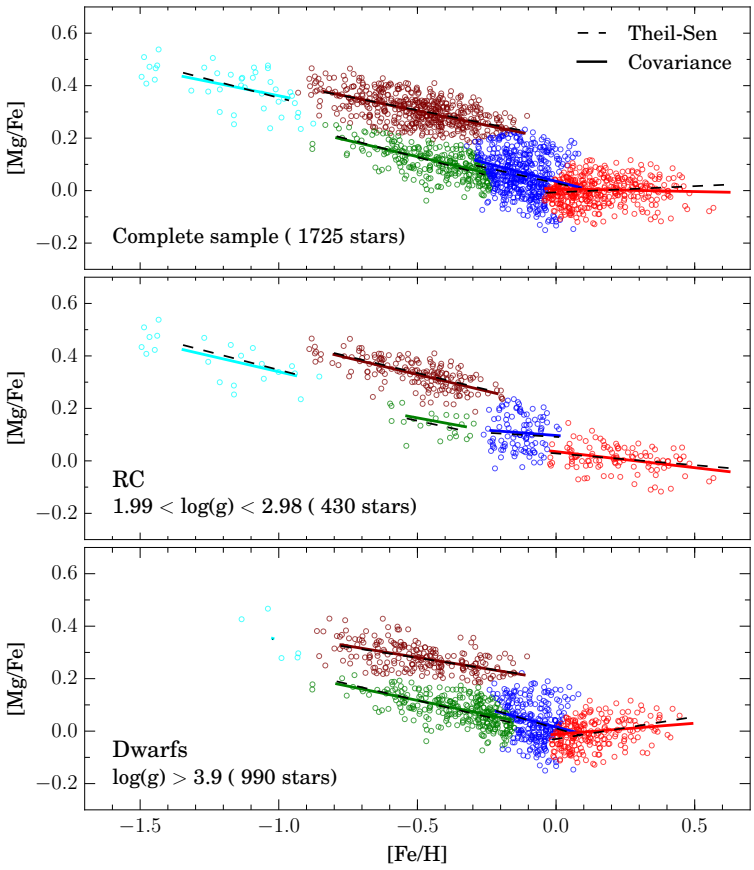


Figure 4.5: GMM decomposition performed on the complete GES working sample (*upper panel*), RC stars (*middle panel*), and dwarfs (*lower panel*). Solid black lines represent trend lines determined for each GMM group from the mean and covariance of the respective mode of the Gaussian mixture. Dashed black lines stand for trends computed directly from the datapoints.

Group	m (Total)	m (RC)	m (Dwarfs)
Cyan	-0.27±0.064	-0.27±0.059	-0.88±1.147
Brown	-0.21±0.014	-0.25±0.020	-0.16±0.022
Green	-0.28±0.020	-0.23±0.110	-0.25±0.019
Blue	-0.23±0.054	-0.06±0.115	-0.29±0.095
Red	0.05±0.018	-0.09±0.035	0.17±0.032

Table 4.2: Slopes of the linear models fitted to the data in Fig. 4.5. The slopes are estimated using the Theil-Sen estimator on each GMM group of the whole working sample (Col. 2), the RC sample alone (Col. 3), and dwarfs (Col. 4). Reported errors are estimated by bootstrapping.

These slope differences can be explained as an effect of comparing stars at different physical regimes, since the ranges in T_{eff} and $\log(g)$ of RC and dwarfs are different. Differences in the atmospheric models and line formation modeling at the respective physical regimes can lead to slightly different results by including different systematics. We checked for this possibility by constructing explicit plots between [Mg/Fe] and atmospheric parameters. No clear correlations were found. Still, some age differences (that cannot be verified here) could imply differences in the chemical enrichment patterns. A more plausible explanation for this effect comes by considering the spatial distribution of RC and dwarf stars in our sample. Red clump stars mostly sample regions inside the solar annulus at $R_{GC} < 7$ kpc, while dwarfs span a smaller range around the solar position. In this sense, the observed slope differences could arise as an effect of different chemical evolutions with R_{GC}.

Another interesting feature in Fig. 4.5 is the density gap that appears in the RC sequence at solar metallicity, where the dwarf sample presents an overdensity. A plausible explanation could be related with the GES selection function. RC stars are indeed intrinsically bright, falling out of the magnitude limits of the photometric selection when they are close. These excluded stars are precisely those that could have characteristic metallicities of the solar neighborhood. As a consequence, they remain undersampled in the respective distribution in the [Mg/Fe] vs. [Fe/H] plane.

On the other hand, as our RC stars are mainly sampling internal regions ($R_{GC} \lesssim 7.5$ kpc) of the disk, the observed thin disk stars should preferentially be metal-rich members. This can explain the scarcity of low-α metal-poor stars at [Fe/H]~ -0.25 dex in the middle panel of Fig. 4.5.

Overall, we can conclude that our GMM decomposition in the [Mg/Fe] vs. [Fe/H] is essentially the same when RC and dwarfs subsamples are compared. This demonstrates that chemical patterns depend only on the spatial distribution of the sampled population, with no relevant biases from the GES selection function.

4.3.3 Comparison with APOGEE-RC data

Our GMM analysis, illustrated in Fig. 4.4, allows us to decompose our working sample into five subgroups that highlight the number density and slope variations in the abundance-metallicity plane. In particular, the thin (low-α) and thick (high-α) disk sequences are separated by an underdensity at [Mg/Fe]$\sim 0.1 - 0.3$ dex depending on metallicity. This abundance gap, also seen in SEGUE data, has been characterized as an artifact arising from a sampling that is biased by the survey selection function [Ivezić *et al.* 2008, Bovy *et al.* 2012]. [Anders *et al.* 2014] first confirmed the existence of the gap using APOGEE first-year data, suggesting that selection effects cannot account for the dip in the data. This was later confirmed by [Nidever *et al.* 2014] and [Hayden *et al.* 2015], who expanded the three radial bins discussed in [Anders *et al.* 2014] to more bins in the Z direction.

Sampling bias effects are difficult to characterize for a given survey. We showed in the previous section that no biases are introduced in the GES sample by including a mixture of dwarf and giant stars in it. On the other hand, a comparison between results coming from two different surveys, with different selection functions, can shed light

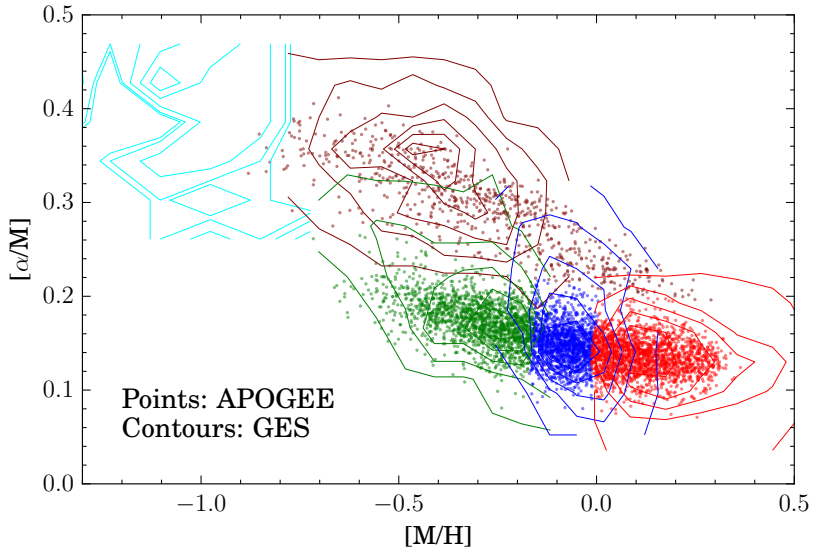


Figure 4.6: GMM decomposition of Gaia-ESO survey and APOGEE samples in the [α/M] vs. [M/H] plane. Points depict the APOGEE working sample. Contour lines draw the density distribution of Gaia-ESO survey GMM data groups. A vertical shift of Δ[α/M] = 0.1 dex was applied to the APOGEE sample to obtain a better agreement between the two data sets. Color coding is set to be consistent with the one used to represent data groups throughout this chapter.

on the relevant factors affecting the homogeneous sampling of the underlying stellar populations, and their relative impact.

With this idea in mind, we compared the results presented in the previous subsection with an equivalent analysis carried out on the APOGEE-RC working sample presented in Sect. 4.1.2. To this end, we analyzed the APOGEE sample in the [α/M] vs. [M/H] plane, given that these are parameters calibrated with respect to external spectroscopic references, [Mészáros *et al.* 2013].

The resulting GMM data group distributions are displayed with color points in Fig. 4.6. As in Fig. 4.4 for the GES sample, the APOGEE sample is separated into subgroups associated with the thin and thick disk sequences. Since the selection function of APOGEE is biased against metal-poor stars at [Fe/H] < -0.9 dex, given the survey color cut at $(\mathrm{J-K})_0 \geq 0.5$ ([Zasowski *et al.* 2013]), there are no data points in the halo region of the abundance-metallicity plane, and consequently, there is no GMM component accounting for them as in the Gaia-ESO sample. The centroids and marginalized dispersions of the resulting model components are listed in the rightmost columns of Table 4.1.

To compare our GES results with APOGEE, we computed contour plots in the abundance-metallicity plane from the [α/Fe] and [M/H] values provided in GES data. As pointed out in Sect. 4.1.2, in APOGEE, [α/M] and [M/H] are part of the set of recommended fundamental parameters. We verified that the [α/Fe] ratio available for

GES data is compatible with the [α/M] provided by APOGEE. This is given by the fact that differences between global metallicity [M/H] and iron abundance [Fe/H] are more conceptual than empirical in both surveys, so we can use these quantities indistinctly.

We proceed to compute GES contour plots in the abundance-metallicity plane. To this end we use the GMM classification in the [Mg/Fe] vs. [Fe/H] plane (Fig. 4.4) to separate the sample. After assigning group membership labels to the stars in the sample, we considered them in the [α/Fe] vs. [M/H] plane. We used the data distribution on this plane to calculate contours delineating their number density distribution. We overplot them as color lines on top of the APOGEE data in Fig. 4.6. This figure shows that the qualitative agreement is quite satisfactory after applying a vertical shift of $\Delta[\alpha/\mathrm{M}] = 0.1$ dex to the APOGEE sample. The difference is probably caused by the different chemical calibration strategy or the different definition of global metallicity adopted by the two surveys. The dispersion of GES contours is larger (but contours delineating high-density regions are tight to the APOGEE distribution) than that characteristic of APOGEE data, but the general agreement is very good. In particular, the thin disk is separated into three subgroups in both cases, with qualitatively comparable shapes.

We recall that the Gaia-ESO and APOGEE surveys constitute two different and independent observational approaches. They have a different selection function, the observations are carried with different instruments, spectral ranges, resolutions, parameter determinations, and calibrations. In spite of these conceptual and design differences, the distributions in the abundance-metallicity plane are qualitatively comparable, which demonstrates that possible observational biases do not create serious artifacts in the sample distributions. In conclusion, we can clearly see that the definition of the different sequences, halo and disks, with their associated substructures as defined by the GES sample, are confirmed from APOGEE data. The availability of a sample of common stars would provide a precious opportunity to increase synergy between the two surveys by allowing a direct comparison of fundamental parameters and abundances as well the definition of a common scale to combine results in a consistent way.

4.4 The metal-poor thin disk

Given the different sequences identified in the abundance-metallicity plane, we explore their spatial and kinematic distributions to compare them. This approach might provide interesting insights to understand their eventually different origins and/or chemodynamical evolution. We focused particularly on the metal-poor thin disk at [Fe/H]< -0.25 dex, as highlighted by one of the GMM components (green points in Fig. 4.4). It contains stars for which recent studies claimed a possible evolution disconnected from the one of the thick and metal-rich thin disk ([Haywood *et al.* 2013, Snaith *et al.* 2015].)

Figure 4.7 displays the general distribution of our sample in the |Z| vs. R_{GC} plane. As usual, points and profiles are colored according to the GMM groups as defined in Fig. 4.4. This figure shows a tendency for the metal-poor thin disk stars to be more distributed towards outer radial regions (as seen also in other works, e.g., [Bovy *et al.* 2012], [Anders *et al.* 2014]). The metal-rich thin disk group presents an excess of stars toward inner radial regions. This is consistent with the radial metallicity gradient of the thin

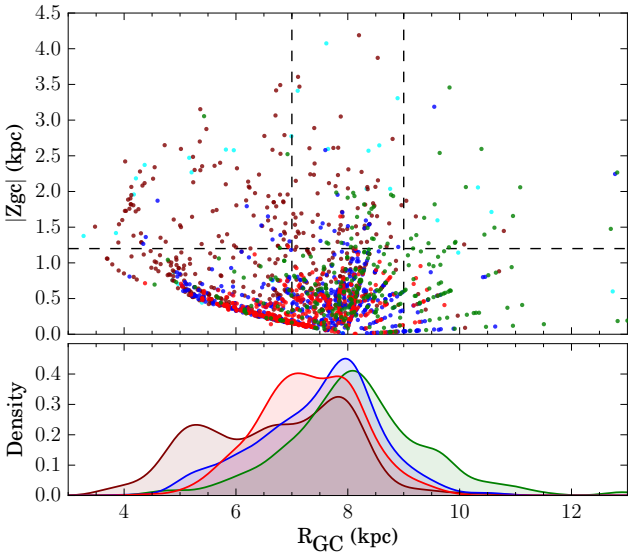


Figure 4.7: *Upper panel:* Distribution of the GES working sample in the $|Z|$ vs. R_{GC} plane. The points are colored as in Fig 4.4. Two vertical dashed lines delimit the solar region $7 < R_{GC} < 9$ kpc, while an horizontal dashed line is drawn at $|Z| = 1.2$ kpc. *Lower panel:* Normalized generalized histograms (kernel 0.5 kpc) showing the Galactocentric radial distribution of the main GMM data groups (excluding the halo stars; cyan group). They are computed using only stars with $|Z| < 1.2$ kpc to reduce the effect of undersampled regions far from the Galactic plane.

disk, and is qualitatively compatible with predictions from the chemodynamical model presented in [Minchev *et al.* 2013] (e.g., their Figure 3). Finally, the thick disk group shows a distribution extending well into the inner regions, but also with important contribution at the solar radii, although clearly less important outside the solar circle (as suggested also by the first-year APOGEE data; [Anders *et al.* 2014]).

4.4.1 Definition of a robust-membership subsample

Before proceeding with the analysis of the spatial distribution and kinematical profiles of the stars in the different GMM groups, we can stop to consider what our GMM sample classification imposes on our data set. As explained in Sect. 4.3, the data classification into GMM groups, as depicted by the different colors in Fig. 4.4, was performed by taking for each star the maximum of the set of responsibilities for this observation to be explained by each one of the five GMM components. This simple labeling process does not take into account the fact that some points, because of their position in the abundance-metallicity plane, are intrinsically prone to be explained with similar probabilities by two or even more components. Even if the errors in [Fe/H] and [Mg/Fe] are very small, these points will have a higher level of uncertainty in their classification with respect to other points located out of these component-intersection regions. This is illustrated in the upper panel of Fig. 4.8 were stars are color coded according to the maximum probability from the set of five responsibilities. We can see that in the regions were two or more GMM components intersect each other, the value of the maximum responsibility drops to less than 50%. This means that any of the GMM components explains exclusively and strongly this feature, so that its classification based in the maximum responsibility is intrinsically uncertain.

In order to study the distribution of physical properties of the GMM groups, |Z| here, for example, it is important to ensure that we work with a sample whose members

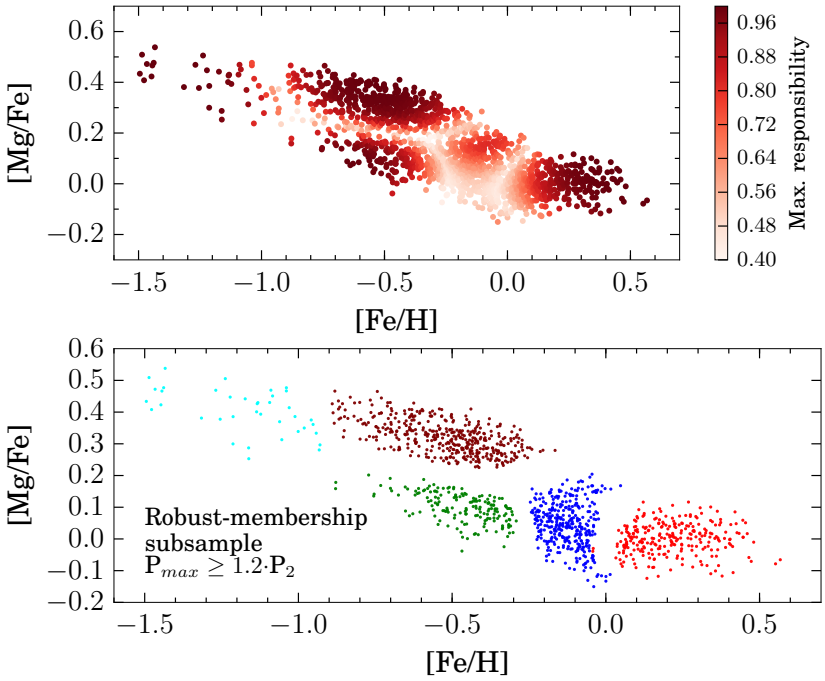


Figure 4.8: Responsibilities from GMM components for stars in the [Mg/Fe] vs. [Fe/H] plane. *Upper panel:* points are color-coded according to the value of the maximum probability from the set of five responsibilities. *Lower panel:* the sample is color-coded as in Fig. 4.4. Only stars strongly explained by one of the GMM components are kept, as explained in the main text.

are strongly explained by the components they are classified in. We devise a criterion which allow us to keep just stars with more certain classification. To this end, we performed 2000 Monte Carlo resamplings of the complete sample by generating repetitions for each star from their error ellipsoid in [Fe/H] and [Mg/Fe][4]. For each resampling, we computed the responsibility vector for each star. Since the individual position of the stars change in the abundance-metallicity plane in each repetition, their set of responsibilities changes as well. From the set of resamplings, we computed for each star the set of mean responsibilities and their associated dispersions. For a given star, if P_1 and σ_1 are the highest responsibility and its dispersion, and P_2 the second highest responsibility, then

$$|P_1 - P_2| > N\sigma_1$$

defines a criterion that allows us to keep stars whose highest responsibility is at a statistically significant distance from the second highest responsibility.

We adopted $N = 1.2$ to define a statistical subsample composed of 1252 stars (from the initial GES sample of 1725 stars). It is illustrated in the lower panel of Fig. 4.8. As expected, this criterion removes stars located in [Fe/H] and [Mg/Fe] plane regions where GMM groups intersect.

[4]The primary quantities and errors determined in iDR2 are [Fe/H] and [Mg/H]. This implies error correlations in the Monte Carlo realizations in the [Mg/Fe] vs. [Fe/H] plane, which we took into account.

4.4.2 Vertical distribution of disk stars

It is interesting to check how the disk GMM groups depicted in Fig. 4.4 are distributed in distance with respect to the plane. To perform this exercise, we assume symmetry with respect to the Galactic mid-plane and use the absolute value of Z to increase statistics.

Figure 4.7 shows the general predominance of thick disk and halo group stars at larger distances from the plane. On the other hand, the distribution of thin disk stars is less distinguishable since they crowd close to the plane. To obtain a cleaner picture, we can calculate a central tendency estimate to summarize the behavior of |Z| with respect to some other property such as [Fe/H] or [Mg/Fe].

In Fig. 4.9 we use the above defined robust-membership subsample to make explicit plots of |Z| as a function of [Fe/H] and [Mg/Fe]. For each GMM data group, we computed the median of |Z| values in equally populated bins in [Fe/H] or [Mg/Fe] (with a minimum of 40 for the green and a maximum of 90 datapoints for the blue groups). The resulting curves are displayed in the upper panels of Fig. 4.9 using square symbols and the same colors as in Fig. 4.4.

Given the errors in [Fe/H] and [Mg/Fe] and the highest responsibility-based labeling criterion, our sample can be affected by some degree of missclassification, despite the statistical cleaning performed above. We estimate its effect on the curves of Fig. 4.9. To do this, we computed 2000 Monte Carlo resamplings of the stars in the [Mg/Fe] vs. [Fe/H] plane. For each repetition, we classified the sample into the GMM groups defined by the original sample and computed the median curves for each component. From the complete set of curves for each GMM component, we determined deviations from the median trends. The shaded error bands in Fig.4.9 represent the deviations at the 1σ and 2σ level from the median tendency of the Monte Carlo resampled curves.

The upper left panel of Fig. 4.9 shows that the metal-intermediate and metal-rich groups of the thin disk (blue and red components) present a monotonous slight decrease of the mean |Z| with metallicity. In addition, the mean |Z| values of the metal poor thin disk (green) are on average 0.2 kpc higher than the more metal-rich thin disk. In this sense, the metal-poor thin disk appears to be of intermediate thickness with respect to the thick and metal-rich thin disks (although the measurement of scale heights is beyond our scope here).

If we use [Mg/Fe] as a proxy for the age of thick disk stars -what is justified by the tight correlation between them found for instance by [Haywood *et al.* 2013] in a solar neighborhood sample- we can see in the upper right panel of Fig. 4.9 a decline in the thick disk thickness with age. Older stars are distributed at larger distances from the plane. In spite of the less clear correlation between age and [Mg/Fe] for thin disk stars in [Haywood *et al.* 2013], similar trends with |Z| can be suggested for the thin disk sequence. The likely old (Mg-enhanced) stars of the metal-poor thin disk present mean |Z| values that are comparable to the younger part of the thick disk. The two GMM families standing for the metal-intermediate and metal-rich thin disk define a continuous decrement in thickness with age. Although the metal-rich thin disk stars are a continuation of the metal-intermediate stars in the |Z| vs. metallicity plane, they are not in the |Z| vs. [Mg/Fe] plane. Indeed, it has been found that many of the solar neighborhood metal-rich stars are in fact old ([Trevisan *et al.* 2011]).

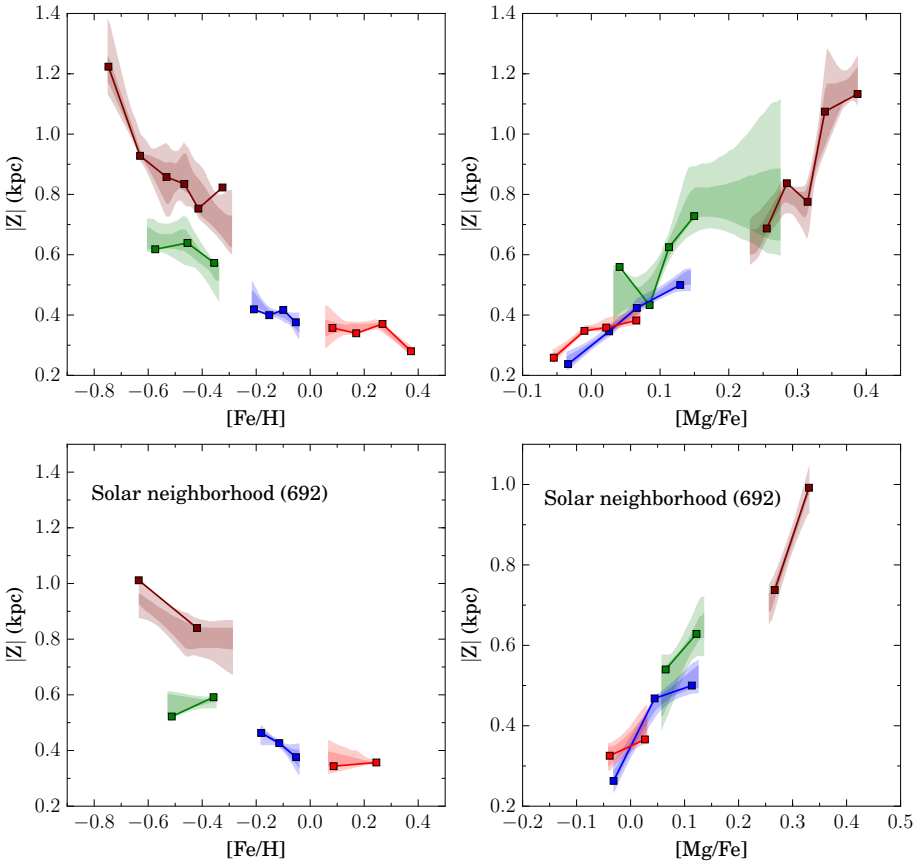


Figure 4.9: Vertical distribution of disk stars as a function of [Fe/H] and [Mg/Fe]. Colors according to the GMM groups as in Fig. 4.4. *Upper panel:* whole robust-membership subsample. *Lower panel:* robust-membership subsample in solar neighborhood. The curve+points correspond to the median values of stars separated [Fe/H] or [Mg/Fe] bins equally populated. Error bands at the 1σ and 2σ level are computed by Monte Carlo resamplings to take into account the effect of errors in metallicity and abundances on the sample classification.

The above results remain valid if instead of using the whole robust-membership subsample, we restrict it to solar neighborhood members at $7 < R_{GC} < 9$ kpc, the region depicted by the two vertical dashed lines in the upper panel of Fig. 4.7. This is illustrated in the lower panels of Fig. 4.9. The size of our sample (692 stars) does not allow us to draw strong particular conclusions concerning the solar neighborhood nor to trace radial variations in the properties described above, but reinforce the general picture emerged from the whole robust-membership subsample.

These qualitative comparisons are in relative terms and do not aim to provide an absolute idea of the scale height of the disk components.

In conclusion, from a statistically well-defined sample of stars classified into the GMM groups, we find that the metal-poor thin disk presents a characteristic thickness intermediate between those of the metal-rich thin and thick disks. The effects of star misclassification, given the errors on [Fe/H] and [Mg/Fe] of the stars in the sample, are

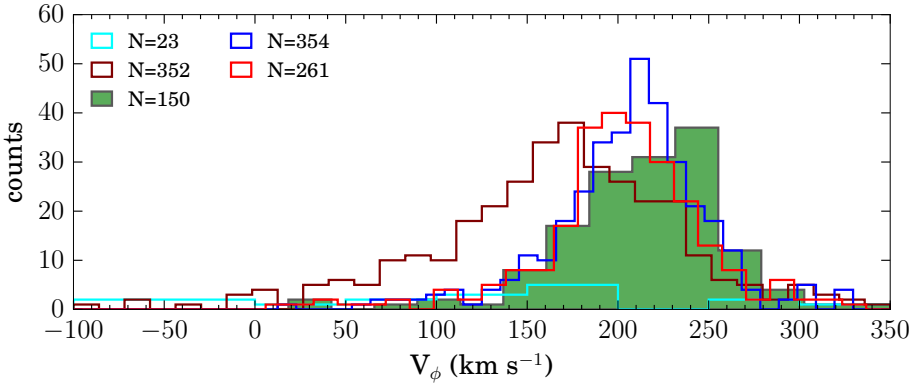


Figure 4.10: V_ϕ velocity distributions of the GMM groups. Only stars from the robust-membership subsample are considered.

small, enforcing the statistical significance of the reported differences.

4.4.3 Galactic rotational velocity of disk stars

Kinematical data were adopted from [Guiglion *et al.* 2015], where cylindrical velocity components were calculated for a larger subsample of ∼6800 stars from the Gaia-ESO survey iDR2. We use them here to characterize kinematically our robust-membership subsample. We refer to [Guiglion *et al.* 2015] for further details about computation of kinematic quantities.

As a first kinematic characterization of our robust-membership subsample, we checked the density distributions of V_ϕ for the GMM families. They are displayed in Fig. 4.10. Narrow distributions with peaks around $V_\phi \sim 200-210$ km s^{-1} stand for the metal-rich thin disk GMM groups, while a broader distribution centered at lower $V_\phi \sim 170$ km s^{-1} is found for the thick disk stars. The metal-poor group attributed to the halo/thick disk presents a very broad distribution spanning all the velocity range, which is compatible with their expected spheroidal kinematics.

In Fig. 4.11 we display the azimuthal velocity component V_ϕ as a function of the cylindrical Galactocentric radius R_{GC}. Only stars from the robust-membership subsample defined in Sect. 4.4.1 with $5 < R_{GC} < 10$ kpc were used to avoid undersampling outside these limits (see Fig. 4.7). The four curves stand for the median tendency of the stars in each GMM data group. Error bands are computed in the same way as in Fig. 4.9 to take into account the effects of sample misclassification.

The analysis and interpretation of kinematical data can be complicated by the fact that errors in stellar parameters, distances, and proper motions propagate to the computed Galactocentric velocities, eventually introducing strong outliers. The position of points defining curves in Fig. 4.11 corresponds to the median of stars separated in equally populated bins in R_{GC}[5]. The use of medians is convenient in this case to take advantage of its robustness with respect to strong influential outliers. To further ensure the robustness of the observed patterns, we cleaned the sample by removing stars with

[5]Bin populations are: brown 70 points, green 33 points, blue 90 points and red 70 points.

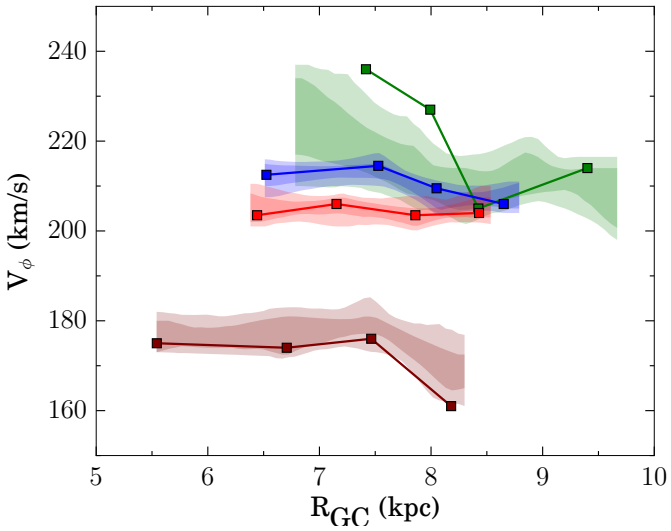


Figure 4.11: Azimuthal velocity component V_ϕ as a function of the Galactocentric radius R_{GC}. Colors as in Fig. 4.4. For each GMM data family, a central tendency curve is constructed by separating the dataset into a number of equally populated bins in R_{GC}. Median values inside each bin determine the position of the dots in the curves. Only stars with $5 < R_{GC} < 10$ kpc are considered, to avoid undersampled bins in the extremes of the distribution. Error bands are computed at the 1σ and 2σ level by Monte Carlo resamplings to take into account the effect of errors in metallicity and abundances on the sample classification.

an accuracy in V_ϕ lower than a given cutoff. Different values were tried in consideration of the error distribution of V_ϕ. We verified that no differences were introduced by allowing points with relatively higher inaccuracies in the sample. In Fig. 4.11 we use stars with accuracies better than 90 km s^{-1}, thereby removing completely the tail of high-inaccuracy stars without reducing the sample size too much. Most of the eliminated stars belong to the thick disk. After all these cuts, the robust-membership subsample used in Fig. 4.11 is reduced to 1026 stars.

Different tendencies are observed for the azimuthal velocity of the GMM components. A decreasing profile out of $R_{GC} \sim 7$ kpc is observed for thick disk stars, in agreement with ([Guiglion *et al.* 2015], their Fig. 12). The two metal-intermediate and metal-rich (blue and red) thin disk groups display nearly flat profiles centered at ~ 210 km s^{-1}. A distinct pattern is displayed by the metal-poor thin disk group of stars (green), with a peak at $V_\phi \sim 235$ km s^{-1} for stars in the range ∼7-8 kpc. This bin contains stars in the metal-rich side of the group with [Fe/H] distributed mostly between -0.3 and -0.5 dex. A decrease in V_ϕ is observed for this group at distances $R_{GC} > 8$ kpc, where the stars span a wider metallicity range to [Fe/H]~ -0.8 dex.

If we consider the current Galactocentric radius distributions in Fig. 4.7 as a blurred version of the distribution of their guiding radii, we can figure out a possible explanation for the pattern observed in Fig. 4.11. The metal-rich group stars (red) are more dominated by stars with inner guiding radii and hence display a slower rotation profile.

The metal-intermediate group stars (blue) are more concentrated on the solar radius and hence are closer on average to the solar value of 220 km s^{-1}. On the other hand, the metal-poor group contains a larger number of stars that would have guiding radii in the outer regions. The fact that they appear at smaller current Galactocentric distances can be due to orbital blurring in the sense of epicyclic motion, or because their orbits are eccentric. In this sense, stars at current distances close to the Sun will have higher azimuthal velocities as we found here.

The aspect of the error bands shows that, in general, misclassification does not significantly affect our results. A larger deviation of the error-band profile with respect to the median tendency of the sample is observed in the metal-poor thin disk group. This effect can be explained by stars that because of their relatively larger errors in the [Mg/Fe] vs. [Fe/H] plane, change of classification between thick disk and metal-poor thin disk during the Monte Carlo resamplings. Stars with thick disk kinematics being classified as metal-poor thin disk can pull down its median V_ϕ values. This effect is expected to be stronger for distant stars because of their a priori larger errors in abundance and metallicity. In spite of this, the median tendency in V_ϕ of the Monte Carlo resamplings of the metal-poor thin disk can still be separated from those of the metal-rich thin disk groups in the region $R_{GC} < 8$ kpc. This reinforces the significance of the differences found between the robust-membership subsample profiles of these groups.

Complementing information from Figs. 4.9 and 4.11 can be used to further highlight the differences between the metal-rich and metal-poor regions of the thin disk. In the following, we discuss this in the context of some other recent results and models.

4.5 Implications for disk formation models

The study of the disk(s) abundance patterns and their spatial and temporal dependency is one of the pathways to understand the formation history and subsequent evolution of the structures assembled in the Galactic disk system. A chemical classification of the disk stars from their distribution in the plane [α/Fe] vs. [Fe/H] has proven to be a fruitful way to separate clean samples of thin and thick disk stars with less superposition in the distribution of other properties.

Our GMM analysis allowed us to separate a selected Gaia-ESO survey iDR2 subsample in a way compatible with other approaches that separate thin and thick disk sequences by following the minimum density in [Mg/Fe] in several metallicity bins (as in [Recio-Blanco *et al.* 2014, Mikolaitis *et al.* 2014]), or used a pure maximum likelihood procedure ([Kordopatis *et al.* 2015]). In addition, our approach reveals some number density and slope variations of the thin disk sequence in the abundance-metallicity plane.

In this sense, if we consider the metal-rich and metal-intermediate part of the thin disk sequence (two of the three GMM groups into which the thin disk sequence is separated; [Fe/H]>-0.25 dex), with most of their stars located at $R_{GC} < 8.5$ kpc (Fig. 4.7), we see that they constitute a sequence with a slope break point at solar metallicity. The qualitative similarity between RC and dwarf distributions in the [Mg/Fe] vs. [Fe/H] plane (Fig. 4.5) shows that this slope variation is present at different Galactocentric

radial distances. These observations suggest that the chemical enrichment history of the thin disk might present some critical transition at solar metallicity.

In addition to the metal-intermediate and metal-rich thin disk groups, our cluster analysis led us to further separate a group at its metal-poor end, with [Fe/H] < -0.25 dex. Stars in this region of the [α/Fe] vs. [Fe/H] plane have been the subject of recent debates concerning some particular properties that place them in a transition status between the thin and thick disks ([Haywood *et al.* 2013]). Our data, as illustrated in Fig. 4.7, show that the radial distribution of these stars is shifted to larger current distances with respect to those of the thick, of the metal-intermediate, and of the metal-rich thin disk groups. From the more radially extended APOGEE DR12 sample of [Hayden *et al.* 2015] (also [Anders *et al.* 2014]), it is also possible to see that α-poor stars with [Fe/H]~ -0.4 to -0.5 dex are widely dominant in number at larger Galactocentric distances (their Fig. 4). Coming back to our results, the spatial distribution of metal-poor thin disk stars with respect to the plane distinguishes them from the more metal-rich internal parts, since the characteristic |Z| median values are in general higher over the whole abundance and metallicity extent (Fig. 4.9). Their azimuthal velocity distribution, as seen in Fig. 4.11, displays a complex pattern; while its stars at $7 \leq R_{GC} \leq 8$ kpc are markedly different, with a V_ϕ peaking at ~ 235 km s^{-1}, the more external $R_{GC} > 8$ kpc stars display slower rotation. In an inside-out formation scenario for the thin disk, these properties of the metal-poor group could be explained by considering them as a more warped distribution of the younger populations toward the outer disk. Actually, simulations predict that coeval populations always flare ([Minchev *et al.* 2015]). If the outer metal-poor thin disk is build up from the superposition of young populations flaring at larger Galactocentric distances, its scale height will naturally be larger than the one of the stars in the inner disk. The fact that these stars are distributed at larger distances from the plane could then also explain their smaller azimuthal velocities at large R_{GC}.

While this is a plausible explanation, some evidence indicates that the stars in the metal-poor end of the thin disk are in fact old ([Haywood *et al.* 2013]), which is qualitatively supported by the average higher Mg enhancements compared with the more metal-rich portion of the thin disk. Moreover, the study of low-redshift disk galaxies has revealed the presence of old stars dominating their stellar population in the outer disk regions ([Yoachim *et al.* 2012, Zheng *et al.* 2015]). Individual age determinations are in this context a key ingredient to test the viability of this scenario.

In the metal-poor thin disk, some of the slow rotator stars at $R_{GC} \geq 8$ kpc have metallicities of [Fe/H] < -0.65 dex. They are in a low number density region of the α-metallicity space, which is partially an intersection of the metal-poor thick disk and halo sequences. In the same region, [Navarro *et al.* 2011] identified a group of stars with cold kinematics, interpreted as tidal debris from a disrupted dwarf galaxy. This is in the same line of the low$-\alpha$ accreted halo sequence described in [Nissen & Schuster 2010]. Because the three GMM groups partially intersect in this region, and as a result of the errors in [Mg/Fe] and [Fe/H], we cannot reject the possibility that some of these stars at [Fe/H] < -0.65 in our metal-poor thin disk subsample correspond to the metal-rich tip of the accreted halo, misclassified as metal-poor thin disk. Alternatively, these stars could sample a true kinematically cold accreted component of the external thin disk.

Even if this is the case, their small number is not enough to distort the results we found for the metal-poor thin disk.

In consequence, given the results of our analysis, it might be suggested that the metal-poor thin disk stars sample a special population of outer disk stars whose evolution might be different from that of the inner disk. As shown by [Haywood *et al.* 2013] (their Fig. 17), these stars draw in the [α/Fe] vs. Age plane a sequence parallel to that of the local thin disk. As seen in Fig. 4.11, they rotate faster than the thick and thin disks in the solar neighborhood, decreasing toward thin disk values at larger radial distances. In addition, from Fig. 8 of [Guiglion *et al.* 2015], it is possible to read a positive correlation of σ_r, σ_ϕ and σ_Z with [Mg/Fe] for these stars. This evidence, if we assume that [Mg/Fe] is a proxy for the stellar age (although probably less true than for the thick disk), can be seen as an indication of a population that was kinematically hotter in the past and cooled down during posterior evolution. In the same vein as the hypothesis considered by [Haywood *et al.* 2013], this population could be composed of stars formed preferentially in the external regions of the thin disk from a relatively low surface density gas distribution. If the gas was additionally polluted by the nucleosynthesis products of the chemical evolution of the thick disk, stars form at low metallicity from a pre-enriched medium of [α/Fe] level comparable to that of the thick disk. The relatively mild increase of velocity dispersion with [Mg/Fe] is compatible with a population evolving by self-enrichment at the same time as settling in a flatter structure while increasing its rotational speed. The indication of a decrease of |Z| with [Mg/Fe] visible in Fig. 4.9 might be interpreted as a signature of an evolution in isolation, with few or no accretion events. This would agree with the dynamical analysis of [Ruchti *et al.* 2015], who found scarce evidence for an accreted component in this region of the abundance-metallicity plane.

In principle, our results might also be compatible with the general idea of an inside-out formation scenario. In the outer regions, the longer infall timescales lead to a slower chemical enrichment as a result of the lower gas density. The outer regions settle on a longer timescale, and consequently an increase of velocity dispersion and |Z| with age would also be expected (as in any model that assumes the formation of the disk by slow gas accretion). As discussed in [Chiappini *et al.* 2001], in the case of a double disk component (thick and thin understood as dual different star formation rates), the outer regions would be contaminated by a previous component (thick disk/inner halo) because there the chemical enrichment could have never been efficient enough. If the formation proceeds inside-out, then younger populations form with increasing scale length. This would imply a negative age gradient with Galactocentric distance, with younger populations dominating at the outskirts of the disk (so in conflict with the ages determined in [Haywood *et al.* 2013] for the metal-poor thin disk).

Considering the limitations imposed by the scarcity of stronger observational constraints, in particular, of age distributions, it is difficult to distinguish between these two broad scenarios. If the external thin disk started to form stars by the end of the thick disk formation from material polluted by its nucleosynthesis products, its evolution could proceed almost dissociated from the inside-out formation taking place in inner regions. We could expect it to be composed mostly of old stars. In contrast, younger average ages are expected if the external disk is the product of a pure inside-out

formation from a media contaminated by the halo or thick disk. Current evidence concerning ages in the Milky Way [Haywood *et al.* 2013] and in external galaxies [Yoachim *et al.* 2012, Zheng *et al.* 2015] seems to favor a formation of the outer thin disk proceeding in parallel to its inner regions.

In summary, our analysis leads us to characterize the metal-poor end of the thin disk as a distinct population, with different spatial and kinematic distributions with respect to those of the thick and the more metal-rich part of the thin disk. The size of our sample, and the intrinsic limitations of our data (difficulty of determining accurate distance, kinematics, and ages) prevent us from providing stronger detailed conclusions.

We hope that the new perspectives provided by the recent large spectroscopic surveys will trigger new theoretical efforts aiming at reconciling the observations with a new generation of chemodynamical models. Precise distances and proper motions from the forthcoming Gaia satellite, fundamental parameters from spectroscopic follow-up campaigns, and ages derived from the combination of these datasets will help us to clearly define the spatial and kinematic distributions for stars in a larger spatial volume. The analysis of their correlation with chemistry and ages will open very promising avenues to construct a definitive coherent picture of the structure, formation, and evolution of the Galactic components.

4.6 Summary and conclusions

We made use of the iDR2 of the Gaia-ESO survey to probe the Galactic disk system in $\sim$ 130 lines-of-sight at low and high latitudes. We selected a subsample of 1725 stars by rejecting stars with low S/N values and large uncertainties in stellar parameters, metallicity and in abundance ratio [Mg/Fe]. This subsample spans a spatial region depicted in Fig 4.7 that is mainly sampled in the ranges $5 < R_{GC} < 10$ kpc, and $|Z| < 2$ kpc.

We demonstrated the usefulness of a clustering approach to separate subsamples from their distribution in the abundance-metallicity plane. This mathematical procedure allowed us to identify and characterize subgroups in data-structure in a probabilistic way, defined by changes in slope and/or variations in the star number density.

In summary, our main results and conclusions are:

1. A Gaussian mixture model decomposition allowed us to find subgroups in the [Mg/Fe] vs. [Fe/H] plane (Fig. 4.4). Five data groups were identified and associated with Galactic populations; the metal-rich end of the halo, the thick disk sequence, and three subgroups associated with the thin disk sequence. The separation between thin and thick disks is compatible with previous procedures based on estimation of the minimum of the [Mg/Fe] distribution in metallicity bins.

2. A comparative GMM analysis between our sample and a subsample of $\sim$ 6100 APOGEE-RC stars yielded qualitatively comparable results. This allows us to conclude that the sequences and features observed in the abundance-metallicity plane, and as a consequence, the outcome of our GMM analysis on the GES sample, might not be strongly biased by the selection function of the survey.

3. The GMM decomposition does not depend on stellar types: Qualitatively similar distributions were indeed obtained for dwarf and RC subsamples. However, a different slope was found in the metal-rich end of the thin disk sequence. This could be explained as a consequence of the different radial regions sampled by the two groups of stars.

4. The metal-poor-end group of the thin disk, with [Fe/H] < -0.25 dex, displays distinct properties with respect to the rest of the thin disk metal-rich stars; it seems to have a qualitatively higher scale height and a larger rotational velocity component V_ϕ (Figs. 4.9 and 4.11).

5. Our findings, together with some other recent analysis of the Gaia-ESO iDR2 sample ([Guiglion *et al.* 2015]; [Ruchti *et al.* 2015]) and age considerations ([Yoachim *et al.* 2012, Haywood *et al.* 2013, Zheng *et al.* 2015]), seem to favor a scenario in which the metal-poor thin disk formed in the outskirts, independently of, or in parallel, to the inside-out formation taking place in the inner regions of the disk. It might correspond to a self-enriched population, formed from pristine gas polluted by material expelled from the thick disk. Posterior evolution might led these stars to settle from a relatively hot structure into a more disk-like one, increasing the azimuthal velocity and decreasing the velocity dispersions and scale height. The smooth changes of |Z| and V_ϕ with respect to [Mg/Fe] suggested by the data indicate a population that evolved in isolation, with few or no accretion events.

The chemical characterization of stellar populations has proven to be a fruitful way to separate stellar samples in a way that allows studying their unbiased kinematical and structural distributions. This provides physically meaningful insights to understand their possible different chemodynamical histories.

In essence, our main results confirm the division of $\alpha-$ rich/poor sequences to define the thin and thick disk populations as devised in previous studies. At the same time, our further separation of a metal-poor group of thin disk stars allows us to characterize it as a special substructure. Its particular structural and kinematic properties reveal a population with a chemodynamical evolution possibly disconnected from that of the metal-rich thin disk.

Chapter 5

The richness of diversity: Unveiling the composite nature of the Galactic bulge

Contents

5.1 Data sample . . . 114
5.1.1 Selected bulge fields . . . 114
5.1.2 Fundamental parameters . . . 115
5.1.3 Distances and reddenings . . . 118
5.2 Metallicity distribution function . . . 119
5.2.1 Samples in Baade's window . . . 120
5.2.2 Bimodality of the bulge MDF . . . 120
5.2.3 MDF variations with spatial location . . . 123
5.2.4 Double RC in magnitude distributions . . . 124
5.2.5 Metal-poor stars . . . 125
5.3 Trends in the [Mg/Fe] vs. [Fe/H] plane . . . 127
5.3.1 The metal-poor bulge knee . . . 129
5.4 Kinematics of chemically defined components . . . 129
5.4.1 Bulge rotation curve . . . 130
5.4.2 Kinematics at the peaks of the double RC . . . 131
5.4.3 Velocity dispersion . . . 132
5.4.4 Interpretation of metal-rich stars kinematics . . . 134
5.4.5 Interpretation of metal-poor stars kinematics . . . 134
5.5 Summary . . . 134

Abstract: The observational evidence from the Gaia-ESO survey concerning the bulge metallicity, kinematics and chemical abundances is described. The bulge metallicity distribution function is clearly bimodal across the spatial region sampled by the GES fields, with the proportion of metal-rich to metal-poor stars decreasing with the distance from the plane. There is not evident field-to-field variation in the sequences in the abundance-metallicity plane. The bulge presents a general cylindrical rotation for stars of all metallicities. Concerning the velocity dispersion,

the metal-poor stars presents an isotropic hot kinematics, while metal-rich stars decrease their dispersion with distance from the plane, a signature of bar-driven kinematics. This chapter is based on results published in A&A, 569, 103 (Rojas-Arriagada et al. 2014) and A&A submitted (Rojas-Arriagada 2016b).

In the previous chapters, we developed a careful description of all the ingredients, observations and analysis tools necessary to perform a thorough study of the Galactic bulge. We present here a detailed discussion about what we have learned about the bulge stellar populations in the context of other Galactic structures, as sampled by the Gaia-ESO survey.

5.1 Data sample

As explained in Chap. 2, an increasing number of bulge targets have been observed up to the Gaia-ESO survey iDR4 as part of the inner Galaxy-bulge subprogram. Two research papers have been published in the context of this thesis making use of these data, [Rojas-Arriagada *et al.* 2014] presenting results coming from the iDR1 and [Rojas-Arriagada *et al.* 2016a] from the latest internal data release (iDR4). As a superset of the iDR1 sample, in the following we will mostly refer to the results obtained from the iDR4, noting when appropriate what was first inferred from the iDR1 data analysis[1].

It is noteworthy to mention here, that all the results coming from the iDR4 are fully compatible, expanding and strengthening, what was obtained from the iDR1 analysis. Having said this, we present the main characteristics of the adopted iDR4 bulge dataset.

5.1.1 Selected bulge fields

The fourth internal data release of the Gaia-ESO survey contains a subset of 2320 stars distributed in 11 pointings toward the bulge region. The positions of the observed fields are illustrated in Fig. 5.1 on top of an extinction map constructed using data from the extinction maps of [Schlegel *et al.* 1998]. We can see that they are distributed nearly in the area $-10^\circ \leq l \leq 10^\circ$ and $-10^\circ \leq b \leq -4^\circ$.

Five of these fields were already observed during the first 9 months of the Gaia-ESO survey, and released as part of the iDR1 (orange symbols in Fig. 5.1). The remaining six fields (green symbols) were observed during the subsequent periods up to the iDR4[2]. The main bulge sample of 2320 stars was selected using the Gaia-ESO survey photometric VVV-based selection function described in Chap. 2. For comparison purposes, a sample of 228 RGB and RC stars in Baade's window was adopted from [Zoccali *et al.* 2008] and [Hill *et al.* 2011]. These literature stars were re-observed and analyzed in the same way as the rest of the Gaia-ESO survey bulge targets, and added to the main sample, making a total of 2548 stars. The selection function of these literature stars differs from that of the main bulge sample. In particular, [Zoccali *et al.* 2008] selected stars in the RGB approximately one magnitude over the RC, sampling the whole color range

[1] For a comparison between iDR1 and iDR4 parameters, see Annex A.

[2] More fields were planned and observed. They will become available in the next internal data release iDR5

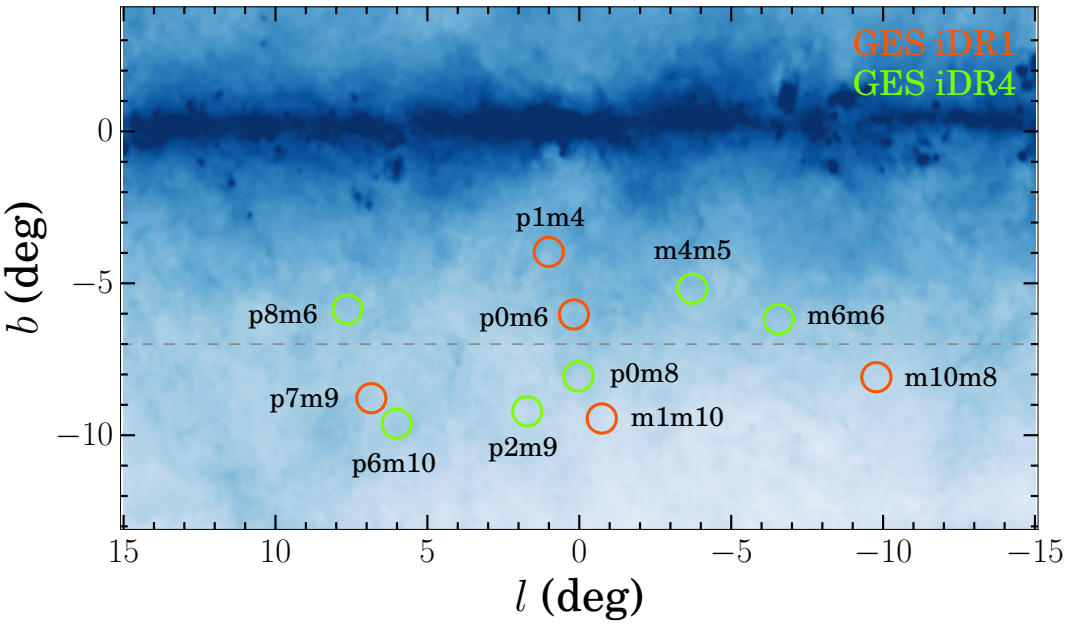


Figure 5.1: Approximate position of the 11 bulge fields analyzed in this thesis. Five red circles depict the fields already observed in the iDR1 while six green circles stand for the extra fields observed up to the iDR4. Each field is labelled according to the name coding adopted elsewhere and based in Galactic coordinates. The background image corresponds to an extinction map of the bulge region according to the [Schlegel *et al.* 1998] prescription. The color density code saturates close to the plane, where the dust obscuration is high. An horizontal dashed gray line indicates $b = -7°$, used to divide the sample into "close" and "far" to the plane fields.

as seen from V,I photometry. Instead, [Hill *et al.* 2011] selected RC stars with the requirements of $K_0 > 12$ mag and $(J-K)_0 > 0.5$ mag. We refer to Annex B for a comparison between atmospheric parameters determined by GES and published ones. The main characteristics of the observed fields are given in Table 5.1. In this table and hereafter, we refer the fields by a name convention using their Galactic coordinates (l,b) and the p/m letter coding the $\pm$ sign, to assemble their names. In this way, Baade's window, with $(l, b) = (1, -4)$ will is named p1m4. From Col. 2, we can read that most of the fields were observed at least two times, given that one GIRAFFE pointing represents ~ 110 science targets. Instead, there are two fields (m4m5 and p0m8) that were observed once. We should be careful while analyzing these fields in order to take into account the eventual effects of low number statistics implied by their moderately scarce sampling. They will be completed in forthcoming data releases.

5.1.2 Fundamental parameters

The whole data processing cascade, from target selection, instrumental setup, data reduction, fundamental parameter determination and abundance measurements is described in detail in Chap. 2. In the left panel of Fig. 5.2 we display the HR diagram

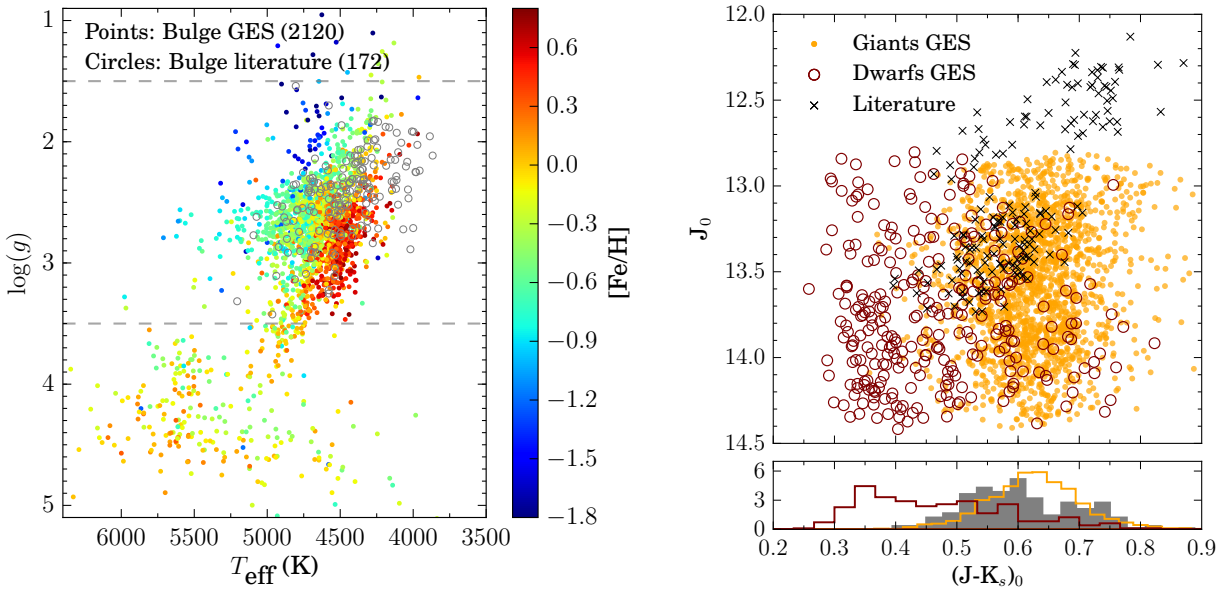


Figure 5.2: *Left panel:* HR diagram of the bulge sample for stars for which iron determinations from FeI lines are available (2292 out of 2548 observed stars). Stars selected with the Gaia-ESO photometric selection function are depicted as full circles color coded by metallicity. The subset of RC and RGB literature stars are depicted as gray open circles. Two dashed gray lines mark $\log(g) = 1.5$ and 3.5 dex. *Right panel:* Color-magnitude diagram of the bulge sample. Stars with $\log(g) > 3.5$ dex are marked as brown open circles, while those with $\log(g) < 3.5$ dex as filled orange circles. The literature sample of RC and RGB stars (all of them with $\log(g) < 3.5$ dex) are depicted with black crosses. The bottom subpanel illustrates the density distribution of these three groups of stars, color coded as in the main panel.

from the fundamental parameters of stars for which iron determinations from FeI lines are available. Essentially all of them have also magnesium determinations from MgI lines. We can verify the general good quality of the stellar parametrization, as far as the main HR features, main sequence, turn off, red giant branch and red clump are clearly distinguishable. The metallicity stratification of the sample is also visible, specially in the RGB/RC region. The sample of literature stars is located preferentially at lower surface gravity than the bulk of RC bulge stars, as expected for a mixture of RGB and RC stars, with a tendency to include in proportion more metal-rich stars than the general bulge sample. We will quantify this effect below when studying the bulge MDF.

From the comparison between the left and right panels of Fig. 5.2, it is apparent that the nature of the Gaia-ESO survey bulge selection function leads, as anticipated in Chap. 2, to a sample with some contamination from main-sequence stars. In particular, the right panel illustrates the distribution of bulge targets in the color magnitude diagram once their spectroscopic nature has been determined. The dichotomy between giant, mostly RC, and dwarf stars is clearly visible. Dwarf main-sequence interlopers are preferentially located in the blue side of the CMD, at the locus where the plume of disk dwarf stars is visible in a general bulge field CMD (c.f Fig. 2.3 Chap. 2). On the other

Field name	N_{fld}	l	b	$\overline{SN}$	E(J-K)$_{G11}$	E(J-K)$_s$	% Giants
p1m4	369	1.00	-3.97	364	0.26	0.20	97.3
p0m6	204	0.18	-6.03	254	0.14	0.17	88.2
m1m10	187	-0.74	-9.45	340	0.03	0.06	70.1
p7m9	221	6.85	-8.87	244	0.10	0.11	90.5
m10m8	310	-9.78	-8.09	347	0.03	0.08	75.5
m4m5	94	-3.72	-5.18	192	0.19	0.18	94.7
m6m6	206	-6.57	-6.18	168	0.13	0.13	91.8
p0m8	98	0.03	-8.06	310	0.06	0.07	82.7
p2m9	105	1.71	-9.22	362	0.08	0.08	77.1
p8m6	302	7.63	-5.86	250	0.22	0.20	94.0
p6m9	196	6.01	-9.62	279	0.09	0.08	81.1

Table 5.1: Characteristics of the bulge fields. Signal-to-noise ratios are the field average. E(J-K)$_{G11}$ corresponds to the reddening as computed from the extinction maps of [Gonzalez *et al.* 2011] in a box of 30 arcmin side centered in the respective (l, b) coordinates. N_{fld} is the number of stars observed in each field. E(J-K$_s$) are field average reddening values estimated from the individual star reddenings simultaneously determined with spectro-photometric distances using out isochrone fitting algorithm. Finally, %Giants provides the ratio of giant stars ($\log(g) < 3.5$) with respect to the total number of stars per field.

hand, stars spectroscopically classified as RC members are mostly distributed toward red colors with a peak at $(J-K)_0 = 0.6-0.65$ mag, as explicitly shown by the histograms in the bottom subpanel. In addition, a weak tail of RC stars extends towards bluer colors where they are outnumbered by the foreground contaminants. These stars are important since they should correspond to the small fraction of the most of metal-poor stars detectable in the bulge using RC stars as stellar population probes. In fact, the GES selection function was designed with a color sampling able to catch these metal-poor members even at the cost of including a larger proportion of foreground contaminants. To illustrate this, we display in Fig. 5.3 the dereddened $J-K$ color distribution of the bulge targets with $\log(g) < 3.5$. The bars are color coded according to the mean metallicity of the stars falling is each color bin. As expected, the distribution follows both, the color density distribution of the bulge RC and a color-metallicity correlation. In particular, it is clear that the most metal-poor bins, with mean metallicity lower than $-0.7/-0.8$ dex, are all of them located at $(J-K)_0 < 0.5$. The detection of these metal-poor stars was the goal behind the generous blue limit of the GES selection function. We demonstrate here that in fact this decision produced a valuable harvest of metal-poor bulge stars: They account for the 4.5% of the total RC bulge sample.

The good correspondence between the location of stars in the HR and CMD diagrams constitutes a science verification of the consistence of the stellar parametrization. At the same time, the distribution of stars in the HR diagram allows us to isolate a sample of bulge RC stars based in their $\log(g)$ values. We select stars with $1.5 < \log(g) < 3.5$ dex,

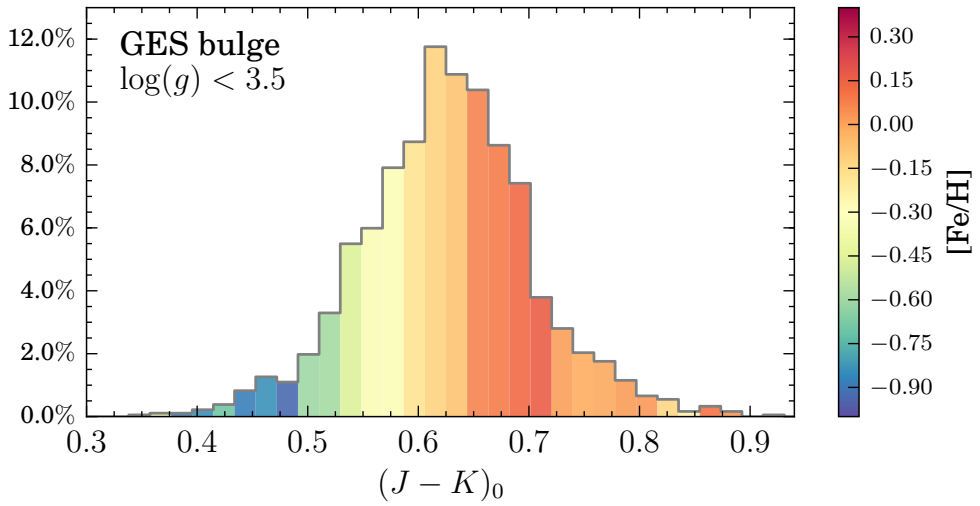


Figure 5.3: Histogram of the $J-K$ color distribution of bulge targets with $\log(g) < 3.5$ dex. The vertical scale of the bars is given in terms of percentage of the total sample. A color code depicts the mean metallicity of stars falling in each color bin.

to eliminate main-sequence stars and giants for which stellar parametrization could suffer from modeling uncertainties. It contains mostly RC, with a contribution of RGB stars, and is composed by 1987 stars, including comparison ones.

5.1.3 Distances and reddenings

We calculate individual line-of-sight spectro-photometric distances and reddenings for the whole bulge sample with FeI measurements, including stars with all surface gravities. To this end, we used the code and procedures described in Chap. 3. Typical internal errors in distance are of the order of 25-30%. Using (l,b) star positions, we further compute their Galactocentric Cartesian coordinates X_{GC}, Y_{GC} and Z_{GC}, and their cylindrical Galactocentric radial distances R_{GC}. The distribution of the latter is shown in Fig. 5.4, separately for the giant and dwarf portions of the sample. We can see how the stars found to be foreground main-sequence contaminants, based on their $\log(g)$ values, are in fact located mostly at 6-8 kpc, close to or in the solar neighborhood. On the other hand, the presumed RC bulge stars are found in a narrow distribution with a peak at ~ 1.5 kpc. We do not expect this maximum to be at $R_{GC} = 0$ kpc given that most of our fields are several degrees apart from the Galactic plane. The availability of Galactocentric radial distances, and the characteristics of their distribution, lead us to use them to introduce a radial distance cut, defining a working sample of likely bulge stars. To this end, we adopt the limit $R_{GC} = 3.5$ kpc. This restriction is applied to the sample of bulge RC stars already defined from their $\log(g)$ values. The resulting working bulge sample is composed by 1583 stars.

From the reddenings simultaneously computed with distances for each star, we estimate the mean reddenings for the 11 bulge fields. The results are quoted in the Col. 7 of Table 5.1. We can compare these results with the figures estimated from the reddening

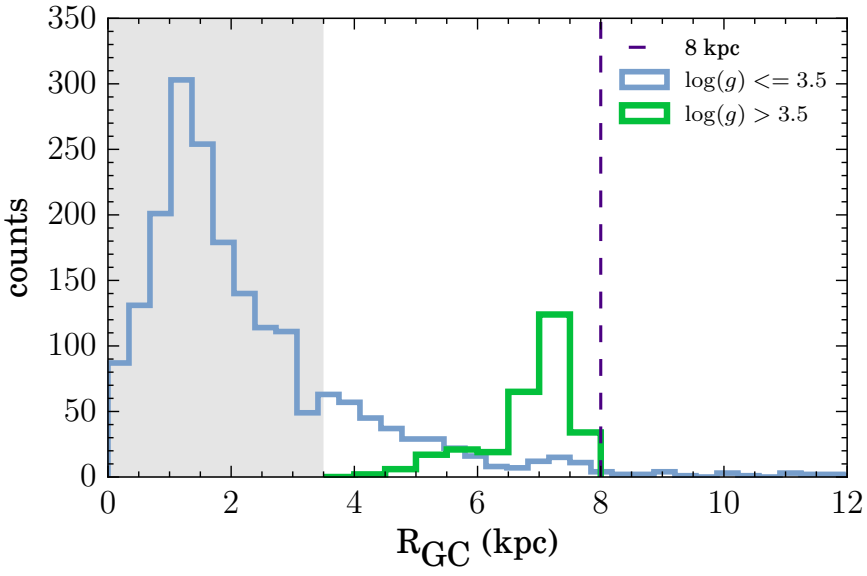


Figure 5.4: Histogram of the Galactocentric radial distance distribution of bulge targets with $\log(g) < 3.5$ (blue solid line) and $\log(g) > 3.5$ dex (green solid line). The shaded gray area depicts the radial region adopted to define a working sample of likely bulge RC stars. A vertical dashed line indicates the Sun's position.

photometric map of [Gonzalez *et al.* 2011], In Col. 6 of Table 5.1. They were computed in a box of 30 arcmin side centered at the nominal coordinates of each fields. The two sets of estimates compare quite well. In fact, the mean difference between them is of $\overline{\Delta \mathrm{E(J\text{-}K)}} = 0.003$ mag, with the spectroscopic determinations being slightly larger in average.

In summary, we have described the general properties of the whole sample of bulge pointings collected up to the fourth internal data release of the Gaia-ESO survey. Our preliminary data analysis leads us to define a working sample of likely bulge RC members with trustworthy stellar parametrization. This sample contains members for which $1.5 \leq \log(g) \leq 3.5$ dex and $R_{GC} = 3.5$ kpc, containing 1583 stars. We devote the rest of this chapter to the detailed analysis of this subsample.

5.2 Metallicity distribution function

The study of the bulge metallicity distribution function, its shape and variations with (l,b) is an important tool to unveil the complexities inherent to the eventual mix of stellar populations coexisting in the central kiloparsecs of the Galaxy. The bimodal or even multimodal nature of the MDF and its variations, especially with b, have been described in the recent literature [Zoccali *et al.* 2008, Hill *et al.* 2011, Bensby *et al.* 2013, Ness *et al.* 2013a, Gonzalez *et al.* 2015]. The Gaia-ESO survey has contributed to this endeavor, enlarging the number of observed fields in high resolution, and so allowing to confirm, extend and strengthen the characterization of the metal distribution across the bulge region.

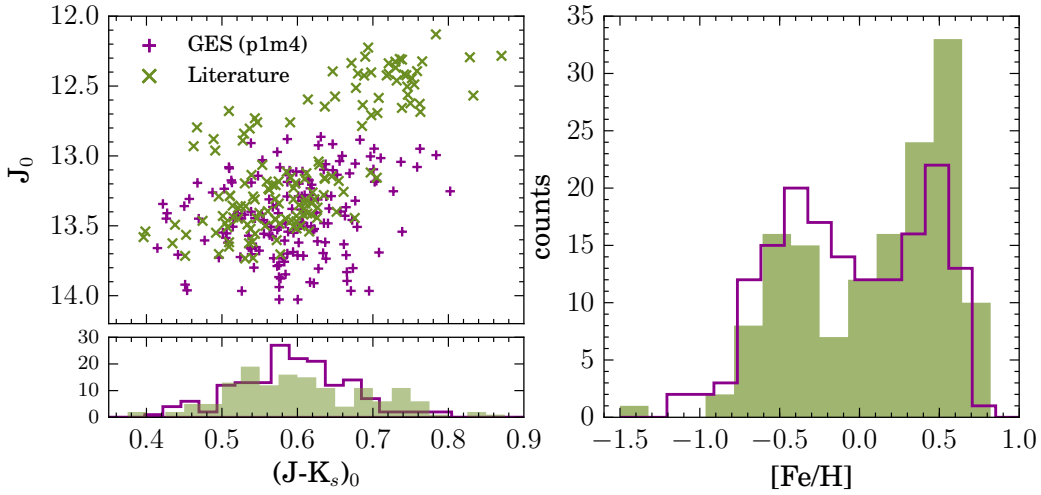


Figure 5.5: Comparison of metallicity distribution between the literature and GES bulge samples in the Baade's window. *Left panel:* CMD diagram of the two set of stars. The bottom subpanel displays the color distribution of both samples. *Right panel:* MDF of the stars selected with the GES selection function (violet solid line), and the literature sample (green filled histogram).

5.2.1 Samples in Baade's window

As explained above, we defined a working sample of RC stars likely located in the bulge, defined as the region with $R_{GC} \leq 3.5$ kpc. A small fraction of these stars correspond to the literature sample of RC and RGB stars in Baade's window, whose selection function differs with respect to the one of the GES. At this point, our intent is to make a characterization of the shape of the MDF across the bulge region, as sampled by our 11 fields. Given the selection function of the literature sample, we anticipated that its MDF should the biased toward metal-rich stars. We explicitly characterize this in Fig. 5.5 by comparing the literature sample and the GES field sample in Baade's window (p1m4). In the left panel, we see how the two sets are distributed in the CMD. The RGB portion of the calibrated sample is clearly visible on average one magnitude over the bulk of RC stars. Their color distributions are depicted in the bottom insert, and highlights the differences between the two selections. The respective MDFs are displayed in the right panel. Being qualitatively comparable, the literature sample has in fact a larger proportion of metal-rich stars with respect to the GES p1m4 sample. Given these differences and our intent of perform a comparison as homogeneous as possible, we exclude from this part of the analysis the sample of literature stars.

5.2.2 Bimodality of the bulge MDF

Let's focus now on the examination of the MDF. As a first glimpse on the bulge MDF, we split the working sample into two groups of fields which are close or far from the plane, respectively. Given the (l,b) spatial distribution of the fields (Fig. 5.1), we define a limit at $b = 7°$, depicted as a gray dashed line in Fig. 5.1. In this way, both halves

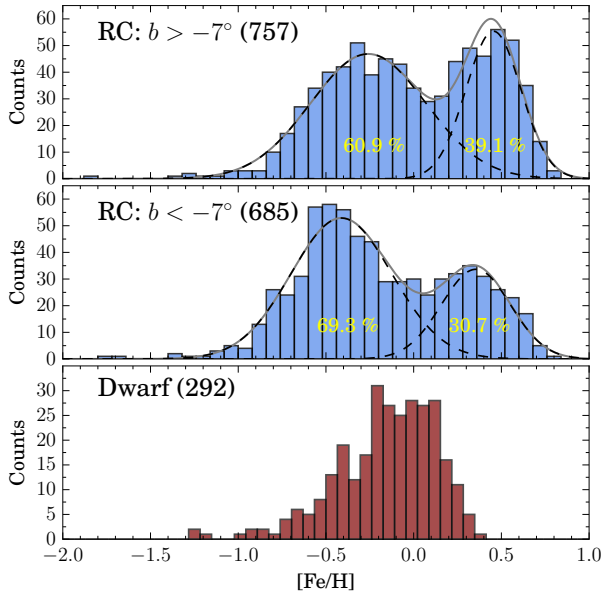


Figure 5.6: *Upper panel:* combined MDF of fields located close to the Galactic plane ($b \geq -7°$). *Middle panel:* combined MDF of fields located far from the Galactic plane ($b \leq -7°$). The results of a GMM analysis on the two distributions are depicted by black dashed lines (individual components) and solid gray lines (summed envelope). *Lower panel:* MDF of stars classified as dwarfs according to their $\log(g)$ values. In the upper panels, the percentage of stars classified in each of the two GMM groups is quoted on top of the respective mode. In all panels, the total number of stars is indicated in parenthesis.

contain similar number of fields. While it is true that this exercise can blur specific MDF field-to-field variations, it allows us to increase the number statistics to investigate the general characteristics of the bulge MDF. The two subsamples are displayed in the upper and middle panels of Fig. 5.6. From this figure, two facts are immediately apparent: first, the MDFs present a bimodal distribution with a narrow metal-rich component peaking at super-solar metallicities, and the other broader and metal-poor located at [Fe/H] $\lesssim 0.0$ dex. Secondly, the relative proportion of stars comprising the two peaks changes with Galactic latitude. In fact, the size of the metal-rich component decreases in favor of the metal-poor one while going far from the Galactic plane.

To quantify these facts, we perform a Gaussian Mixture Models decomposition on the two MDFs. In both cases, the Akaike Information Criterion, used for model selection, gave preference for a two-component solution with a high relative probability. Close to the plane, the narrow ($\sigma = 0.16$ dex) metal-rich GMM component represents the 36% of the probability density of the model, while the broader metal-poor ($\sigma = 0.33$ dex) one the remaining 64%. On the other hand, for the fields far from the plane, the metal-rich component ($\sigma = 0.35$ dex) and the metal-poor ($\sigma = 0.29$ dex) one accounts for the 30% the 70% of the relative weights, respectively. As a consistency check on the statistical significance of the GMM procedure, we calculate in each panel the percentage of stars classified in each of the two modes of the respective model. The classification is based on the individual responsibilities: given a bimodal Gaussian solution, for each star there is an associated pair of values, the responsibilities, giving the probability of each Gaussian component of explaining this observation. In our case, we adopted a simple classification scheme, assigning stars to each mode based on the larger of its responsibilities. The percentages calculated in this way are indicated in the upper and middle panels of Fig. 5.6 on top of the respective GMM modes. The values quoted above for each panel, concerning the relative probability density of the model modes, compares

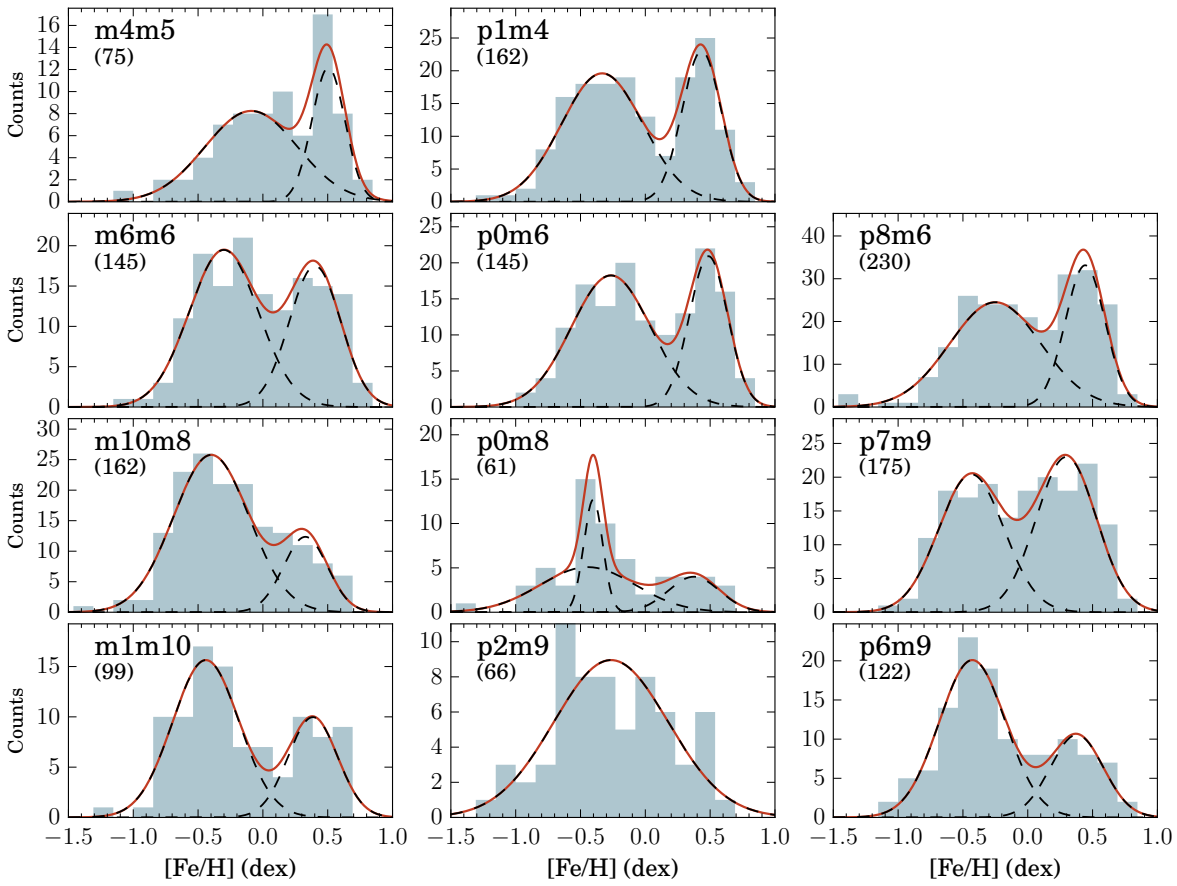


Figure 5.7: Metallicity distribution functions of the 11 bulge fields. Blue filled histograms stand for the individual distributions, with the number of stars quoted in each panel. An independent GMM decomposition, performed in each field MDF, is depicted by black dashed lines (individual modes) and a red solid line (composite profile). The distribution of the fields in the panels try to approximately mimic their position in (l,b) (c.f. Fig. 5.1).

quite well with the percentages of stars classified in the respective groups. The small differences arises from the fact that the data resolution is limited by the finite size of the sample, while the model is intended to characterize the underlying parent distribution density. The respective figures are expected to be comparable, but not identical.

As a qualitative comparison, in the lower panel of Fig. 5.6 we display the MDF of the sources classified as dwarfs according to their $\log(g)$ values. They are mostly solar neighborhood members, as seen in Fig. 5.4. It is clear that these stars have a MDF with a significantly different shape with respect to the bulge sample. Their MDF has a long tail toward low metallicity, partially due to the contribution of the local thick disk, and a sharp decline toward [Fe/H] = 0.4 dex. The distribution presents a strong peak at solar metallicity, precisely at the locus where the dip in the bimodality of the bulge MDF is located.

Table 5.2: Parameters of the best GMM model for each field where two components were found. MP and MR subscripts refer to the metal-poor and metal-rich Gaussian components, respectively.

Field name	$\overline{[Fe/H]}_{MP}$	σ_{MP}	Weight$_{MP}$	$\overline{[Fe/H]}_{MR}$	σ_{MR}	Weight$_{MR}$
m4m5	-0.09	0.36	0.65	0.51	0.13	0.35
p1m4	-0.33	0.31	0.64	0.43	0.15	0.36
m6m6	-0.30	0.27	0.60	0.40	0.20	0.40
p0m6	-0.27	0.31	0.64	0.49	0.15	0.36
p8m6	-0.25	0.35	0.63	0.44	0.15	0.37
m10m8	-0.40	0.29	0.78	0.33	0.17	0.22
p7m9	-0.44	0.25	0.49	0.30	0.23	0.51
m1m10	-0.44	0.26	0.68	0.39	0.19	0.32
p6m10	-0.43	0.26	0.70	0.38	0.20	0.30

From the above general analysis a clear bimodal shape of the bulge MDFs, rather different than that of the local disk, is established. The good number statistics given by the combination of fields close and far from the plane, is important to identify the global MDF characteristics as a first step toward a more detailed analysis. In Fig. 5.7 we display the MDFs of the 11 bulge fields. Individual GMM decompositions were independently attempted in each field. In qualitative agreement with Fig. 5.6, the preferred GMM model has two components, a narrow metal-rich plus a broader metal-poor one. This is the case for most of the fields, but with two exceptions, namely p0m8 and p2m9. As commented above, these fields were observed just once up to the iDR4, thus having less than 70 stars after the likely bulge RC members were selected from their original samples (Table 5.1). In these cases, the data does not provide strong statistical evidence to constrain a model, precluding the GMM on giving strong assessments. In Table. 5.2, we present the set of parameters characterizing the Gaussian modes in the nine fields where the data favor a bimodal solution.

5.2.3 MDF variations with spatial location

When comparing the MDF shape variations with respect to the spatial (l,b) location of the fields, a general decline in the number of metal-rich in favor of metal-poor stars with increasing distance from the Galactic plane is visible. A closer examination, reveals that along with this latitudinal metallicity variation, there is an asymmetry with respect to the minor axis. In fact, while comparing fields at each side of the minor axis in Fig. 5.7, the metal-rich MDF component is systematically stronger in fields at positive longitudes than those at similar b but negative longitudes. This is consistent with the asymmetry observed in the photometric metallicity map of [Gonzalez *et al.* 2013]. The asymmetry can be attributed to a perspective effect, given the spatial distribution of the bulge/bar described in Chap. 7. Since at positive (negative) longitudes, the line-of-sight intersects the near (far) sides of the bar, the stars at positive longitudes are on average closer to the observer, and hence to the plane, than those at negative longitudes and same

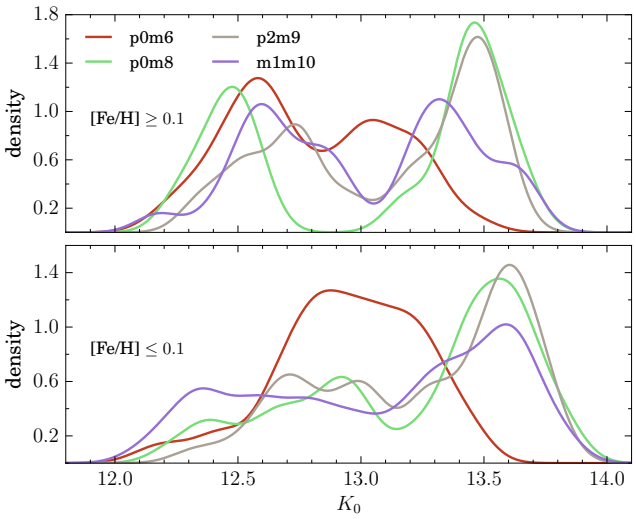


Figure 5.8: Double RC in the magnitude distribution of bulge stars as a function of metallicity. *Upper panel:* generalized histograms (Gaussian kernel of 0.09 mag) of the extinction corrected K_s magnitude for stars with [Fe/H] $\geq$ 0.1 dex. *Lower panel:* generalized histograms (Gaussian kernel of 0.09 mag) of the extinction corrected K_s magnitudes for stars with [Fe/H] $\leq$ 0.1 dex. The same color code is used to identify the different fields in both panels.

b. Given the intrinsic decrease of metallicity while moving far from the Galactic plane, then an asymmetry in metallicity with (l,b) can be drawn from the geometrical one.

To quantify these trends, we can compute a number of metallicity gradients: First, from the GMM profiles, we determine the metallicity at which the peaks of the two populations are located in each field (with the exception of p0m8 and p2m9). Then, we compute metallicity gradients with l and b independently for the two populations. We also compute mean field metallicity gradients with l and b. From these estimates, we found negligible gradients with l for both, metal-rich and metal-poor populations, but noticeable variations with b, with gradients of -0.18 dex/kpc and -0.31 dex/kpc, respectively. A gradient of -0.24 dex/kpc is found for the variation of the mean field metallicity with b. These values were computed by assuming all the fields centers projected on a plane at 8 kpc (to be consistent with other studies and allow comparison). Our results are compatible with the presence of internal vertical gradients in both metallicity populations, with the gradient of the metal-poor fraction being $\sim$ 60 percent larger than that displayed by the metal-rich stars. In this sense, the global metallicity gradients, traditionally measured from the mean field metallicity variations with b, can be interpreted as the interplay of two effects; the variation of the relative proportion in which both populations contribute to the global field MDF, plus the presence of internal gradients in both components. As a reference, if we compute a vertical gradient in similar fashion, but adopting the results for fields at $b = -4°, -6°, -12°$ from [Zoccali *et al.* 2008], we find a gradient of -0.24 dex/kpc, in excellent agreement with the value derived from the median values of our fields. Also, the photometric metallicity map of [Gonzalez *et al.* 2013] indicates a vertical gradient of -0.28 dex/kpc, again in agreement with the global gradient found here.

5.2.4 Double RC in magnitude distributions

The use of RC stars as probes of bulge stellar populations reports an opportunity to characterize their spatial distribution and eventual correlations with kinematics and chemistry. In fact, it is well known that RC stars can be used as standard candles,

allowing us to use their apparent magnitudes as a proxy of distance (e.g [Alves 2000]). Since K_s photometry is weakly affected by dust obscuration, we use it to construct magnitude distributions. This exercise echoes what has been done in recent years to map the bulge structure in stellar density, and its variations with metallicity. In Fig. 5.8 we display the generalized histograms of the VVV extinction corrected K_s magnitude distributions of fields where the double RC feature is present according to the density maps of [Wegg & Gerhard 2013] (p0m6, p0m8, p2m9 and m1m10). We correct for extinction in field-by-field basis, adopting the extinction law of [Cardelli *et al.* 1989] and the mean field values computed with our isochrone fitting algorithm and reported in the 7th column of Table 5.1. The upper and lower panels display the magnitude distributions of metal-rich and metal-poor stars in each field, respectively. From the comparison between both sets of profiles, it is clear that an enhanced bimodality is drawn by the metal-rich stars. The difference in magnitude between the two peaks changes from field to field, being smaller closer to the plane, and so tracing the distance between the near and far arms of the X-shape bulge. On the other hand, metal-poor stars present nearly flat magnitude distributions, with some tendency, especially in the outermost fields, to have a peak at faint magnitudes. The latter because the volume observed is bigger at larger distances due to the cone effect.

It has been suggested that an enhanced bimodality for metal-rich stars can arise, or be inflated by stellar evolutionary effects ([Nataf *et al.* 2014]). The RGB is redder than the RC, but both become bluer with decreasing metallicity. This implies that the relative contamination of the RC sample with RGB members can increase as a function of metallicity given a color cut in the survey selection function. From a PARSEC isochrone of 10 Gyr and [Fe/H] $= -1.5$ dex (so, at the metal-poor end of the bulge MDF) the RC lies at $J - K = 0.40$ mag, redder than the selection color cut at $J - K = 0.38$ mag. Consequently, our sample might be free of this potential bias. On the other hand, the ratio of RC relative to RGB stars is an increasing function of metallicity, meaning that, for example, a sample with [M/H] ~ -1.3 dex should be 1.75 times larger than one at [M/H] ~ 0.4 dex to display features with the same statistical significance. In the combined set of stars from the p0m6, p0m8, p2m9 and m1m10 fields, the ratio between stars lower and higher than solar metallicity is 1.65, which ensures that this bias source might not be relevant in our case. A third potential bias comes from a metallicity dependence of both, the magnitude and the strength of the red giant branch bump. these factors can conspire to increase the signal of the faint magnitude peak at high metallicity. While it is true that the exact modeling of the impact of this effect is complicated, this effect could just increase the difference between the peaks, and could not necessarily invalidate the qualitative presence of two peaks in the magnitude distribution.

5.2.5 Metal-poor stars

An important aspect to consider while examining the metallicity distribution of bulge stars is to explore its metal-poor end, given that these stars should correspond to the oldest detectable members. We tackle this issue by considering the metal-poor tail of the MDF of the whole working sample with [Fe/H] ≤ -1.0 dex. Nevertheless, we

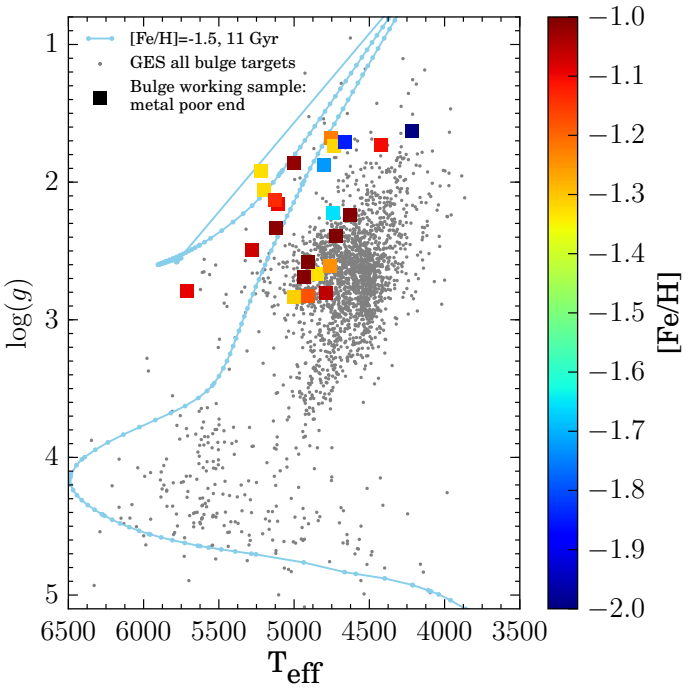


Figure 5.9: Location in the HR diagram of metal-poor bulge working sample stars. The whole GES bulge targets, without any surface gravity or distance cuts, is displayed with gray dots. The metal-poor stars of the bulge working sample with [Fe/H] ≤ -1.0 dex, are highlighted with a color code according to their metallicity. A PARSEC isochrone of [Fe/H] $= -1.5$ dex and 11 Gyr is also displayed as a reference.

should keep in mind that, while exploring the bulge MDF using red clump stars, a possible cut in the metal-poor end might be introduced by stellar evolutionary effects. With decreasing metallicity, stars eventually undergo the helium burning phase in the Horizontal Branch instead of in the RC. The exact metallicity limit depends on very poorly modeled processes such as the mass-loss rate, which prevents a precise estimate from theoretical calculations. On the other hand, we already saw that the photometric selection limits imposed by the GES selection function do not bias the MDF against the more metal-poor stars, because we expect to include first-ascent RGB stars in the sample as well.

Figure 5.9 illustrates the distribution of bulge stars in the HR diagram. The background sample corresponds to the whole GES bulge sample, without cuts in surface gravity or distance. On top of it, the metal-poor stars of the bulge working sample with [Fe/H] ≤ -1.0 dex, are highlighted and color coded according to metallicity. As expected, all metal-poor stars are located toward the blue edge of the whole sample, with the most-metal-poor ones sitting at higher surface gravities than the mean. A PARSEC isochrone of [Fe/H] $= -1.5$ dex and 11 Gyr overplotted on top of the data, confirms that in fact, these stars are located in the expected locus of RGB and RC old metal-poor stars. Considering that we have limited our spatial sampling to be inside $R_{GC} = 3.5$ kpc, the two most metal-poor stars attain metallicities of -1.9 and -2.0 dex. In addition, our sample shows that the incidence of stars with [Fe/H] ≤ -1.0 dex is 1.7% and only 0.3% for stars with [Fe/H] ≤ -1.5 dex. For comparison, the respective values from [Ness *et al.* 2013a] are 4.4% and 0.7%. It is difficult, without the availability of public ARGOS catalogs, to point out if the slightly larger proportion of metal-poor stars in the ARGOS sample, considering that the color cut is fixed at $J - K = 0.38$ in both surveys, comes from the inclusion of some halo contaminants, or it is just an effect

of different metallicity scales of both surveys. In any case, these low ratios stress the importance of constructing large samples to increase the statistical significance of the metal-poor tail, as well as the dedicated observational efforts of hunting them. Such metal-poor and very metal-poor stars are authentic bulge fossils encoding information of the very early stages of Galactic evolution.

In conclusion, the analysis of the bulge MDF, given the spatial coverage provided by GES data, provided us with a first general approximation to understand it in terms of stellar populations. A bimodal nature of the MDF, already clear from the qualitative examination of the histograms have been established and characterized by means of a Gaussian mixture modeling. A metal-rich narrow plus a metal-poor broad components are ubiquitous over the bulge sampled area except in the fields where the small available samples make difficult to obtain strong statistical assessments. Metal-rich stars decline in favor of metal poor while increasing the distance from the Galactic plane. At the same time, both components seem to present internal metallicity gradients with b. The interplays between both effects produce the general vertical gradients characterized in the literature. In the following, we aim to further characterize the MDF metallicity groups by including α-abundances and kinematics into the analysis.

5.3 Trends in the [Mg/Fe] vs. [Fe/H] plane

Beyond the study of metallicity distributions, the availability of elemental abundances from high resolution spectroscopy provide us with an important tool to further disentangle and characterize the eventual mix of stellar populations sitting in the bulge. In fact, the trends displayed by stars of any stellar population in the [α/Fe] vs. [Fe/H] plane encode important information regarding the IMF and the star formation history of its stellar content. This has been particularly critical in Galactic bulge studies, as it has been used in attempts to associate the bulge with other Galactic components, in particular the thick disk [Zoccali *et al.* 2006, Lecureur *et al.* 2007, Fulbright *et al.* 2007, Meléndez *et al.* 2008, Alves-Brito *et al.* 2010, Bensby *et al.* 2013, Johnson *et al.* 2014, Gonzalez *et al.* 2015].

Unlike the first internal GES data release, the iDR4 provided metallicity along with abundance measurements for several species. We focus here on the distribution in the [Mg/Fe] vs. [Fe/H] plane. We adopted this plane because the abundance determinations for the α-element magnesium seem to be less affected by errors in stellar parameters and because visual inspection show that the features we are interested in are more clearly defined with this element than with other available α-species. Moreover, as for the oxygen, magnesium is expected to be produced exclusively by SN II explosions.

In Fig. 5.10, we display the [Mg/Fe] vs. [Fe/H] distributions of the different fields and the whole working sample. Unlike the subset used to characterize the MDF, we adopt here the whole working sample, including also the Baade's window literature RGB and RC stars previously discarded. Now, we are interested in characterizing sequences in the [Mg/Fe] vs. [Fe/H] plane and not density distributions, so that the archive stars, with their density number biased toward metal-rich stars does not represent a problem.

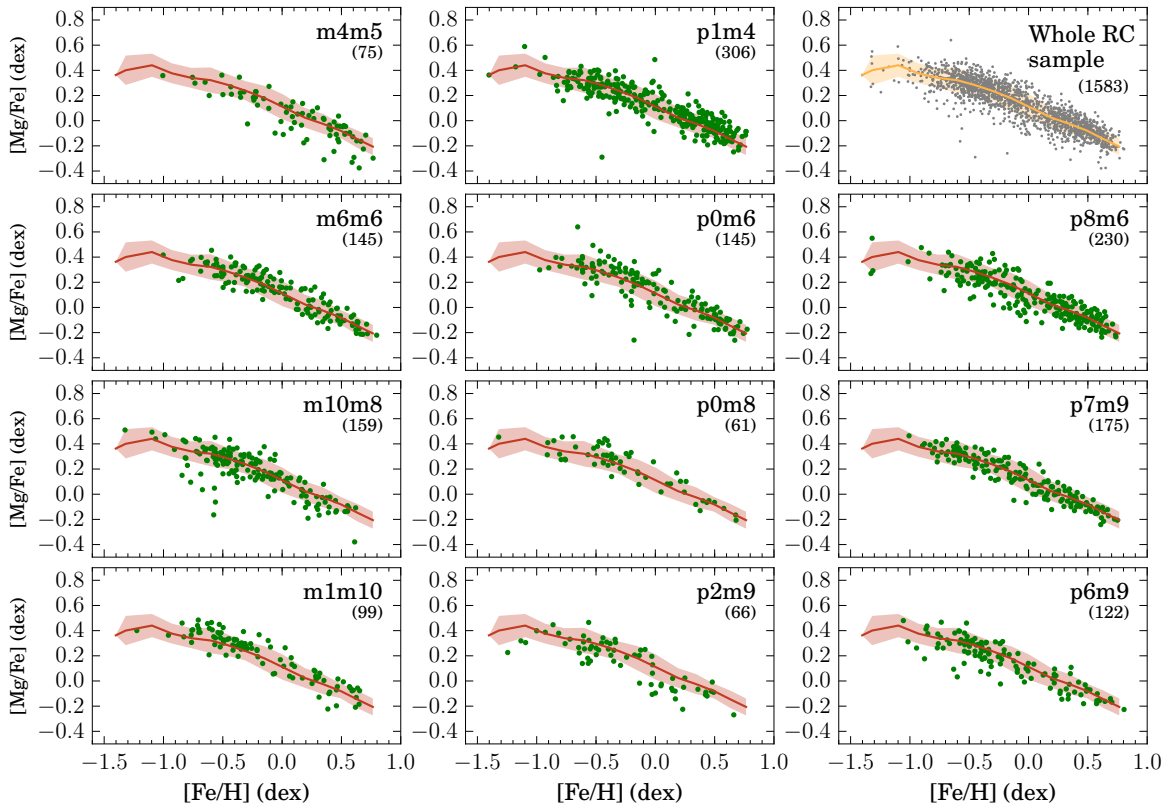


Figure 5.10: Distribution of bulge stars in the [Mg/Fe] vs. [Mg/Fe] plane. *Upper rightmost panel:* whole working sample as gray points. A fiducial median profile and 1σ dispersion band is constructed over several metallicity bins. *Remaining panels:* individual field distributions (green filled points) and fiducial profile and dispersion band of the whole working sample (red line and shaded area). The number of available stars is quoted in parenthesis. The order of the panels aims at mimicking the field distribution in the (l,b) plane.

In fact, they draw a sequence comparable to that of the stars selected with the GES selection function in Baade's window (p1m4).

The upper rightmost panel of Fig. 5.10 displays the whole sample together with a median profile and 1σ dispersion band calculated over several small bins in metallicity. This fiducial trend is then overplotted in the other panels on top of the individual field distributions. The different samples compare well with the fiducial trend, with no significant deviations from it throughout the sampled bulge region. Nevertheless, a smaller number of off-trend low-alpha stars are present in some fields. They are visible mainly in external bulge fields such as m10m8 and p6m9. These stars cannot be thin disk contaminants given that they lie mostly at metallicities around or lower than [Fe/H] $= -0.5$ dex, which is too metal-poor even for the local thin disk (which is also excluded as a contamination source, given the distance cut used to define our working sample). Moreover, they cannot be thick disk stars because of their low alpha enhancements. On the other hand, their stellar parameters and associated errors are

comparable in quality with respect to the rest of the sample. The scarce number of such weak outliers limits a further characterization so that it is not possible to draw a conclusion about their eventual different nature.

5.3.1 The metal-poor bulge knee

In Fig 5.10, it can be seen that, in every field, the [Mg/Fe] vs. [Fe/H] trends tend to flatten at metallicities lower than $-0.4/-0.5$ dex. This is an expected feature from the time-delay model, according to which the *alpha-* enhancement levels start to decline strongly with [Fe/H] after the onset of supernovae Ia polluters. This produces a "knee" in the [α/Fe] vs. [Fe/H] trend whose location provides constraints on the formation time scale of the stellar system.

In Fig. 5.11 we display the whole bulge working sample. From the analysis of the MDF, the existence of two metallicity populations in the bulge is strongly suggested. A visual inspection gives the impression of a slightly flatter distribution at supersolar metallicities, which might be understood as a different behavior of the metal-rich and metal-poor populations. Even if the effect is null, or too small to be quantified given the size and error distribution of our sample, it is convenient to exclude supersolar metallicity stars while trying to characterize the metal-poor population.

In Fig. 5.11, we display a best fit trend model intended to determine the position of the "knee". The adopted model consists in two linear trends sharing a common point, the "knee", letting the other parameters free to be determined by minimizing an appropriate cost function. Guided by the above discussion, we perform the fit in the range $-1.5 \leq$ [Fe/H] ≤ 0.1, which is highlighted as a shaded area in Fig. 5.11. The fit is implemented by means of χ^2 minimization, and errors are taken into account by performing 1000 Monte Carlo resamplings from the individual errors in [Mg/Fe]. We can see that, given the sample size and the data dispersion in [Mg/Fe] (which is not excluded to be mostly astrophysical, see next sections), we cannot constrain the "knee" position better than ~ 0.1 dex, with the resulting value being $[\mathrm{Fe/H}]_{\mathrm{knee}} = -0.37 \pm 0.09$ dex.

As shown above, the two metallicity components discernible in the bulge MDF, present different behaviors when examined in the [Mg/Fe] vs. [Fe/H] plane. The metal-rich component displays a single linear trend somehow flatter than the subsolar metallicity stars. These metal-poor stars display a long sequence spanning more than 1.5 dex in metallicity with a slope break compatible with the qualitative predictions of the time delay model. In the following, we will consider kinematic information to explore potential further difference between the two bulge populations.

5.4 Kinematics of chemically defined components

The kinematical characterization of the bulge populations can be used to highlight the potential different formation and evolution histories of its metal-rich and metal-poor bulge components.

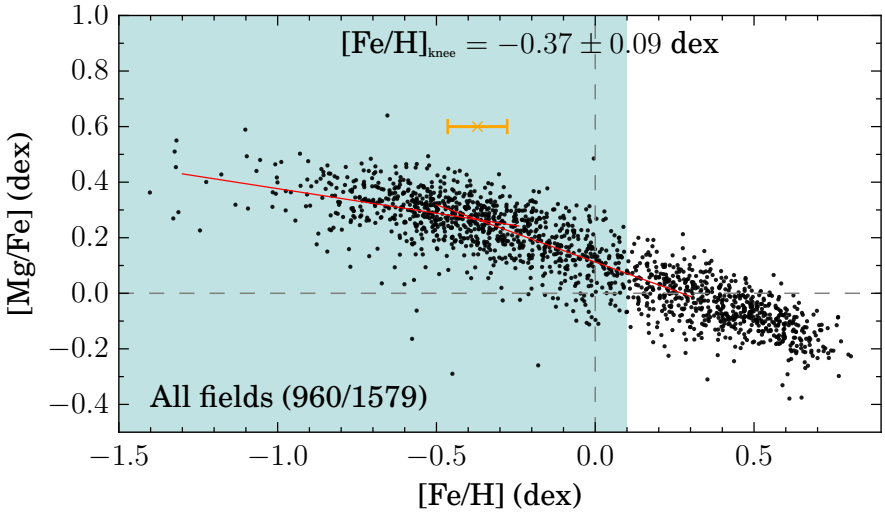


Figure 5.11: Determination of the bulge "knee" position in the [Mg/Fe] vs. [Fe/H] plane. The whole working sample is depicted by black dots. A bilinear model, fitted to the metal-poor bulge fraction of the sample (highlighted with a shaded blue area), is shown with red solid lines. The number of stars included in the fit, and the resulting "knee" position and errorbar, are quoted in the figure. An orange errorbar draw the "knee" position.

5.4.1 Bulge rotation curve

In Fig. 5.12 we use the mean field Galactocentric velocities (see Chap. 3) to construct the rotation curve drawn by our 11 bulge fields. For comparison, we added profiles standing for the results of the BRAVA [Rich *et al.* 2007b, Howard *et al.* 2009, Kunder *et al.* 2012] and GIBS [Zoccali *et al.* 2014] radial velocity surveys in longitude strips at $b = -4°, -6°$ and $-8°$, covering most of the latitude extent of our sample. In accordance with the conclusions drawn above, concerning the bimodal nature of the bulge MDF, we split our sample into metal-rich and metal-poor components. To this end, we adopted limits at [Fe/H] = 0.15 and 0.10 dex for the fields close and far from the plane, respectively. The characteristic s shape of the rotation curve reflects the projection of velocity vectors on the line of sight. The near independence of the shape of the rotation curve with latitude, the so called cylindrical rotation, has been regarded as evidence of a secular evolution origin of the bulge. In particular, if the bulge originated from the buckling instability of a rotating bar, it is expected to show little differences in the mean rotation velocity measured at different distances from the Galactic plane while viewed edge-on. A tendency of the rotation curves to be steeper at lower latitudes has been characterized [Howard *et al.* 2009, Zoccali *et al.* 2014]. Such rotation pattern is naturally explained by models as an effect of the non zero position angles of the bar with respect to the Sun-Galactic center line-of-sight [Shen *et al.* 2010, Martinez-Valpuesta & Gerhard 2013]

In a general picture, Fig. 5.12 shows that the mean velocity of our fields is in good agreement with the curves traced by the larger number of BRAVA and GIBS fields. However, a detailed comparison seems to suggest that the metal-poor stars draw a

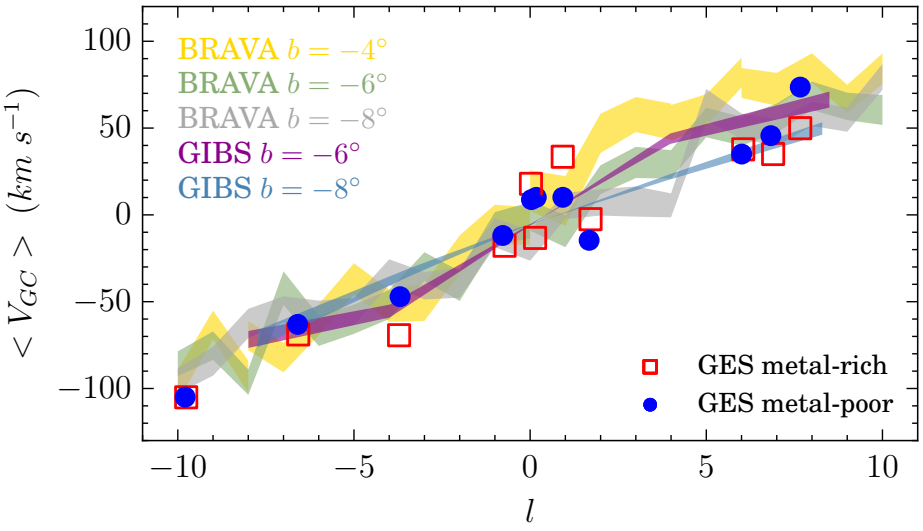


Figure 5.12: Bulge rotation curves from GES, GIBS and BRAVA samples. Several fields in the range of latitudes sampled by GES were selected from GIBS ($b = -6°$ and $-8°$) and BRAVA ($b = -4°$, $-6°$ and $-8°$) surveys. Colorbands stand for the rotation curves in each latitude strip. Their width is determined by the standard error of the mean in each field of the strip. Red squares and blue circles stand for the mean velocities estimated from metal-rich and metal-poor GES stars in each field, respectively.

profile with less dispersion than the one displayed by metal-rich stars, when compared to the BRAVA and GIBS profiles. For the metal-poor bulge, this fact simply states its near cylindrical rotation. For the metal-rich portion, instead, this highlights field-to-field differences around the general cylindrical rotation pattern. As we have seen from their magnitude distribution, these stars trace the X-shape structure in spatial number density. Given the complex mix of family orbits intersecting each other to build up this structure, we can expect that stream motions along the arms of the X-shape will lead to deviations in velocity around the main rotational pattern.

5.4.2 Kinematics at the peaks of the double RC

An additional way to study the aforementioned stream motions is possible by comparing velocities of stars at the bright (close side) and faint (far side) peaks of the magnitude distributions for the fields displaying the double RC feature. In line with previous studies in the literature [De Propris *et al.* 2011, Uttenthaler *et al.* 2012, Vásquez *et al.* 2013], we attempt to characterize the stream motions by comparing the mean Galactocentric velocities of stars around the peaks of the magnitude distribution. Given the size of our sample, this exercise may suffer from low number statistics, as evidenced by the relative size of the Errorbars. The results of this exercise in the four studied fields are reported in Table 5.3. With the exception of p0m6, there is not statistically significant differences in velocity for the bright and faint groups of metal-rich stars. These results are in agreement with previous works for p0m8 [De Propris *et al.* 2011] and m1m10 [Uttenthaler *et al.* 2012]. The structure of the X-shape bulge is complex, as composed

		V_{GC} bright	V_{GC} faint
p0m6	Mean	-37.7 ± 17.9	12.0 ± 19.6
	σ	91.1 ± 12.6	94.0 ± 13.9
	Number	26	33
p0m8	Mean	6.0 ± 21.6	18.5 ± 18.1
	σ	52.9 ± 15.3	51.1 ± 12.8
	Number	6	8
p2m9	Mean	-35.7 ± 27.5	-18.0 ± 18.7
	σ	61.4 ± 19.4	52.8 ± 13.2
	Number	5	8
m1m10	Mean	-10.2 ± 14.7	-33.6 ± 13.1
	σ	54.5 ± 10.3	49.1 ± 9.3
	Number	14	14

Table 5.3: Galactocentric velocities of stars located in the bright and faint peaks of the metal-rich magnitude distribution in fields displaying the double RC feature. Units in km s^{-1}.

by the superposition of several stable family orbits. Radial velocity measurements in a significant number of fields, covering the area where the double RC is visible, might help us to unravel the nature and spatial distribution of these orbit streams.

5.4.3 Velocity dispersion

Coming back to the general analysis of radial velocities, we can further gain insight into the metallicity dependence on kinematics by studying the velocity dispersion patterns. In Fig. 5.13, we display the Galactocentric velocity dispersion trends of our fields color coded according to their Galactic latitude. Given the small individual velocity errors compared with the dispersion reported here, we did not correct for the individual uncertainties while computing velocity dispersions. With such negligible uncertainties, the error in the velocity dispersion can be taken as $\sigma/\sqrt{2N}$. Figure 5.13 shows that the metal-poor field components appear to be kinematically hot throughout the whole sampled area, with values around $\sigma V_{GC} = 100km\ s{-}1$. Instead, the metal-rich component has a velocity dispersion that is higher close to the plane and decreases systematically with b.

To see these results more in perspective, Fig. 5.14 displays the [Mg/Fe] vs. [Fe/H] distributions of the working sample, separating it in fields close and far from the Plane. We split each subsample in small boxes in [Fe/H] and [Mg/Fe] and the resulting velocity dispersion values are color coded as indicated in the figure. On average, metal-rich and metal-poor parcels are kinematically homogeneous in inner fields, while for outer ones the metal-rich end is clearly kinematically colder. It is worth to note that, from this figure, there is no evidence of kinematic variations with [Mg/Fe] at fixed metallicity.

Taken at once, all the above characterization depicts an inhomogeneous and more complex spatial orbital distribution for the structure traced by the metal-rich stars.

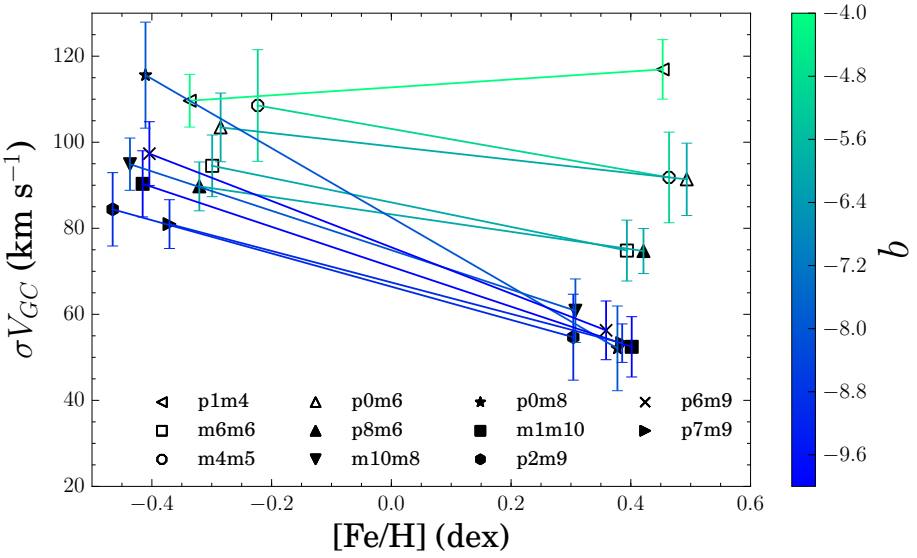


Figure 5.13: Velocity dispersion of metal-rich and metal-poor bulge stars. The different markers stand for the velocity dispersion and errorbar computed from the metal-rich or metal-poor components of each field. Markers standing for the same field are connected by a line which is color coded according to b.

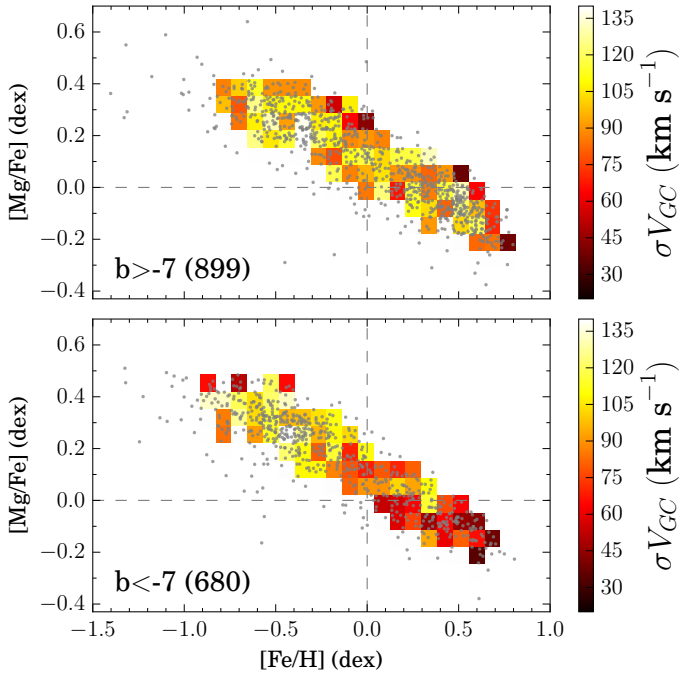


Figure 5.14: Velocity dispersion distribution in the [Mg/Fe] vs. [Fe/H] plane. The sample is divided in small parcels inside which the velocity dispersion is calculated. They are color coded as indicated by the colorbars. Two gray dashed lines indicate in each panel the Sun's position for reference. *Upper panel:* fields close to the plane with $b > -7°$. *Lower panel:* fields far from the plane with $b < -7°$. The number of stars is given in parenthesis in each panel.

5.4.4 Interpretation of metal-rich stars kinematics

We can understand the observed kinematical properties of metal-rich stars in terms of the orbital structure of the B/P bulge that is found to be observationally traced by them. A buckling bar instability driven formation results in a rearranged dynamical system consisting of many types of stellar orbit families. The global structure of this mix of orbits is complex, for example, as depicted in Figures 3 and 8 of [Martinez-Valpuesta *et al.* 2006]. One of the possible stable orbit families, the x1, sometimes dub *banana-like* orbits, has profiles that are up-bended or down-bended if seen edge-on, building up an X-shaped structure. In this context, the observed velocity dispersion variation of metal-rich stars with b might arise from the different mixture of orbit families on the line-of-sight. In the central parts of the bulge, the different families of orbits intersect each other, building up a large velocity dispersion in these fields. In contrast, far from the plane, the line-of-sight intersect the arms of the X in external regions, dominated by relatively homogeneous stream motions, as seen above. This naturally leads to lower velocity dispersions.

5.4.5 Interpretation of metal-poor stars kinematics

On the other hand, Figures 5.13 and 5.14 hint at a metal-poor bulge component that is kinematically homogeneous in the surveyed area. Guided by this, we take all metal-poor stars to construct the velocity dispersion profile displayed in Fig. 5.15. A 1σ error band is displayed as a shaded area. An interesting trend is clearly visible, with the velocity dispersion increasing and then decreasing symmetrically with metallicity around [Fe/H] ~ -0.5 dex. It is worth to note that the maximum dispersion of this profile is reached at the metallicity of the "knee" of the [Mg/Fe] vs. [Fe/H] relation. This is illustrated by the dashed gray line and the shaded area depicting the position and 1σ error in the "knee" position, respectively.

It is clear that the bulge kinematics correlates and reinforces the metallicity groups identified in the MDF, and characterized in the [Mg/Fe] vs. [Fe/H] plane. In addition, a striking kinematical signature in the kinematically hot metal-poor bulge correlates in metallicity with the "knee" position found for this population.

As observational evidence have steadily accumulated, the nature of the Galactic bulge has proven to be very complex. It is not enough with giving a chemical identification and characterization of the possible multiple components sitting together at the central kiloparsecs of the Galaxy. Instead, a multiple approach, from the point of view of detailed chemical abundances, kinematics, and spatial distribution, specially emphasizing on their correlations, should be adopted.

5.5 Summary

In essence, all the pieces of evidence discussed here leads us to consider the Galactic bulge as a composite structure due to the coexistence of at least two stellar populations. We propose here a list with the main points raised in this chapter:

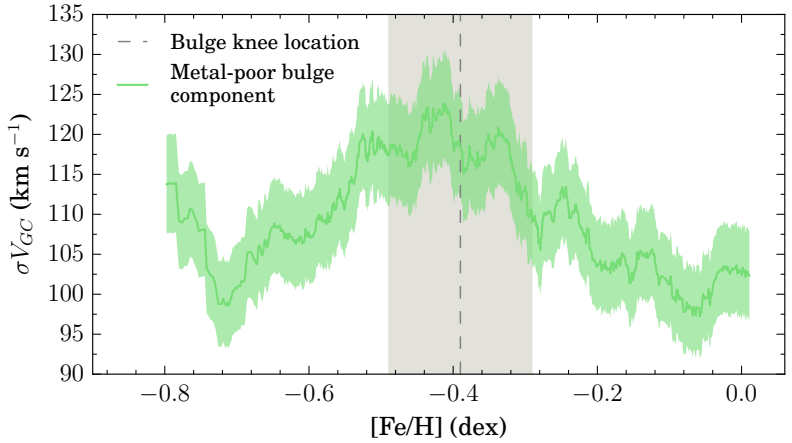


Figure 5.15: Velocity dispersion vs. metallicity profile for the metal-poor bulge. A running median with binsize of 170 datapoints is used to construct the curve depicted by the green solid line. A 1σ errorband around the mean is given by the green shaded area. The position and errorbar in [Fe/H] of the bulge "knee" in the [Mg/Fe] vs. [Fe/H] plane are indicated by a vertical dashed line and gray shaded area.

1. The bulge presents a bimodal metallicity distribution function across the whole sampled area. The proportion of metal-rich and metal-poor stars building up the MDF, changes mainly as a function of b, with metal-poor ones dominating far from the Galactic plane. In addition, internal metallicity gradients are found in both bulge subcomponents.

2. In turn, the bulge MDF is clearly different with respect to that of the disk in the solar neighborhood.

3. The double RC feature in the magnitude distribution is only drawn by stars in the metal-rich subpopulation, those with [Fe/H] $\gtrsim 0.1$ dex.

4. The two most metal-poor stars in the bulge sample attain metallicities of -1.9 and -2.0 dex. The incidence of stars with [Fe/H] ≤ -1.0 dex is of 1.7%, and of 0.3% for stars with [Fe/H] ≤ -1.5 dex.

5. Bulge stars are distributed in the [Mg/Fe] vs. [Fe/H] plane as a continuous tight sequence. No deviations from the median trend are found in the studied fields. The "knee" of this sequence is found at $[\mathrm{Fe/H}]_{\mathrm{knee}} = -0.37 \pm 0.09$ dex.

6. The metal-rich bulge subpopulation presents disk-like kinematics, while the metal-poor appears isotropic and kinematically hot. No variations of σV_{GC} are found in both subpopulations as a function of [Mg/Fe].

Going beyond in the analysis, a proper characterization of the bulge stellar populations should take a place in the context of other Galactic stellar populations. We tackle this problem in the next chapter.

Chapter 6

The bulge stellar populations and formation as seen by the GES

Contents

6.1 How many bulge components? 138
6.2 The bulge MDF in the literature 139
6.3 Metallicity gradients in perspective 141
6.4 Beyond a metallicity characterization: the origin of bulge populations 141
6.4.1 The metal-rich bulge 142
6.4.2 The metal-poor bulge 142
6.5 A dissipative collapse origin of the bulge? 143
6.5.1 Interpretation of bulge chemical patterns from a chemical evolution model 143
6.6 A secular origin of the bulge? 145
6.6.1 Chemical similarities between the thick disk and the bulge 145
6.7 Summary 152

Abstract: The different observational pieces of evidence presented in the last chapter are discussed in the context of proposed scenarios for bulge formation. The metal-rich bulge seems to dominate close to the plane, display the double RC and presents bar-like kinematics. We associate it with the bar B/P bulge formed as the product of secular evolution of the early thin disk. On the other hand, the origin of the metal-poor bulge is still difficult to asses. Its spatial distribution, kinematics and α- enhancement levels argue for a early rapid formation dominated by massive stars. On the other hand, its α- enhancement levels are comparable to those of the thick disk, though the position of the so called "knee" might be located at slightly larger metallicity. In this sense, the bulge might be whether the product of an early dissipative collapse or of the secular evolution of the early thick disk. More precise determinations of the "knee" position in both populations, as well as measurements of SFR sensitive r- and s-elements are needed to complete the picture.

It is clear that metallicity alone is not enough to unravel the complexities inherent to the stellar populations sitting in the central kiloparsecs of the Milky Way. All the

accumulated observational evidences, chemical abundances, kinematics and spatial distributions have been collected with an increasing level of detail, but often leading to contradictory conclusions concerning the nature of the bulge. Once this conundrum was recognized, several efforts to conciliate observational evidence and interpretations from N-body simulations and chemical evolution models have been done.

In the previous chapter chapter, we have reviewed all the observational evidence concerning metallicity, kinematics and chemical abundances of the bulge. A great deal of progress both in the number of stars and sampled fields as in the quality of stellar parameters and derived abundances, has been reached along the different GES data releases up to the current iDR4. We have profited of this exquisite sample to conduct a thorough study of the bulge stellar population in the context of the Milky Way stellar populations. To achieve this goal, we have used in addition to the bulge sample a subsample of good quality data coming from the disk pointings of the survey.

In the following, we discuss what we have learned from the analysis of the different pieces of evidence. As we will see, the interpretation of these results leads to firmly establish a composite nature for the Galactic bulge. Of course, the picture is still not complete, despite the great degree of progress reached in this work and in the literature in general. Accordingly, we will discuss also which pieces of evidence, specially from the observational point of view are still needed to make our way towards a thorough understanding of the complex origin of the Galactic bulge.

6.1 How many bulge components?

Early suggestions from the analysis of high resolution spectroscopic data ([Zoccali *et al.* 2008]) pointed out for a bimodal or even multimodal nature of the bulge MDF. A quantification of the number and characteristics of such metallicity components was first provided in [Hill *et al.* 2011]. In that work, the authors identified a clear bimodality with a narrow metal-rich component at supersolar metallicity and a broader metal-poor one. A step forward in terms of spatial coverage and number statistics is given by the results of the ARGOS survey. From their GMM decomposition ([Ness *et al.* 2013a]), they found up to five components building up the MDF in different proportions depending of latitude. Three components, dubbed A, B and C, are thought to trace the thin and thick disk contribution to the bulge stellar population budget. On the other hand, the weak D and E components are defined as disk interlopers or halo contaminants in their sightlines. The results of this work have been adopted de facto in the literature as a comparison in subsequent observational efforts, as well as for models trying to reproduce global and specific chemo-kinematic bulge trends. Our results, as well as the qualitative analysis of several high resolution works in the literature (see next section), seem to challenge this picture in the sense of simplifying it: no more than two components seem to be enough to appropriately describe the bulge MDF when samples are carefully cleaned from disk foreground sources and halo intruders at the metal-poor end.

Our early work based in the first GES data release, revealed a systematic bimodal nature of the MDF in the five analyzed fields. As we shown in this Chapter, the same result emerges from the analysis of the iDR4, that with respect to the iDR1

contains more stars, with more robust stellar parametrization and a larger (l,b) spatial coverage. In fact, from a Gaussian Mixture Models analysis, the bulge MDF appears as a bimodal distribution, comprising a narrow super-solar metal-rich (with a peak around [Fe/H] = 0.4 dex) and a broad metal-poor (with a peak around [Fe/H]=-0.4 dex) components. This bimodal nature is verified in all the individual fields, except in those limited by small number statistics (Fig. 5.7). In all these cases, the AIC criterion used for model selection, gave preference for a two-component model with a high relative probability. In terms of information theory, this means than the metallicity distribution, as given by the number an quality of the data in each field, can be explained by a two-Gaussian mixture with a minimum loss of information, though with a minimized tendency of overfitting. Moreover, as we show below, this is in general the case when performing a similar analysis on high resolution samples available in the recent literature.

6.2 The bulge MDF in the literature

It has been demonstrated in this thesis the usefulness of the Gaussian Mixture Models as a way to perform statistically robust analysis on the MDF structure. In particular, this approach has proven to be efficient unfolding the substructure visible in the bulge MDF. Our intent here is to present the GMM analysis of several MDFs observed and analyzed in different works. This compilation is not exhaustive, and is limited to studies obtaining samples in high resolution. The specific targets, RC, RGB or microlensed dwarfs, are selected in different ways in each study, as well as the instrument, spectral coverage, resolution and analysis method. The specific details can be found in the respective research papers as listed below. We have limited ourselves to perform a GMM analysis on the MDF as directly available from the on-line data published in the VisieR catalog service[1]. In this sense, we adopt a qualitative approach since we cannot ensure -and it is probably not the case- that all the cited works share a common metallicity scale. Nevertheless, we focus here on the number of components obtained in each case.

In Fig. 6.1, we present the best model fit on the MDF coming from 6 different works:

- [Zoccali *et al.* 2008]: 473 K giants located at ~ 1 mag above the RC and selected along the whole color range of the RGB. Observed with FLAMES-GIRAFFE at $R \sim 20000$.
- [Hill *et al.* 2011]: 220 RC stars observed with FLAMES-GIRAFFE at $R \sim 20000$.
- [Johnson *et al.* 2012b]: 62 RGB and RC stars observed with the Hydra multifiber spectrograph at the Blanco 4m telescope. $R \sim 25000$
- [Uttenthaler *et al.* 2012]: 401 RGB stars Observed with FLAMES-GIRAFFE at $R \sim 17000$.
- [Bensby *et al.* 2013]: 58 microlensed dwarfs observed as ToO, mostly with UVES, but also with HIRES and MIKE. Spectral resolution ranging between $R = 46000$ (UVES) to $R = 64000$ (MIKE).

[1] http://vizier.u-strasbg.fr/

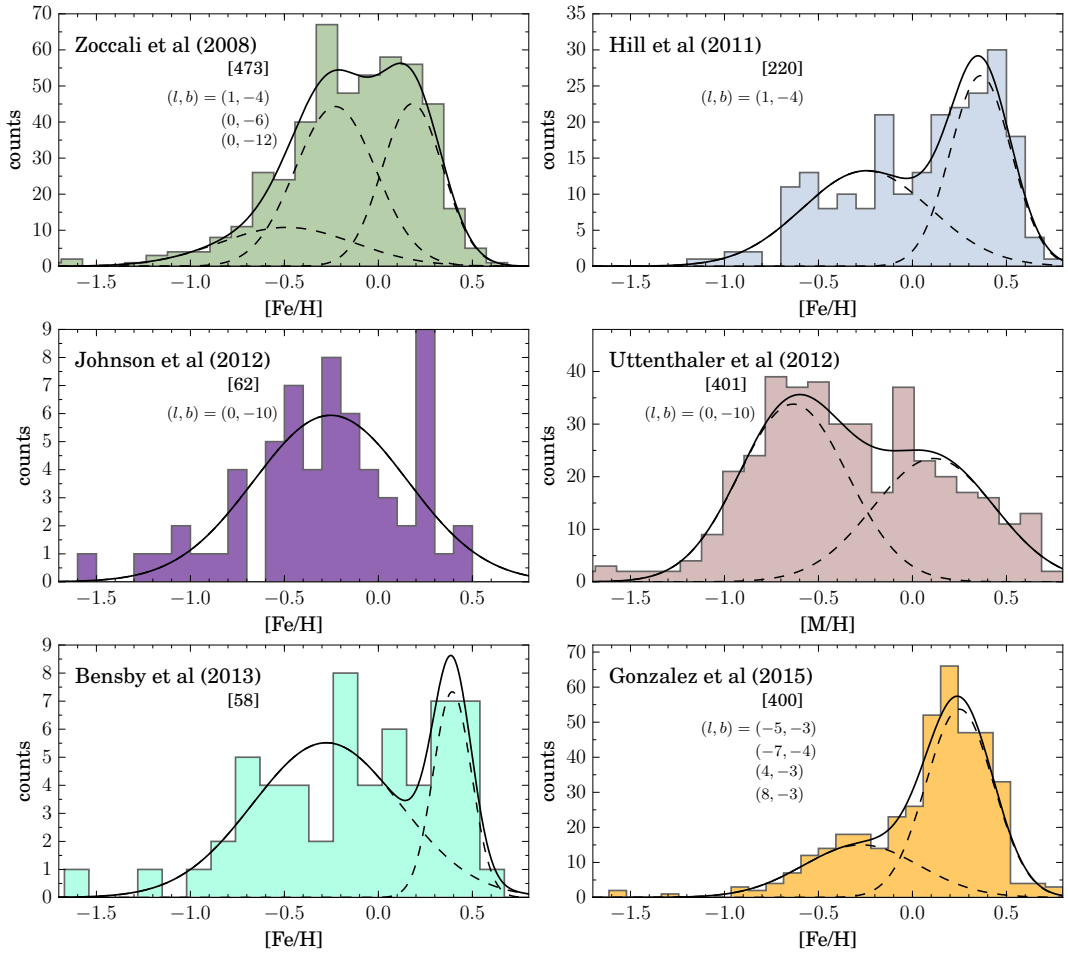


Figure 6.1: GMM decomposition of bulge MDFs taken from literature. The metallicity values measured from six different high resolution samples are depicted by histograms in the different panels. Some of the works are from a single field ([Hill *et al.* 2011, Johnson *et al.* 2012b, Uttenthaler *et al.* 2012]) while others are the combination of vertical ([Zoccali *et al.* 2008]), horizontal ([Gonzalez *et al.* 2015]) strips. The [Bensby *et al.* 2013] sample is composed by scattered targets across the bulge region. The number of targets is indicated in brackets.

- [Gonzalez *et al.* 2015]: 400 RC stars observed with FLAMES-GIRAFFE at $R \sim 22500$. (the high resolution strip of the GIBS survey).

As it can be readily seen, the information criterion used for model selection (AIC, see Chap. 3) usually prefers two-component solutions. The exceptions are two. The MDF of [Zoccali *et al.* 2008] is composed by the combination of three fields along the bulge's minor axis. We verified that in the individual fields the solutions are comparable to the global one presented here. In fact, the fields at $b = -4°$ and $b = -6°$ are both trimodal, while the one at $b = -12°$ results in a single-peaked solution, mainly due to its small number statistics.

The MDF from [Gonzalez *et al.* 2015] offers an interesting verification on the domi-

nance of metal-rich stars close to the plane. The combined MDF comes from four fields in a strip at $b = -3°$. We can see clearly the strong metal-rich peak and the minor contribution of the broader metal-poor component.

6.3 Metallicity gradients in perspective

The suggestion about the presence of vertical gradients in the bulge region date back to the work of [Minniti *et al.* 1995]. This decrease of mean metallicity with latitude along the minor axis was fist confirmed based on high resolution spectroscopy by [Zoccali *et al.* 2008]. In this way, the existence of a metallicity gradient for $b \leq 1 - 4°$ was established. However, such a gradient would be absent at latitudes lower than $b = -4°$ [Rich *et al.* 2007a, Rich *et al.* 2012]. A first general picture of the metallicity distribution and gradients through the bulge region comes from the photometric metallicity map of [Gonzalez *et al.* 2013]. This work confirms the general trend with latitude as characterized from the small spectroscopic samples, although not covering regions inside $|b| = -4°$. As already shown in [Zoccali *et al.* 2008], the vertical gradient arises from the variation of the relative density of metal-poor and metal-rich stars, rather than from a solid shift of the MDF with latitude. The analysis of the spatially extended ARGOS data leads [Ness *et al.* 2013a] to further emphasize this picture

The analysis of GES bulge data presented in this chapter allows us to confirm this general picture and further characterize it. In fact, there is a systematic change of the relative proportion of stars belonging to each one of the two MDF populations. This ratio changes chiefly as a function of b, with metal-poor stars dominating far from the Galactic plane. In this sense, the variation of the mean metallicity with latitude can be interpreted as the interplay between two effects. It is a global trend build up from the variation of metal-poor stars in detriment of metal-rich ones, plus the effect of the internal gradients in each population.

It is worth to emphasize here that the identification of these two effects is important to interpret the potential structural and formation differences between metal-rich and metal-poor bulge stars. On one side, the dominance of metal-poor stars far from the plane, and the absence of RC split among them, indicates that the structure traced by these stars might be spherical and more spatially extended than the B/P bulge traced by metal-rich stars. On the other hand, the existence of individual metallicity gradients in both groups of stars, should be considered while attempting to draw conclusions about their possibly different origins.

6.4 Beyond a metallicity characterization: the origin of bulge populations

The systematic bimodality of the MDF across our sampled area, as well as the apparently different spatial distributions of stars in each group -as revealed from the gradients with b and the presence or not of the double RC feature- made an important first step toward a consistent multicomponent description of the Galactic bulge. Extra pieces of

information were incorporated while looking for correlations with kinematics and alpha element enhancements, further stressing the likely different nature of both populations

We show that the line-of-sight Galactocentric velocity dispersion correlates with metallicity. Metal-poor stars display a high velocity dispersion, around 100 km s^{-1}, nearly independent of (l, b). Instead, metal-rich stars present a more complex behavior. The stars close to the plane are kinematically as hot as the bulge. But their velocity dispersion decreases systematically as the distance from the plane increases, reaching at high latitudes values typical of the thin disk.

6.4.1 The metal-rich bulge

Two different origins can be proposed for the stars belonging to the metal-rich and the metal-poor MDF components. Metal-rich stars participate in the B/P bulge and present bar-like kinematics. We associate them with a population formed by secular evolution of the disk via bar formation and buckling instabilities. No major controversy can be found in the literature concerning this hypothesis, since all observational evidence so far accumulated, as well as the outcome of dynamical models, seem to be consistent with this picture. As a structure formed in a secular timescale, it is possible, and even expected, that it contains a fraction of young stars. Historically, global bulge age determinations have hinted for a stellar population uniformly old of about 10 Gyr [Ortolani *et al.* 1995, Feltzing & Gilmore 2000, Kuijken & Rich 2002, Zoccali *et al.* 2003, Clarkson *et al.* 2008]. In contrast, by studying a sample of microlensed bulge dwarfs, [Bensby *et al.* 2013] found that nearly 22% of the sample is younger than 5 Gyr, most of them metal-rich stars. In the same way, an internal vertical metallicity gradient, as the one reported here, is predicted by N-body simulations of secular bulge formation as an effect of the mapping in the vertical direction of horizontal [Martinez-Valpuesta & Gerhard 2013], vertical [Bekki & Tsujimoto 2011], or a mix of both [Di Matteo *et al.* 2015] metallicity gradients initially present in the disk. The issue of a pure thin disk or thin+thick disk origin of these stars have also been raised by claiming that, to account properly for the detailed chemical and kinematical observed properties and correlations, a composite disk model should be adopted [Di Matteo *et al.* 2015]. A disk parenthood for the bulge metal-rich stars finds also qualitative support from the distribution of these stars in the [Mg/Fe] vs. [Fe/H] plane. In fact, we show here that the metal-rich end of the thin disk sequence overlaps the metal-rich bulge one at [Fe/H] $\gtrsim 0.15$ dex.

6.4.2 The metal-poor bulge

When it comes to the characterization and determination of the origin of the metal-poor bulge, two main ideas are in competition. On one side, the classical hypothesis of dissipative collapse is invoked as able to explain kinematic, structural and chemical patters seen in these stars. A second scenario proposes that the metal-poor bulge is merely the product of the redistribution of thick disk stars into the central Galactic regions as the product of secular dynamics. Let's examine in the next section what we can tell from our results about each of these possibilities.

6.5 A dissipative collapse origin of the bulge?

We found that metal-poor RC stars do not participate in the B/P bulge, dominate in number density far from the plane, and display isotropic kinematics. These properties are compatible with a stellar population formed at early epochs from the dissipative collapse of a primordial cloud accompanied by a strong burst of stellar formation, namely, a classical spheroid. A reinforcement on the potential spheroidal spatial distribution these metal-poor stars comes from the fact that RR Lyrae stars, as tracers of metal-poor old stellar populations, have been shown to display an axisymmetric spatial distribution, uncorrelated with the bar position angle [Dékány *et al.* 2013], and a high velocity dispersion of around 130 km s° [Gratton 1987, Kunder *et al.* 2016].

The presence of an internal radial metallicity gradient, as well as a high velocity dispersion, are expected features from a dissipative collapse formation process. Moreover, the general enhancement of alpha elements and the metallicity at which the "knee" of the sequence in the [Mg/Fe] vs. [Fe/H] plane takes place, are both possible to interpret as a consequence of the interplay between SN II vs. SN Ia explosion timescales in a rapid formation process. In fact, when adopting a chemical evolution model to reproduce these observational signatures, we found that it fits satisfactorily the data under the assumption of fast chemical evolution ($t \leq 1$ Gyr), dominated by massive stars and characterized by a high star formation efficiency.

In the work of [Shen *et al.* 2010], the bulge rotation and dispersion curves from the BRAVA project are suitably reproduced with a N-body simulation which limits the mass contribution of a possible classical bulge to be less than 8%. Such bulge single disk origin scenario is not compatible with our results. The mean proportion of stars belonging to each one of the MDF components is weighted toward metal-poor stars. Although our data set may not be fully adequate to make strong assessments on the mass contribution of both populations to the global bulge mass budget (the sample is not large enough, not enough spatial coverage, specially in the inner bulge), the data clearly hints for a bulge composed by a similar fraction of metal-poor and metal-rich stars. Moreover, from the observed mass-metallicity relation for galactic spheroids [Gallazzi *et al.* 2005], a system with mean metallicity around -0.4 dex, as the metal-poor component, should have a mass of $\sim 10^{10}$ $M_{\odot}$, a value comparable to the total bulge mass, as estimated from observations [Valenti *et al.* 2015].

A dissipative collapse has also been suggested for the bulge from the chemical modeling of its MDF ([Matteucci & Brocato 1990]). In the following we use a chemical evolution model to put constraints on the formation timescale from our GES data.

6.5.1 Interpretation of bulge chemical patterns from a chemical evolution model

The modeling of observational data by means of a chemical evolution model provides an interesting opportunity to give constraints on the formation timescale of a stellar system. We attempt here to constrain the bulge scale formation by adopting a model for a bulge formed by a fast dissipative collapse with a strong early burst of stellar formation. To this end, we adopted the model of [Grieco *et al.* 2012]. In particular,

in this work, two bursts of star formation are invoked to model the metal rich and metal poor modes of the bulge MDF. We adopt here the model corresponding to the metal-poor bulge. The model assumes a gas infall law given by

$$\left(\frac{d\sigma_{\rm gas}}{dt}\right)_{\rm infall} = A(r)X_{\rm i}e^{-t/T_{\rm inf}}, \tag{6.1}$$

where $X_{\rm i}$ is the abundance of a generic chemical element i in the infall gas. The chemical composition of the infall gas is assumed to be primordial or slightly enhanced from the halo formation. $T_{\rm inf}$ is the infall timescale, fixed by reproducing present day abundances (MDF), SFR and stellar mass. $A(r)$ is a parameter fixed by reproducing the current average total bulge surface mass density. The parametrization of the star formation rate is adopted as a Schmidt-Kennicutt law:

$$\psi(t) = \nu\sigma_{\rm gas}^{k} \tag{6.2}$$

with k the law index, and ν the star formation efficiency (i.e the star formation rate per unit mass of gas). The model includes a Salpeter IMF, constant in space and time, which allows to reproduce well the MDF of the metal-poor bulge population. The set of yields are adopted from [Maeder 1992], [Woosley & Weaver 1995], [van den Hoek & Groenewegen 1997] and [Meynet & Maeder 2002].

Several models were run adjusting parameters to better reproduce the trends drawn by bulge stars in the [Mg/Fe] vs. [Fe/H] plane. The best model is displayed in Fig. 6.2, where it is compared to the whole bulge working sample. This model assumes a short timescale for the gas infall $T_{\rm inf} = 0.1$ Gyr and a very efficient star formation, with $k = 1$ and $\nu = 25$ Gyr^{-1}. The main characteristics of the bulge sequence (enhancement levels, "knee" location) are well reproduced by this model. We can see that, for [Fe/H] ≥ -1.5 dex, the predicted [Mg/Fe] abundance ratio steadily decreases with metallicity. This behavior increases from [Fe/H] $\gtrsim -0.4$ dex, which is comparable with the observed locus of the "knee", as determined directly from the sample (Fig. 5.11). The overall formation time scale, as read from the upper axis of Fig. 6.2, indicates a rather rapid chemical enrichment of the bulge, taking place on a total timescale of 0.5-0.7 Gyr. Such a short timescale is compatible with a monolithic assembly of the metal-poor bulge. It is worth noting that, formally, the model predicts a continuous enrichment of the gas up to super-solar metallicities. However, the number fraction of such super-solar stars is low compared to populations with lower metallicities. In this way, from the point of view of the CEM, it is not excluded that the bulge contains a fraction of metal-rich in-situ-born stars. In this sense, the ensemble of bulge metal-rich stars could constitute a composite population of stars formed in-situ plus a larger dominant fraction of stars with disk origin, currently located in this region as a product of secular bar-driven dynamics.

In essence, chemical evolution models provide us with an opportunity to directly interpret observed chemical abundance patterns in terms of the interplay between the relative contributions of different polluters and timescales. The CEM we adopted here assumes a dissipative collapse as the main process of mass assembly and chemical evolution of the bulge metal-poor stellar population. Under this paradigm, the model reproduces well the bulge metallicity-abundance distribution interpreting it as a population that formed at early epochs in a short timescale ≤ 1 Gyr.

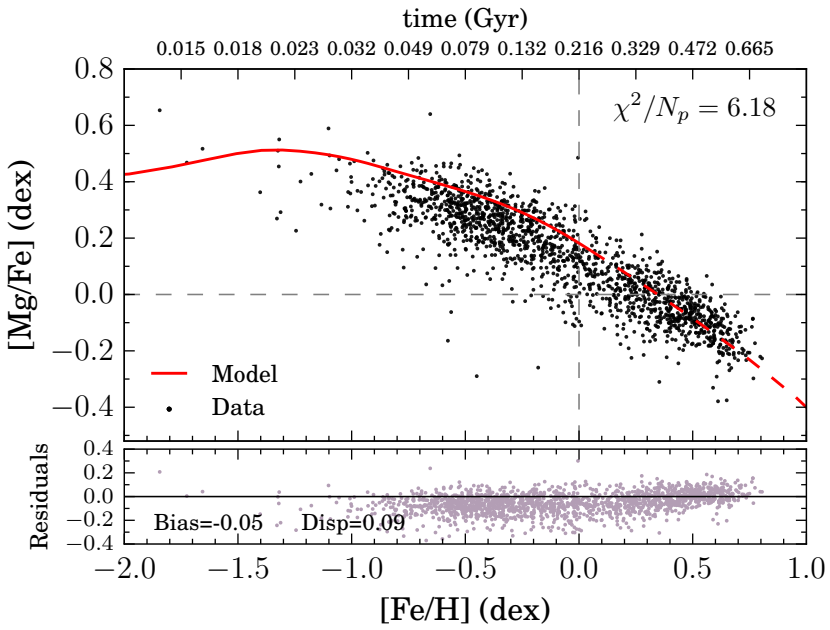


Figure 6.2: Comparison between the bulge data (black dots) and the predicted sequence (red line) from the adopted chemical evolution model. The line changes from solid to dashed to emphasize that the model parameters are adjusted to fit the metal-poor bulge MDF component. *Main panel:* The evolution in time of the modeled quantities is indicated by the scale at the top of the panel. A normalized χ^2 between the model and data is quoted in the panel. *Small panel:* Residuals between the data and the model.

6.6 A secular origin of the bulge?

In a second view, the comparable α- enhancement levels, along with the similar "knee" position of the bulge and thick disk sequences, can be interpreted as signatures of common origin, or at least, of a similar chemodynamical evolution of these populations. In fact, if this is the case, the two stellar population would not only share a similar IMF but also comparable star formation rates. In this sense, such chemical similarities without a causal connection, would seem to be a too fine-tuned coincidence to happens just by chance. We study here the relation between the bulge and the thick disk as seen by GES data.

6.6.1 Chemical similarities between the thick disk and the bulge

In the previous chapter, we presented observational evidence unfolding a bulge composite nature. The bimodality of the MDF suggests the existence of two stellar components with different characteristic metallicities. A different spatial distribution is suggested from the observed variation in the relative proportion in which both components contribute to build up the MDF at different fields: metal-rich stars dominate close to the plane with metal-poor ones being more extended. An additional correlation of kine-

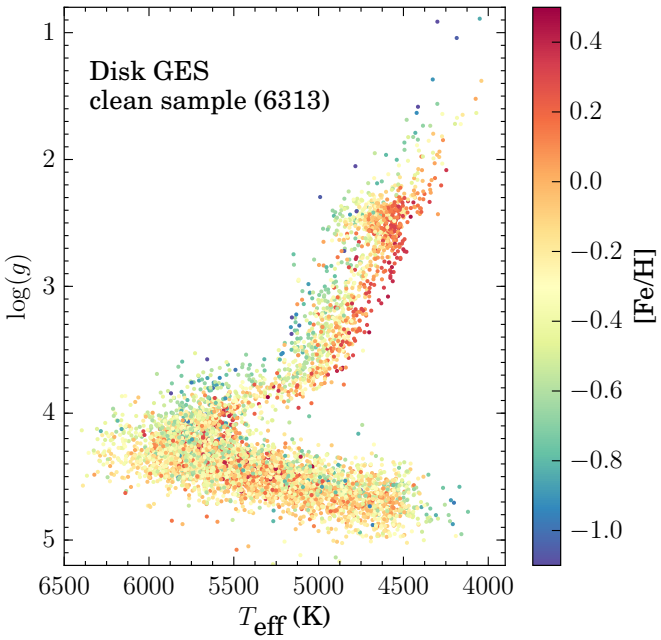


Figure 6.3: HR diagram of the selected sample of disk stars. Several cuts in SNR and errors in stellar parameters and abundances were applied as described in the text. The points are color-coded according to the metallicity.

matics with metallicity strengthens the case. The metal-poor component appears to be systematically hot throughout the area sampled by our fields. In contrast, the kinematic behavior of the metal-rich component is highly dependent on the specific position of the fields, being generally hotter close to the plane and cooler with increasing (l,b). The latter depicts an inhomogeneous and more spatial orbital distribution for the structure traced by these metal-rich stars. The case for a composite bulge seems therefore to be well established. Let us now turn to the problem of setting this paradigm into the more general picture of Galactic components.

The chemical characterization of disk stars in the [α/Fe] vs. [Fe/H] plane has proven to be a very useful tool to distinguish and characterize thin vs. thick disk stars samples [Adibekyan *et al.* 2013, Haywood *et al.* 2013, Recio-Blanco *et al.* 2014, Kordopatis *et al.* 2015, Hayden *et al.* 2015]. In fact, the photospheric chemical composition is expected to be a more reliable physical property than, for example, kinematics, since the chemical composition of low mass stars is a more preserved quantity than kinematics in the complex dynamical evolution of a stellar system [Freeman & Bland-Hawthorn 2002]. In general, the chemical characterization of the different Galactic components allows us to compare them in order to figure out at which extent their formation and subsequent chemical evolution can be connected. In this line, several efforts have been made in the literature to compare the disk stellar populations, in particular the thick disk, with the bulge [Zoccali *et al.* 2006, Lecureur *et al.* 2007, Fulbright *et al.* 2007, Meléndez *et al.* 2008, Alves-Brito *et al.* 2010, Bensby *et al.* 2013, Gonzalez *et al.* 2015]. These studies have been based on the comparison of bulge and local thick disk samples. The general conclusion emerging from this debate is that the thick disk seems to have similar enrichment levels compared to the bulge, which suggests a possible connection between both Galactic components.

As described in Chap. 2, the Gaia-ESO survey observes stars in all the main Galac-

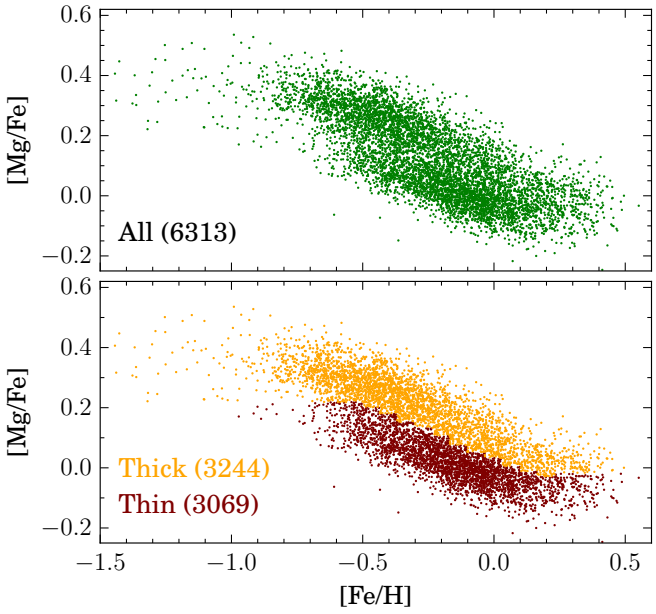


Figure 6.4: Selected disk subsample in the [Mg/Fe] vs. [Fe/H] plane. *Upper panel:* Whole selected sample of 6313 stars. The number count underdensity between thin and thick disk sequences is clearly visible. *Lower panel:* A sample separation into thin and thick disk sequences is performed as described in the text, and color coded accordingly. The total number of stars in each sequence is quoted in parenthesis.

tic components, with a significantly number of its pointings intended to characterize the thin and thick disk populations. We recall also, that the disk samples in the Gaia-ESO survey are observed both with the HR10 and HR21 GIRAFFE setups, but a careful fundamental parameter homogenization, based on benchmark stars, ensures compatibility between the parameters and abundances determined from this setup combination with respect to the HR21-based ones of the bulge sample.

We take advantage of this large homogeneous data set to perform a comparison with our bulge sample. From the entire disk sample, we select stars satisfying $SNR \geq 45$, $\Delta T_{teff} \leq 150$ K, $\Delta \log(g) \leq 0.23$ dex, Δ[M/H] ≤ 0.20 dex, Δ[Fe/H] ≤ 0.1 dex and Δ[Mg/H] ≤ 0.08 dex. In this way, we define a clean disk sample with trustworthy stellar parametrization and abundance measurements. It is composed of 6313 stars. As can be seen in Fig. 6.3, these stars cover all the main evolutionary stages of low mass stars, from the main-sequence, to the turn-off and giant sequences, including the RC. As we will see below, this is very important since the availability of giants allows both to sample larger distances than the solar neighborhood, and to explicitly check that no chemical systematics are introduced in our analysis by comparing dwarfs and giants.

The distribution of our selected disk sample in the [Mg/Fe] vs. [Fe/H] plane is shown in the upper panel of Fig. 6.4. A number count underdensity between α-enhanced (thick) and low-α (thin) disk sequences is clearly visible over the metallicity range $-0.7 \leq$ [Fe/H] ≤ 0.0 dex. Around solar metallicity, the thick disk sequence merges the thin disk one, hence the separation becomes more uncertain. Given this density structure, a separation between the thin and thick disk sequences has been performed by following the dip in [Mg/Fe] in several metallicity bins. To this end, we used a K-means clustering algorithm across narrow metallicity bins. For metallicities lower than [Fe/H] $-$ 0.6 dex and higher than [Fe/H] $=$ 0.30 dex, the classification becomes uncertain, so that we simply separate stars with respect to the limit Mg value of the

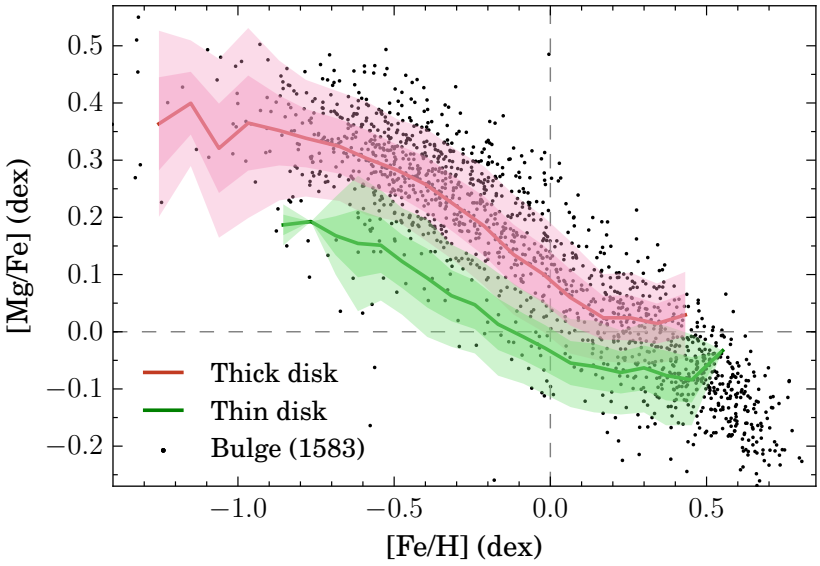


Figure 6.5: Bulge sample stars (black dots), mean trend (solid lines), and 1σ and 2σ dispersion bands (shaded areas) for the thin (green) and thick (red) disk profiles in the [Mg/Fe] vs. [Fe/H] plane.

latest computed bin. The separated subsamples are depicted with different colors in the lower panel of Fig. 6.4.

As a first qualitative comparison between the disk and bulge in the [Mg/Fe] vs. [Fe/H] plane, we construct median profiles and dispersion bands at the 1σ and 2σ levels for the thin and thick disk sequences. We overplot the resulting profiles on top of the bulge sample distribution in Fig. 6.5. We can see that over the whole metallicity range spanned by the thick disk, bulge and thick disk stars have comparable [Mg/Fe] enhancement levels. Nevertheless, a larger dispersion in [Mg/Fe] of bulge stars relative to thick disk ones is apparent along the whole metallicity range. Although this can be a real feature, revealing differences in chemical evolution between both populations, we cannot rule out the possibility that this effect comes from the lesser spectral information available from the HR21 setup for the bulge compared to the HR10+HR21 available for the thick disk sample. It is worth noting that the metal rich end of the thin disk sequence seems to overlap with the metal-rich bulge at [Fe/H] ≥ 0.1 dex.

The previous comparison suggests a chemical similarity between the bulge and the thick disk given that both populations seem to present comparable levels of α- enhancement, and in general, similar trends in the [Mg/Fe] vs. [Fe/H] plane. We attempt to make more detailed assessments by comparing the location in metallicity of the "knee" in both sequences. Unlike previous attempts in this direction, our thick disk sample spans a broader extent in Galactocentric radii, sampling regions well outside the solar neighborhood. This can be seen in Fig. 6.6, where the spatial distribution in the R_{GC} vs. $|Z_{GC}|$ plane of bulge and disk samples is displayed. The distribution of thick disk stars (red points) is concentrated in the solar cylinder but extends to larger distances, with a good number of stars even up to 4 kpc. Given the likely variable vertical distribu-

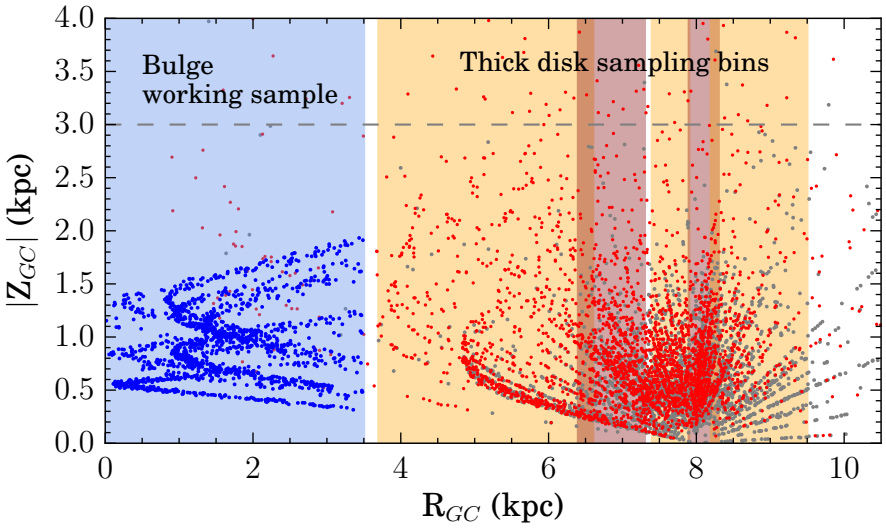


Figure 6.6: Spatial distribution of the bulge and disk samples in the $|Z_{GC}|$ vs. R_{GC} plane. Bulge, thick disk and thin disk stars are depicted by blue, red and gray points, respectively. A blue shaded area highlights the spatial selection (with $R_{GC} \leq 3.5$ kpc) used to define the bulge working sample. Analogously, several alternate orange and red shared areas depict the radial bins used to split the thick disk sample. An horizontal gray dashed line indicates the limit $|Z_{GC}| \leq 3$ kpc imposed to ensure constancy of $|Z_{GC}|$ through the different radial bins.

tion of stars at different R_{GC}, because of the sightlines at increasing values of Galactic latitude, we select stars with $|Z_{GC}| \leq 3$ kpc to ensure constancy of $|Z_{GC}|$ along the sampled radial range.

We split the thick disk sample into five radial portions of approximately the same number of stars in order to probe radial variations in the position of the [Mg/Fe] vs. [Fe/H] "knee". As we did for the bulge sample, we fit a bilinear model to the thick disk sequence in each radial bin. In each case, we used stars in the range $-1.0 \leq$ [Fe/H] $\leq$ 0.1 dex in order to avoid low density count levels in the metal-poor end and the region where the thin and thick disk sequence separation is more uncertain (i.e. around solar metallicity). The results for the five radial bins are displayed in the panels a-e of Fig. 6.7. The metallicity at which the "knee" is located, and the respective error from 1000 Monte Carlo samplings on the individual [Mg/Fe] errors, is quoted in each respective panel. We can see that, accounting for the errorbars, the position of the thick disk "knee" does not change through the sampled radial region, despite a small trend is apparent (panel f). A radial constancy of the thick disk profile in the [α/Fe] vs. [Fe/H] plane has been already suggested from APOGEE data [Nidever *et al.* 2014, Hayden *et al.* 2015].

Unfortunately, our current level number statistics at inner Galactocentric radius, and possibly, the level of uncertainty in our abundance measurements does not allow us to establish unequivocally whether the thick disk presents or not chemical radial variations. The position of the "knee" is a proxy for the star formation rate at which the system formed stars out of the initial gas, In this sense, a decrease of the metallicity

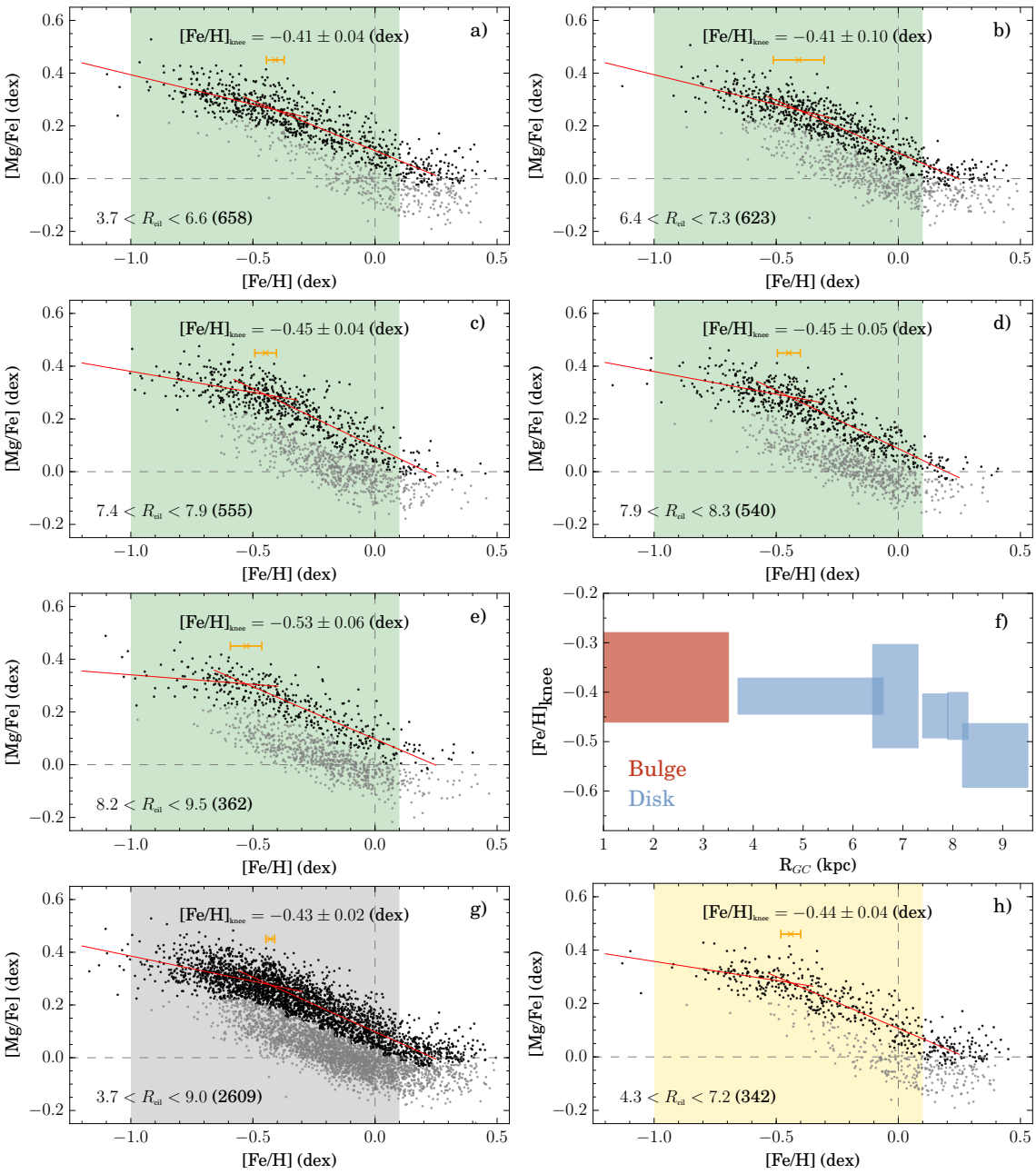


Figure 6.7: Determination of the "knee" in the [Mg/Fe] vs. [Fe/H] plane for the thick disk. *Panels a-e:* Gray and black points depict thin and thick disk stars. A shaded area highlights the metallicity range used to perform a bilinear model fit of the thick disk sequence in five different radial bins. The number of thick disk stars used to perform the fit is indicated in parenthesis. The best fit model in each radial bin is displayed with red lines overlaid on of the thick disk sample. The [Fe/H] location of the model "knee", together with its error, is quoted in each panel and sketched with an orange errorbar. *Panel f :* [Fe/H] position of the "knee" as a function of Galactocentric distance. *Panel g:* general thick disk sample, including all the stars in the panels a-e. *Panel h:* subsample of RC stars.

position of the "knee" with R_{GC} would imply an inside-out formation (which would be necessary to conciliate with the observed absence of a radial metallicity gradient [Mikolaitis *et al.* 2014]), while a constancy of its position a formation given by a single star burst.

We attempt at increasing the accuracy of the metallicity position of the thick disk "knee" by performing a bilinear fit on the whole thick disk sample (sample's mean Galactocentric radius $R_{GC} = 7.1$ kpc). We obtain a value of $[Fe/H]_{knee} = -0.43 \pm 0.02$ dex, which we can consider as representative of the thick disk from the Gaia-ESO survey sample (Fig. 6.7 panel g). Finally, in panel g of Fig. 6.7, we display a fit performed on the subsample of RC thick disk stars (sample's mean Galactocentric radius $R_{GC} = 5.6$ kpc). The result $[Fe/H]_{knee} = -0.44 \pm 0.04$ dex, again in agreement with all the previous determinations, demonstrates that no systematics are likely to be introduced in our analysis by using results coming from dwarf and giant stars. If we compare the thick disk value of the "knee" position with the one of the bulge sequence, a difference of $\Delta[Fe/H] = 0.06$ dex is found. This difference is small with respect to the size of the errorbars of both determinations (0.09 and 0.02 dex, respectively) making difficult to make a strong assessment for its statistical significance. However, if nonzero, this difference would have an upper limit of $\Delta[Fe/H]_{knee} = 0.18$ dex at a confidence level of 95%.

We found a small difference of 0.06 dex, which might be compatible with zero if the errorbars in the individual "knee" positions are taken into account. From the size of these errorbars, we estimate that the difference, if real, might be smaller than 0.18 dex. By the same token, the bulge and thick disk sequences share in the [Mg/Fe] vs. [Fe] a common locus up to solar metallicity. This result is fully compatible with [Alves-Brito *et al.* 2010]. In this study, from a strict differential analysis of red giants with very similar parameters, a similarity in the alpha enhancements of the bulge and local thick disk is found in the range $-1.5 \leq [Fe/H] \leq -0.3$ dex. Not to be overlooked though is the fact that in our dataset, a larger [Mg/Fe] dispersion in the whole metallicity range is suggested for the bulge with respect to the thick disk. Finally, many recent N-body simulations have shown that it is possible to reproduce general kinematic and chemical bulge patterns from models explaining the bulge as the product of disk evolution [Shen *et al.* 2010, Martinez-Valpuesta & Gerhard 2013, Di Matteo *et al.* 2014]. However it is only in [Di Matteo *et al.* 2015] that an original thick disk contribution comes to play a role in the bulge formation.

In summary, a chemical similarity between the bulge and the thick disk is suggested by the data. A detailed examination of compatibility between both sequences is beyond the statistical resolution of the present sample. Nevertheless, some caution should be taken while considering the facts exposed here; although similar enhancement levels are found for both populations, the bulge exhibits a larger dispersion in [Mg/Fe] around the mean, a result to be confirmed with a more homogeneous dataset. And similarly, although the "knee" position of both sequences is comparable inside the errors, an eventual difference as large as 0.18 dex suggests that the "knee" of the bulge can be in fact located at a higher metallicity than the one of the thick disk. As a proxy of the SFR, the relative position of the "knee" between the bulge and the thick disk can provide a fundamental constrain on their formation timescales, and eventually establish a clear

difference between both populations.

Given what our data suggest, but being aware that no firm assessments can be done at this point on the origin of the metal-poor bulge, we propose a possible formation scenario. If we assume that the difference in the "knee" position between the bulge and thick disk sequences is not null, we can draw a tentative picture of the bulge formation by interpreting the observational evidence in terms of two stellar populations: The in-situ-formed bulge population is the product of a fast dissipative collapse in the early epochs of Milky Way evolution. As characterized by a strong SFR, the chemical enrichment of the gas may have reached super-solar metallicities before gas exhaustion, with the majority of stars produced around -0.5 dex. This metal-poor population should be currently seen as a spheroid centrally concentrated and supported by isotropic random orbital motions. On the other hand, secular disk instabilities lead to the formation of a bar out of the early inner disk. The redistribution of mass and angular momentum driven by the bar, may explain the dynamics of these metal-rich stars, globally displaying a X-shape morphology. In this sense, it is possible that a small fraction of the metal-rich stars are in fact endemic from the central regions of the Galaxy, being currently outnumbered by stars with their origin in the early disk.

A semantic issue is then raised. In fact, we legitimately could call bulge all stellar populations currently present in the central kiloparsecs of the Milky Way, regardless of their origin and specific evolutionary histories.

6.7 Summary

To understand the nature of the bulge it is fundamental to put it in the context of other Galactic components. In this chapter we considered evidence from the literature, chemical evolution models, as well as the comparison of bulge and disk chemical patterns to draw arguments favoring each one of the bulge formation scenarios.

We list here a number of facts and conclusions we have discussed:

1. Data taken from the literature, with their different observational approaches and analysis strategies, confirm in most of the cases the bimodal (or multimodal) nature of the bulge MDF.

2. The variation of the mean metallicity with latitude -the vertical gradient- can be understood as the interplay between the increase of metal-poor stars in detriment of metal-rich ones, plus the effect of the internal gradients in each population.

3. The metal-rich end of the thin disk sequence overlies the metal-rich bulge subpopulation in the [Mg/Fe] vs. [Fe/H] plane. Analogously, the thick disk and metal-poor bulge sequences share nearly the same locus.

4. A small variation in the "knee" position with Galactocentric distance is found for the thick disk, although is not statistically significant considering the errorbars of individual measurements.

5. A small difference of Δ[Fe/H] = 0.06 dex is found between the thick disk and metal-poor bulge "knee" position, with the later located at higher metallicities.

6. A chemical evolution model was used to fit the whole bulge sequence in the [Mg/Fe] vs. [Fe/H] plane. It assumes a prompt fast dissipative collapse of a primordial cloud, in a timescale $\leq$ 1 Gyr, accompanied by an strong burst of stellar formation.

7. We associate the metal-rich bulge subpopulation with the B/P bulge formed by the secular evolution of the early thin disk.

8. Our evidence suggests that the metal-poor bulge subpopulation might correspond to a classical bulge build out from the dissipative collapse of a primordial cloud in a short timescale. We emphasize that, from the evidence presented in this work, we cannot rule out an eventual thick disk origin of the metal-poor bulge subpopulation. For example, the statistical significance of the difference in the "knee" location reported here, has still to be firmly established.

Much progress have been done in the last decade in our understanding of the Galactic bulge. Not only the complexities of the problem have been recognized, but also many pieces of evidence, previously contradictory, are taking place in a coherent general picture of its origin and evolution. The Gaia-ESO survey is currently providing a valuable opportunity to characterize the bulge stellar populations and set them in the more general context of the Galactic components. Altogether, a composite picture of the Galactic bulge can be unambiguously established, with all the presented evidence pointing to the presence of at least two different subpopulations currently coexisting in the central regions of the Milky Way.

Chapter 7

General conclusions, perspectives and future work

Contents

7.1 General summary and conclusions 155
7.2 Towards solving the puzzle of bulge formation 157
7.3 Future work prospects 160

7.1 General summary and conclusions

In this thesis, we have used data from the Gaia-ESO survey to study the nature of the Galactic bulge and disk system. Our aim was to characterize them from the point of view of their kinematics, metallicity and elemental abundance distributions.

We list here our main conclusions to give a brief global overview of the results obtained in the course of this thesis.

Concerning the disk system:

1. The distribution of disk stars in the metallicity-abundance plane displays a gap which separates and defines two sequences, an α-rich associated with the thick disk and an α-poor associated with the thin disk. These sequences are well separated up to [Fe/H]=-0.1 dex. At larger metallicities, the sequences merge and it becomes more difficult to define a separation between them.

2. A Gaussian mixture models algorithm was successfully used to separate stars in the abundance-metallicity plane in five groups accounting for the main Galactic components: the metal-rich end of the halo, the thick disk, and three subgroups for the thin disk sequence. The same decomposition is obtained while analyzing in the same way a sample of red clump stars from APOGEE.

3. The metal-rich part of the thin disk with [Fe/H]$>$-0.25 dex (as depicted by two of the three thin disk GMM groups) presents a change in the slope in the abundance-metallicity plane at solar metallicity. This holds true for the distribution of RC stars which are sampling mostly the inner Galactocentric radial regions.

4. The metal-poor end of the thin disk with [Fe/H]<-0.25 dex presents a Galactocentric radial distance distribution shifted to larger distances with respect to the more metal-rich thin disk ([Fe/H]>-0.25 dex) and the thick disk. Moreover, it presents indications of a scaleheight intermediate between those of the thick and the more metal rich thin disk, and displays higher mean azimuthal velocity than the latter.

5. These metal-poor thin disk stars might have formed and evolved in parallel and/or dissociated from the inside-out formation taking place in the inner parts of the thin disk. In this context, their α-enhancement levels might be due to their origin from pre-enriched gas by the outflows of the thick disk or the inner halo.

6. The thick disk presents α-enhancement levels compatible with a faster formation timescale compared to that of the thin disk. While studying the distribution of thick disk stars in the abundance-metallicity plane, we found indications for a decrease in the "knee" metallicity with Galactocentric distance, with a difference of Δ[Fe/H] = 0.12 dex between the innermost and outermost distance bins. While there is a clear variation along the successive distance bins, the size of the individual errorbars hampers a definitive assessment on the statistical significance of this variation.

Concerning the bulge:

1. The bulge metallicity distribution function is bimodal over the whole area sampled by the GES fields (11 fields in the area $-10^\circ \leq l \leq +10^\circ$ and $-10^\circ \leq b \leq -4^\circ$). This is assessed both by visual inspection as well as from the results of applying a Gaussian mixture models algorithm on the data.

2. In general terms, the metal-rich component is narrow, with a peak at $\langle$[Fe/H]$\rangle \approx +0.2$ dex. The metal-poor component is broader, with a peak at $\langle$[Fe/H]$\rangle \approx -0.4$ dex. The relative ratio between the two modes of the MDF changes as a function of the latitude, with metal-poor stars dominating at higher latitudes.

3. The metal-rich stars display bar-like kinematics and a bimodality in their RC magnitude distribution, a feature which is tightly associated with the X-shape bulge. They overlap with the metal-rich end of the thin disk sequence in the [Mg/Fe] vs. [Fe/H] plane.

4. The metal-poor stars display isotropic hot kinematics and do not display the double RC feature in their magnitude distribution. Their Mg enhancements are comparable to those of the thick disk sequence. The "knee" of the bulge sequence is located at [Fe/H] $= -0.37 \pm 0.09$ dex, being 0.06 dex higher than that of the thick disk.

5. A chemical evolution model suitably fits the bulge sequence in the abundance-metallicity plane by assuming a fast intense burst of stellar formation, taking place at early epochs

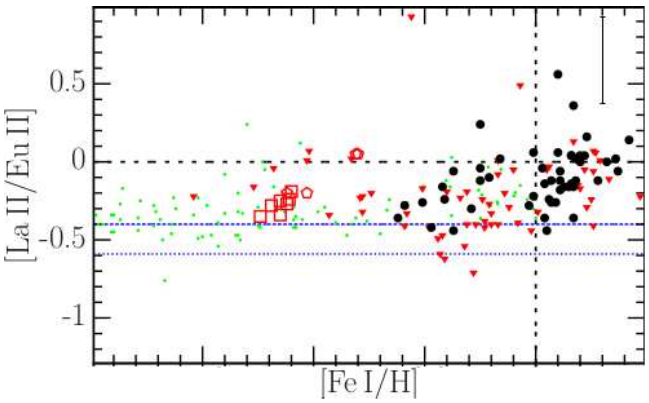


Figure 7.1: [La/Eu] vs. [Fe/H] distributions for several samples compiled from literature: black filled circles red filled triangles and red crosses: bulge stars; red empty squares: M62; red empty pentagons: NGC 6522; green small dots: thick disk. The dotted and dashed blue lines stand for pure r-process values from [Arlandini *et al.* 1999] and [Sneden *et al.* 2008]. Figure reproduced from [Van der Swaelmen *et al.* 2016]

6. Given all these evidences from the GES data, and in agreement with the literature, we associate the metal-rich bulge with the B/P bulge formed by secular bar-driven evolution of the early thin disk.

7. Concerning the origin of the metal-poor bulge, two different scenarios can be proposed based on our observational evidence. On one hand, the bulge MDF and α-enhancement levels are compatible with an early prompt formation in a star burst regime, dominated by massive stars. This might place the bulge as one of the first structures to be assembled in the Milky Way, with exception of the stellar halo, and so might precede the formation epoch of the thick disk. On the other hand, the chemical similarities between bulge and thick disk stars suggest that the bulge could be the product of the secular evolution of the early thick disk. The level at which we are able to resolve the position of the "knee" in the bulge and thick disk sequences, is not enough precise to rule out a comparable SFR and so an eventual parenthood between these structures.

The work conducted in this thesis shaded light over many points concerning the nature and possible origins of the disk and bulge systems. Nevertheless, some issues are left open for future analysis of upcoming GES data releases, or by the acquisition and analysis of tailored datasets.

7.2 Towards solving the puzzle of bulge formation

It is clear from the discussions presented in the previous chapters, and the conclusions drawn above, that up to now, there is not a final word concerning the origin of the metal-poor bulge population. So, what would we need to clearly disentangle its nature and origin?

1. Large spectroscopic surveys, as GES, have the virtue of superseding the limitation given by the individual star measurement uncertainties by providing large samples

to greatly increase number statistics. In this context, it would be desirable to have a sample of disk stars containing a minimum number of objects per Galactocentric radial distance bin all the way down to the inner Galaxy. The convenience of such a sampling is twofold: it would allow us to test for radial variations of the "knee" position of the thick disk sequence in the abundance-metallicity plane, which is fundamental to understand its formation process and evolution. And if such variations are detected, we would be able to compare the inner thick disk with the bulge to establish or discard any parenthood between them.

2. A large sampling of the bulge, including the inner regions which largely affected by dust obscuration, would allow to improve our understanding of the spatial variations of properties of metal-poor and metal-rich populations, as well as providing a firm statistical base to perform the aforementioned comparison with inner thick disk populations.

3. Even with small samples, if we observe bulge and thick disk stars with similar stellar parameters, let's say, just RC stars, and with the same instrumental setup, then we minimize the introduction of systematics due to stellar physics or spectral line formation modeling in the analysis. In this case, we would be in conditions to carefully compare the distribution of bulge and disk stars in the abundance-metallicity plane, looking for the eventually slight differences imprinted by similar but unrelated formation processes. Moreover, this would allow to test whether the abundance dispersion of different elements at a given metallicity is larger in the bulge than in the thick disk. A lack of scatter in the observed sequences in the abundance-metallicity plane would indicate a formation with no IMF variations and good mixing. A statistically significant difference in this property would therefore provide important constraints on the specific processes responsible for the formation of both structures.

4. In the same vein, if accurate determinations of the SFR sensitive r- and s-process element abundances are available for stars with similar stellar parameters, we could use their ratios, such as [La/Eu] or [Ba/Fe] for example, to set a precise chemical clock on the relative speed of stellar formation in the thick disk and bulge populations. In fact, enhancement differences in r- and s-process element abundances have been proposed as evidence of different formation timescales between both structures [Johnson *et al.* 2012b, Van der Swaelmen *et al.* 2016]. To illustrate this point, we display in Fig. 7.1, reproduced from [Van der Swaelmen *et al.* 2016], the distribution of several samples in the [La/Eu] vs. [Fe/H] plane, as compiled from literature. If the formation of a given stellar population is fast, AGB stars will not have time to pollute the ISM, and the stars will be overabundant in r-process elements such as Eu (which are produced mostly during SN II explosions). On the other hand, a rise in the [La/Eu] ratio with metallicity would indicate a formation timescale slow enough to allow s-process elements to pollute the ISM over successive stellar generations. Unfortunately, current efforts in this direction are based on the comparison of bulge giants and local samples, which limits our ability to draw firm conclusions given that the solar neighborhood is

not necessarily representative of the stellar populations in the inner kiloparsecs.

5. Another fundamental ingredient would be given by the availability of individual stellar ages, which can be estimated from distances, fundamental parameters and metallicity. In this context, Gaia is regarded as the cornucopia of Galactic Archaeology as it is expected to provide a large scale census of the stellar content of the Galaxy in a large spatial volume. However, we should be aware that in the case of the bulge, the characteristics of the data to be provided will depart from the nominal performances.

   Indeed, the traditional observational problems while observing towards the bulge, the strong patchy extinction and the severe crowding, normally limits the ability of resolving individually all the sources in a given field with low spatial resolution instruments. Despite its tremendous potential and technical capabilities, Gaia is not exempt of these problems. In fact, the astrometric instrument is designed to cope with object densities up to 750 000 stars/deg^2. Towards the Galactic bulge, and in particular, in low extinction regions, the density of sources down to the Gaia flux limit ($G = 20$) can reach the order of millions of sources per square degree. In such cases, the crowding is larger than the assumed density for the Gaia's on-board processing resources, resulting in a lower completitude, with a performance degradation for faint stars. For example, by simulating the observational completitude in Baade's window (with a surface source density of $3{\cdot}10^6$ stars/deg^2), we can verify that the completitude drops to a 50% percent level at $G = 19$. On the other hand, high extinction alleviates the crowding problem but stars, specially those at the distance of the bulge, can become to faint to be observed.

   The interplay between extinction and star density towards the bulge determines a complex pattern of the regions where distances of stars down to the central kiloparsecs and beyond will be determined. All things considered, the expected Gaia performances in the bulge is to provide distances for $G < 16$, proper motions for $G < 20$, spectrophotometry for $G < 20$ and radial velocities for $G_{\rm RVS} < 16$.

   At $G = 16$, with red clump stars one can reach distances well inside and beyond the bulge at $|b| \gtrsim 4 - 5$. For a $G = 16$ star at 8 kpc, the expected performances are $\sigma_\pi/\pi = 40\%$, $\sigma_\mu = 1$ km s^{-1}, $\sigma_{V_{\rm rad}} = 15$ km s^{-1}.

   Despite the fact that the astrometric precision will be somehow lower for bulge than for disk stars, the tremendous value and scientific impact of the dataset is evident. In particular, distances for targets down to $G = 16$, will allow for studies of the tridimensional structure of the bar and the interface between the bulge, the thick disk and the halo. Moreover, distances can be used together with fundamental parameters and metallicities, whether provided by Gaia itself or obtained from high resolution spectroscopic follow up, to derive ages. The direct comparison of the age distributions of the bulge, the local and inner thin and thick disks, will provide crucial information to reconstruct their star formation histories, and allow to place them in a chronological sequence.

   The availability of precise enough proper motions down to $G = 20$, will provide

a way to separate and characterize disk and bulge stars overlying in the CMDs of bulge fields. The ability of discriminating disk from bulge stars based in their proper motions, will allow for detailed studies of the extinction towards the bulge by comparing the relative distribution of disk and bulge stars in the CMD diagram.

In addition, proper motions will allow to reconstruct the six dimensional phase-space when combined with radial velocities, whether from the RVS or from spectroscopic follow up. Such dataset will allow for dynamical studies of the brightest bulge stars to compare them with the thick disk with the hope of detecting variations at the interface between both structures.

6. Finally, it is of fundamental importance to complement all the observational efforts done in Galactic stellar populations, with an appropriate set of chemical evolution models and N-body simulations, helping us to interpret data, as well as with observations of external galaxies, which provides the necessary comparisons. As described throughout this thesis, these kind of theoretical and observational efforts have proven to constitute a rewarding avenue to pursue the ultimate goal of understanding the history of Milky Way assembling. For example, the composite nature of galaxy bulges, as the one proposed for the Milky Way, has been pointed out by several authors, both as a classical+pseudobulge paradigm [Samland & Gerhard 2003, Athanassoula 2005, Obreja *et al.* 2013, Fiacconi *et al.* 2015]), or as a thin+thick disk system ([Di Matteo *et al.* 2015]). Observations of external galaxies have also provided evidence for classical+pseudobulge structures [Erwin 2008, Gadotti 2009, Nowak *et al.* 2010, Kormendy & Barentine 2010, Williams *et al.* 2011]. as well as for pure disk systems ([Kormendy *et al.* 2010]).

After completion of this thesis, I will take a postdoctoral position at the Instituto de Astrofísica of Pontificia Universidad Católica de Chile (IA-PUC) to keep working on Galactic stellar populations in collaboration with the group of Manuela Zoccali, in turn involved in the VVV and APOGEE-2 teams.

I describe briefly below how I will try to tackle some of the aforementioned observational challenges in the coming years.

7.3 Future work prospects

APOGEE

The second Apache Point Observatory Galactic Evolution Experiment APOGEE-2 (of which M. Zoccali is Co-I member) is a large spectroscopic survey planned as an extension of the APOGEE-1 survey. As presented in Chap. 7, APOGEE-1 targeted $\sim$ 100 000 giant stars in all Galactic components, observing at the Sloan foundation 2.5m telescope at the Apache Point Observatory (APO, New Mexico), and obtaining NIR spectra in the H band ($1.51-1.70\mu m$), with high resolution ($R = 22\,500$) and high SNR (typically ≥ 100). Using dedicated pipelines, stellar parameters $\log(g)$, $T_{\rm eff}$, [Fe/H] and [α/Fe], abundances of 15 chemical species to 0.1 dex precision, and precise radial velocities, have been derived from this high quality data set ([Majewski *et al.* 2015]). Under the

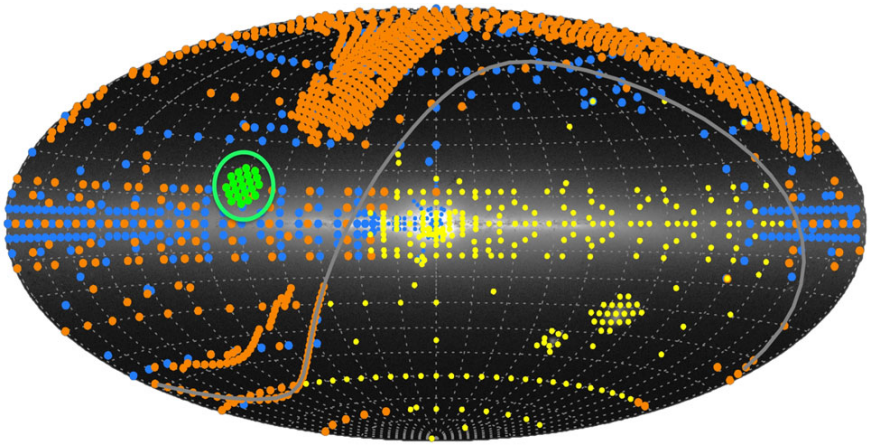


Figure 7.2: APOGEE-2 planned footprint. Green points: Kepler pointings; blue points: APOGEE-1 pointings; orange points: APOGEE-2/north pointings; yellow points: APOGEE-2/south pointings. Figure reproduced from the survey webpage http://www.sdss.org/surveys/apogee-2/.

same philosophy, APOGEE-2 will extend the APOGEE-1 sample size by more than one order of magnitude, and also its sky coverage by including observations from the southern hemisphere. To this end, a twin spectrograph of that at APO will be placed in the du Pont telescope at Las Campanas Observatory, Chili, to start observations in late 2016. A southern sky coverage extension is fundamental, as it will allow to cover the whole bulge area at low airmass. This means that APOGEE-2 will be able not only to further map the disk, but also to probe the bulge region down to the midplane and Galactic center. In fact, as a NIR survey, it can explore all latitudes down to the most extincted central regions of the bulge. This is the first time that such a systematic coverage is done. In Fig. 7.2, we reproduce the planned footprint of the survey.

I will participate in the science exploitation of APOGEE-2 data. Certainly it represents an excellent opportunity to perform exciting research on the bulge and the disk system by applying the lessons learned from the work preformed with the Gaia-ESO survey data. The puzzle of bulge formation has many pieces, and not all of them are currently in their definitive place. We expect that APOGEE-2 will provide means to test important science cases: map the bulge and identify its stellar populations and variations with distance from the plane, explore unexamined regions at the halo/bulge/disk interface to look for population discontinuities between these structures, characterize disk incursions into the bulge region, characterize populations in terms of their detailed kinematic profiles, exploit chemo-kinematical correlations to detect any underlying merger components -which would be a signature of ΛCDM formation- etc. And of course, it will be eventually the source of many serendipitous discoveries. I am particularly interested in using this dataset to attempt unveiling the origin of the metal-poor portion of the bulge. The large spatial coverage, precise radial velocities, and the possibility to explore chemical profiles beyond alpha elements, represents an unique opportunity to find and characterize the stellar populations coexisting at the central kiloparsecs of the Galaxy. The final goal is to establish firm constraints to be incorporated in formation models

aiming to explain the bulge and Galaxy assembling and growth in a consistent global picture, consistent with what we learned from the observation of external galaxies and cosmological theories in general.

It is worth to mention that besides the data coming from the APOGEE-2 Survey, we plan to take advantage of the 10% Chilean reserved time of the APOGEE-2/south spectrograph to perform a customized bulge survey. The regular APOGEE survey imposes constraints on the exposure time and the general observation strategy that are an appropriate compromise to attain the different science cases of the survey. In the case of the bulge, these specifications translate into an observed sample composed mainly by bright red giant stars. By performing a customized bulge survey, we can focus in some particular science cases, such as the determination of metallicity, chemical abundances and kinematics of the bar at the inner degrees to be compared with the general trends at the well sampled regions far from the plane.

Gaia ESO survey

From my work inside the Gaia-ESO Survey, both in the data product generation and quality control, as in the scientific exploitation, I gained experience on large survey spectroscopic data mining. Moreover, as Co-I of this collaboration, I have both, access to the data and a thorough understanding of its creation, contents, strengths and shortcomings. As for the iDR4, I will be involved in the generation of the iDR5 (planned for late 2016) recommended set of fundamental parameters, metallicity and detailed chemical abundances from my work inside the WG10. As an incremental data release, the fifth internal data release will provide larger data sets, both for the bulge and the disk, than those we use in the course of this thesis. In the case of the disk, this larger dataset might allow us to conduct a detailed study on the radial variations of the thick disk high-α sequence, in particular on the possible variations of the metallicity position of the "knee". As we discussed before, such a variation would challenge the thick disk formation as a turbulent process producing stars from a well mixed initial gas disk.

In the case of the bulge, the iDR5 will provide observations in 23 fields[1], twice as those available up to the iDR4. Our quest for a detailed characterization of the stellar populations sitting in the bulge, will greatly benefit from the analysis of this rich dataset. A thorough comparison of the bulge and disk stars will be attempted on the basis of the detailed comparative analysis of the whole set of available detailed abundances (Mg, Si, Ca, Ti and Al).

The APOGEE (1 and 2) and the Gaia-ESO Survey share similar objectives and observational approaches. It is important to take advantage of their complementary nature, so we can fully profit of the synergy between both datasets.

[1]Following our usual field notation, the fields are: p1m4, m0m7, m10m8, m1m10, m1m8, m4m5, m6m6, m7m7, p0m5, p0m6, p0m8, p0m9, p2m9, p3m3, p3m4, p3m5, p3m6, p3m7, p5m6, p6m9, p7m6, p7m9 and p8m6

Gaia

Needless to mention at this point the enormous relevance of the results that Gaia will start providing from its first data release, planned for September 14 2016, onwards. With the availability of accurate distances and proper motions for a disk sample as that analyzed in this thesis, we will be able to tackle several issues which still remains observationally unconstrained. We can use the positional and velocity information to integrate orbits and compare the orbital parameter distributions of metal-poor thin disk stars with respect to their more metal-rich counterparts and with the thick disk. In this way, we might be able to perform a comparison similar to that presented in Fig. 4.7, but using the computed guiding radius. This analysis might help to better understand the nature of these seemingly outer disk stars, and to put constraints on the amount of radial migration allowed by the data.

From my work with GES data, I developed tools allowing for the determination of spectro-photometric distances. In the same way, my future work with Gaia in combination with GES and APOGEE data, will provide the context and the opportunity to work on the problem of determining ages. As commented above, ages are a fundamental ingredient to reconstruct the temporal sequence of events involved in the Milky Way formation. I will exploit this opportunity by constructing appropriate analysis tools.

In the case of the bulge, by mid 2017, Gaia will provide (starting from the DR2) groundbreaking astrometric data we can use to fruitfully complement the spectroscopic campaigns. At that point, the final bulge dataset from the Gaia-ESO survey will be available, ensuring a timely analysis exploiting its full potential as combined with the astrometric data.

MOONS

It is worth to mention that towards 2018-2019, it will take place the first light of the MOONS spectrograph. This is a third generation instrument for the VLT which is expected to greatly contribute to the field of Galactic archaeology. The general characteristics of the spectroscopic data (resolution, observed spectral region, as described in Chap. 7) to be produced with this instrument, are quite comparable with those of APOGEE. In this sense, our work with APOGEE will tailor our experience to analyze MOONS data. Importantly, my postdoc host institution (IA-PUC) is part of the consortium in charge of its construction. To take advantage of this opportunity, I expect to contribute in the definition of the science cases to be tackled during the instrument GTO, and in using the data to complement the science done with APOGEE-2 and the Gaia-ESO Survey.

VVV and VVVX

Last, but not least, I have been involved in the VVV survey, and I am part of the proposal for its extension, the VVVX. I expect to devote part of my research time in the data quality control, and the analysis of light curves. In a broad sense, this science is a very important complement of bulge studies, because it enables us to use the standard candle nature of some variable stars as probes for the spatial structure of bulge stellar

populations. In particular, we can try to extend studies using RR Lyrae as tracers of the metal-poor old stellar populations in the bulge, and use Cepheids as tracers for the metal-rich young portion.

In addition, proper motions will be available for the entire bulge region, allowing for the kinematic analysis of cleaned bulge samples. Up to the third data release, VVV source catalogs provide aperture photometry. Instead, in the DR4, psf-photometry is expected to be provided. This is relevant for us since psf-photometry performs better than aperture photometry in crowded fields as those in the bulge. By combining VVV psf-photometry and VVV proper motions, we might then be in condition to perform detailed CMD-based studies on the properties of stellar populations, bulge and disk, overlying in the field CMDs. Such kind of studies will harmoniously complement the efforts of characterizing the central Galactic regions by means of chemistry and kinematics, as provided by spectroscopic data.

Models and simulations

This thesis represents an observational approach to the Galactic bulge. Nevertheless, we cannot miss the fruitful synergy which is possible to obtain from the interplay of models predicting observations and observations constraining models. In my future work with GES and APOGEE, I will pursue for such interactions. The detailed chemical information provided by both surveys, represents an interesting opportunity to interpret chemical abundance patterns of different stellar populations in terms of chemical evolution models. In this thesis, we used the chemical evolution of [Grieco *et al.* 2012] to interpret the trend of metal-poor bulge stars in the abundance-metallicity plane. We will continue this kind of analysis with the group of F. Matteucci to fully exploit the wealth of data for several chemical species provided by GES and APOGEE.

On the other hand, the complex kinematics of bulge populations and the correlations with metallicity, represents an interesting opportunity to compare with N-body model predictions. For example, it would be extremely interesting to compare observed kinematics as a function of metallicity with the predictions of models advocating for a thick disk origin of the bulge ([Di Matteo *et al.* 2015]), as well as with other theoretical alternatives (single disk or a merger origin). The steadily increasing number of bulge stars with high resolution spectroscopy are a valuable resource to test in detail the ability of different models on predicting their complex chemo-kinematic relations.

The previous discussion is intended to provide a foresight view of the research I am planning to conduct in the coming years. Of course, deviations from this are expected as the product of serendipitous discoveries, as well as from the increasing understanding we expect to grasp from the analysis of all these datasets. Indeed, exciting times for exploring and (re)discovering the nature, origin and evolution of our host Galaxy are coming.

Appendix A

Comparison of iDR1 and iDR4 fundamental parameters

As presented in Chap. 2, the Gaia-ESO survey produces incremental data releases. In each one a new determination of fundamental parameters and abundances is produced homogeneously for the whole data set. The study of the bulge has been carried on in this thesis on the basis of the first and fourth internal data releases. Here, we present a short comparison between the fundamental parameters produced in both of them.

We briefly recall here how parameters were determined in each data release. The recommended parameters $T_{\rm eff}$, $\log(g)$ and global metallicity [M/H] in the first internal data release were determined with the MATISSE algorithm [Recio-Blanco *et al.* 2006]. No other methods were applied to the data. To correct the derived atmospheric parameters from possible bias, and set the zero point of the metallicity scale, we used in [Rojas-Arriagada *et al.* 2014] a set of benchmark stars selected by the GES consortium [Jofré *et al.* 2015]. We constructed relations between the nominal atmospheric values for the benchmark stars versus those estimated with MATISSE in the same way as for the bulge sample stars. The obtained relations enabled us to move our original parameters onto the benchmark scale. The calibration fits are displayed in Fig. A.1, with the respective relations given as follows:

$$T_{eff\ calib} = 1.269 \cdot T_{eff\ MATISSE} - 1301.17$$

$$\log(g)_{calib} = 1.22 \cdot \log(g)_{MATISSE} - 0.959$$

$$[M/H]_{calib} = 0.862 \cdot [M/H]_{MATISSE} - 0.036$$

Instead, in the iDR4, an homogenization of the results from three independent procedures (see Chap. 2) was carried on to produce the recommended fundamental parameters and elemental abundances for several species, including the Fe and Mg used in this thesis.

We limit here our analysis to the set of stars observed up to the first internal data release. This selection includes stars in the p1m4, p0m6, p7m9, m1m10 and m10m8 bulge fields (orange symbols in Fig. 5.1). Figure A.2 display the HR diagram of this sample as seen from iDR1 (left) and iDR4 (right) fundamental parameters. The color scale accounts for metallicity, [M/H] for iDR1 and [Fe/H] in the case of the iDR4. We can see that in general, both parametrization display the main HR features, the main-sequence, the turn-off, the RGB, and in particular, the RC.

From the left panel, the iDR1 seems to suffer of a certain degree of error correlations between $T_{\rm eff}$ and $\log(g)$. In the whole sample distribution, this introduces some degeneracy of parameters along the RGB, distorting the shape of the RC and blurring

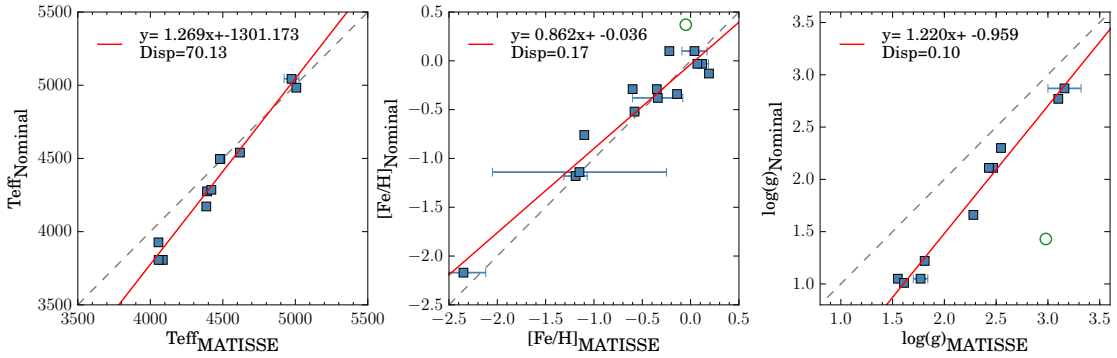


Figure A.1: Calibration of iDR1 parameters respect to the benchmark sample. Fundamental parameters obtained for a sample of benchmark stars with MATISSE are compared with their values as provided by [Jofré *et al.* 2015]. After sigma clipping offset points (green open circles), linear relations were computed. They allow to transform parameters from the MATISSE scale onto the one of the benchmarks. The coefficients of the fit as well as the dispersion of data round the trend are quoted in each panel.

its qualitatively expected metallicity distribution. The multi-pipeline analysis implemented in the iDR4 is able to tackle at a good degree these problems. As it can be seen in the right panel the shape of the main-sequence (its slope) and the RC (its roundness and metallicity structure) are better defined respect to the iDR1.

A more detailed comparison between both data releases is displayed in Fig. A.3. The fundamental parameters, as derived in each instance, are compared each other. In the three cases a general reasonable agreement is visible. For $T_{\rm eff}$ and [M/H] the biases are small, well inside the typical spectroscopic errors. Instead, the dispersion is relatively large in both cases. For $\log(g)$ the situation is less neat. The bulk of RC stars are over the 1:1, but a number of stars clumps in an offset position. Moreover, the dwarfs appear with a systematical shift, with iDR4 parameters being larger.

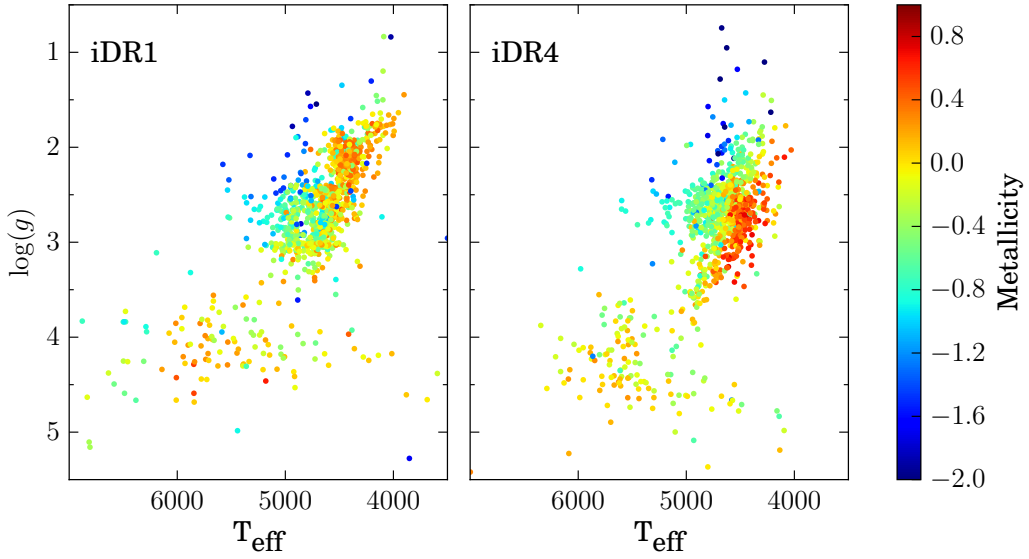


Figure A.2: HR diagram of stars present in iDR1 and iDR4 samples. Left and right panels display the distribution of stars according to the parameters provided in the first and fourth internal data releases, respectively. In both cases the samples are limited to the stars observed in the iDR1 (c.f. Fig. 5.1). Color points are color coded according to their respective metallicity [M/H] in the case of the iDR1 and [Fe/H] for the iDR4.

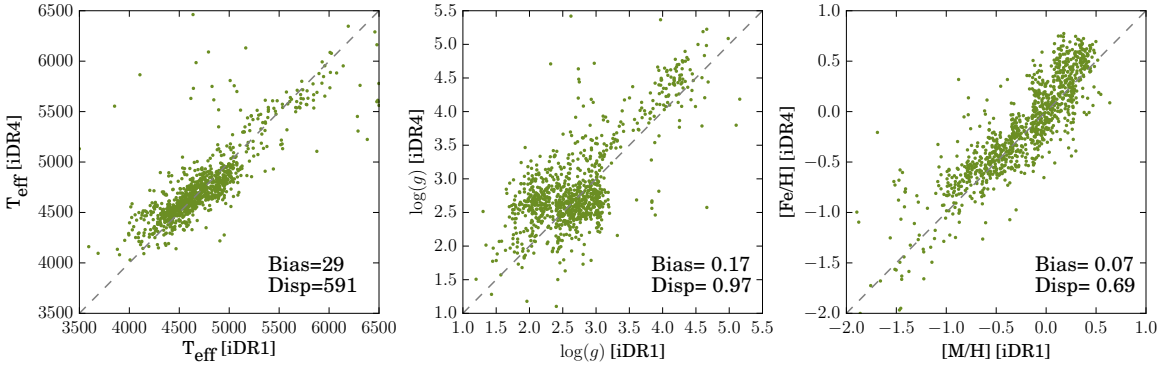


Figure A.3: Explicit comparison of fundamental parameters $T_{\rm eff}$, $\log(g)$ and metallicity of stars observed in first and fourth internal data releases. A dashed gray line depicted the 1:1 relation. The bias and dispersion are quoted in each panel.

Appendix B

The bulge comparison sample

As described in Chap. 2 and 5, together with the main sample of RC bulge stars selected with the GES photometric selection function, a comparison sample in Baade's window was taken from the literature. In particular, a subset of the RC stars published in [Hill *et al.* 2011], and a subset of the RBG ones published in [Zoccali *et al.* 2008], were reobserved with the same instrumental setup, and analyzed in the same Way as the rest of the GES targets. The idea is to perform an a posteriori comparison to verify the consistence of parameters, in particular metallicity, derived and recommended by the GES consortium. We focus here in the metallicity estimations.

In the upper panels of Fig. B.1 we compare the metallicity values published in [Hill *et al.* 2011] with respect to those coming from the iDR1 (left panel) and iDR4 (right panel). The original sample in [Hill *et al.* 2011] is of $\sim$ 220 RC stars. The stars with available parameters from GES constitute a small subset of 105 and 94 stars from the iDR1 and the iDR4, respectively. In both cases, the dispersion is relatively high, larger than typical spectroscopic errors. On the other hand, the bias is larger for the iDR1 than for the iDR4, being the latter smaller than typical spectroscopic errors.

In the lower panel of Fig. B.1 we compare the metallicity derived in iDR4 with those published in [Zoccali *et al.* 2008]. The original Baade's window sample of [Zoccali *et al.* 2008] is of $\sim$ 200 K-giant stars observed at $\sim$ 1 mag over the RC. None of them was observed up to the iDR1, and just 39 are available from the iDR4. The comparison between iDR4 and [Zoccali *et al.* 2008] metallicities shows a relative good agreement, with a small mean bias and a reasonable dispersion respect to typical spectroscopic errors.

This brief analysis shows that metallicity values derived by the GES consortium are robust and comparable with at least two independent studies of bulge stellar populations based in high resolution spectroscopy.

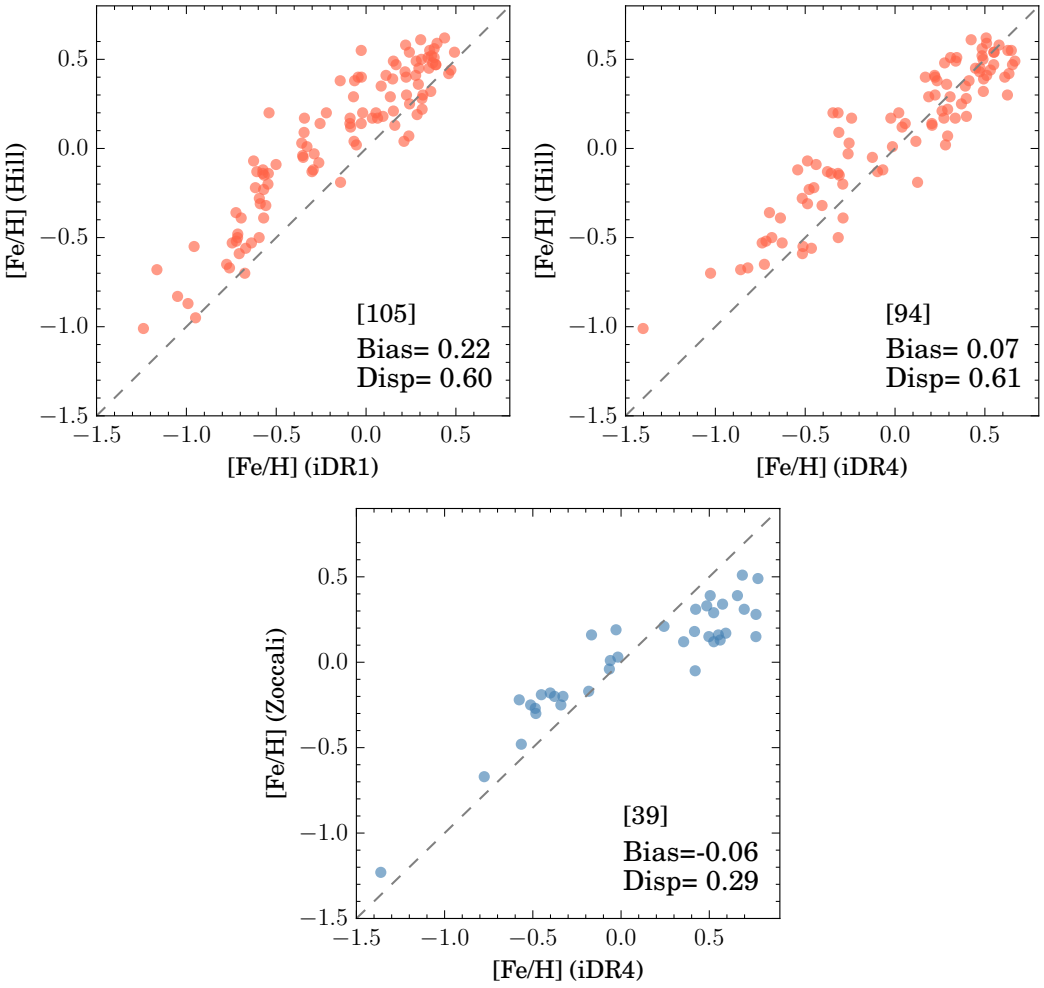


Figure B.1: Comparison of metallicity determinations from GES and literature for the bulge comparison sample. *Upper panels:* comparison of iDR1 left and iDR4 right values respect to those published in [Hill *et al.* 2011], *Lower panel:* comparison of iDR4 values respect to those published in [Zoccali *et al.* 2008]. In each case, the number of stars used for the comparison is quoted in square brackets.

Appendix C

Mathematical bits

C.1 Covariance Matrix

The covariance matrix is a matrix whose (i, j) element gives the covariance between the i an j components of a random vector. In fact, it is an object containing all the information needed to characterize the dependence between two random variables (RV). We describe here the covariance matrix for 2D dependent and correlated data.
The variance of a RV is a measure of the deviation from the mean for a random variable. It corresponds to the expected average of the squared deviation from its mean

$$Var(z) = E[(z - E[z])(z - E[z])] = \sum_{i=1}^{n} \frac{(z_i - \bar{z})^2}{(n-1)} = \sigma^2,$$

where the second expression is the corresponding *sample estimator*.
The covariance of two random variables is a measure of how much they change together. It corresponds to the expected average of the product of their deviations from their respective means

$$Cov(x, y) = E[(x - E[x])(y - E[y])] = \sum_{i=1}^{n} \frac{(x_i - \bar{x})(y_i - \bar{y})}{(n-1)},$$

where $E[a]$ is the expectation value of the random variable a. Again the second expression is the sampling estimator.
This is a generalization of the concept of variance. It is clear that

$$Cov(x, x) = Var(x)$$

As the name says, $Cov(x, y)$ is a measure of the lineal "co-variation" of the two random variables x and y. In particular:

- $Cov(x, y) > 0$: If x increases, y increases also.
- $Cov(x, y) < 0$: If x increases, y decreases.
- $Cov(x, y) = 0$: If x increases, $y$does not change. Bot random variables are *uncorrelated*.

Where the actual values are difficult to interpret. A more convenient way to express is in its standardized form

$$r = \frac{Cov(x, y)}{\sqrt{Var(x) \cdot Var(y)}}$$

called the Pearson's correlation of x and y. It takes values in the range [-1,1].

With those elements we can define the covariance matrix as

$$\Sigma_{x,y} = \begin{bmatrix} Var(x) & Cov(x,y) \\ Cov(y,x) & Var(y) \end{bmatrix} \tag{C.1}$$

where $Cov(x,y) = Cov(y,x)$. For N-dimensional data, the covariance matrix is a NxN matrix. The covariance matrix defines the shape of the data; the diagonal spread is captured by the covariance, while the axis spread by the variances. As a object giving a generalization of the notion of variance, if we want to know the variance V_u of the projection of the whole data distribution with covariance matrix Σ on the unit vector $\vec{u}$ we need to compute:

$$V_u = \vec{u}^T \Sigma \vec{u}$$

In fact, we can think the covariance matrix as storing all possible projection variances in all directions.

Geometrical interpretation: The covariance matrix can be decomposed into transformation matrices. The leftmost panel of Figure C.1 displays a sample of white data, i.e. data from a normal distribution of non-correlated random variables. The other panels show that other bivariate distributions can be seen as the result of rotation and scaling operations applied to the original white data. In particular, it can be proved that the covariance matrix can be decomposed in a scaling

$$\Sigma = \begin{bmatrix} Var(x) & 0 \\ 0 & Var(y) \end{bmatrix} \tag{C.2}$$

and rotation matrix

$$\Sigma = \begin{bmatrix} \cos(\phi) & -\sin(\phi) \\ \sin(\phi) & \cos(\phi) \end{bmatrix} \tag{C.3}$$

where ϕ is the angle of the tilted distribution. Then the correlation matrix can be write down as

$$\Sigma = R \Sigma R^T.$$

Another interpretation arises by considering the rightmost panel of Figure C.1. The eigenvectors of a given matrix represents the directions in which the variance of the data is maximized. The variance given by the square of the corresponding eigenvalues. In figure C.1, the eigenvectors $\vec{e}_i$ are represented by red arrows with their size indicating the standard deviation $\sigma_i = \lambda_i$. From the covariance matrix Σ_c it is possible to construct a transformation matrix mapping a white distribution into one with the same covariance matrix. To do this, one can define a rotation matrix

$$R_t = \begin{bmatrix} \vec{e_1}_x & \vec{e_2}_x \\ \vec{e_1}_y & \vec{e_2}_y \end{bmatrix} \tag{C.4}$$

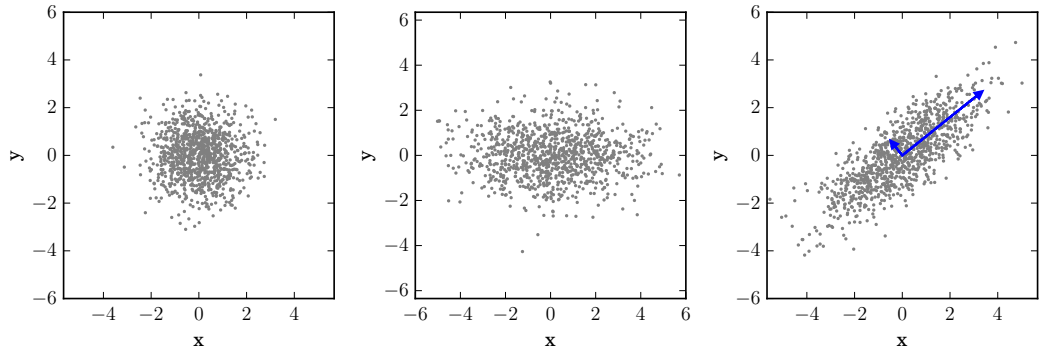


Figure C.1: Bivariate distributions. From left to right: white noise of non correlated normal distributed data. Uncorrelated data with the dispersion in the x axis scaled by 2. Positive correlated data

with the columns given by the eigenvectors of Σ_c, and a scaling matrix

$$S_t = \begin{bmatrix} \sqrt{\lambda_1} & 0 \\ 0 & \sqrt{\lambda_2} \end{bmatrix} \tag{C.5}$$

given by the square root of the corresponding eigenvalues. Then, the transformation matrix corresponds to

$$T_{RS} = R_t S_t.$$

C.2 Bivariate normal distribution

The bivariate normal distribution is a statistical distribution with joint probability density function of the random variables x and y given by

$$f(x,y) = \frac{1}{2\pi\sigma_x\sigma_y\sqrt{1-\rho^2}} \exp\left[-\frac{q(x,y)}{2}\right],$$

with

$$q(x,y) = \left(\frac{1}{1-\rho^2}\right)\left[\left(\frac{x-\mu_x}{\sigma_x}\right)^2 - 2\rho\left(\frac{x-\mu_x}{\sigma_x}\right)\left(\frac{y-\mu_y}{\sigma_y}\right) + \left(\frac{y-\mu_y}{\sigma_y}\right)^2\right].$$

Here μ_x and μ_y give the center of the distribution, σ_x and σ_y the standard deviation of the data in the x and y direction. the factor ρ is called the correlation between the random variables and can be expressed as

$$\rho = \frac{Cov(xy)}{\sigma_x\sigma_y}$$

where $Cov(x,y)$ is the covariace between x and y.
The region R defined by the valid ranges of the random variables x and y is a plane

called the support of the pdf. The joint probability function should be

$$\int \int_R f(x,y)dxdy = 1$$

If the correlation is zero ($\rho = 0$), the random variables are independent and the joint pdf can be factorized in the normal pdf of x and the normal pdf of y

$$f(x,y) = f_x(x)f_y(y).$$

The marginal probabilities are defined as

$$P(x) = \int_{-\infty}^{\infty} f(x,y)dy = \frac{1}{\sqrt{2\pi}\sigma_x} e^{-(x-\mu_x)^2/(2\sigma_x^2)}$$

and

$$P(y) = \int_{-\infty}^{\infty} f(x,y)dx = \frac{1}{\sqrt{2\pi}\sigma_y} e^{-(y-\mu_y)^2/(2\sigma_y^2)}$$

C.3 Anderson-Darling test

This statistic is a modification of the Kolmogorov-Smirnov test. It is used to test if a sample data comes from a population with an specific distribution. In the particular case of the distributions in Fig. 4.1, were we used, the null hypothesis H_0 is that the data comes from a normal distribution with unknown mean and variance.

C.4 p-values

A p-value is defined in frequentist statistics as the probability of obtaining a result from a statistic test (for example a two sample Kolmogorov-Smirnov test) at least as extreme (i.e. more improbable) or as close to the one observed assuming that the null hypothesis H_0 is true. In turn, the null hypothesis, is a statistical hypothesis that is tested for possible rejection under the assumption that is true. It represents observations arising by chance. We reject H_0 when the p-value is lower than a predetermined significance level, often 0.05. Then, the observed result is highly unlikely under H_0.

In Fig. C.2, the concept is illustrated. The solid black line represents the probability density of all the possible outcomes of the statistic test computed under the null hypothesis. The observed result is depicted with a black dot. The p-value correspond to the area which includes all the possible results that are more unlikely (or at least as improbable as the observed one) to be obtained than the observed result.

C.5 Student t-test

The t-student test can be used when the test statistic follows a t-student distribution. In a nutshell, a Student t-distribution is the distribution of the location of the population mean relative to the sample mean when considering a sample drawn from a normally

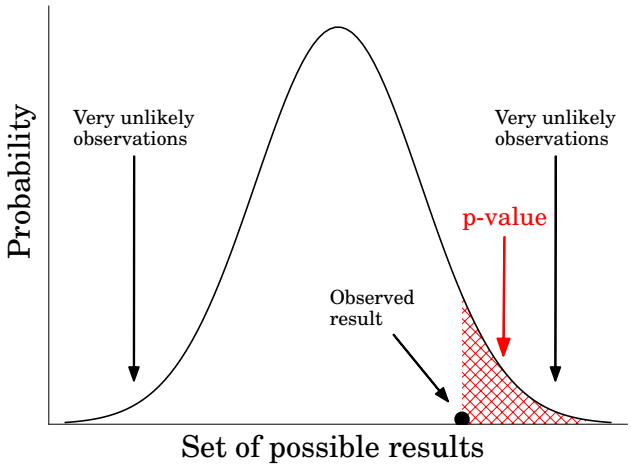


Figure C.2: Illustration of the p-value of an observed sample result. The vertical axis is the probability density of each possible outcome of the statistic test computed under the null hypothesis H_0. The $p-$value corresponds to the shaded area under the curve from the observed result towards more "extreme" results.

distributed population in situations where the sample is small and the population standard deviation is unknown. The t-distribution has a probability density function given by

$$p(t) = \frac{\Gamma\left(\frac{\nu+1}{2}\right)}{\sqrt{\nu\pi}\Gamma\left(\frac{\nu}{2}\right)}\left(1+\frac{t^2}{\nu}\right)^{-\frac{\nu+1}{2}},$$

with ν being the degrees of freedom and Γ the gamma function. The t-student distribution is different for each sample size. In the limit where the sample size is of infinite size we retrieve the normal distribution

$$p(t) = \frac{1}{\sqrt{2\pi}}e^{\frac{-t^2}{2}}.$$

The Student t-test can be used to determine if two datasets are significantly different from each other, or to assess the statistical significance of the difference between two sample means.

Bibliography

[Abadi *et al.* 2003] M. G. Abadi, J. F. Navarro, M. Steinmetz and V. R. Eke. *Simulations of Galaxy Formation in a Λ Cold Dark Matter Universe. II. The Fine Structure of Simulated Galactic Disks.* ApJ, vol. 597, pages 21–34, November 2003. (Cited en pages 7 et 15.)

[Adibekyan *et al.* 2012] V. Z. Adibekyan, S. G. Sousa, N. C. Santos, E. Delgado Mena, J. I. González Hernández, G. Israelian, M. Mayor and G. Khachatryan. *Chemical abundances of 1111 FGK stars from the HARPS GTO planet search program. Galactic stellar populations and planets.* A&A, vol. 545, page A32, September 2012. (Cited en page 75.)

[Adibekyan *et al.* 2013] V. Z. Adibekyan, P. Figueira, N. C. Santos, A. A. Hakobyan, S. G. Sousa, G. Pace, E. Delgado Mena, A. C. Robin, G. Israelian and J. I. González Hernández. *Kinematics and chemical properties of the Galactic stellar populations. The HARPS FGK dwarfs sample.* A&A, vol. 554, page A44, June 2013. (Cited en pages v, 31, 32, 33, 75, 76, 95 et 146.)

[Allende Prieto *et al.* 2006] C. Allende Prieto, T. C. Beers, R. Wilhelm, H. J. Newberg, C. M. Rockosi, B. Yanny and Y. S. Lee. *A Spectroscopic Study of the Ancient Milky Way: F- and G-Type Stars in the Third Data Release of the Sloan Digital Sky Survey.* ApJ, vol. 636, pages 804–820, January 2006. (Cited en page 55.)

[Alves-Brito *et al.* 2010] A. Alves-Brito, J. Meléndez, M. Asplund, I. Ramírez and D. Yong. *Chemical similarities between Galactic bulge and local thick disk red giants: O, Na, Mg, Al, Si, Ca, and Ti.* A&A, vol. 513, page A35, April 2010. (Cited en pages 24, 127, 146 et 151.)

[Alves 2000] D. R. Alves. *K-Band Calibration of the Red Clump Luminosity.* ApJ, vol. 539, pages 732–741, August 2000. (Cited en pages 20 et 125.)

[Anders *et al.* 2014] F. Anders, C. Chiappini, B. X. Santiago, H. J. Rocha-Pinto, L. Girardi, L. N. da Costa, M. A. G. Maia, M. Steinmetz, I. Minchev, M. Schultheis, C. Boeche, A. Miglio, J. Montalbán, D. P. Schneider, T. C. Beers, K. Cunha, C. Allende Prieto, E. Balbinot, D. Bizyaev, D. E. Brauer, J. Brinkmann, P. M. Frinchaboy, A. E. García Pérez, M. R. Hayden, F. R. Hearty, J. Holtzman, J. A. Johnson, K. Kinemuchi, S. R. Majewski, E. Malanushenko, V. Malanushenko, D. L. Nidever, R. W. O'Connell, K. Pan, A. C. Robin, R. P. Schiavon, M. Shetrone, M. F. Skrutskie, V. V. Smith, K. Stassun and G. Zasowski. *Chemodynamics of the Milky Way. I. The first year of APOGEE data.* A&A, vol. 564, page A115, April 2014. (Cited en pages 32, 98, 100 et 108.)

[Arlandini *et al.* 1999] C. Arlandini, F. Käppeler, K. Wisshak, R. Gallino, M. Lugaro, M. Busso and O. Straniero. *Neutron Capture in Low-Mass Asymptotic Giant Branch Stars: Cross Sections and Abundance Signatures.* ApJ, vol. 525, pages 886–900, November 1999. (Cited en page 157.)

[Arp 1965] H. Arp. *Properties of the Galactic Nucleus in the Direction of NGC 6522.* ApJ, vol. 141, page 43, January 1965. (Cited en page 17.)

[Athanassoula 2005] E. Athanassoula. *On the nature of bulges in general and of box/peanut bulges in particular: input from N -body simulations.* MNRAS, vol. 358, no. 4, pages 1477–1488, April 2005. (Cited en pages 16, 22 et 160.)

[Audouze & Tinsley 1976] J. Audouze and B. M. Tinsley. *Chemical evolution of galaxies.* ARA&A, vol. 14, pages 43–79, 1976. (Cited en page 12.)

[Baade 1951] W. Baade. *Galaxies - Present Day Problems.* Publications of Michigan Observatory, vol. 10, page 7, 1951. (Cited en pages 17 et 26.)

[Bailer-Jones *et al.* 2013] C. A. L. Bailer-Jones, R. Andrae, B. Arcay, T. Astraatmadja, I. Bellas-Velidis, A. Berihuete, A. Bijaoui, C. Carrión, C. Dafonte, Y. Damerdji, A. Dapergolas, P. de Laverny, L. Delchambre, P. Drazinos, R. Drimmel, Y. Frémat, D. Fustes, M. García-Torres, C. Guédé, U. Heiter, A.-M. Janotto, A. Karampelas, D.-W. Kim, J. Knude, I. Kolka, E. Kontizas, M. Kontizas, A. J. Korn, A. C. Lanzafame, Y. Lebreton, H. Lindstrøm, C. Liu, E. Livanou, A. Lobel, M. Manteiga, C. Martayan, C. Ordenovic, B. Pichon, A. Recio-Blanco, B. Rocca-Volmerange, L. M. Sarro, K. Smith, R. Sordo, C. Soubiran, J. Surdej, F. Thévenin, P. Tsalmantza, A. Vallenari and J. Zorec. *The Gaia astrophysical parameters inference system (Apsis). Pre-launch description.* A&A, vol. 559, page A74, November 2013. (Cited en page 36.)

[Barbuy *et al.* 2006] B. Barbuy, M. Zoccali, S. Ortolani, Y. Momany, D. Minniti, V. Hill, A. Renzini, R. M. Rich, E. Bica, L. Pasquini and R. K. S. Yadav. *VLT-UVES analysis of two giants in the bulge metal-poor globular cluster HP-1. Analysis of two giants in HP-1.* A&A, vol. 449, pages 349–358, April 2006. (Cited en page 29.)

[Barbuy *et al.* 2007] B. Barbuy, M. Zoccali, S. Ortolani, D. Minniti, V. Hill, A. Renzini, E. Bica and A. Gómez. *NGC 6558: A Blue Horizontal Branch Moderately Metal-Poor Globular Cluster in the Bulge.* AJ, vol. 134, page 1613, October 2007. (Cited en page 29.)

[Barbuy *et al.* 2009] B. Barbuy, M. Zoccali, S. Ortolani, V. Hill, D. Minniti, E. Bica, A. Renzini and A. Gómez. *VLT-FLAMES analysis of 8 giants in the bulge metal-poor globular cluster NGC 6522: oldest cluster in the Galaxy?. Analysis of 8 giants in NGC 6522.* A&A, vol. 507, pages 405–415, November 2009. (Cited en page 29.)

[Barnes 1988] J. E. Barnes. *Encounters of disk/halo galaxies.* ApJ, vol. 331, pages 699–717, August 1988. (Cited en page 15.)

[Beaulieu *et al.* 2000] S. F. Beaulieu, K. C. Freeman, A. J. Kalnajs, P. Saha and H. Zhao. *Dynamics of the Galactic Bulge Using Planetary Nebulae.* AJ, vol. 120, pages 855–871, August 2000. (Cited en page 22.)

[Bekki & Tsujimoto 2011] K. Bekki and T. Tsujimoto. *Formation of the Galactic bulge from a two-component stellar disc: explaining cylindrical rotation and a vertical metallicity gradient.* MNRAS, vol. 416, pages L60–L64, September 2011. (Cited en pages 19 et 142.)

[Bensby *et al.* 2003] T. Bensby, S. Feltzing and I. Lundström. *Elemental abundance trends in the Galactic thin and thick disks as traced by nearby F and G dwarf stars.* A&A, vol. 410, pages 527–551, November 2003. (Cited en page 32.)

[Bensby *et al.* 2004] T. Bensby, S. Feltzing and I. Lundström. *Oxygen trends in the Galactic thin and thick disks.* A&A, vol. 415, pages 155–170, February 2004. (Cited en page 25.)

[Bensby *et al.* 2005] T. Bensby, S. Feltzing, I. Lundström and I. Ilyin. *α-, r-, and s-process element trends in the Galactic thin and thick disks.* A&A, vol. 433, pages 185–203, April 2005. (Cited en page 25.)

[Bensby *et al.* 2013] T. Bensby, J. C. Yee, S. Feltzing, J. A. Johnson, A. Gould, J. G. Cohen, M. Asplund, J. Meléndez, S. Lucatello, C. Han, I. Thompson, A. Gal-Yam, A. Udalski, D. P. Bennett, I. A. Bond, W. Kohei, T. Sumi, D. Suzuki, K. Suzuki, S. Takino, P. Tristram, N. Yamai and A. Yonehara. *Chemical evolution of the Galactic bulge as traced by microlensed dwarf and subgiant stars. V. Evidence for a wide age distribution and a complex MDF.* A&A, vol. 549, page A147, January 2013. (Cited en pages v, 24, 25, 30, 119, 127, 139, 140, 142 et 146.)

[Bensby *et al.* 2014] T. Bensby, S. Feltzing and M. S. Oey. *Exploring the Milky Way stellar disk. A detailed elemental abundance study of 714 F and G dwarf stars in the solar neighbourhood.* A&A, vol. 562, page A71, February 2014. (Cited en pages 24, 25, 30, 31, 76 et 77.)

[Bland-Hawthorn & Gerhard 2016] J. Bland-Hawthorn and O. Gerhard. *The Galaxy in Context: Structural, Kinematic and Integrated Properties.* ArXiv e-prints, February 2016. (Cited en pages 8 et 9.)

[Blitz & Spergel 1991] L. Blitz and D. N. Spergel. *Direct evidence for a bar at the Galactic center.* ApJ, vol. 379, pages 631–638, October 1991. (Cited en page 21.)

[Blommaert & Groenewegen 2007] J. A. D. L. Blommaert and M. A. T. Groenewegen. *The Galactic Bulge Mira Population.* In A. Vallenari, R. Tantalo, L. Portinari and A. Moretti, editeurs, From Stars to Galaxies: Building the Pieces to Build Up the Universe, volume 374 of *Astronomical Society of the Pacific Conference Series*, page 193, December 2007. (Cited en page 29.)

[Bournaud & Combes 2002] F. Bournaud and F. Combes. *Gas accretion on spiral galaxies: Bar formation and renewal.* A&A, vol. 392, pages 83–102, September 2002. (Cited en page 16.)

[Bournaud *et al.* 2005] F. Bournaud, F. Combes and B. Semelin. *The lifetime of galactic bars: central mass concentrations and gravity torques.* MNRAS, vol. 364, pages L18–L22, November 2005. (Cited en page 16.)

[Bovy *et al.* 2012] J. Bovy, H.-W. Rix, C. Liu, D. W. Hogg, T. C. Beers and Y. S. Lee. *The Spatial Structure of Mono-abundance Sub-populations of the Milky Way Disk.* ApJ, vol. 753, page 148, July 2012. (Cited en pages 31, 98 et 100.)

[Bovy *et al.* 2014] J. Bovy, D. L. Nidever, H.-W. Rix, L. Girardi, G. Zasowski, S. D. Chojnowski, J. Holtzman, C. Epstein, P. M. Frinchaboy, M. R. Hayden, T. S. Rodrigues, S. R. Majewski, J. A. Johnson, M. H. Pinsonneault, D. Stello, C. Allende Prieto, B. Andrews, S. Basu, T. C. Beers, D. Bizyaev, A. Burton, W. J. Chaplin, K. Cunha, Y. Elsworth, R. A. García, D. A. García-Herńandez, A. E. García Pérez, F. R. Hearty, S. Hekker, T. Kallinger, K. Kinemuchi, L. Koesterke, S. Mészáros, B. Mosser, R. W. O'Connell, D. Oravetz, K. Pan, A. C. Robin, R. P. Schiavon, D. P. Schneider, M. Schultheis, A. Serenelli, M. Shetrone, V. Silva Aguirre, A. Simmons, M. Skrutskie, V. V. Smith, K. Stassun, D. H. Weinberg, J. C. Wilson and O. Zamora. *The APOGEE Red-clump Catalog: Precise Distances, Velocities, and High-resolution Elemental Abundances over a Large Area of the Milky Way's Disk.* ApJ, vol. 790, page 127, August 2014. (Cited en pages 32, 89 et 95.)

[Bragaglia *et al.* 2012] A. Bragaglia, R. G. Gratton, E. Carretta, V. D'Orazi, C. Sneden and S. Lucatello. *Searching for multiple stellar populations in the massive, old open cluster Berkeley 39.* A&A, vol. 548, page A122, December 2012. (Cited en page 33.)

[Bureau & Freeman 1999] M. Bureau and K. C. Freeman. *The Nature of Boxy/Peanut-Shaped Bulges in Spiral Galaxies.* AJ, vol. 118, pages 126–138, July 1999. (Cited en pages 16 et 21.)

[Bureau *et al.* 2006] M. Bureau, G. Aronica, E. Athanassoula, R.-J. Dettmar, A. Bosma and K. C. Freeman. *K-band observations of boxy bulges - I. Morphology and surface brightness profiles.* MNRAS, vol. 370, pages 753–772, August 2006. (Cited en page 22.)

[Burstein 1979] D. Burstein. *Structure and origin of S0 galaxies. III - The luminosity distribution perpendicular to the plane of the disks in S0's.* ApJ, vol. 234, pages 829–836, December 1979. (Cited en page 9.)

[Cardelli *et al.* 1989] J. A. Cardelli, G. C. Clayton and J. S. Mathis. *The relationship between infrared, optical, and ultraviolet extinction.* ApJ, vol. 345, pages 245–256, October 1989. (Cited en page 125.)

[Carollo *et al.* 2010] D. Carollo, T. C. Beers, M. Chiba, J. E. Norris, K. C. Freeman, Y. S. Lee, Ž. Ivezić, C. M. Rockosi and B. Yanny. *Structure and Kinematics of the Stellar Halos and Thick Disks of the Milky Way Based on Calibration Stars*

from Sloan Digital Sky Survey DR7. ApJ, vol. 712, pages 692–727, March 2010. (Cited en page 9.)

[Casagrande *et al.* 2011] L. Casagrande, R. Schönrich, M. Asplund, S. Cassisi, I. Ramírez, J. Meléndez, T. Bensby and S. Feltzing. *New constraints on the chemical evolution of the solar neighbourhood and Galactic disc(s). Improved astrophysical parameters for the Geneva-Copenhagen Survey.* A&A, vol. 530, page A138, June 2011. (Cited en pages 75 et 76.)

[Chabrier 2003] G. Chabrier. *Galactic Stellar and Substellar Initial Mass Function.* PASP, vol. 115, pages 763–795, July 2003. (Cited en page 72.)

[Chiappini *et al.* 2001] C. Chiappini, F. Matteucci and D. Romano. *Abundance Gradients and the Formation of the Milky Way.* ApJ, vol. 554, pages 1044–1058, June 2001. (Cited en page 109.)

[Chiappini 2009] C. Chiappini. *The chemical evolution of the Galactic thick and thin disks.* In J. Andersen, Nordströara, B. m and J. Bland-Hawthorn, editeurs, IAU Symposium, volume 254 of *IAU Symposium*, pages 191–196, March 2009. (Cited en page 31.)

[Cirasuolo *et al.* 2011] M. Cirasuolo, J. Afonso, R. Bender, P. Bonifacio, C. Evans, L. Kaper, E. Oliva and L. Vanzi. *MOONS: The Multi-Object Optical and Near-infrared Spectrograph.* The Messenger, vol. 145, pages 11–13, September 2011. (Cited en page 43.)

[Clarkson *et al.* 2008] W. Clarkson, K. Sahu, J. Anderson, T. E. Smith, T. M. Brown, R. M. Rich, S. Casertano, H. E. Bond, M. Livio, D. Minniti, N. Panagia, A. Renzini, J. Valenti and M. Zoccali. *Stellar Proper Motions in the Galactic Bulge from Deep Hubble Space Telescope ACS WFC Photometry.* ApJ, vol. 684, pages 1110–1142, September 2008. (Cited en pages v, 28 et 142.)

[Clarkson *et al.* 2011] W. I. Clarkson, K. C. Sahu, J. Anderson, R. M. Rich, T. E. Smith, T. M. Brown, H. E. Bond, M. Livio, D. Minniti, A. Renzini and M. Zoccali. *The First Detection of Blue Straggler Stars in the Milky Way Bulge.* ApJ, vol. 735, page 37, July 2011. (Cited en page 28.)

[Coelho & Gadotti 2011] P. Coelho and D. A. Gadotti. *Bars Rejuvenating Bulges? Evidence from Stellar Population Analysis.* ApJ, vol. 743, page L13, December 2011. (Cited en page 16.)

[Combes & Sanders 1981] F. Combes and R. H. Sanders. *Formation and properties of persisting stellar bars.* A&A, vol. 96, pages 164–173, March 1981. (Cited en page 16.)

[Cyburt *et al.* 2016] R. H. Cyburt, B. D. Fields, K. A. Olive and T.-H. Yeh. *Big bang nucleosynthesis: Present status.* Reviews of Modern Physics, vol. 88, no. 1, page 015004, January 2016. (Cited en page 7.)

[Dalton *et al.* 2012] G. Dalton, S. C. Trager, D. C. Abrams, D. Carter, P. Bonifacio, J. A. L. Aguerri, M. MacIntosh, C. Evans, I. Lewis, R. Navarro, T. Agocs, K. Dee, S. Rousset, I. Tosh, K. Middleton, J. Pragt, D. Terrett, M. Brock, C. Benn, M. Verheijen, D. Cano Infantes, C. Bevil, I. Steele, C. Mottram, S. Bates, F. J. Gribbin, J. Rey, L. F. Rodriguez, J. M. Delgado, I. Guinouard, N. Walton, M. J. Irwin, P. Jagourel, R. Stuik, G. Gerlofsma, R. Roelfsma, I. Skillen, A. Ridings, M. Balcells, J.-B. Daban, C. Gouvret, L. Venema and P. Girard. *WEAVE: the next generation wide-field spectroscopy facility for the William Herschel Telescope.* In Ground-based and Airborne Instrumentation for Astronomy IV, volume 8446 of Proc. SPIE, page 84460P, September 2012. (Cited en page 42.)

[Dame *et al.* 2001] T. M. Dame, D. Hartmann and P. Thaddeus. *The Milky Way in Molecular Clouds: A New Complete CO Survey.* ApJ, vol. 547, pages 792–813, February 2001. (Cited en pages v et 21.)

[de Jong *et al.* 2010] J. T. A. de Jong, B. Yanny, H.-W. Rix, A. E. Dolphin, N. F. Martin and T. C. Beers. *Mapping the Stellar Structure of the Milky Way Thick Disk and Halo Using SEGUE Photometry.* ApJ, vol. 714, pages 663–674, May 2010. (Cited en page 49.)

[de Jong *et al.* 2012] R. S. de Jong, O. Bellido-Tirado, C. Chiappini, É. Depagne, R. Haynes, D. Johl, O. Schnurr, A. Schwope, J. Walcher, F. Dionies, D. Haynes, A. Kelz, F. S. Kitaura, G. Lamer, I. Minchev, V. Müller, S. E. Nuza, J.-C. Olaya, T. Piffl, E. Popow, M. Steinmetz, U. Ural, M. Williams, R. Winkler, L. Wisotzki, W. R. Ansorge, M. Banerji, E. Gonzalez Solares, M. Irwin, R. C. Kennicutt, D. King, R. G. McMahon, S. Koposov, I. R. Parry, D. Sun, N. A. Walton, G. Finger, O. Iwert, M. Krumpe, J.-L. Lizon, M. Vincenzo, J.-P. Amans, P. Bonifacio, M. Cohen, P. Francois, P. Jagourel, S. B. Mignot, F. Royer, P. Sartoretti, R. Bender, F. Grupp, H.-J. Hess, F. Lang-Bardl, B. Muschielok, H. Böhringer, T. Boller, A. Bongiorno, M. Brusa, T. Dwelly, A. Merloni, K. Nandra, M. Salvato, J. H. Pragt, R. Navarro, G. Gerlofsma, R. Roelfsema, G. B. Dalton, K. F. Middleton, I. A. Tosh, C. Boeche, E. Caffau, N. Christlieb, E. K. Grebel, C. Hansen, A. Koch, H.-G. Ludwig, A. Quirrenbach, L. Sbordone, W. Seifert, G. Thimm, T. Trifonov, A. Helmi, S. C. Trager, S. Feltzing, A. Korn and W. Boland. *4MOST: 4-metre multi-object spectroscopic telescope.* In Ground-based and Airborne Instrumentation for Astronomy IV, volume 8446 of Proc. SPIE, page 84460T, September 2012. (Cited en page 43.)

[De Pascale *et al.* 2014] M. De Pascale, C. C. Worley, P. de Laverny, A. Recio-Blanco, V. Hill and A. Bijaoui. *The AMBRE project: Parameterisation of FGK-type stars from the ESO:HARPS archived spectra.* A&A, vol. 570, page A68, October 2014. (Cited en page 75.)

[De Propris *et al.* 2011] R. De Propris, R. M. Rich, A. Kunder, C. I. Johnson, A. Koch, S. Brough, C. J. Conselice, M. Gunawardhana, D. Palamara, K. Pimbblet and D. Wijesinghe. *Separating the Conjoined Red Clump in the Galactic Bulge: Kinematics and Abundances.* ApJ, vol. 732, page L36, May 2011. (Cited en page 131.)

[De Silva *et al.* 2015] G. M. De Silva, K. C. Freeman, J. Bland-Hawthorn, S. Martell, E. W. de Boer, M. Asplund, S. Keller, S. Sharma, D. B. Zucker, T. Zwitter, B. Anguiano, C. Bacigalupo, D. Bayliss, M. A. Beavis, M. Bergemann, S. Campbell, R. Cannon, D. Carollo, L. Casagrande, A. R. Casey, G. Da Costa, V. D'Orazi, A. Dotter, L. Duong, A. Heger, M. J. Ireland, P. R. Kafle, J. Kos, J. Lattanzio, G. F. Lewis, J. Lin, K. Lind, U. Munari, D. M. Nataf, S. O'Toole, Q. Parker, W. Reid, K. J. Schlesinger, A. Sheinis, J. D. Simpson, D. Stello, Y.-S. Ting, G. Traven, F. Watson, R. Wittenmyer, D. Yong and M. Žerjal. *The GALAH survey: scientific motivation.* MNRAS, vol. 449, pages 2604–2617, May 2015. (Cited en page 42.)

[de Vaucouleurs 1964] G. de Vaucouleurs. *Interpretation of velocity distribution of the inner regions of the Galaxy.* In F. J. Kerr, editeur, The Galaxy and the Magellanic Clouds, volume 20 of *IAU Symposium*, page 195, 1964. (Cited en page 21.)

[Debattista *et al.* 2006] V. P. Debattista, L. Mayer, C. M. Carollo, B. Moore, J. Wadsley and T. Quinn. *The Secular Evolution of Disk Structural Parameters.* ApJ, vol. 645, pages 209–227, July 2006. (Cited en page 22.)

[Dékány *et al.* 2013] I. Dékány, D. Minniti, M. Catelan, M. Zoccali, R. K. Saito, M. Hempel and O. A. Gonzalez. *VVV Survey Near-infrared Photometry of Known Bulge RR Lyrae Stars: The Distance to the Galactic Center and Absence of a Barred Distribution of the Metal-poor Population.* ApJ, vol. 776, page L19, October 2013. (Cited en page 143.)

[Dékány *et al.* 2015] I. Dékány, D. Minniti, D. Majaess, M. Zoccali, G. Hajdu, J. Alonso-García, M. Catelan, W. Gieren and J. Borissova. *The VVV Survey Reveals Classical Cepheids Tracing a Young and Thin Stellar Disk across the Galaxy Bulge.* ApJ, vol. 812, page L29, October 2015. (Cited en page 29.)

[Di Matteo *et al.* 2014] P. Di Matteo, M. Haywood, A. Gómez, L. van Damme, F. Combes, A. Hallé, B. Semelin, M. D. Lehnert and D. Katz. *Mapping a stellar disk into a boxy bulge: The outside-in part of the Milky Way bulge formation.* A&A, vol. 567, page A122, July 2014. (Cited en page 151.)

[Di Matteo *et al.* 2015] P. Di Matteo, A. Gómez, M. Haywood, F. Combes, M. D. Lehnert, M. Ness, O. N. Snaith, D. Katz and B. Semelin. *Why the Milky Wayâs bulge is not only a bar formed from a cold thin disk.* A&A, vol. 577, page A1, April 2015. (Cited en pages 19, 34, 142, 151, 160 et 164.)

[Di Matteo 2016] P. Di Matteo. *The Disc Origin of the Milky Way Bulge.* PASA, vol. 33, page e027, June 2016. (Cited en page 34.)

[Dwek *et al.* 1995] E. Dwek, R. G. Arendt, M. G. Hauser, T. Kelsall, C. M. Lisse, S. H. Moseley, R. F. Silverberg, T. J. Sodroski and J. L. Weiland. *Morphology, near-infrared luminosity, and mass of the Galactic bulge from COBE DIRBE observations.* ApJ, vol. 445, pages 716–730, June 1995. (Cited en pages 21 et 22.)

[Eggen *et al.* 1962] O. J. Eggen, D. Lynden-Bell and A. R. Sandage. *Evidence from the motions of old stars that the Galaxy collapsed.* ApJ, vol. 136, page 748, November 1962. (Cited en page 14.)

[Eisenstein *et al.* 2011] D. J. Eisenstein, D. H. Weinberg, E. Agol, H. Aihara, C. Allende Prieto, S. F. Anderson, J. A. Arns, É. Aubourg, S. Bailey, E. Balbinot and et al. *SDSS-III: Massive Spectroscopic Surveys of the Distant Universe, the Milky Way, and Extra-Solar Planetary Systems.* AJ, vol. 142, page 72, September 2011. (Cited en page 31.)

[Ellison *et al.* 2011] S. L. Ellison, P. Nair, D. R. Patton, J. M. Scudder, J. T. Mendel and L. Simard. *The impact of gas inflows on star formation rates and metallicities in barred galaxies.* MNRAS, vol. 416, pages 2182–2192, September 2011. (Cited en page 16.)

[Elmegreen 1999] B. G. Elmegreen. *Galactic Bulge Formation as a Maximum Intensity Starburst.* ApJ, vol. 517, pages 103–107, May 1999. (Cited en page 15.)

[Erwin *et al.* 2015] P. Erwin, R. P. Saglia, M. Fabricius, J. Thomas, N. Nowak, S. Rusli, R. Bender, J. C. Vega Beltrán and J. E. Beckman. *Composite bulges: the co-existence of classical bulges and discy pseudo-bulges in S0 and spiral galaxies.* MNRAS, vol. 446, pages 4039–4077, February 2015. (Cited en page 16.)

[Erwin 2008] P. Erwin. *The coexistence of classical bulges and disky pseudobulges in early-type disk galaxies.* In M. Bureau, E. Athanassoula and B. Barbuy, editeurs, Formation and Evolution of Galaxy Bulges, volume 245 of *IAU Symposium*, pages 113–116, July 2008. (Cited en page 160.)

[Falcón-Barroso *et al.* 2004] J. Falcón-Barroso, R. Bacon, M. Bureau, M. Cappellari, R. L. Davies, E. Emsellem, D. Krajnović, H. Kuntschner, R. McDermid, R. F. Peletier and P. T. de Zeeuw. *A SAURON look at galaxy bulges.* Astronomische Nachrichten, vol. 325, pages 92–95, February 2004. (Cited en page 22.)

[Famaey & McGaugh 2013] B. Famaey and S. McGaugh. *Challenges for ΛCDM and MOND.* Journal of Physics Conference Series, vol. 437, no. 1, page 012001, April 2013. (Cited en page 7.)

[Feltzing & Gilmore 2000] S. Feltzing and G. Gilmore. *Age and metallicity gradients in the Galactic Bulge. A differential study using HST/WFPC2.* A&A, vol. 355, pages 949–965, March 2000. (Cited en page 142.)

[Feltzing *et al.* 2003] S. Feltzing, T. Bensby and I. Lundström. *Signatures of SN Ia in the galactic thick disk. Observational evidence from alpha -elements in 67 dwarf stars in the solar neighbourhood.* A&A, vol. 397, pages L1–L4, January 2003. (Cited en page 30.)

[Fiacconi *et al.* 2015] D. Fiacconi, R. Feldmann and L. Mayer. *The Argo simulation - II. The early build-up of the Hubble sequence.* MNRAS, vol. 446, pages 1957–1972, January 2015. (Cited en page 160.)

[Fisher & Drory 2016] D. B. Fisher and N. Drory. *An Observational Guide to Identifying Pseudobulges and Classical Bulges in Disc Galaxies.* Galactic Bulges, vol. 418, page 41, 2016. (Cited en page 16.)

[Freeman & Bland-Hawthorn 2002] K. Freeman and J. Bland-Hawthorn. *The New Galaxy: Signatures of Its Formation.* ARA&A, vol. 40, pages 487–537, 2002. (Cited en pages 31 et 146.)

[Freeman 2012] K. C. Freeman. *The HERMES Project: Reconstructing Galaxy Formation.* In W. Aoki, M. Ishigaki, T. Suda, T. Tsujimoto and N. Arimoto, editeurs, Galactic Archaeology: Near-Field Cosmology and the Formation of the Milky Way, volume 458 of *Astronomical Society of the Pacific Conference Series*, page 393, August 2012. (Cited en page 42.)

[Friedli *et al.* 1994] D. Friedli, W. Benz and R. Kennicutt. *On the influence of bars and star formation on galactic abundance gradients.* ApJ, vol. 430, pages L105–L108, August 1994. (Cited en page 19.)

[Frinchaboy *et al.* 2013] P. M. Frinchaboy, B. Thompson, K. M. Jackson, J. O'Connell, B. Meyer, G. Zasowski, S. R. Majewski, S. D. Chojnowksi, J. A. Johnson, C. Allende Prieto, T. C. Beers, D. Bizyaev, H. Brewington, K. Cunha, G. Ebelke, A. E. García Pérez, F. R. Hearty, J. Holtzman, K. Kinemuchi, E. Malanushenko, V. Malanushenko, M. Marchante, S. Mészáros, D. Muna, D. L. Nidever, D. Oravetz, K. Pan, R. P. Schiavon, D. P. Schneider, M. Shetrone, A. Simmons, S. Snedden, V. V. Smith and J. C. Wilson. *The Open Cluster Chemical Analysis and Mapping Survey: Local Galactic Metallicity Gradient with APOGEE Using SDSS DR10.* ApJ, vol. 777, page L1, November 2013. (Cited en page 33.)

[Fuhrmann 2011] K. Fuhrmann. *Nearby stars of the Galactic disc and halo - V.* MNRAS, vol. 414, pages 2893–2922, July 2011. (Cited en page 30.)

[Fukugita *et al.* 1998] M. Fukugita, C. J. Hogan and P. J. E. Peebles. *The Cosmic Baryon Budget.* ApJ, vol. 503, page 518, August 1998. (Cited en page 14.)

[Fulbright *et al.* 2007] J. P. Fulbright, A. McWilliam and R. M. Rich. *Abundances of Baade's Window Giants from Keck HIRES Spectra. II. The Alpha and Light Odd Elements.* ApJ, vol. 661, pages 1152–1179, June 2007. (Cited en pages 24, 127 et 146.)

[Fustes *et al.* 2012] D. Fustes, D. Ordóñez, C. Dafonte, M. Manteiga and B. Arcay. Distributed Genetic Algorithm for Feature Selection in Gaia RVS Spectra: Application to ANN Parameterization, page 127. 2012. (Cited en page 37.)

[Fux 1999] R. Fux. *3D self-consistent N-body barred models of the Milky Way. II. Gas dynamics.* A&A, vol. 345, pages 787–812, May 1999. (Cited en pages 17, 21 et 22.)

[Gadotti 2009] D. A. Gadotti. *Structural properties of pseudo-bulges, classical bulges and elliptical galaxies: a Sloan Digital Sky Survey perspective.* MNRAS, vol. 393, pages 1531–1552, March 2009. (Cited en page 160.)

[Gallazzi *et al.* 2005] A. Gallazzi, S. Charlot, J. Brinchmann, S. D. M. White and C. A. Tremonti. *The ages and metallicities of galaxies in the local universe.* MNRAS, vol. 362, pages 41–58, September 2005. (Cited en page 143.)

[Garcia Perez *et al.* 2014] A. Garcia Perez, C. Allende-Prieto, K. M. Cunha, J. A. Holtzman, J. Johnson, S. Majewski, S. Meszaros, R. P. Schiavon, M. D. Shetrone, V. V. Smith and SDSS-III/APOGEE Collaboration. *The APOGEE Stellar Parameters and Chemical Abundances Pipeline (ASPCAP).* In American Astronomical Society Meeting Abstracts 223, volume 223 of *American Astronomical Society Meeting Abstracts*, page 440.07, January 2014. (Cited en page 89.)

[Gazzano *et al.* 2013] J.-C. Gazzano, G. Kordopatis, M. Deleuil, P. de Laverny, A. Recio-Blanco and V. Hill. *Characterisation of the Galactic thin disc with CoRoT targets.* A&A, vol. 550, page A125, February 2013. (Cited en page 95.)

[Genovali *et al.* 2014] K. Genovali, B. Lemasle, G. Bono, M. Romaniello, M. Fabrizio, I. Ferraro, G. Iannicola, C. D. Laney, M. Nonino, M. Bergemann, R. Buonanno, P. François, L. Inno, R.-P. Kudritzki, N. Matsunaga, S. Pedicelli, F. Primas and F. Thévenin. *On the fine structure of the Cepheid metallicity gradient in the Galactic thin disk.* A&A, vol. 566, page A37, June 2014. (Cited en page 33.)

[Gesicki *et al.* 2014] K. Gesicki, A. A. Zijlstra, M. Hajduk and C. Szyszka. *Accelerated post-AGB evolution, initial-final mass relations, and the star-formation history of the Galactic bulge.* A&A, vol. 566, page A48, June 2014. (Cited en page 29.)

[Gilmore & Reid 1983] G. Gilmore and N. Reid. *New light on faint stars. III - Galactic structure towards the South Pole and the Galactic thick disc.* MNRAS, vol. 202, pages 1025–1047, March 1983. (Cited en pages 9, 30, 31 et 88.)

[Gilmore *et al.* 2012] G. Gilmore, S. Randich, M. Asplund, J. Binney, P. Bonifacio, J. Drew, S. Feltzing, A. Ferguson, R. Jeffries, G. Micela, I. Negueruela, T. Prusti, H.-W. Rix, A. Vallenari, E. Alfaro, C. Allende-Prieto, C. Babusiaux, T. Bensby, R. Blomme, A. Bragaglia, E. Flaccomio, P. François, M. Irwin, S. Koposov, A. Korn, A. Lanzafame, E. Pancino, E. Paunzen, A. Recio-Blanco, G. Sacco, R. Smiljanic, S. Van Eck and N. Walton. *The Gaia-ESO Public Spectroscopic Survey.* The Messenger, vol. 147, pages 25–31, March 2012. (Cited en pages 31 et 38.)

[Girardi *et al.* 2000] L. Girardi, A. Bressan, G. Bertelli and C. Chiosi. *Evolutionary tracks and isochrones for low- and intermediate-mass stars: From 0.15 to 7 M_{sun}, and from Z=0.0004 to 0.03.* A&AS, vol. 141, pages 371–383, February 2000. (Cited en page 71.)

[Gonzalez *et al.* 2011] O. A. Gonzalez, M. Rejkuba, M. Zoccali, E. Valenti and D. Minniti. *Reddening and metallicity maps of the Milky Way bulge from VVV and 2MASS. I. The method and minor axis maps.* A&A, vol. 534, page A3, October 2011. (Cited en pages 50, 117 et 119.)

[Gonzalez *et al.* 2013] O. A. Gonzalez, M. Rejkuba, M. Zoccali, E. Valent, D. Minniti and R. Tobar. *Reddening and metallicity maps of the Milky Way bulge from VVV and 2MASS. III. The first global photometric metallicity map of the Galactic bulge*. A&A, vol. 552, page A110, April 2013. (Cited en pages v, 18, 19, 123, 124 et 141.)

[Gonzalez *et al.* 2015] O. A. Gonzalez, M. Zoccali, S. Vasquez, V. Hill, M. Rejkuba, E. Valenti, A. Rojas-Arriagada, A. Renzini, C. Babusiaux, D. Minniti and T. M. Brown. *The GIRAFFE Inner Bulge Survey (GIBS). II. Metallicity distributions and alpha element abundances at fixed Galactic latitude*. A&A, vol. 584, page A46, December 2015. (Cited en pages 119, 127, 140 et 146.)

[Gratton 1987] R. G. Gratton. *Radial velocities of RR Lyrae stars in the Baade Window*. MNRAS, vol. 224, pages 175–178, January 1987. (Cited en page 143.)

[Grevesse *et al.* 2007] N. Grevesse, M. Asplund and A. J. Sauval. *The Solar Chemical Composition*. Space Sci. Rev., vol. 130, pages 105–114, June 2007. (Cited en pages 11, 57 et 61.)

[Grieco *et al.* 2012] V. Grieco, F. Matteucci, A. Pipino and G. Cescutti. *Chemical evolution of the Galactic bulge: different stellar populations and possible gradients*. A&A, vol. 548, page A60, November 2012. (Cited en pages 143 et 164.)

[Guiglion *et al.* 2015] G. Guiglion, A. Recio-Blanco, P. de Laverny, G. Kordopatis, V. Hill, Š. Mikolaitis, I. Minchev, C. Chiappini, R. F. G. Wyse, G. Gilmore, S. Randich, S. Feltzing, T. Bensby, E. Flaccomio, S. E. Koposov, E. Pancino, A. Bayo, M. T. Costado, E. Franciosini, A. Hourihane, P. Jofré, C. Lardo, J. Lewis, K. Lind, L. Magrini, L. Morbidelli, G. G. Sacco, G. Ruchti, C. C. Worley and S. Zaggia. *The Gaia-ESO Survey: New constraints on the Galactic disc velocity dispersion and its chemical dependencies*. A&A, vol. 583, page A91, November 2015. (Cited en pages 105, 106, 109 et 111.)

[Gustafsson *et al.* 2008] B. Gustafsson, B. Edvardsson, K. Eriksson, U. G. Jørgensen, Å. Nordlund and B. Plez. *A grid of MARCS model atmospheres for late-type stars. I. Methods and general properties*. A&A, vol. 486, pages 951–970, August 2008. (Cited en page 57.)

[Habing *et al.* 2006] H. J. Habing, M. N. Sevenster, M. Messineo, G. van de Ven and K. Kuijken. *The distribution of maser stars in the inner Milky Way: the effect of a weak, rotating bar*. A&A, vol. 458, pages 151–162, October 2006. (Cited en page 22.)

[Harris 1996] W. E. Harris. *A Catalog of Parameters for Globular Clusters in the Milky Way*. AJ, vol. 112, page 1487, October 1996. (Cited en page 77.)

[Hartwick 1987] F. D. A. Hartwick. *The structure of the Galactic halo*. In G. Gilmore and B. Carswell, editeurs, NATO Advanced Science Institutes (ASI) Series C, volume 207 of *NATO Advanced Science Institutes (ASI) Series C*, pages 281–290, 1987. (Cited en page 9.)

[Hayden *et al.* 2014] M. R. Hayden, J. A. Holtzman, J. Bovy, S. R. Majewski, J. A. Johnson, C. Allende Prieto, T. C. Beers, K. Cunha, P. M. Frinchaboy, A. E. García Pérez, L. Girardi, F. R. Hearty, Y. S. Lee, D. Nidever, R. P. Schiavon, K. J. Schlesinger, D. P. Schneider, M. Schultheis, M. Shetrone, V. V. Smith, G. Zasowski, D. Bizyaev, D. Feuillet, S. Hasselquist, K. Kinemuchi, E. Malanushenko, V. Malanushenko, R. O'Connell, K. Pan and K. Stassun. *Chemical Cartography with APOGEE: Large-scale Mean Metallicity Maps of the Milky Way Disk.* AJ, vol. 147, page 116, May 2014. (Cited en page 33.)

[Hayden *et al.* 2015] M. R. Hayden, J. 2012, J. A. Holtzman, D. L. Nidever, J. C. Bird, D. H. Weinberg, B. H. Andrews, S. R. Majewski, C. Allende Prieto, F. Anders, T. C. Beers, D. Bizyaev, C. Chiappini, K. Cunha, P. Frinchaboy, D. A. García-Herńandez, A. E. García Pérez, L. Girardi, P. Harding, F. R. Hearty, J. A. Johnson, S. Mészáros, I. Minchev, R. O'Connell, K. Pan, A. C. Robin, R. P. Schiavon, D. P. Schneider, M. Schultheis, M. Shetrone, M. Skrutskie, M. Steinmetz, V. Smith, J. C. Wilson, O. Zamora and G. Zasowski. *Chemical Cartography with APOGEE: Metallicity Distribution Functions and the Chemical Structure of the Milky Way Disk.* ApJ, vol. 808, page 132, August 2015. (Cited en pages 33, 98, 108, 146 et 149.)

[Haywood *et al.* 2013] M. Haywood, P. Di Matteo, M. D. Lehnert, D. Katz and A. Gómez. *The age structure of stellar populations in the solar vicinity. Clues of a two-phase formation history of the Milky Way disk.* A&A, vol. 560, page A109, December 2013. (Cited en pages 9, 32, 33, 34, 100, 103, 108, 109, 111 et 146.)

[Haywood *et al.* 2016] M. Haywood, P. Di Matteo, O. Snaith and A. Calamida. *Hiding its age: the case for a younger bulge.* ArXiv e-prints, June 2016. (Cited en page 28.)

[Herschel 1785] W. Herschel. *On the Construction of the Heavens.* Philosophical Transactions of the Royal Society of London Series I, vol. 75, pages 213–266, 1785. (Cited en page 5.)

[Hill *et al.* 2011] V. Hill, A. Lecureur, A. Gómez, M. Zoccali, M. Schultheis, C. Babusiaux, F. Royer, B. Barbuy, F. Arenou, D. Minniti and S. Ortolani. *The metallicity distribution of bulge clump giants in Baade's window.* A&A, vol. 534, page A80, October 2011. (Cited en pages 19, 57, 58, 66, 114, 115, 119, 138, 139, 140, 169 et 170.)

[Howard *et al.* 2009] C. D. Howard, R. M. Rich, W. Clarkson, R. Mallery, J. Kormendy, R. De Propris, A. C. Robin, R. Fux, D. B. Reitzel, H. S. Zhao, K. Kuijken and A. Koch. *Kinematics at the Edge of the Galactic Bulge: Evidence for Cylindrical Rotation.* ApJ, vol. 702, pages L153–L157, September 2009. (Cited en page 130.)

[Ibata *et al.* 2013] R. A. Ibata, G. F. Lewis, A. R. Conn, M. J. Irwin, A. W. McConnachie, S. C. Chapman, M. L. Collins, M. Fardal, A. M. N. Ferguson, N. G. Ibata, A. D. Mackey, N. F. Martin, J. Navarro, R. M. Rich, D. Valls-Gabaud

and L. M. Widrow. *A vast, thin plane of corotating dwarf galaxies orbiting the Andromeda galaxy.* Nature, vol. 493, pages 62–65, January 2013. (Cited en page 7.)

[Immeli *et al.* 2004] A. Immeli, M. Samland, O. Gerhard and P. Westera. *Gas physics, disk fragmentation, and bulge formation in young galaxies.* A&A, vol. 413, pages 547–561, January 2004. (Cited en page 15.)

[Ivezić *et al.* 2008] Ž. Ivezić, B. Sesar, M. Jurić, N. Bond, J. Dalcanton, C. M. Rockosi, B. Yanny, H. J. Newberg, T. C. Beers, C. Allende Prieto, R. Wilhelm, Y. S. Lee, T. Sivarani, J. E. Norris, C. A. L. Bailer-Jones, P. Re Fiorentin, D. Schlegel, A. Uomoto, R. H. Lupton, G. R. Knapp, J. E. Gunn, K. R. Covey, J. A. Smith, G. Miknaitis, M. Doi, M. Tanaka, M. Fukugita, S. Kent, D. Finkbeiner, J. A. Munn, J. R. Pier, T. Quinn, S. Hawley, S. Anderson, F. Kiuchi, A. Chen, J. Bushong, H. Sohi, D. Haggard, A. Kimball, J. Barentine, H. Brewington, M. Harvanek, S. Kleinman, J. Krzesinski, D. Long, A. Nitta, S. Snedden, B. Lee, H. Harris, J. Brinkmann, D. P. Schneider and D. G. York. *The Milky Way Tomography with SDSS. II. Stellar Metallicity.* ApJ, vol. 684, pages 287–325, September 2008. (Cited en page 98.)

[Jofré *et al.* 2015] P. Jofré, U. Heiter, C. Soubiran, S. Blanco-Cuaresma, T. Masseron, T. Nordlander, L. Chemin, C. C. Worley, S. Van Eck, A. Hourihane, G. Gilmore, V. Adibekyan, M. Bergemann, T. Cantat-Gaudin, E. Delgado-Mena, J. I. González Hernández, G. Guiglion, C. Lardo, P. de Laverny, K. Lind, L. Magrini, S. Mikolaitis, D. Montes, E. Pancino, A. Recio-Blanco, R. Sordo, S. Sousa, H. M. Tabernero and A. Vallenari. *Gaia FGK benchmark stars: abundances of α and iron-peak elements.* A&A, vol. 582, page A81, October 2015. (Cited en pages 56, 61, 165 et 166.)

[Johnson *et al.* 2012a] C. I. Johnson, R. Rich, A. Kunder, R. de Propris, C. Kobayashi and A. Koch. *The Chemical Composition of RGB Stars in Off-Axis Bulge Fields.* In American Astronomical Society Meeting Abstracts #219, volume 219 of *American Astronomical Society Meeting Abstracts*, page 152.11, January 2012. (Cited en page 19.)

[Johnson *et al.* 2012b] C. I. Johnson, R. M. Rich, C. Kobayashi and J. P. Fulbright. *Constraints on the Formation of the Galactic Bulge from Na, Al, and Heavy-element Abundances in Plaut's Field.* ApJ, vol. 749, page 175, April 2012. (Cited en pages 139, 140 et 158.)

[Johnson *et al.* 2014] Christian I. Johnson, R. Michael Rich, Chiaki Kobayashi, Andrea Kunder and Andreas Koch. *LIGHT, ALPHA, AND Fe-PEAK ELEMENT ABUNDANCES IN THE GALACTIC BULGE.* ApJ, vol. 148, no. 4, page 67, September 2014. (Cited en page 127.)

[Jordi *et al.* 2006] C. Jordi, E. Høg, A. G. A. Brown, L. Lindegren, C. A. L. Bailer-Jones, J. M. Carrasco, J. Knude, V. Straižys, J. H. J. de Bruijne, J.-F. Claeskens,

R. Drimmel, F. Figueras, M. Grenon, I. Kolka, M. A. C. Perryman, G. Tautvaišienė, V. Vansevičius, P. G. Willemsen, A. Bridžius, D. W. Evans, C. Fabricius, M. Fiorucci, U. Heiter, T. A. Kaempf, A. Kazlauskas, A. Kučinskas, V. Malyuto, U. Munari, C. Reylé, J. Torra, A. Vallenari, K. Zdanavičius, R. Korakitis, O. Malkov and A. Smette. *The design and performance of the Gaia photometric system.* MNRAS, vol. 367, pages 290–314, March 2006. (Cited en page 36.)

[Jordi *et al.* 2010] C. Jordi, M. Gebran, J. M. Carrasco, J. de Bruijne, H. Voss, C. Fabricius, J. Knude, A. Vallenari, R. Kohley and A. Mora. *Gaia broad band photometry.* A&A, vol. 523, page A48, November 2010. (Cited en page 36.)

[Jurić *et al.* 2008] M. Jurić, Ž. Ivezić, A. Brooks, R. H. Lupton, D. Schlegel, D. Finkbeiner, N. Padmanabhan, N. Bond, B. Sesar, C. M. Rockosi, G. R. Knapp, J. E. Gunn, T. Sumi, D. P. Schneider, J. C. Barentine, H. J. Brewington, J. Brinkmann, M. Fukugita, M. Harvanek, S. J. Kleinman, J. Krzesinski, D. Long, E. H. Neilsen Jr., A. Nitta, S. A. Snedden and D. G. York. *The Milky Way Tomography with SDSS. I. Stellar Number Density Distribution.* ApJ, vol. 673, pages 864–914, February 2008. (Cited en pages 8 et 9.)

[Kordopatis *et al.* 2011] G. Kordopatis, A. Recio-Blanco, P. de Laverny, G. Gilmore, V. Hill, R. F. G. Wyse, A. Helmi, A. Bijaoui, M. Zoccali and O. Bienaymé. *A spectroscopic survey of thick disc stars outside the solar neighbourhood.* A&A, vol. 535, page A107, November 2011. (Cited en pages 30, 69, 84 et 89.)

[Kordopatis *et al.* 2015] G. Kordopatis, R. F. G. Wyse, G. Gilmore, A. Recio-Blanco, P. de Laverny, V. Hill, V. Adibekyan, U. Heiter, I. Minchev, B. Famaey, T. Bensby, S. Feltzing, G. Guiglion, A. J. Korn, Š. Mikolaitis, M. Schultheis, A. Vallenari, A. Bayo, G. Carraro, E. Flaccomio, E. Franciosini, A. Hourihane, P. Jofré, S. E. Koposov, C. Lardo, J. Lewis, K. Lind, L. Magrini, L. Morbidelli, E. Pancino, S. Randich, G. G. Sacco, C. C. Worley and S. Zaggia. *The Gaia-ESO Survey: characterisation of the [α/Fe] sequences in the Milky Way discs.* A&A, vol. 582, page A122, October 2015. (Cited en pages 31, 83, 97, 107 et 146.)

[Kormendy & Barentine 2010] J. Kormendy and J. C. Barentine. *Detection of a Pseudobulge Hidden Inside the "Box-shaped Bulge" of NGC 4565.* ApJ, vol. 715, pages L176–L179, June 2010. (Cited en page 160.)

[Kormendy & Kennicutt 2004] J. Kormendy and R. C. Kennicutt Jr. *Secular Evolution and the Formation of Pseudobulges in Disk Galaxies.* ARA&A, vol. 42, pages 603–683, September 2004. (Cited en page 16.)

[Kormendy *et al.* 2010] J. Kormendy, N. Drory, R. Bender and M. E. Cornell. *Bulgeless Giant Galaxies Challenge Our Picture of Galaxy Formation by Hierarchical Clustering.* ApJ, vol. 723, pages 54–80, November 2010. (Cited en page 160.)

[Kraljic *et al.* 2012] K. Kraljic, F. Bournaud and M. Martig. *The Two-phase Formation History of Spiral Galaxies Traced by the Cosmic Evolution of the Bar Fraction.* ApJ, vol. 757, page 60, September 2012. (Cited en page 16.)

[Kroupa *et al.* 2010] P. Kroupa, B. Famaey, K. S. de Boer, J. Dabringhausen, M. S. Pawlowski, C. M. Boily, H. Jerjen, D. Forbes, G. Hensler and M. Metz. *Local-Group tests of dark-matter concordance cosmology . Towards a new paradigm for structure formation.* A&A, vol. 523, page A32, November 2010. (Cited en page 7.)

[Kuijken & Merrifield 1995] K. Kuijken and M. R. Merrifield. *Establishing the connection between peanut-shaped bulges and galactic bars.* ApJ, vol. 443, pages L13–L16, April 1995. (Cited en pages 16 et 21.)

[Kuijken & Rich 2002] K. Kuijken and R. M. Rich. *Hubble Space Telescope WFPC2 Proper Motions in Two Bulge Fields: Kinematics and Stellar Population of the Galactic Bulge.* AJ, vol. 124, pages 2054–2066, October 2002. (Cited en pages 28 et 142.)

[Kunder *et al.* 2012] A. Kunder, A. Koch, R. M. Rich, R. de Propris, C. D. Howard, S. A. Stubbs, C. I. Johnson, J. Shen, Y. Wang, A. C. Robin, J. Kormendy, M. Soto, P. Frinchaboy, D. B. Reitzel, H. Zhao and L. Origlia. *The Bulge Radial Velocity Assay (BRAVA). II. Complete Sample and Data Release.* AJ, vol. 143, page 57, March 2012. (Cited en pages 22 et 130.)

[Kunder *et al.* 2016] A. Kunder, R. M. Rich, J. Storm, D. M. Nataf, R. De Propris, A. R. Walker, G. Bono, C. I. Johnson, J. Shen and Z. Y. Li. *Before the Bar: Kinematic Detection of A Spheroidal Metal-Poor Bulge Component.* ArXiv e-prints, March 2016. (Cited en page 143.)

[Lagioia *et al.* 2014] E. P. Lagioia, A. P. Milone, P. B. Stetson, G. Bono, P. G. Prada Moroni, M. Dall'Ora, A. Aparicio, R. Buonanno, A. Calamida, I. Ferraro, R. Gilmozzi, G. Iannicola, N. Matsunaga, M. Monelli and A. Walker. *On the Kinematic Separation of Field and Cluster Stars across the Bulge Globular NGC 6528.* ApJ, vol. 782, page 50, February 2014. (Cited en page 29.)

[Larson 1976] R. B. Larson. *Models for the formation of disc galaxies.* MNRAS, vol. 176, pages 31–52, July 1976. (Cited en page 33.)

[Lecureur *et al.* 2007] A. Lecureur, V. Hill, M. Zoccali, B. Barbuy, A. Gómez, D. Minniti, S. Ortolani and A. Renzini. *Oxygen, sodium, magnesium, and aluminium as tracers of the galactic bulge formation.* A&A, vol. 465, pages 799–814, April 2007. (Cited en pages 24, 25, 127 et 146.)

[Licquia *et al.* 2015] T. C. Licquia, J. A. Newman and J. Brinchmann. *Unveiling the Milky Way: A New Technique for Determining the Optical Color and Luminosity of Our Galaxy.* ApJ, vol. 809, page 96, August 2015. (Cited en page 7.)

[Lindqvist *et al.* 1992a] M. Lindqvist, H. J. Habing and A. Winnberg. *OH/IR stars close to the Galactic Centre. II - Their spatial and kinematic properties and the mass distribution within 5-100 PC from the galactic centre.* A&A, vol. 259, pages 118–127, June 1992. (Cited en page 29.)

[Lindqvist *et al.* 1992b] M. Lindqvist, A. Winnberg, H. J. Habing and H. E. Matthews. *OH/IR stars close to the Galactic Centre. I - Observational data.* A&AS, vol. 92, pages 43–62, January 1992. (Cited en page 29.)

[Liszt & Burton 1980] H. S. Liszt and W. B. Burton. *The gas distribution in the central region of the Galaxy. III - A barlike model of the inner-Galaxy gas based on improved H I data.* ApJ, vol. 236, pages 779–797, March 1980. (Cited en page 21.)

[Lloyd Evans 1976] T. Lloyd Evans. *Red variables in the central bulge of the Galaxy. I. The period distribution of Mira variables.* MNRAS, vol. 174, January 1976. (Cited en page 29.)

[López-Corredoira *et al.* 2005] M. López-Corredoira, A. Cabrera-Lavers and O. E. Gerhard. *A boxy bulge in the Milky Way. Inversion of the stellar statistics equation with 2MASS data.* A&A, vol. 439, pages 107–110, August 2005. (Cited en page 21.)

[Luo *et al.* 2015] A.-L. Luo, Y.-H. Zhao, G. Zhao, L.-C. Deng, X.-W. Liu, Y.-P. Jing, G. Wang, H.-T. Zhang, J.-R. Shi, X.-Q. Cui, Y.-Q. Chu, G.-P. Li, Z.-R. Bai, Y. Wu, Y. Cai, S.-Y. Cao, Z.-H. Cao, J. L. Carlin, H.-Y. Chen, J.-J. Chen, K.-X. Chen, L. Chen, X.-L. Chen, X.-Y. Chen, Y. Chen, N. Christlieb, J.-R. Chu, C.-Z. Cui, Y.-Q. Dong, B. Du, D.-W. Fan, L. Feng, J.-N. Fu, P. Gao, X.-F. Gong, B.-Z. Gu, Y.-X. Guo, Z.-W. Han, B.-L. He, J.-L. Hou, Y.-H. Hou, W. Hou, H.-Z. Hu, N.-S. Hu, Z.-W. Hu, Z.-Y. Huo, L. Jia, F.-H. Jiang, X. Jiang, Z.-B. Jiang, G. Jin, X. Kong, X. Kong, Y.-J. Lei, A.-H. Li, C.-H. Li, G.-W. Li, H.-N. Li, J. Li, Q. Li, S. Li, S.-S. Li, X.-N. Li, Y. Li, Y.-B. Li, Y.-P. Li, Y. Liang, C.-C. Lin, C. Liu, G.-R. Liu, G.-Q. Liu, Z.-G. Liu, W.-Z. Lu, Y. Luo, Y.-D. Mao, H. Newberg, J.-J. Ni, Z.-X. Qi, Y.-J. Qi, S.-Y. Shen, H.-M. Shi, J. Song, Y.-H. Song, D.-Q. Su, H.-J. Su, Z.-H. Tang, Q.-S. Tao, Y. Tian, D. Wang, D.-Q. Wang, F.-F. Wang, G.-M. Wang, H. Wang, H.-C. Wang, J. Wang, J.-N. Wang, J.-L. Wang, J.-P. Wang, J.-X. Wang, L. Wang, M.-X. Wang, S.-G. Wang, S.-Q. Wang, X. Wang, Y.-N. Wang, Y. Wang, Y.-F. Wang, Y.-F. Wang, P. Wei, M.-Z. Wei, H. Wu, K.-F. Wu, X.-B. Wu, Y.-Z. Wu, X.-Z. Xing, L.-Z. Xu, X.-Q. Xu, Y. Xu, T.-S. Yan, D.-H. Yang, H.-F. Yang, H.-Q. Yang, M. Yang, Z.-Q. Yao, Y. Yu, H. Yuan, H.-B. Yuan, H.-L. Yuan, W.-M. Yuan, C. Zhai, E.-P. Zhang, H.-W. Zhang, J.-N. Zhang, L.-P. Zhang, W. Zhang, Y. Zhang, Y.-X. Zhang, Z.-C. Zhang, M. Zhao, F. Zhou, X. Zhou, J. Zhu, Y.-T. Zhu, S.-C. Zou and F. Zuo. *The first data release (DR1) of the LAMOST regular survey.* Research in Astronomy and Astrophysics, vol. 15, page 1095, August 2015. (Cited en page 42.)

[Maeder 1992] A. Maeder. *Stellar yields as a function of initial metallicity and mass limit for black hole formation.* A&A, vol. 264, pages 105–120, October 1992. (Cited en page 144.)

[Majewski *et al.* 2011] S. R. Majewski, G. Zasowski and D. L. Nidever. *Lifting the Dusty Veil with Near- and Mid-infrared Photometry. I. Description and Applications*

of the Rayleigh-Jeans Color Excess Method. ApJ, vol. 739, page 25, September 2011. (Cited en page 89.)

[Majewski *et al.* 2015] S. R. Majewski, R. P. Schiavon, P. M. Frinchaboy, C. Allende Prieto, R. Barkhouser, D. Bizyaev, B. Blank, S. Brunner, A. Burton, R. Carrera, S. D. Chojnowski, K. Cunha, C. Epstein, G. Fitzgerald, A. E. Garcia Perez, F. R. Hearty, C. Henderson, J. A. Holtzman, J. A. Johnson, C. R. Lam, J. E. Lawler, P. Maseman, S. Meszaros, M. Nelson, D. Coung Nguyen, D. L. Nidever, M. Pinsonneault, M. Shetrone, S. Smee, V. V. Smith, T. Stolberg, M. F. Skrutskie, E. Walker, J. C. Wilson, G. Zasowski, F. Anders, S. Basu, S. Beland, M. R. Blanton, J. Bovy, J. R. Brownstein, J. Carlberg, W. Chaplin, C. Chiappini, D. J. Eisenstein, Y. Elsworth, D. Feuillet, S. W. Fleming, J. Galbraith-Frew, R. A. Garcia, D. Anibal Garcia-Hernandez, B. A. Gillespie, L. Girardi, J. E. Gunn, S. Hasselquist, M. R. Hayden, S. Hekker, I. Ivans, K. Kinemuchi, M. Klaene, S. Mahadevan, S. Mathur, B. Mosser, D. Muna, J. A. Munn, R. C. Nichol, R. W. O'Connell, A. C. Robin, H. Rocha-Pinto, M. Schultheis, A. M. Serenelli, N. Shane, V. Silva Aguirre, J. S. Sobeck, B. Thompson, N. W. Troup, D. H. Weinberg and O. Zamora. *The Apache Point Observatory Galactic Evolution Experiment (APOGEE).* ArXiv e-prints, September 2015. (Cited en pages 41 et 160.)

[Marinova & Jogee 2007] I. Marinova and S. Jogee. *Characterizing Bars at z ˜ 0 in the Optical and NIR: Implications for the Evolution of Barred Disks with Redshift.* ApJ, vol. 659, pages 1176–1197, April 2007. (Cited en page 16.)

[Martinez-Valpuesta & Gerhard 2013] I. Martinez-Valpuesta and O. Gerhard. *Metallicity Gradients Through Disk Instability: A Simple Model for the Milky Way's Boxy Bulge.* ApJ, vol. 766, page L3, March 2013. (Cited en pages 19, 34, 130, 142 et 151.)

[Martinez-Valpuesta *et al.* 2006] I. Martinez-Valpuesta, I. Shlosman and C. Heller. *Evolution of Stellar Bars in Live Axisymmetric Halos: Recurrent Buckling and Secular Growth.* ApJ, vol. 637, pages 214–226, January 2006. (Cited en pages 16, 22 et 134.)

[Matsunaga *et al.* 2009] N. Matsunaga, T. Kawadu, S. Nishiyama, T. Nagayama, H. Hatano, M. Tamura, I. S. Glass and T. Nagata. *A near-infrared survey of Miras and the distance to the Galactic Centre.* MNRAS, vol. 399, pages 1709–1729, November 2009. (Cited en page 29.)

[Matteucci & Brocato 1990] Francesca Matteucci and Enzo Brocato. *Metallicity distribution and abundance ratios in the stars of the Galactic bulge.* ApJ, vol. 365, page 539, December 1990. (Cited en pages 15 et 143.)

[Matteucci & Chiappini 2001] F. Matteucci and C. Chiappini. *The evolution of the oxygen abundance in the Galaxy.* New A Rev., vol. 45, pages 567–570, July 2001. (Cited en page 91.)

[Matteucci & Recchi 2001] F. Matteucci and S. Recchi. *On the Typical Timescale for the Chemical Enrichment from Type Ia Supernovae in Galaxies.* ApJ, vol. 558, pages 351–358, September 2001. (Cited en page 13.)

[McMahon *et al.* 2013] R. G. McMahon, M. Banerji, E. Gonzalez, S. E. Koposov, V. J. Bejar, N. Lodieu, R. Rebolo and VHS Collaboration. *First Scientific Results from the VISTA Hemisphere Survey (VHS).* The Messenger, vol. 154, pages 35–37, December 2013. (Cited en page 49.)

[McWilliam & Rich 1994] A. McWilliam and R. M. Rich. *The first detailed abundance analysis of Galactic bulge K giants in Baade's window.* ApJS, vol. 91, pages 749–791, April 1994. (Cited en pages 17, 18 et 24.)

[McWilliam & Zoccali 2010] A. McWilliam and M. Zoccali. *Two Red Clumps and the X-shaped Milky Way Bulge.* ApJ, vol. 724, pages 1491–1502, December 2010. (Cited en page 21.)

[Meléndez *et al.* 2008] J. Meléndez, M. Asplund, A. Alves-Brito, K. Cunha, B. Barbuy, M. S. Bessell, C. Chiappini, K. C. Freeman, I. Ramírez, V. V. Smith and D. Yong. *Chemical similarities between Galactic bulge and local thick disk red giant stars.* A&A, vol. 484, pages L21–L25, June 2008. (Cited en pages 24, 127 et 146.)

[Mészáros *et al.* 2013] S. Mészáros, J. Holtzman, A. E. García Pérez, C. Allende Prieto, R. P. Schiavon, S. Basu, D. Bizyaev, W. J. Chaplin, S. D. Chojnowski, K. Cunha, Y. Elsworth, C. Epstein, P. M. Frinchaboy, R. A. García, F. R. Hearty, S. Hekker, J. A. Johnson, T. Kallinger, L. Koesterke, S. R. Majewski, S. L. Martell, D. Nidever, M. H. Pinsonneault, J. O'Connell, M. Shetrone, V. V. Smith, J. C. Wilson and G. Zasowski. *Calibrations of Atmospheric Parameters Obtained from the First Year of SDSS-III APOGEE Observations.* AJ, vol. 146, page 133, November 2013. (Cited en pages 89 et 99.)

[Meynet & Maeder 2002] G. Meynet and A. Maeder. *Stellar evolution with rotation. VIII. Models at $Z = 10^{-5}$ and CNO yields for early galactic evolution.* A&A, vol. 390, pages 561–583, August 2002. (Cited en page 144.)

[Mikolaitis *et al.* 2014] Š. Mikolaitis, V. Hill, A. Recio-Blanco, P. de Laverny, C. Allende Prieto, G. Kordopatis, G. Tautvaišiene, D. Romano, G. Gilmore, S. Randich, S. Feltzing, G. Micela, A. Vallenari, E. J. Alfaro, T. Bensby, A. Bragaglia, E. Flaccomio, A. C. Lanzafame, E. Pancino, R. Smiljanic, M. Bergemann, G. Carraro, M. T. Costado, F. Damiani, A. Hourihane, P. Jofré, C. Lardo, L. Magrini, E. Maiorca, L. Morbidelli, L. Sbordone, S. G. Sousa, C. C. Worley and S. Zaggia. *The Gaia-ESO Survey: the chemical structure of the Galactic discs from the first internal data release.* A&A, vol. 572, page A33, December 2014. (Cited en pages 9, 31, 33, 57, 83, 107 et 151.)

[Minchev *et al.* 2013] I. Minchev, C. Chiappini and M. Martig. *Chemodynamical evolution of the Milky Way disk. I. The solar vicinity.* A&A, vol. 558, page A9, October 2013. (Cited en page 100.)

[Minchev *et al.* 2015] I. Minchev, M. Martig, D. Streich, C. Scannapieco, R. S. de Jong and M. Steinmetz. *On the Formation of Galactic Thick Disks.* ApJ, vol. 804, page L9, May 2015. (Cited en page 108.)

[Minniti *et al.* 1992] D. Minniti, S. D. M. White, E. W. Olszewski and J. M. Hill. *Rotation of the Galactic bulge.* ApJ, vol. 393, pages L47–L50, July 1992. (Cited en page 22.)

[Minniti *et al.* 1995] D. Minniti, E. W. Olszewski, J. Liebert, S. D. M. White, J. M. Hill and M. J. Irwin. *The metallicity gradient of the Galactic bulge*.* MNRAS, vol. 277, pages 1293–1311, December 1995. (Cited en pages 18 et 141.)

[Minniti *et al.* 1998] D. Minniti, T. Vandehei, K. H. Cook, K. Griest and C. Alcock. *Detection of Lithium in a Main-Sequence Bulge Star Using Keck I as a 15 Meter Diameter Telescope.* ApJ, vol. 499, pages L175–L178, June 1998. (Cited en page 29.)

[Minniti *et al.* 2010] D. Minniti, P. W. Lucas, J. P. Emerson, R. K. Saito, M. Hempel, P. Pietrukowicz, A. V. Ahumada, M. V. Alonso, J. Alonso-Garcia, J. I. Arias, R. M. Bandyopadhyay, R. H. Barbá, B. Barbuy, L. R. Bedin, E. Bica, J. Borissova, L. Bronfman, G. Carraro, M. Catelan, J. J. Clariá, N. Cross, R. de Grijs, I. Dékány, J. E. Drew, C. Fariña, C. Feinstein, E. Fernández Lajús, R. C. Gamen, D. Geisler, W. Gieren, B. Goldman, O. A. Gonzalez, G. Gunthardt, S. Gurovich, N. C. Hambly, M. J. Irwin, V. D. Ivanov, A. Jordán, E. Kerins, K. Kinemuchi, R. Kurtev, M. López-Corredoira, T. Maccarone, N. Masetti, D. Merlo, M. Messineo, I. F. Mirabel, L. Monaco, L. Morelli, N. Padilla, T. Palma, M. C. Parisi, G. Pignata, M. Rejkuba, A. Roman-Lopes, S. E. Sale, M. R. Schreiber, A. C. Schröder, M. Smith, L. S. Jr., M. Soto, M. Tamura, C. Tappert, M. A. Thompson, I. Toledo, M. Zoccali and G. Pietrzynski. *VISTA Variables in the Via Lactea (VVV): The public ESO near-IR variability survey of the Milky Way.* New A, vol. 15, pages 433–443, July 2010. (Cited en pages 43 et 50.)

[Mouret *et al.* 2007] S. Mouret, D. Hestroffer and F. Mignard. *Asteroid masses and improvement with Gaia.* A&A, vol. 472, pages 1017–1027, September 2007. (Cited en page 35.)

[Nakasato & Nomoto 2003] N. Nakasato and K. Nomoto. *Three-dimensional Simulations of the Chemical and Dynamical Evolution of the Galactic Bulge.* ApJ, vol. 588, pages 842–851, May 2003. (Cited en page 17.)

[Nassau & Blanco 1958] J. J. Nassau and V. M. Blanco. *M-Type Stars and Red Variables in the Galactic Center.* ApJ, vol. 128, page 46, July 1958. (Cited en page 17.)

[Nataf *et al.* 2010] D. M. Nataf, A. Udalski, A. Gould, P. Fouqué and K. Z. Stanek. *The Split Red Clump of the Galactic Bulge from OGLE-III.* ApJ, vol. 721, pages L28–L32, September 2010. (Cited en page 21.)

[Nataf *et al.* 2014] D. M. Nataf, S. Cassisi and E. Athanassoula. *On the correlation between metallicity and the X-shaped morphology of the Milky Way bulge.* MNRAS, vol. 442, pages 2075–2080, August 2014. (Cited en page 125.)

[Navarro *et al.* 2011] J. F. Navarro, M. G. Abadi, K. A. Venn, K. C. Freeman and B. Anguiano. *Through thick and thin: kinematic and chemical components in the solar neighbourhood.* MNRAS, vol. 412, pages 1203–1209, April 2011. (Cited en pages 30, 31 et 108.)

[Ness *et al.* 2013a] M. Ness, K. Freeman, E. Athanassoula, E. Wylie-de-Boer, J. Bland-Hawthorn, M. Asplund, G. F. Lewis, D. Yong, R. R. Lane and L. L. Kiss. *ARGOS - III. Stellar populations in the Galactic bulge of the Milky Way.* MNRAS, vol. 430, pages 836–857, April 2013. (Cited en pages v, 20, 23, 34, 119, 126, 138 et 141.)

[Ness *et al.* 2013b] M. Ness, K. Freeman, E. Athanassoula, E. Wylie-de-Boer, J. Bland-Hawthorn, M. Asplund, G. F. Lewis, D. Yong, R. R. Lane, L. L. Kiss and R. Ibata. *ARGOS - IV. The kinematics of the Milky Way bulge.* MNRAS, vol. 432, pages 2092–2103, July 2013. (Cited en pages 23 et 24.)

[Ness *et al.* 2014] M. Ness, V. P. Debattista, T. Bensby, S. Feltzing, R. Roškar, D. R. Cole, J. A. Johnson and K. Freeman. *Young Stars in an Old Bulge: A Natural Outcome of Internal Evolution in the Milky Way.* ApJ, vol. 787, page L19, June 2014. (Cited en page 30.)

[Nidever *et al.* 2014] D. L. Nidever, J. Bovy, J. C. Bird, B. H. Andrews, M. Hayden, J. Holtzman, S. R. Majewski, V. Smith, A. C. Robin, A. E. García Pérez, K. Cunha, C. Allende Prieto, G. Zasowski, R. P. Schiavon, J. A. Johnson, D. H. Weinberg, D. Feuillet, D. P. Schneider, M. Shetrone, J. Sobeck, D. A. García-Hernández, O. Zamora, H.-W. Rix, T. C. Beers, J. C. Wilson, R. W. O'Connell, I. Minchev, C. Chiappini, F. Anders, D. Bizyaev, H. Brewington, G. Ebelke, P. M. Frinchaboy, J. Ge, K. Kinemuchi, E. Malanushenko, V. Malanushenko, M. Marchante, S. Mészáros, D. Oravetz, K. Pan, A. Simmons and M. F. Skrutskie. *Tracing Chemical Evolution over the Extent of the Milky Way's Disk with APOGEE Red Clump Stars.* ApJ, vol. 796, page 38, November 2014. (Cited en pages 32, 98 et 149.)

[Nissen & Schuster 2010] P. E. Nissen and W. J. Schuster. *Two distinct halo populations in the solar neighborhood. Evidence from stellar abundance ratios and kinematics.* A&A, vol. 511, page L10, February 2010. (Cited en pages 9 et 108.)

[Nordström *et al.* 2004] B. Nordström, M. Mayor, J. Andersen, J. Holmberg, F. Pont, B. R. Jørgensen, E. H. Olsen, S. Udry and N. Mowlavi. *The Geneva-Copenhagen survey of the Solar neighbourhood. Ages, metallicities, and kinematic properties of ∼14 000 F and G dwarfs.* A&A, vol. 418, pages 989–1019, May 2004. (Cited en pages 18 et 75.)

[Nowak *et al.* 2010] N. Nowak, J. Thomas, P. Erwin, R. P. Saglia, R. Bender and R. I. Davies. *Do black hole masses scale with classical bulge luminosities only? The case of the two composite pseudo-bulge galaxies NGC 3368 and NGC 3489.* MNRAS, vol. 403, pages 646–672, April 2010. (Cited en page 160.)

[Obreja *et al.* 2013] A. Obreja, R. Domínguez-Tenreiro, C. Brook, F. J. Martínez-Serrano, M. Doménech-Moral, A. Serna, M. Mollá and G. Stinson. *A Two-phase Scenario for Bulge Assembly in ΛCDM Cosmologies.* ApJ, vol. 763, page 26, January 2013. (Cited en pages 17 et 160.)

[Ortolani *et al.* 1995] S. Ortolani, A. Renzini, R. Gilmozzi, G. Marconi, B. Barbuy, E. Bica and R. M. Rich. *Near-coeval formation of the Galactic bulge and halo inferred from globular cluster ages.* Nature, vol. 377, pages 701–704, October 1995. (Cited en pages 26, 27 et 142.)

[Pagel & Patchett 1975] B. E. J. Pagel and B. E. Patchett. *Metal abundances in nearby stars and the chemical history of the solar neighborhood.* MNRAS, vol. 172, pages 13–40, July 1975. (Cited en page 12.)

[Pasquini *et al.* 2000] L. Pasquini, G. Avila, E. Allaert, P. Ballester, P. Biereichel, B. Buzzoni, C. Cavadore, H. Dekker, B. Delabre, F. Ferraro, V. Hill, A. Kaufer, H. Kotzlowski, J.-L. Lizon, A. Longinotti, S. Moureau, R. Palsa and S. Zaggia. *FLAMES: a multi-object fiber facility for the VLT.* In M. Iye and A. F. Moorwood, editeurs, Optical and IR Telescope Instrumentation and Detectors, volume 4008 of *Society of Photo-Optical Instrumentation Engineers (SPIE) Conference Series*, pages 129–140, August 2000. (Cited en page 52.)

[Peletier *et al.* 2007] R. F. Peletier, J. Falcón-Barroso, R. Bacon, M. Cappellari, R. L. Davies, P. T. de Zeeuw, E. Emsellem, K. Ganda, D. Krajnović, H. Kuntschner, R. M. McDermid, M. Sarzi and G. van de Ven. *The SAURON project - XI. Stellar populations from absorption-line strength maps of 24 early-type spirals.* MNRAS, vol. 379, pages 445–468, August 2007. (Cited en page 16.)

[Perlmutter *et al.* 1999] S. Perlmutter, G. Aldering, G. Goldhaber, R. A. Knop, P. Nugent, P. G. Castro, S. Deustua, S. Fabbro, A. Goobar, D. E. Groom, I. M. Hook, A. G. Kim, M. Y. Kim, J. C. Lee, N. J. Nunes, R. Pain, C. R. Pennypacker, R. Quimby, C. Lidman, R. S. Ellis, M. Irwin, R. G. McMahon, P. Ruiz-Lapuente, N. Walton, B. Schaefer, B. J. Boyle, A. V. Filippenko, T. Matheson, A. S. Fruchter, N. Panagia, H. J. M. Newberg, W. J. Couch and T. S. C. Project. *Measurements of Ω and Λ from 42 High-Redshift Supernovae.* ApJ, vol. 517, pages 565–586, June 1999. (Cited en page 6.)

[Perryman *et al.* 1997] M. A. C. Perryman, L. Lindegren, J. Kovalevsky, E. Hoeg, U. Bastian, P. L. Bernacca, M. Crézé, F. Donati, M. Grenon, M. Grewing, F. van Leeuwen, H. van der Marel, F. Mignard, C. A. Murray, R. S. Le Poole, H. Schrijver, C. Turon, F. Arenou, M. Froeschlé and C. S. Petersen. *The HIPPARCOS Catalogue.* A&A, vol. 323, July 1997. (Cited en page 34.)

[Perryman *et al.* 2001] M. A. C. Perryman, K. S. de Boer, G. Gilmore, E. Høg, M. G. Lattanzi, L. Lindegren, X. Luri, F. Mignard, O. Pace and P. T. de Zeeuw. *GAIA: Composition, formation and evolution of the Galaxy.* A&A, vol. 369, pages 339–363, April 2001. (Cited en page 34.)

[Planck Collaboration *et al.* 2015] Planck Collaboration, P. A. R. Ade, N. Aghanim, M. Arnaud, M. Ashdown, J. Aumont, C. Baccigalupi, A. J. Banday, R. B. Barreiro, J. G. Bartlett and et al. *Planck 2015 results. XIII. Cosmological parameters.* ArXiv e-prints, February 2015. (Cited en page 6.)

[Prugniel *et al.* 2001] P. Prugniel, G. Maubon and F. Simien. *The formation of galaxy bulges: Spectrophotometric constraints.* A&A, vol. 366, pages 68–82, January 2001. (Cited en page 16.)

[Raha *et al.* 1991] N. Raha, J. A. Sellwood, R. A. James and F. D. Kahn. *A dynamical instability of bars in disk galaxies.* Nature, vol. 352, page 411, August 1991. (Cited en page 16.)

[Ramírez *et al.* 2000] S. V. Ramírez, A. W. Stephens, J. A. Frogel and D. L. DePoy. *Metallicity of Red Giants in the Galactic Bulge from Near-Infrared Spectroscopy.* AJ, vol. 120, pages 833–844, August 2000. (Cited en pages 17, 18 et 19.)

[Rattenbury *et al.* 2007] N. J. Rattenbury, S. Mao, T. Sumi and M. C. Smith. *Modelling the Galactic bar using OGLE-II red clump giant stars.* MNRAS, vol. 378, pages 1064–1078, July 2007. (Cited en page 22.)

[Recio-Blanco *et al.* 2006] A. Recio-Blanco, A. Bijaoui and P. de Laverny. *Automated derivation of stellar atmospheric parameters and chemical abundances: the MATISSE algorithm.* MNRAS, vol. 370, pages 141–150, July 2006. (Cited en pages 55 et 165.)

[Recio-Blanco *et al.* 2014] A. Recio-Blanco, P. de Laverny, G. Kordopatis, A. Helmi, V. Hill, G. Gilmore, R. Wyse, V. Adibekyan, S. Randich, M. Asplund, S. Feltzing, R. Jeffries, G. Micela, A. Vallenari, E. Alfaro, C. Allende Prieto, T. Bensby, A. Bragaglia, E. Flaccomio, S. E. Koposov, A. Korn, A. Lanzafame, E. Pancino, R. Smiljanic, R. Jackson, J. Lewis, L. Magrini, L. Morbidelli, L. Prisinzano, G. Sacco, C. C. Worley, A. Hourihane, M. Bergemann, M. T. Costado, U. Heiter, P. Joffre, C. Lardo, K. Lind and E. Maiorca. *The Gaia-ESO Survey: the Galactic thick to thin disc transition.* A&A, vol. 567, page A5, July 2014. (Cited en pages 8, 30, 31, 32, 33, 83, 107 et 146.)

[Recio-Blanco *et al.* 2016] A. Recio-Blanco, P. de Laverny, C. Allende Prieto, D. Fustes, M. Manteiga, B. Arcay, A. Bijaoui, C. Dafonte, C. Ordenovic and D. Ordoñez Blanco. *Stellar parametrization from Gaia RVS spectra.* A&A, vol. 585, page A93, January 2016. (Cited en page 37.)

[Reddy *et al.* 2006] B. E. Reddy, D. L. Lambert and C. Allende Prieto. *Elemental abundance survey of the Galactic thick disc.* MNRAS, vol. 367, pages 1329–1366, April 2006. (Cited en pages 18, 25 et 30.)

[Rich & Origlia 2005] R. M. Rich and L. Origlia. *The First Detailed Abundances for M Giants in Baade's Window from Infrared Spectroscopy.* ApJ, vol. 634, pages 1293–1299, December 2005. (Cited en page 24.)

[Rich *et al.* 2007a] R. M. Rich, L. Origlia and E. Valenti. *The First Detailed Abundances for M Giants in the Inner Bulge from Infrared Spectroscopy.* ApJ, vol. 665, pages L119–L122, August 2007. (Cited en pages 19 et 141.)

[Rich *et al.* 2007b] R. M. Rich, D. B. Reitzel, C. D. Howard and H. Zhao. *The Bulge Radial Velocity Assay: Techniques and a Rotation Curve.* ApJ, vol. 658, pages L29–L32, March 2007. (Cited en pages 22 et 130.)

[Rich *et al.* 2012] R. M. Rich, L. Origlia and E. Valenti. *Detailed Abundances for M Giants in Two Inner Bulge Fields from Infrared Spectroscopy.* ApJ, vol. 746, page 59, February 2012. (Cited en pages 19 et 141.)

[Rich 1988] R. M. Rich. *Spectroscopy and abundances of 88 K giants in Baade's Window.* AJ, vol. 95, pages 828–865, March 1988. (Cited en page 18.)

[Rieke & Lebofsky 1985] G. H. Rieke and M. J. Lebofsky. *The interstellar extinction law from 1 to 13 microns.* ApJ, vol. 288, pages 618–621, January 1985. (Cited en page 50.)

[Robotham *et al.* 2012] A. S. G. Robotham, I. K. Baldry, J. Bland-Hawthorn, S. P. Driver, J. Loveday, P. Norberg, A. E. Bauer, K. Bekki, S. Brough, M. Brown, A. Graham, A. M. Hopkins, S. Phillipps, C. Power, A. Sansom and L. Staveley-Smith. *Galaxy And Mass Assembly (GAMA): in search of Milky Way Magellanic Cloud analogues.* MNRAS, vol. 424, pages 1448–1453, August 2012. (Cited en page 7.)

[Rodriguez-Fernandez & Combes 2008] N. J. Rodriguez-Fernandez and F. Combes. *Gas flow models in the Milky Way embedded bars.* A&A, vol. 489, pages 115–133, October 2008. (Cited en page 21.)

[Rojas-Arriagada *et al.* 2014] A. Rojas-Arriagada, A. Recio-Blanco, V. Hill, P. de Laverny, M. Schultheis, C. Babusiaux, M. Zoccali, D. Minniti, O. A. Gonzalez, S. Feltzing, G. Gilmore, S. Randich, A. Vallenari, E. J. Alfaro, T. Bensby, A. Bragaglia, E. Flaccomio, A. C. Lanzafame, E. Pancino, R. Smiljanic, M. Bergemann, M. T. Costado, F. Damiani, A. Hourihane, P. Jofré, C. Lardo, L. Magrini, E. Maiorca, L. Morbidelli, L. Sbordone, C. C. Worley, S. Zaggia and R. Wyse. *The Gaia-ESO Survey: metallicity and kinematic trends in the Milky Way bulge.* A&A, vol. 569, page A103, September 2014. (Cited en pages 114 et 165.)

[Rojas-Arriagada *et al.* 2016a] A. Rojas-Arriagada, A. Recio-Blanco, P. de Laverny, M. Schultheis, G. Guiglion, Š. Mikolaitis, G. Kordopatis, V. Hill, G. Gilmore, S. Randich, E. J. Alfaro, T. Bensby, S. E. Koposov, M. T. Costado, E. Franciosini, A. Hourihane, P. Jofré, C. Lardo, J. Lewis, K. Lind, L. Magrini, L. Monaco, L. Morbidelli, G. G. Sacco, C. C. Worley, S. Zaggia and C. Chiappini.

The Gaia-ESO Survey: Separating disk chemical substructures with cluster models. Evidence of a separate evolution in the metal-poor thin disk. A&A, vol. 586, page A39, February 2016. (Cited en page 114.)

[Rojas-Arriagada *et al.* 2016b] A. Rojas-Arriagada, M. Zoccali, S. Vásquez, V. Ripepi, I. Musella, M. Marconi, A. Grado and L. Limatola. *High resolution spectroscopic analysis of seven giants in the bulge globular cluster NGC 6723.* A&A, vol. 587, page A95, March 2016. (Cited en pages 25 et 26.)

[Ruchti *et al.* 2011] G. R. Ruchti, J. P. Fulbright, R. F. G. Wyse, G. F. Gilmore, O. Bienaymé, J. Bland-Hawthorn, B. K. Gibson, E. K. Grebel, A. Helmi, U. Munari, J. F. Navarro, Q. A. Parker, W. Reid, G. M. Seabroke, A. Siebert, A. Siviero, M. Steinmetz, F. G. Watson, M. Williams and T. Zwitter. *Observational Properties of the Metal-poor Thick Disk of the Milky Way and Insights into its Origins.* ApJ, vol. 737, page 9, August 2011. (Cited en pages 69 et 84.)

[Ruchti *et al.* 2015] G. R. Ruchti, J. I. Read, S. Feltzing, A. M. Serenelli, P. McMillan, K. Lind, T. Bensby, M. Bergemann, M. Asplund, A. Vallenari, E. Flaccomio, E. Pancino, A. J. Korn, A. Recio-Blanco, A. Bayo, G. Carraro, M. T. Costado, F. Damiani, U. Heiter, A. Hourihane, P. Jofré, G. Kordopatis, C. Lardo, P. de Laverny, L. Monaco, L. Morbidelli, L. Sbordone, C. C. Worley and S. Zaggia. *The Gaia-ESO Survey: a quiescent Milky Way with no significant dark/stellar accreted disc.* MNRAS, vol. 450, pages 2874–2887, July 2015. (Cited en pages 109 et 111.)

[Sadler *et al.* 1996] E. M. Sadler, R. M. Rich and D. M. Terndrup. *K Giants in Baade's Window. II. The Abundance Distribution.* AJ, vol. 112, page 171, July 1996. (Cited en pages 17 et 18.)

[Saito *et al.* 2011] R. K. Saito, M. Zoccali, A. McWilliam, D. Minniti, O. A. Gonzalez and V. Hill. *Mapping the X-shaped Milky Way Bulge.* AJ, vol. 142, page 76, September 2011. (Cited en page 21.)

[Saito *et al.* 2012] R. K. Saito, M. Hempel, D. Minniti, P. W. Lucas, M. Rejkuba, I. Toledo, O. A. Gonzalez, J. Alonso-García, M. J. Irwin, E. Gonzalez-Solares, S. T. Hodgkin, J. R. Lewis, N. Cross, V. D. Ivanov, E. Kerins, J. P. Emerson, M. Soto, E. B. Amôres, S. Gurovich, I. Dékány, R. Angeloni, J. C. Beamin, M. Catelan, N. Padilla, M. Zoccali, P. Pietrukowicz, C. Moni Bidin, F. Mauro, D. Geisler, S. L. Folkes, S. E. Sale, J. Borissova, R. Kurtev, A. V. Ahumada, M. V. Alonso, A. Adamson, J. I. Arias, R. M. Bandyopadhyay, R. H. Barbá, B. Barbuy, G. L. Baume, L. R. Bedin, A. Bellini, R. Benjamin, E. Bica, C. Bonatto, L. Bronfman, G. Carraro, A. N. Chenè, J. J. Clariá, J. R. A. Clarke, C. Contreras, A. Corvillón, R. de Grijs, B. Dias, J. E. Drew, C. Fariña, C. Feinstein, E. Fernández-Lajús, R. C. Gamen, W. Gieren, B. Goldman, C. González-Fernández, R. J. J. Grand, G. Gunthardt, N. C. Hambly, M. M. Hanson, K. G. Hełminiak, M. G. Hoare, L. Huckvale, A. Jordán, K. Kinemuchi, A. Longmore, M. López-Corredoira, T. Maccarone, D. Majaess, E. L. Martín, N. Masetti, R. E.

Mennickent, I. F. Mirabel, L. Monaco, L. Morelli, V. Motta, T. Palma, M. C. Parisi, Q. Parker, F. Peñaloza, G. Pietrzyński, G. Pignata, B. Popescu, M. A. Read, A. Rojas, A. Roman-Lopes, M. T. Ruiz, I. Saviane, M. R. Schreiber, A. C. Schröder, S. Sharma, M. D. Smith, L. Sodré, J. Stead, A. W. Stephens, M. Tamura, C. Tappert, M. A. Thompson, E. Valenti, L. Vanzi, N. A. Walton, W. Weidmann and A. Zijlstra. *VVV DR1: The first data release of the Milky Way bulge and southern plane from the near-infrared ESO public survey VISTA variables in the Vía Láctea.* A&A, vol. 537, page A107, January 2012. (Cited en pages 43 et 44.)

[Samland & Gerhard 2003] M. Samland and O. E. Gerhard. *The formation of a disk galaxy within a growing dark halo.* A&A, vol. 399, no. 3, pages 961–982, March 2003. (Cited en pages 17 et 160.)

[Scannapieco & Tissera 2003] C. Scannapieco and P. B. Tissera. *The effects of mergers on the formation of disc-bulge systems in hierarchical clustering scenarios.* MNRAS, vol. 338, pages 880–890, February 2003. (Cited en page 15.)

[Scannapieco *et al.* 2012] C. Scannapieco, M. Wadepuhl, O. H. Parry, J. F. Navarro, A. Jenkins, V. Springel, R. Teyssier, E. Carlson, H. M. P. Couchman, R. A. Crain, C. Dalla Vecchia, C. S. Frenk, C. Kobayashi, P. Monaco, G. Murante, T. Okamoto, T. Quinn, J. Schaye, G. S. Stinson, T. Theuns, J. Wadsley, S. D. M. White and R. Woods. *The Aquila comparison project: the effects of feedback and numerical methods on simulations of galaxy formation.* MNRAS, vol. 423, pages 1726–1749, June 2012. (Cited en page 7.)

[Schaller *et al.* 1992] G. Schaller, D. Schaerer, G. Meynet and A. Maeder. *New grids of stellar models from 0.8 to 120 solar masses at Z = 0.020 and Z = 0.001.* A&AS, vol. 96, pages 269–331, December 1992. (Cited en page 10.)

[Schlegel *et al.* 1998] D. J. Schlegel, D. P. Finkbeiner and M. Davis. *Maps of Dust Infrared Emission for Use in Estimation of Reddening and Cosmic Microwave Background Radiation Foregrounds.* ApJ, vol. 500, page 525, June 1998. (Cited en pages 49, 114 et 115.)

[Schultheis *et al.* 2015] M. Schultheis, G. Kordopatis, A. Recio-Blanco, P. de Laverny, V. Hill, G. Gilmore, E. J. Alfaro, M. T. Costado, T. Bensby, F. Damiani, S. Feltzing, E. Flaccomio, C. Lardo, P. Jofre, L. Prisinzano, S. Zaggia, F. Jimenez-Esteban, L. Morbidelli, A. C. Lanzafame, A. Hourihane, C. Worley and P. Francois. *The Gaia-ESO Survey: Tracing interstellar extinction.* A&A, vol. 577, page A77, May 2015. (Cited en page 89.)

[Sesar *et al.* 2011] B. Sesar, M. Jurić and Ž. Ivezić. *The Shape and Profile of the Milky Way Halo as Seen by the Canada-France-Hawaii Telescope Legacy Survey.* ApJ, vol. 731, page 4, April 2011. (Cited en page 9.)

[Shen *et al.* 2010] J. Shen, R. M. Rich, J. Kormendy, C. D. Howard, R. De Propris and A. Kunder. *Our Milky Way as a Pure-disk Galaxy: A Challenge for Galaxy*

Formation. ApJ, vol. 720, pages L72–L76, September 2010. (Cited en pages 21, 22, 34, 130, 143 et 151.)

[Sheth *et al.* 2008] K. Sheth, D. M. Elmegreen, B. G. Elmegreen, P. Capak, R. G. Abraham, E. Athanassoula, R. S. Ellis, B. Mobasher, M. Salvato, E. Schinnerer, N. Z. Scoville, L. Spalsbury, L. Strubbe, M. Carollo, M. Rich and A. A. West. *Evolution of the Bar Fraction in COSMOS: Quantifying the Assembly of the Hubble Sequence.* ApJ, vol. 675, pages 1141–1155, March 2008. (Cited en page 16.)

[Sheth *et al.* 2012] K. Sheth, J. Melbourne, D. M. Elmegreen, B. G. Elmegreen, E. Athanassoula, R. G. Abraham and B. J. Weiner. *Hot Disks and Delayed Bar Formation.* ApJ, vol. 758, page 136, October 2012. (Cited en page 16.)

[Sjouwerman *et al.* 1998] L. O. Sjouwerman, H. J. van Langevelde, A. Winnberg and H. J. Habing. *A new sample of OH/IR stars in the Galactic center.* A&AS, vol. 128, pages 35–65, February 1998. (Cited en page 29.)

[Snaith *et al.* 2015] O. Snaith, M. Haywood, P. Di Matteo, M. D. Lehnert, F. Combes, D. Katz and A. Gómez. *Reconstructing the star formation history of the Milky Way disc(s) from chemical abundances.* A&A, vol. 578, page A87, June 2015. (Cited en pages 33 et 100.)

[Sneden *et al.* 2008] C. Sneden, J. J. Cowan and R. Gallino. *Neutron-Capture Elements in the Early Galaxy.* ARA&A, vol. 46, pages 241–288, September 2008. (Cited en pages 12 et 157.)

[Soubiran *et al.* 2003] C. Soubiran, O. Bienaymé and A. Siebert. *Vertical distribution of Galactic disk stars. I. Kinematics and metallicity.* A&A, vol. 398, pages 141–151, January 2003. (Cited en page 31.)

[Steinmetz *et al.* 2006] M. Steinmetz, T. Zwitter, A. Siebert, F. G. Watson, K. C. Freeman, U. Munari, R. Campbell, M. Williams, G. M. Seabroke, R. F. G. Wyse, Q. A. Parker, O. Bienaymé, S. Roeser, B. K. Gibson, G. Gilmore, E. K. Grebel, A. Helmi, J. F. Navarro, D. Burton, C. J. P. Cass, J. A. Dawe, K. Fiegert, M. Hartley, K. S. Russell, W. Saunders, H. Enke, J. Bailin, J. Binney, J. Bland-Hawthorn, C. Boeche, W. Dehnen, D. J. Eisenstein, N. W. Evans, M. Fiorucci, J. P. Fulbright, O. Gerhard, U. Jauregi, A. Kelz, L. Mijović, I. Minchev, G. Parmentier, J. Peñarrubia, A. C. Quillen, M. A. Read, G. Ruchti, R.-D. Scholz, A. Siviero, M. C. Smith, R. Sordo, L. Veltz, S. Vidrih, R. von Berlepsch, B. J. Boyle and E. Schilbach. *The Radial Velocity Experiment (RAVE): First Data Release.* AJ, vol. 132, pages 1645–1668, October 2006. (Cited en page 30.)

[Stonkutė *et al.* 2016] E. Stonkutė, S. E. Koposov, L. M. Howes, S. Feltzing, C. C. Worley, G. Gilmore, G. R. Ruchti, G. Kordopatis, S. Randich, T. Zwitter, T. Bensby, A. Bragaglia, R. Smiljanic, M. T. Costado, G. Tautvaišienė, A. R. Casey, A. J. Korn, A. C. Lanzafame, E. Pancino, E. Franciosini, A. Hourihane, P. Jofré, C. Lardo, J. Lewis, L. Magrini, L. Monaco, L. Morbidelli, G. G. Sacco and

L. Sbordone. *The Gaia-ESO Survey: the selection function of the Milky Way field stars.* MNRAS, April 2016. (Cited en pages 49, 50 et 54.)

[Tinsley 1976] B. M. Tinsley. *Chemical evolution in the solar neighborhood. II - Statistical constraints, finite stellar lifetimes, and inhomogeneities.* ApJ, vol. 208, pages 797–811, September 1976. (Cited en page 12.)

[Trevisan *et al.* 2011] M. Trevisan, B. Barbuy, K. Eriksson, B. Gustafsson, M. Grenon and L. Pompéia. *Analysis of old very metal rich stars in the solar neighbourhood.* A&A, vol. 535, page A42, November 2011. (Cited en page 103.)

[Tsikoudi 1979] V. Tsikoudi. *Photometry and structure of lenticular galaxies. I - NGC 3115.* ApJ, vol. 234, pages 842–853, December 1979. (Cited en page 9.)

[Tumlinson 2010] J. Tumlinson. *Chemical Evolution in Hierarchical Models of Cosmic Structure. II. The Formation of the Milky Way Stellar Halo and the Distribution of the Oldest Stars.* ApJ, vol. 708, pages 1398–1418, January 2010. (Cited en page 52.)

[Uttenthaler *et al.* 2012] S. Uttenthaler, M. Schultheis, D. M. Nataf, A. C. Robin, T. Lebzelter and B. Chen. *Constraining the structure and formation of the Galactic bulge from a field in its outskirts. FLAMES-GIRAFFE spectra of about 400 red giants around (l, b) = (0°, -10°).* A&A, vol. 546, page A57, October 2012. (Cited en pages 19, 131, 139 et 140.)

[Valenti & Piskunov 1996] J. A. Valenti and N. Piskunov. *Spectroscopy made easy: A new tool for fitting observations with synthetic spectra.* A&AS, vol. 118, pages 595–603, September 1996. (Cited en page 55.)

[Valenti *et al.* 2013] E. Valenti, M. Zoccali, A. Renzini, T. M. Brown, O. A. Gonzalez, D. Minniti, V. P. Debattista and L. Mayer. *Stellar ages through the corners of the boxy bulge.* A&A, vol. 559, page A98, November 2013. (Cited en pages 10 et 28.)

[Valenti *et al.* 2015] E. Valenti, M. Zoccali, O. A. Gonzalez, D. Minniti, J. Alonso-Garcia, E. Marchetti, M. Hempel, A. Renzini and M. Rejkuba. *Stellar density profile and mass of the Milky Way Bulge from VVV data.* ArXiv e-prints, October 2015. (Cited en pages 14 et 143.)

[van den Hoek & Groenewegen 1997] L. B. van den Hoek and M. A. T. Groenewegen. *New theoretical yields of intermediate mass stars.* A&AS, vol. 123, June 1997. (Cited en page 144.)

[Van der Swaelmen *et al.* 2016] M. Van der Swaelmen, B. Barbuy, V. Hill, M. Zoccali, D. Minniti, S. Ortolani and A. Gómez. *Heavy elements Ba, La, Ce, Nd, and Eu in 56 Galactic bulge red giants.* A&A, vol. 586, page A1, February 2016. (Cited en pages 157 et 158.)

[van Leeuwen 2007] F. van Leeuwen. *Validation of the new Hipparcos reduction.* A&A, vol. 474, pages 653–664, November 2007. (Cited en page 74.)

[van Loon *et al.* 2003] J. T. van Loon, G. F. Gilmore, A. Omont, J. A. D. L. Blommaert, I. S. Glass, M. Messineo, F. Schuller, M. Schultheis, I. Yamamura and H. S. Zhao. *Infrared stellar populations in the central parts of the Milky Way galaxy.* MNRAS, vol. 338, pages 857–879, February 2003. (Cited en page 29.)

[Vanhollebeke *et al.* 2006] E. Vanhollebeke, J. A. D. L. Blommaert, M. Schultheis, B. Aringer and A. Lançon. *Near-IR spectroscopy of OH/IR stars in the Galactic centre.* A&A, vol. 455, pages 645–652, August 2006. (Cited en page 29.)

[Vásquez *et al.* 2013] S. Vásquez, M. Zoccali, V. Hill, A. Renzini, O. A. González, E. Gardner, V. P. Debattista, A. C. Robin, M. Rejkuba, M. Baffico, M. Monelli, V. Motta and D. Minniti. *3D kinematics through the X-shaped Milky Way bulge.* A&A, vol. 555, page A91, July 2013. (Cited en page 131.)

[Wegg & Gerhard 2013] C. Wegg and O. Gerhard. *Mapping the three-dimensional density of the Galactic bulge with VVV red clump stars.* MNRAS, vol. 435, pages 1874–1887, November 2013. (Cited en pages v, 21, 22, 23 et 125.)

[Weiland *et al.* 1994] J. L. Weiland, R. G. Arendt, G. B. Berriman, E. Dwek, H. T. Freudenreich, M. G. Hauser, T. Kelsall, C. M. Lisse, M. Mitra, S. H. Moseley, N. P. Odegard, R. F. Silverberg, T. J. Sodroski, W. J. Spiesman and S. W. Stemwedel. *COBE diffuse infrared background experiment observations of the galactic bulge.* ApJ, vol. 425, pages L81–L84, April 1994. (Cited en page 21.)

[Weinberg 1992] M. D. Weinberg. *Detection of a large-scale stellar bar in the Milky Way.* ApJ, vol. 384, pages 81–94, January 1992. (Cited en page 21.)

[Whitelock & Catchpole 1992] P. Whitelock and R. Catchpole. *The shape of the bulge from IRAS Miras.* In L. Blitz, editeur, The Center, Bulge, and Disk of the Milky Way, volume 180 of *Astrophysics and Space Science Library*, pages 103–110, 1992. (Cited en page 21.)

[Whitelock *et al.* 1991] P. Whitelock, M. Feast and R. Catchpole. *IRAS sources and the nature of the Galactic Bulge.* MNRAS, vol. 248, pages 276–312, January 1991. (Cited en page 29.)

[Whitford & Rich 1983] A. E. Whitford and R. M. Rich. *Metal content of K giants in the nuclear bulge of the galaxy.* ApJ, vol. 274, pages 723–732, November 1983. (Cited en page 18.)

[Williams *et al.* 2011] M. J. Williams, M. A. Zamojski, M. Bureau, H. Kuntschner, M. R. Merrifield, P. T. de Zeeuw and K. Kuijken. *The stellar kinematics and populations of boxy bulges: cylindrical rotation and vertical gradients.* MNRAS, vol. 414, pages 2163–2172, July 2011. (Cited en page 160.)

[Woosley & Weaver 1995] S. E. Woosley and T. A. Weaver. *The Evolution and Explosion of Massive Stars. II. Explosive Hydrodynamics and Nucleosynthesis.* ApJS, vol. 101, page 181, November 1995. (Cited en page 144.)

[Yanny *et al.* 2009] B. Yanny, C. Rockosi, H. J. Newberg, G. R. Knapp, J. K. Adelman-McCarthy, B. Alcorn, S. Allam, C. Allende Prieto, D. An, K. S. J. Anderson, S. Anderson, C. A. L. Bailer-Jones, S. Bastian, T. C. Beers, E. Bell, V. Belokurov, D. Bizyaev, N. Blythe, J. J. Bochanski, W. N. Boroski, J. Brinchmann, J. Brinkmann, H. Brewington, L. Carey, K. M. Cudworth, M. Evans, N. W. Evans, E. Gates, B. T. Gänsicke, B. Gillespie, G. Gilmore, A. Nebot Gomez-Moran, E. K. Grebel, J. Greenwell, J. E. Gunn, C. Jordan, W. Jordan, P. Harding, H. Harris, J. S. Hendry, D. Holder, I. I. Ivans, Ž. Ivezič, S. Jester, J. A. Johnson, S. M. Kent, S. Kleinman, A. Kniazev, J. Krzesinski, R. Kron, N. Kuropatkin, S. Lebedeva, Y. S. Lee, R. French Leger, S. Lépine, S. Levine, H. Lin, D. C. Long, C. Loomis, R. Lupton, O. Malanushenko, V. Malanushenko, B. Margon, D. Martinez-Delgado, P. McGehee, D. Monet, H. L. Morrison, J. A. Munn, E. H. Neilsen Jr., A. Nitta, J. E. Norris, D. Oravetz, R. Owen, N. Padmanabhan, K. Pan, R. S. Peterson, J. R. Pier, J. Platson, P. Re Fiorentin, G. T. Richards, H.-W. Rix, D. J. Schlegel, D. P. Schneider, M. R. Schreiber, A. Schwope, V. Sibley, A. Simmons, S. A. Snedden, J. Allyn Smith, L. Stark, F. Stauffer, M. Steinmetz, C. Stoughton, M. SubbaRao, A. Szalay, P. Szkody, A. R. Thakar, T. Sivarani, D. Tucker, A. Uomoto, D. Vanden Berk, S. Vidrih, Y. Wadadekar, S. Watters, R. Wilhelm, R. F. G. Wyse, J. Yarger and D. Zucker. *SEGUE: A Spectroscopic Survey of 240,000 Stars with g = 14-20.* AJ, vol. 137, pages 4377–4399, May 2009. (Cited en page 30.)

[Yoachim *et al.* 2012] P. Yoachim, R. Roškar and V. P. Debattista. *Spatially Resolved Spectroscopic Star Formation Histories of nearby Disks: Hints of Stellar Migration.* ApJ, vol. 752, page 97, June 2012. (Cited en pages 108, 110 et 111.)

[Yong *et al.* 2012] D. Yong, B. W. Carney and E. D. Friel. *Elemental Abundance Ratios in Stars of the Outer Galactic Disk. IV. A New Sample of Open Clusters.* AJ, vol. 144, page 95, October 2012. (Cited en page 33.)

[Yoshii 1982] Y. Yoshii. *Density Distribution of Faint Stars in the Direction of the North Galactic Pole.* PASJ, vol. 34, page 365, 1982. (Cited en pages 9, 30 et 88.)

[Zasowski *et al.* 2013] G. Zasowski, J. A. Johnson, P. M. Frinchaboy, S. R. Majewski, D. L. Nidever, H. J. Rocha Pinto, L. Girardi, B. Andrews, S. D. Chojnowski, K. M. Cudworth, K. Jackson, J. Munn, M. F. Skrutskie, R. L. Beaton, C. H. Blake, K. Covey, R. Deshpande, C. Epstein, D. Fabbian, S. W. Fleming, D. A. Garcia Hernandez, A. Herrero, S. Mahadevan, S. Mészáros, M. Schultheis, K. Sellgren, R. Terrien, J. van Saders, C. Allende Prieto, D. Bizyaev, A. Burton, K. Cunha, L. N. da Costa, S. Hasselquist, F. Hearty, J. Holtzman, A. E. García Pérez, M. A. G. Maia, R. W. O'Connell, C. O'Donnell, M. Pinsonneault, B. X. Santiago, R. P. Schiavon, M. Shetrone, V. Smith and J. C. Wilson. *Target Selection for the Apache Point Observatory Galactic Evolution Experiment (APOGEE).* AJ, vol. 146, page 81, October 2013. (Cited en pages 89 et 99.)

[Zhao *et al.* 2012] G. Zhao, Y. Zhao, Y. Chu, Y. Jing and L. Deng. *LAMOST Spectral Survey.* ArXiv e-prints, June 2012. (Cited en page 41.)

[Zhao 1996] H. Zhao. *A steady-state dynamical model for the COBE-detected Galactic bar.* MNRAS, vol. 283, pages 149–166, November 1996. (Cited en page 21.)

[Zheng *et al.* 2015] Z. Zheng, D. A. Thilker, T. M. Heckman, G. R. Meurer, W. S. Burgett, K. C. Chambers, M. E. Huber, N. Kaiser, E. A. Magnier, N. Metcalfe, P. A. Price, J. L. Tonry, R. J. Wainscoat and C. Waters. *The Structure and Stellar Content of the Outer Disks of Galaxies: A New View from the Pan-STARRS1 Medium Deep Survey.* ApJ, vol. 800, page 120, February 2015. (Cited en pages 108, 110 et 111.)

[Zoccali & Minniti 2009] M. Zoccali and D. Minniti. *Formation and Evolution of the Galactic Bulge.* In Revista Mexicana de Astronomia y Astrofisica Conference Series, volume 35 of *Revista Mexicana de Astronomia y Astrofisica Conference Series*, pages 85–90, May 2009. (Cited en page 25.)

[Zoccali *et al.* 2003] M. Zoccali, A. Renzini, S. Ortolani, L. Greggio, I. Saviane, S. Cassisi, M. Rejkuba, B. Barbuy, R. M. Rich and E. Bica. *Age and metallicity distribution of the Galactic bulge from extensive optical and near-IR stellar photometry.* A&A, vol. 399, pages 931–956, March 2003. (Cited en pages v, 17, 18, 27, 28 et 142.)

[Zoccali *et al.* 2006] M. Zoccali, A. Lecureur, B. Barbuy, V. Hill, A. Renzini, D. Minniti, Y. Momany, A. Gómez and S. Ortolani. *Oxygen abundances in the Galactic bulge: evidence for fast chemical enrichment.* A&A, vol. 457, pages L1–L4, October 2006. (Cited en pages 24, 25, 127 et 146.)

[Zoccali *et al.* 2008] M. Zoccali, V. Hill, A. Lecureur, B. Barbuy, A. Renzini, D. Minniti, A. Gómez and S. Ortolani. *The metal content of bulge field stars from FLAMES-GIRAFFE spectra. I. Stellar parameters and iron abundances.* A&A, vol. 486, pages 177–189, July 2008. (Cited en pages v, 18, 19, 20, 58, 114, 119, 124, 138, 139, 140, 141, 169 et 170.)

[Zoccali *et al.* 2014] M. Zoccali, O. A. Gonzalez, S. Vasquez, V. Hill, M. Rejkuba, E. Valenti, A. Renzini, A. Rojas-Arriagada, I. Martinez-Valpuesta, C. Babusiaux, T. Brown, D. Minniti and A. McWilliam. *The GIRAFFE Inner Bulge Survey (GIBS). I. Survey description and a kinematical map of the Milky Way bulge.* A&A, vol. 562, page A66, February 2014. (Cited en page 130.)

[Zwitter *et al.* 2010] T. Zwitter, G. Matijevič, M. A. Breddels, M. C. Smith, A. Helmi, U. Munari, O. Bienaymé, J. Binney, J. Bland-Hawthorn, C. Boeche, A. G. A. Brown, R. Campbell, K. C. Freeman, J. Fulbright, B. Gibson, G. Gilmore, E. K. Grebel, J. F. Navarro, Q. A. Parker, G. M. Seabroke, A. Siebert, A. Siviero, M. Steinmetz, F. G. Watson, M. Williams and R. F. G. Wyse. *Distance determination for RAVE stars using stellar models . II. Most likely values assuming a standard stellar evolution scenario.* A&A, vol. 522, page A54, November 2010. (Cited en pages 69 et 84.)